Ultrafast Spin Dynamics in Ferromagnetic Patterned Nanostructures and Multilayers

Thesis submitted for the degree of

Doctor of Philosophy (Science)

in

Physics (Experimental)

by

Anulekha De

Department of Physics

University of Calcutta

2021

Dedicated to my parents

Mr. Nirmallya Kumar De & Mrs. Krishna De

Abstract

The objectives of the thesis are to investigate the spin-wave (SW) dynamics in ferromagnetic patterned nanostructures and multilayers. We have employed time-resolved magneto-optical Kerr effect (TR-MOKE) and Brillouin light scattering (BLS) techniques to measure the SW dynamics. The experimental results have been modelled by analytical calculations and numerical simulations. The magnonic band structure has been investigated in a binary magnonic crystal in the form of diatomic nanodot array (dipolar-coupled $Ni_{80}Fe_{20}$ nanodots forming a complex double dot basis). A strong anisotropy in the SW dispersion has been observed, which is evident in the iso-frequency curves. We have investigated the ultrafast magnetization dynamics in antidot MCs ($Ni_{80}Fe_{20}$) with complex geometry. The most densely packed hexagonal lattice shows a strong six-fold rotational anisotropy encased with a weak three-fold anisotropy. The quasiperiodic octagonal lattice lacking translation symmetry, along with a complex triangular antidot basis lacking reflection symmetry, exhibits a strong eight-fold rotational anisotropy superposed with a weak three-fold anisotropy. The most primitive square lattice exhibits a strong four-fold rotational anisotropy superposed with a weak three-fold anisotropy. A mode conversion from extended to quantized one and vice versa has been observed with the in-plane bias field orientation. The ultrafast demagnetization in perpendicular magnetic anisotropy (PMA) synthetic antiferromagnets (SAF) comprised of [Co/Pt] multilayers separated by Ru or Ir spacers showed that the spin-transport (ST) of optically excited carriers can have a significant contribution to the ultrafast demagnetization, in addition to spin-flip scattering (SFS) processes. The individual mechanisms can be controlled by specially designing the samples and altering the bias field and excitation fluence. The anisotropic variation of SW dynamics in diamond shaped antidots patterned on PMA [Co/Pd] multilayers has been studied, where in-plane domain structures are formed in narrow shell regions around the antidots due to the Ga+ ion irradiation during the focused ion beam (FIB) milling process of antidot fabrication. The magnetoelastic coupling between surface acoustic waves (SAWs) and SWs in Co nanomagnet array fabricated on $LiNbO_3$ substrate has been observed to selectively stimulate intrinsic SW modes and generate new extrinsic modes, without any bias magnetic field. These observations are important for future spintronic devices.

List of Publications

Included in the Thesis

1. "*Investigation of magnetization dynamics in two dimensional $Ni_{80}Fe_{20}$ diatomic nanodot arrays*"

   A. De, S. Mondal, C. Banerjee, A. K. Chaurasiya, R. Mandal, Y. Otani, R. K. Mitra, and A. Barman

   Journal of Physics D: Applied Physics, 50, 385002 (2017).

2. "*Field-controlled ultrafast magnetization dynamics in two-dimensional nanoscale ferromagnetic antidot arrays*"

   A. De, S. Mondal, S. Sahoo, S. Barman, Y. Otani, R. K. Mitra, and A.Barman

   Beilstein Journal of Nanotechnology, 9, 1123 (2018).

3. "*Shape dependent high frequency spin-wave dynamics in nanoscale magnonic crystals*"

   A. De, S. Mondal, S. Choudhury, S. Sahoo, S. Majumder, S. Barman, Y. Otani, and A. Barman

   Journal of Magnetism and Magnetic Materials, 487, 165263 (2019).

4. "*Anisotropic Spin-Wave Dispersion in two dimensional $Ni_{80}Fe_{20}$ diatomic nanodot arrays*"

   A. De, C. Banerjee, A. K. Chaurasiya, R. Mandal, Y. Otani, R. K. Mitra, and A. Barman,

   Journal of Magnetism and Magnetic Materials, 491, 165557 (2019).

5. "*Extreme Subwavelength Magnetoelastic Electromagnetic Antenna Implemented with Multiferroic Nanomagnets*"

   J. L. Drobitch, **A. De**, K. Dutta, P. K. Pal, A. Adhikari, A. Barman, and S. Bandyopadhyay,

   Advanced Materials Technologies, 5, 2000316 (2020).

6. "*Magnonic Crystals with complex geometry*"

   A. De, K. Dutta, S. Mondal, S. Barman, Y. Otani, and A. Barman

   Physical Review B, 103, 064402 (2021).

7. "*Magnetic Configuration Driven Femtosecond Spin Dynamics in Synthetic Antiferromagnets*",

   A. De, S. S. P. K. Arekapudi, L. Koch, F. Samad, S. N. Panda, B. Böhm, O. Hellwig, and A. Barman

   (*Manuscript Submitted*).

8. "*Resonant Amplification of Intrinsic Magnon Modes and Generation of New Extrinsic Modes in a Two-Dimensional Array of Interacting Multiferroic Nanomagnets by Surface Acoustic Waves*"

   A. De, J. L. Drobitch, S. Barman, S. Bandyopadhyay, and A. Barman

   (*Submitted*).

9. "*Anisotropic Variation of the Spin-Wave Dynamics in Antidot Lattices on $[Co/Pd]_8$ Multilayers with Perpendicular Magnetic Anisotropy*"

   A. De, S. Sahoo, S. Pal, O. Hellwig, and A. Barman

   (*Submitted*).

Relevant Publications Not Included in the Thesis

10. "*All optical detection of picosecond spin-wave dynamics in 2D annular antidot lattice*"

    N. Porwal, S. Mondal, S. Choudhury, **A. De**, J. Sinha, A. Barman and P. K. Datta

    Journal of Physics D: Applied Physics, 51, 055004 (2018).

11. "*Hybrid Magnetodynamical Modes in a Single Magnetostrictive Nanomagnet on a Piezoelectric Substrate Arising from Magnetoelastic Modulation of Precessional Dynamics*"

    S. Mondal, M. A. Abeed, K. Dutta, **A. De**, S. Sahoo, A. Barman, and S. Bandyopadhyay

    ACS Applied Materials and Interfaces, 10, 43970 (2018).

12. "*Observation of angle dependent mode conversion and mode hopping in 2D annular antidot lattices*"

    N. Porwal, **A. De**, S. Mondal, K. Dutta, S. Choudhury, J. Sinha, A. Barman and P. K. Datta

    Scientific Reports, 9, 12138 (2019).

13. "*Magnetization dynamics of nanoscale magnetic materials: A perspective*"

    A. Barman, S. Mondal, S. Sahoo and **A. De**

    Journal of Applied Physics, 128, 170901 (2020).

14. "*Ultrafast Magnetization Dynamics in Diamond Antidot Lattices Supporting Spin-Wave Nanochannels*"

    K. Dutta, **A. De,** S. Barman, Y. Otani, and A. Barman

    (*To be submitted*)

Book Chapters

1. "Tunable picosecond magnetization dynamics in ferromagnetic nanostructures"

   S. Choudhury, S. Mondal, **A. De** and A. Barman

   21st century Nanoscience - A Handbook: Exotic Nanostructures and Quantum Systems (Volume Five), CRC Press, ISBN 9780815356264 - CAT# K346419 (2020)

Acknowledgements

The journey from being a small-town (Burdwan) girl to become a growing research scholar on the verge of accomplishing PhD is indeed a long and memorable one. There has been a lot of ups and downs during my PhD life. Handling those hurdles successfully has been an inspiring journey that I will remember forever. There are several individuals and groups, without whom, this work would not have been completed and I graciously take this pleasant opportunity to acknowledge all of them.

First and foremost, I express my deepest gratitude and respect to my PhD supervisor, Prof. Anjan Barman, for giving me an opportunity to work under his excellent guidance. I sincerely thank him for his tolerance, insight, patience, for his constant help, encouragement, support and care during all these years, above and beyond the call of duty. He is a perfect combination of positivity, professionalism, discipline and intelligence. He taught me each and every detail of the lab culture, the way of planning new experiments, harnessing new ideas, analyzing data and present the results in extremely scientific manner. He always motivated me to work hard and think independently. He is an extremely helpful person with full of humanity, whom I can trust and share my academic, official or even personal difficulties. I have learned a tremendous amount from him which will help me not only in my professional life, but in my personal life too.

I am heartily thankful to my joint supervisor Prof. Rajib Kumar Mitra for his encouragement, motivation, support, valuable discussions, and helpful suggestions.

I sincerely thank Dr. Saswati Barman for her help in LLG Micromagnetic Simulator and for all the moral support during the tough times. My sincere thanks to Dr. Jaivardhan Sinha for fruitful suggestions and making me aware about some contemporary research activities.

I sincerely thank Prof. Olav Hellwig (HZDR, Germany) and his research group for providing various samples in collaboration and useful discussions. I would also like to thank Prof. Yoshichika Otani (RIKEN, Japan) for providing samples. My sincere gratitude to Prof. Supriyo Bandhyopadhyay (Virginia Commonwealth University, USA) and his research group for providing various samples and useful discussions. I also thank Prof. Bandyopadhyay for giving me an opportunity to visit his lab.

I would like to acknowledge all my labmates of '*spintronics and spin dynamics research group'*. I would like to acknowledge Dr. Semanti Pal, and Dr. Ruma Mandal for help in sample fabrication and Dr. Dheeraj Kumar for developing DotMag code and help in numerical

analysis. Thanks to Dr. Chandrima Banerjee, and Dr. Sucheta Mondal for teaching me the experimental and numerical techniques, how to build up lab habits, and how to patiently face the challenges during difficult experiments and simulations. They have been exceedingly loving and caring. Thanks to my other labmates Sourav Sahoo, Avinash Kumar Chaurasiya, Santanu Pan, Koustuv Dutta, Surya Narayan Panda, Kartik Adhikary, Sudip Majumder, Arundhati Adhikari, Amrit Kumar Mondal, Pratap Kumar Pal, Sreya Pal, Soma Dutta, Sourav Kanthal, Payel Bhattacherjee, Dr. Bivas Rana, Dr. Debanjan Polley, Dr. Arnab Ganguly, Dr. Susmita Saha, Dr. Bipul Kumar Mahato, Dr. Sumona Sinha, Dr. Dipak Kumar Das and Dr. Arpan Bhattacharya for their support. I express my love to all those juniors who joined here as project students. Thanks to all the lab members for making the lab such an enjoyable place to work.

I would also like to thank my labmates of '*THz spectroscopy research group'* Dr. Nirnay Samanta, Dr. Debasish Das Mahanta, Dr. Chaitrali Sengupta, Dr. Animesh Patra, Sk Imadul Islam, Partha Pyne, Sumona Pyne, Didhiti Bhattacharya, Saikat Pal, Riya Saha, and Subhajit Singha.

I would like to express my sincere gratitude to all my friends in S. N. Bose National Centre for Basic Sciences. I could never forget the love, care and support I received from Dr. Poulomi Chakraborty, Dr. Debasmita Maiti, Dr. Arghya Das, Dr. Biplab Bhattacherjee, Dr. Sumanta Kundu, Dr. Subhadip Chakraborti, and Dr. Rakesh Das during the tough times of my life. Special thanks to all of them. Also, thanks to Dr. Siddhi Chaudhuri, Damayanti Bagchi, Monalisa Singh Roy, Priyanka Saha, Anwesha Chakraborty, Swarnali Hait, Anupam Gorai, Debayan Mondal, Indranil Chakraborty, Siddhartha Biswas, Dhiraj Tapadar, and Anirban Mukherjee.

I thank Ajay Jha, Jack O'Brien (from the group of Prof. J. M. D. Coey, Trinity College, Dublin, Ireland) and Thanh Binh Nguyen (from the group of Prof. Roy Chantrell and Prof. Richard Evans, University of York, England) for being a part of successful project that won the award for best students-led project proposal during the IEEE summer school 2019 in Virginia Commonwealth University, USA.

Sincere respect to my teachers involved throughout my academic career for their proper guidance and teaching. I am extremely grateful to my teachers Dr. Abhijit Chakraborty, Prof. Sourangshu Mukhopadhyay, and Dr. Tanmoy Banerjee of the University of Burdwan.

I convey my heartiest gratitude to my parents for their unconditional love, support, guidance and encouragement that keeps me going through the successful journey of my research. They are the biggest strength and inspiration of my life. They have sacrificed a lot for me. I express

my sincere respect to my grandparents. My grandfather (Satyanarayan Nandi) is the best teacher of my life. Also, thanks to all other family members for their love. Special thanks to Rahul Bandyopadhyay and his family for love and support. My respect to Dr. Sukanya Chakraborti and love to Swapnil Barman and *Ace*.

Finally, I would like to thank S. N. Bose National Centre for Basic Sciences for giving me an opportunity to work. I acknowledge the technical cell of our Centre for various facilities. I gratefully acknowledge Department of Science and Technology (DST), INSPIRE and S. N. Bose National Centre for Basic Sciences for providing me fellowship for the doctoral research. I also acknowledge the financial support from S. N. Bose National Centre for Basic Sciences, IEEE Magnetic Society, DST-SERB for international travel grants to attend various national and international conferences/schools/visits held in India, Singapore and USA.

Anulekha De,
S. N. Bose National Centre for Basic Sciences,
Kolkata, India.

List of Abbreviations

ADL: Antidot lattice

AFC: Antiferromagnetic coupling

AFM: Atomic force microscope

(A)FM: (Anti) Ferromagnet

AOM: Acousto-optic modulator

BLS: Brillouin light scattering

BZ: Brillouin zone

BBO: Barium beta-borate

(B)MC: (Bi-component) Magnonic crystal

BNM: Binary magnonic cryatal

BS: Beam splitter

CPA: Chirped pulse amplification

CW: Continuous wave

DE: Damon–Eshbach

DMI: Dzyaloshinskii-Moriya interaction

DPSS: Diode pumped solid state

DW: Domain wall

EBE: Electron beam evaporation

EBL: Electron beam lithography

EDX: Energy dispersive X-ray spectroscopy

EM: Electromagnetic

EY: Elliott-Yafet

FDM: Finite difference method

FEM: Finite element method

FFT: Fast Fourier transform

FMR: Ferromagnetic resonance

fs: Femtosecond

FWHM: Full width at half maxima

GMR: Giant magnetoresistance

GVD: Group velocity dispersion

HAMR: Heat assisted magnetic recording

HDD: Hard disc drive

HM: Heavy metal

HWP: Half wave plate

IEC: Interlayer exchange coupling

IP: In-plane

IR: Infra-red

LLG: Landau-Lifshitz-Gilbert

MAMR: Microwave assisted magnetic recording

MC: Magnonic crystal

ME: Magneto-elastic

MFM: Magnetic force microscope

ML: Multilayer

MO: Microscope objective

MOKE: Magneto-optical Kerr effect

MQC: Magnonic quasicrystal

MRAM: Magnetoresistive random access memory

MSBVM: Magnetostatic backward volume mode

MSFVM: Magnetostatic forward volume mode

MSSW: Magnetostatic surface wave

MTJ: Magnetic tunnel junction

N.A.: Numerical aperture

OBD: Optical bridge detector

OISTR: Optically induced spin transport

OOMMF: Object oriented micromagnetic framework

OOP: Out-of-plane

PBC: Periodic boundary condition

PBS: Polarizing beam splitter

PMA: Perpendicular magnetic anisotropy

ps: Picosecond

PSSW: Perpendicular standing spin waves

PWM: Plane wave method

PZT: Piezoelectric transducer

RGA: Regenerative amplifier

RR: Retro-reflector

SAF: Synthetic antiferromagnet

SAW: Surface acoustic wave

SDG: Synchronized delay generator

SEM: Scanning electron microscope

SFS: Spin flip scattering

SHNO: Spin-Hall nano-oscillator

SMOKE: Static magneto-optical Kerr effect

SOC: Spin-orbit coupling

SOT: Spin-orbit torque

ST: Spin transport

STNO: Spin-torque nano-oscillator

STT: Spin transfer torque

SW: Spin-wave

TMR: Tunnel magnetoresistance

TR-MOKE: Time-resolved magneto-optical Kerr effect

(T)FPI: (Tandem) Fabry-Pérot interferometer

VPUF: Verdi pumped ultrafast laser

VSM: Vibrating sample magnetometer

List of Tables

List of Figures

Contents

Chapter 1

1. Introduction

Since the early discovery of the compass, magnetism has become an inseparable feature of everyday life. Over the years, magnetism has seen discovery of many fundamental phenomena and contributed many fascinating technologies. There are mainly three different sources of magnetic moment in a free atom. The diamagnetism is observed due to the change in the orbital moment induced by some external magnetic field. On the other hand, both spin and orbital angular momentum play roles for the occurrence of paramagnetism, ferromagnetism, antiferromagnetism and ferrimagnetism. Langevin developed the theories of diamagnetism and paramagnetism in 1905 [1, 2]. All magnetic effects other than diamagnetism originate due to permanent magnetic moments of the atoms. For paramagnetic materials, the coupling between the atomic magnetic moments is zero, resulting in no net magnetic moment in the absence of applied magnetic field. The theory of ferromagnetism was given by Weiss in 1906 [3]. The hallmark of ferromagnetic materials is that they exhibit spontaneous magnetization even at zero applied magnetic field (the magnetic moments are aligned parallel to each other), developing a net magnetic moment below the Curie temperature (T_C). The spontaneous magnetization is due to the direct exchange interaction between neighbouring magnetic moments. This property can be used to create device components with bistable magnetic states, which can be correlated with binary '0' and '1' for digital applications. The theory regarding the dynamics of the magnetic moments was given by Landau and Liftshitz in 1935 [4], which was further modified by Gilbert in 1955 [5].

Louis Neel first envisioned an antiferromagnetic material as composed of two sublattices, one of whose magnetic moments are antiparallel to those of the other, giving rise to zero or negligible magnetization [6]. The Neel temperature (T_N) of an antiferromagnet is the counterpart of the Curie temperature (T_C) of a ferromagnet ($T_C > T_N$), above which the antiferromagnetic ordering vanishes. The exchange interactions in antiferromagnets are quite different from ferromagnets. Strong antiferromagnetic coupling results due to the indirect exchanges like superexchange [7, 8] and double exchange [9] interactions. Some antiferromagnetic materials (such as Hematite) exhibiting non-zero magnetic moment due to spin canting near absolute zero temperature are known as canted antiferromagnets. Spin canting occurs due to two contrasting factors: isotropic exchange align the spins exactly antiparallel,

while anisotropic exchange arising from strong spin-orbit coupling (SOC) would align the spins perpendicular to each other. Synthetic antiferromagnets (SAF) are artificial antiferromagnets consisting of two or more thin ferromagnetic layers separated by a nonmagnetic spacer layer. In such structures, coupling between the ferromagnetic layers occurs through perpendicular orange peel coupling [10] or oscillatory RKKY coupling [11, 12] or by the coexistence of both. Antiferromagnetically coupled media can act as storage media that switch faster, more secured against external magnetic fields, and have higher storage density. Ferrimagnets possess antiferromagnetic sublattices (antiparallel magnetic moments) but with unequal sublattice magnetizations, hence possess a net magnetic moment. Ferrimagnetism was first observed in materials with spinel crystal structures and were named ferrites (spinel ferrites). It is also exhibited by magnetic garnets and rare-earth (RE) transition metal (TM) alloys. In some ferrimagnets, by tuning parameters such as the chemical composition, temperature, and strain it is possible to reach a state with zero net magnetization, known as the magnetic compensation state. These are called compensated ferrimagnets [13]. Both antiferromagnets and compensated ferrimagnets give opportunities to investigate spin dynamics in terahertz range. However, compared to conventional antiferromagnets, compensated ferrimagnets not only possess the aforementioned speed and density advantages but also allow the use of convenient electrical reading and writing mechanisms due to the existence of inequivalent magnetic sublattices with non-zero magnetizations.

1.1. Effects of Reduced Dimensionality

1.1.1. Ferromagnetic Thin Films

Nanoscale magnetic systems have become a topic of thriving interest to the scientific community in recent times due to their potential applications in a range of multidisciplinary fields like nonvolatile magnetic memory [14, 15], magnetic storage media [16-18], magnetic recording heads [19], magnetic resonance imaging [20], biomedicine and health science [21, 22]. They also offer a span of exotic phenomena and stern challenges. The rapid advancements of nanofabrication, characterization, and numerical simulations during the last two decades have made it possible to explore a plethora of science and technology applications related to dynamics of these systems. Nanoscale magnetic systems are not just ‘small magnets’ but their physical properties are very much different from their bulk counterparts. The growing demand of ‘storing more information within less space’ has increased the quest to study different

properties of nanoscale ferromagnetic media including ultrathin films, multilayers and patterned magnetic media. The invention of magnetic media as data storage and recording technology is the basis of the modern technological revolution, which has dramatically advanced the human life. Nowadays, mankind are habituated in handling gigabytes or terabytes of data in small gadgets like smartphones, tablets, personal computers, laptops, video cameras etc. Fast data volume growth along with user's habit of consuming increasingly more online content have encouraged the scientific community to continuously innovate.

The magnetic hard disk drive (HDD), a key component for data storage in computers as well as larger-scale data servers, has increased in capacity by a phenomenal extent since it was first introduced in the 1956. The first hard drive, the IBM 350, had an areal density of 2000 bit/in^2. Since then, the increase in storage density has matched the Moore's Law published in 1965 (Gordon Moore, Intel's co-founder) [23]. Seagate introduced a HDD with storage density of 1.34 Tbit/in^2 in the year 2015 [24]. In the first few generations of HDDs, a particulate medium (which is essentially a mixture of magnetic particles in a binder) was used. A particulate medium cannot have a high saturation magnetization and also their coercivity could not be tailored easily. Therefore, ferromagnetic thin films were considered as alternatives in the HDDs. A bulk magnetic material has constant physical properties regardless of its size. If the dimensionality of the system is reduced, a thin film is obtained with fundamental magnetic properties substantially different from bulk. With the reduction of film thickness, the surface to volume ratio increases and the interface effects dominates. The properties of ultra-thin films can be excellently tuned by varying the film thickness. Significant steps in the development of thin film media for HDD began with experiments characterizing a single layer thin granular film of *hcp* Co-based alloys deposited onto Cr underlayers where the easy axis of magnetization lies in the film plane [25]. Several other investigations on ultrathin films of Co [26] and Co-based alloys such as CoCr [27], CoPt [28], CoCrRh [29], CoCrPt [30] showed that the magnetization lies perpendicular to film plane.

1.1.2. Magnetic Multilayers

The technological progress with magnetic thin film media started to face difficulties due to the polycrystalline nature of the films. The magnetic properties of these media are strongly dependent on the microstructures of the film such as grain morphology, crystallographic orientation and grain size [31]. Eventually, it was found that instead of single layer thin films, the multilayer (ML) thin films can enhance device performance significantly due to the larger

grain density as well as decreased magnetic exchange coupling between the magnetic layers [32]. Additionally, the material properties near the interface are quite different from the bulk properties. Repetition of interfaces in MLs allows us to prepare a macroscopic bulk sample dominated by the interface properties [33]. Such structure gives rise to some novel properties which are extremely desirable in present day technology. In the year of 1988, the history of magnetism reached a milestone when Albert Fert [34] and Peter Grunberg [35] first experimentally observed giant magnetoresistance (GMR) effect in Fe/Cr multilayer system for which they were jointly awarded Noble prize in 2007. A classic GMR experiment studies a Ferromagnetic/Non-magnetic/Ferromagnetic (FM/NM/FM) multilayer. The resistance of the system depends on the relative orientation of magnetizations of the two ferromagnetic layers, which depends on the non-magnetic layer thickness. Subsequently, tunneling magnetoresistance (TMR)-based read heads started to replace GMR-based read heads. TMR is based on the quantum mechanical phenomenon called electron tunnelling. Instead of metallic barrier, the typical TMR device consists of a very thin insulating barrier sandwiched between two ferromagnetic layers (FM/I/FM). The discovery of GMR has triggered a new dimension of research called '*spintronics*' (SPIN TRansport electrONICS), which deals with encoding data in electron's magnetic moment or spin, rather than electron's charge. Spintronics have the potential to dramatically reduce the obstacles associated with the conventional semiconductor-based technology and may yield some advantages in terms of increased processing speed, lower power consumption due to Joule heat free storage, transfer and processing of information and/or increased on-chip device density. This discovery was a revolutionary breakthrough in technological industry and has enormous application in the present-day magnetic recording industry. In present day, hard drives are very fast, handy and are capable of storing Terabytes of data. GMR or TMR led to the possibility of novel non-volatile magnetic memories, like Magnetoresistive Random Access Memory (MRAM and magnetic HDD. The main drawback of the conventional solid state memories (DRAM and SRAM) in computer chips is volatility. They can store information as long as electricity flows through them. Once power is turned off, the stored information is lost. In contrast, MRAM (relies on tunnel valves) retains data even after the power supply is cut off. Replacing DRAM with MRAM could prevent data loss and enable computers to start instantly without waiting for the software to boot up. MRAM uses a pair of ferromagnetic metallic layers separated by a very thin insulating layer. One ferromagnetic layer has a high coercive field, which remains magnetized, while the other layer has a smaller coercive field, whose magnetization can be easily varied. The orientation of the two magnetic layers defines the 1 or 0 in a binary bit. This basic structure is called a magnetic

tunnel junction (MTJ). Arrays of such MTJs make the memory device. MRAM can perform read and write operations much faster than DRAM using less power, while being a non-volatile memory, it is considered a 'universal memory'. Recently, MRAM is proposed with spin transfer torque (STT)-based magnetization switching called the STT-MRAM. Here 'writing' of a bit is done by a spin-polarized current [36]. Application of spin polarized current to write bits in nonvolatile magnetic memory has become an effective approach because it promises to reduce the unnecessary power consumption in the system in comparison to existing electronic memory devices, including conventional MRAM devices. STT-MRAM devices are faster, more efficient and easier to scale down compared to toggle MRAM. The advancement in longitudinal recording technology started facing difficulties in order to the increase of storage density, which requires the reduction of grain size. However, as the grain size is reduced very much, they fail to retain their magnetic orientation due to random thermal fluctuation even at room temperature due to superparamagnetism. Therefore, alternative materials or methods of recording schemes are needed to move the magnetic recording industry forward. Antiferromagnetically coupled (AFC) media [37] consisting of magnetic layers antiferromagnetically coupled through a thin nonmagnetic spacer are another kind of magnetic media which helped to achieve higher storage density by obstructing the superparamagnetic limit. Eventually, it was observed that the materials with high magnetic anisotropies are even superior candidates than the AFC media in terms of storage capacity. Ferromagnetic MLs with high perpendicular magnetic anisotropy (PMA-MLs) are strong candidates for the recording technology due to the very high and tunable anisotropy, where the interface anisotropy contribution dominates over the bulk contribution to give a preferential perpendicular orientation of the magnetization. The concept of perpendicular magnetic recording (PMR) was introduced by Shun-Ichi Iwasaki in 1976 [38] and PMA was first observed in Co/Pd MLs in 1985 by Carcia *et al.*[39]. It was found that for a fixed Pd layer thickness, it becomes hard to magnetize the ML in the film plane for Co layer thickness < 8 Å and the ML shows perpendicular easy axis of magnetization. As the Co/Pd alloy structures do not exhibit PMA [29], it was inferred that rather than the crystalline anisotropy, the surface anisotropy at the Co/Pd interface and the strain in the Co layer is responsible for the PMA [40]. The saturation magnetization of the Co/Pd ML structure was also found to be significantly higher than that expected from the magnetic moments of the Co layer only. The perpendicular recording can overcome the superparamagnetic limit. Consequently, in perpendicular recording the areal density of data is higher and the bit patterns are magnetostatically more stable as compared to the longitudinal recording. It is thus less affected by thermal fluctuation and other spurious

fields. Earlier literature reveals that longitudinal recording can have maximum storage capacity of 100 GB/in^2, whereas the perpendicular recording offers higher storage capacity of 340 GB/in^2 [41].

An extensive investigation on several ferromagnetic MLs with PMA such as Co/Pd [42], Co/Pt [43], Co/Ni [44] systems have been carried out over the years. PMA is believed to originate from the interface anisotropy due to the broken symmetry and d-d hybridization at the Co/Pd and Co/Pt interfaces [45]. A competition between interface and volume anisotropies leads to a variation of PMA with Co layer thickness in Co/Pd MLs [46]. Plenty of research works [47-54] have been carried out on the formation and evolution of fascinating stripe domains and labyrinth domains depending upon the film thickness in such PMA-ML systems. Study of magnetization reversal of PMA Co/Pt ML establishes the crucial role of anisotropy in determining the reversal behavior [55] A correlation between PMA and Gilbert damping has been predicted [56, 57]. An increase in Gilbert damping with decrease in Co layer thickness in Co/Pt and Co/Pd ML films with PMA has been reported [58]. Insertion of ultrathin metallic (e.g. Ru, Ir) or insulating (e.g. NiO) spacer layers between such PMA Co/Pd or Co/Pt MLs gives rise to antiferromagnetic coupling between the adjacent ferromagnetic layes, which leads to the alteration of the magnetization of the adjacent Co/Pd or Co/Pt MLs with magnetic field [59, 60].

The use of high-anisotropy material causes the problem of writability because it requires very high magnetic field from a write head to switch the magnetization [38]. New techniques like heat-assisted magnetic recording (HAMR) and microwave-assisted magnetic recording (MAMR) are invented to overcome this difficulty. In HAMR technique, the anisotropy and coercivity of the ferromagnetic films can be tuned by local heating using a laser pulse. Magnetization of the laser spotted region of the film can be switched easily without affecting the other parts of the films [61]. This allows writing with less magnetic energy and the use of a smaller write head, thus, achieving a higher storage density. MAMR [62] can solve a few problems that are created with laser-based writing technology in HAMR, such as excessive surface heating and building complexity. The MAMR technology overall looks like ‘improved HAMR’ with the same pros, but lower cons. Now the technology is nearly ready to manufacture. MAMR technology promises to have HDDs with storage capacity of 2 to 5 Tbit/in^2 as compared to 1.3 Tbit/in^2 used on conventional drives.

1.1.2.1. Synthetic Antiferromagnets

According to the Nobel lecture of Louis Neel in 1970, the common perception regarding antiferromagnets were ‘interesting but useless’ [63]. However, antiferromagnetic spintronics is a field that makes antiferromagnets useful and spintronics more interesting. Antiferromagnetic materials are outstanding candidates for the next generation of spintronic applications due to several important features they combine: they are robust against perturbation due to magnetic fields, exhibit faster dynamics (in THz frequency range), have ability to generate and detect spin-polarized electric currents, produce no parasitic stray fields, and are capable to generate large magnetotransport effects. Synthetic antiferromagnets (SAFs) are used to overcome device malfunctions associated with ferromagnetic stray fields when lateral dimensions are reduced (e.g. crosstalks in MRAM due to the mutual interaction between neighbouring cells which are supposed to be isolated from each other). SAFs [64] are built with FM layers periodically interleaved with metallic or insulating spacers, where the magnetization of adjacent FM layers alternates owing to the antiferromagnetic (AF) interlayer exchange coupling (IEC) [65]. The IEC in SAF is much weaker than the direct exchange or superexchange coupling in crystal antiferromagnets, which allows for manipulation of the antiferromagnetic order more easily in SAF [64]. Nowdays, SAFs are frequently being used as pinning layers to harden the operating ferromagnetic layers in spin valves and MTJs [66]. A spin-flop-like reorientation provided the basis for a magnetic-field-writing of the free layer composed of SAF in commercial toggle MRAMs [67]. SAFs can reduce the critical current for switching (to write a bit) while maintaining the thermal stability in MRAMs [68]. Moreover, the switching time can be reduced significantly with the IEC within the free layer of SAF [69]. Spin-current-driven auto-oscillations in SAF structures have also been reported [70]. Several experimental and theoretical studies have demonstrated the motion of domain walls and solitons in SAFs [71-73]. An attraction between the domain walls in the two ferromagnetic layers occuring due to the IEC, leads to increased velocities of the domain walls in SAF structures [74]. The interface between ferromagnetic and nonmagnetic heavy metal gives rise to interfacial DMI which leads to chiral domain walls. In particular, this interfacial DMI stabilizes Neel domain walls that are efficiently driven by spin-orbit torque (SOT) induced by high spin orbit coupling (SOC) in the heavy metal layer. The IEC in SAF structures stabilizes the Neel walls such that they can be driven more efficiently by SOT [72]. The SAF structures led to the discovery of the GMR and thus gave to the birth of modern spintronics. Despite the rapidly growing literatures, the field of ‘synthetic antiferromagnetic spintronics’ is still in its

infancy, making it difficult to predict the future course of research and viable applications. Nonetheless, significant challenges still need to be thoroughly addressed and continued research is required to reach a level of control in this field before SAFs can become active elements of real spintronic devices.

The main challenge of using antiferromagnets in spintronic devices is the lack of mechanisms for realizing efficient reading and writing. Compensated ferrimagnets provide hope to address these obstacles. Recent research has demonstrated fast spin-torque switching, as well as efficient electrical reading with compensated ferrimagnets. Mizukami *et al.* reported long-lived ultrafast spin precession with frequencies up to 0.28 THz in Mn-Ga alloy films with a large perpendicular magnetic anisotropy and low Gilbert damping [75]. Another study reported laser induced magnetization precession with frequencies more than 0.5 THz in Heusler-like nearly compensated ferromagnetic Mn_3Ge alloy films [76]. Observation of giant spin-orbit torque has been reported in half-metallic compensated ferrimagnet Mn_2Ru_xGa with x = 0.7 (MRG), which is sufficient to sustain self-oscillation with negligible damping [77].

1.2. Patterned Nanostructures

The magnetic properties of confined magnetic structures are different from their bulk counterparts and continuous thin films. The dynamic magnetic processes of patterned nanostructures strongly depend on their static magnetization states, which depend not only on the intrinsic material properties such as exchange stiffness constant, saturation magnetization and magnetocrystalline anisotropy, but also on extrinsic geometric properties including shape, size, lattice constant, lattice geometry as well as the ensuing magnetic interactions. For an isolated single or quasi-single domain nanomagnet, the magnetization reversal may occur through the formation of vortex, onion, flower, leaf, C- or S- states depending upon the shape, size and aspect ratio of the nanomagnets [78, 79], whereas, the reversal in multidomain nanomagnets occur through domain wall (DW) dynamics. The nonuniform static magnetization states in magnetic nanostructures may trap spin waves (SWs) locally or quantize them. Patterned nanostructures have witnessed myriads of activities over the last few decades, due to their potential applications in range of multidisciplinary fields such as nonvolatile magnetic memory [80,81], magnetic data storage [82-84], magnetic recording heads [85], spin logic [86], spin-based transistors [87], filters [88], phase shifters [89], multiplexers [90], interferometers [91], spin-Hall nano-oscillators (SHNO) [92], spin-torque nano-oscillators

(STNO) [93], magnonic crystals (MCs) [94, 95], neuromorphic computation [96], magnetic resonance imaging [97], nanobiomedicines [98, 99] etc.

1.2.1. Magnonics

Magnonics is a newly born and rapidly evolving research field in nanomagnetism that provide unprecedented controllability in terms of ultrafast transfer and processing of information through SWs. The concept of SWs in a periodic medium was first introduced by Bloch [100], which are basically collective excitation of spins in a magnetic media. Magnons are the quanta of SWs. The hybridization of magnonics with other physical excitations has led to new fields such as magnon–spintronics, [101] magphonics, [102] magnon–polaritronics [103] etc. Magnonic crystals (MCs) are the pillar of magnonics. The term magnonic crystal was coined by Gulyaev and Nikitov [104]. These are artificially patterned magnetic structures with periodic alteration of magnetic properties, which offer non-volatility, Joule-heat-free transfer and processing of information, faster data processing speed, low energy consumption integrated with a much higher storage density as opposed to the modern semiconductor technology. Further advantages of magnonic devices are reprogrammability, large coherence length, miniaturization to atomic scale, broad bandwidth anisotropic properties, and efficient tunability by various external stimuli. The stark modulation of magnetic properties in MCs brings about changes in coercivity and switching field, induced anisotropies, and collective behaviors of the elements in magnetization reversal. Consequently, SWs get localized or confined due to the periodic distribution of local or internal magnetic field or coherent coupling owing to the periodic arrangement (due to exchange or anisotropic dipolar interaction) which leads towards the formation of dispersive or non-dispersive magnon energy bands as well as partial bands. However, unlike electromagnetic, acoustic or photonic waves, SWs display a diversity of dispersion characteristics. The dispersion of dipole-dominated SWs in ferromagnetic thin films strongly depends on their direction of propagation with respect to the applied magnetic field, giving rise to magnetostatic surface wave or Damon-Eshbach (DE), backward-volume (BV) and forward volume (FV) modes. On the other hand, exchange-dominated perpendicular standing spin wave (PSSW) modes with different nodal planes are found across the thickness of the ferromagnetic films. The upsurge of research interest in this area has been started almost two decades ago and enormous efforts have been made to develop advanced nanofabrication and characterization techniques to deal with the excitation, propagation, control and detection of SWs in MCs. A flurry of research have been performed

in one- [105, 106], two- [107, 108], and three- [109, 110] dimensional MCs with periodic variation of material parameters, [111, 112] external controllers like magnetic field [113], stress [114], charge current, electric field etc. or by structuring the material differently to provoke the modulation in the magnonic band structures as well as the SW dispersion.

In the following sub-sections, brief overviews of different types of MCs investigated in this thesis have been presented.

1.2.1.1. Ferromagnetic Nanodot Arrays

Periodic array of non-interacting ferromagnetic islands (dots) embedded in non-magnetic matrix can be used as bit-patterned media (BPM) where information is stored as the magnetization state of a single magnetic island. For the application in BPM, the essential criterion is to eliminate the magnetostatic interaction, i.e. cross-talks between the individual bits. However, same arrays of ferromagnetic nanodots may be used to transfer information via SWs, when the nanodots are strongly magnetostatically coupled. Intense research on such systems have been performed so far to utilize their SW characteristics as logic devices or non-volatile elements for information storage. In the early theoretical studies of GHz frequency response of ferromagnetic nanodot arrays, the effects of inter-dot dipolar coupling on the dynamics by varying array geometry and magnetic field orientation have been studied [115,116]. The magnetic domain formation gets affected due to the confinement in various directions and different anisotropy energies such as shape anisotropy, configurational anisotropy etc. play crucial role in controlling the SW dynamics of ferromagnetic nanodot arrays. The initial experimental studies on nanodot arrays showed the decomposition of a single FMR peak into multimodal oscillations, whose frequencies strongly depends on the orientation of the external magnetic field and the interparticle interaction [117]. This was followed by BLS studies on cylindrical $Ni_{80}Fe_{20}$ (permalloy or Py) nanodots showing two classes of SW modes, namely, higher-frequency DE-like and lower-frequency BV-like modes [118] and FMR studies perpendicularly magnetized nanodots showing a large number of modes independent of interdot separation stemming from the dipole–exchange interaction [119]. Subsequently, the study of time-resolved precessional magnetization dynamics in square-shaped $Co_{80}Fe_{20}/Ni_{88}Fe_{12}$ bilayer nanodot arrays showed a non-monotonic variation of the precession frequency with dot size owing to a crossover from CM to EM domination below a certain dot diameter [120]. This was followed by important observations like dynamical configurational anisotropy [121] and SW modes in non-ellipsoidal elements with nonuniform ground states

[122]. By frequency-resolved MOKE experiment Shaw *et al*. observed that the intrinsic Gilbert damping parameter remains almost unaffected by the nanopatterning [123]. In 2010, Kruglyak *et al*. detected collective SW modes in an array of closely spaced ferromagnetic nanodots [124]. Further study in square-shaped Py nanodots arranged with varying areal density showed a transition from a single uniform collective mode at a very high areal density through weakly collective dynamics at an intermediate areal density to completely isolated dynamics of the individual nanodots at a very small areal density [125]. Collective modes for a ferromagnetic nanodot array with perpendicular magnetization was shown by Bondarenko *et al.* [126]. A stark variation of collective SW dynamics was observed when the lattice symmetry of circular shaped Py nanodot arrays were varied from square to octagonal through rectangular, hexagonal, and honeycomb lattices [127]. Furthermore, Mondal *et al.* reported the influence of anisotropic dipolar interaction on the SW dynamics of Py nanodot arrays arranged in honeycomb and octagonal lattices with varying lattice constants [128]. Variation of dot shapes like elliptical, half-elliptical, rectangular, triangular, and diamond-shaped nanoelements showed a strong variation in SW spectra due to the modifications of the internal field profiles [129]. A new system of cross-shaped Py nanodots exhibited some very interesting phenomena such as mode softening, mode crossover, mode splitting and merging of SW frequency branches with the strength and orientation of bias magnetic field [130]. Recently, a strong magnon-magnon coupling was reported in similar nanocross array [131]. This field has been rapidly emerging with many more works in spin-texture driven magnonics, hybrid magnonics, short-wavelength magnonics, etc.

1.2.1.2. Ferromagnetic Antidot Arrays

Ferromagnetic antidot (hole) lattices (ADLs), i.e. periodically etched holes on a continuous ferromagnetic film are one of the strongest candidates for reconfigurable MCs. The nonuniformity in magnetization due to the inclusion of periodic holes can strongly affect the precessional switching of such structures, which may play important roles in next-generation magnetic storage and memory devices. The ferromagnetic antidot arrays have some unique advantages over the nanodot arrays. Due to the absence of any small isolated magnetic entity, the antidot systems do not suffer from the superparamagnetic lower limit as opposed to the nanodot systems. Here, the whole film remains exchange coupled, and hence, offers higher SW propagation velocity and longer propagation distance for the SWs as opposed to isolated nanodots. Extensive research on the dynamics of standing and propagating SWs in

ferromagnetic ADLs have led toward important findings. Martyanov *et al.* [132] reported the first experimental study on the magnetization dynamics of Co antidot arrays by ferromagnetic resonance (FMR) technique, which showed evidence that the inhomogeneities in the magnetization distribution around the antidots give rise to the changes of the resonance modes with the in-plane direction of the magnetization. This was followed by the observation of the magnonic normal mode, [133] Bloch-wave mode, and an unusual bias field independent mode [134] in ferromagnetic ADLs. Anisotropic propagation and damping of SWs with bias field orientation [135], complete magnonic band gap for magnetostatic FV modes [136], and high-symmetry SW modes in perpendicularly magnetized ADL [137] were important observations in terms of SW dispersion in ADLs. Subsequently, a flurry of experimental and numerical investigations on the dynamics of standing and propagating SWs in ferromagnetic antidots have led towards important findings, including field controlled confinement, localization, and propagation of SWs [138], splitting of resonant modes [139], mode crossover [140], mode hopping [141], mode softening [142], as well as the formation of magnonic mini bands [143] depending upon the antidot shape [144], lattice constant [145], lattice symmetry [146], base material [147, 148] as well as the strength and orientation of the applied magnetic field [113]. Non-circular antidots have been observed to contribute an additional anisotropic component to the SW dynamics due to the inhomogeneous internal field distribution created by asymmetric demagnetized regions [113, 149]. Defects play important roles in such antidot MCs. A numerical study on defective ADLs showed softening of the localized modes accompanied by an amplification of the extended modes as a result of the local alteration of SW mode profiles due to defects [150]. Another numerical study showed the SW propagation in an ADL with a ring defect [151]. Unconventional structures like magnonic quasicrystals (MQCs) in the form of octagonal lattice of antidots [152], defective honeycomb lattice [153], ADLs with geometrical complexity [154] have been developed in the pursuit of greater tunability of SW spectra and anisotropy. Similar to nanodot arrays this field is also bubbling with new ideas and developments.

1.2.1.3. Magnonic Quasicrystals

Quasicrystals possess long-range ordering without any periodicity, complex form of frustration leading to glassy behavior, and they exhibit exotic rotational symmetry [155]. Recently, MQCs have become a hot topic of research due to their various interesting properties like branching features in the band structure, self-similarity and scaling properties in the transmission spectra

[156], allowed bulk band in place of band gaps [157], appearance of passband [158] etc. The experimental and theoretical concepts of self-generation of dissipative solitons in MQCs active ring resonator have been reported [159]. Heush *et al.* proposed the existence of perfect transmission of SWs in a 1D Thue-Morse MQC, which become sharper with increasing order of quasicrystals [160]. The plane wave method (PWM) investigation of SWs in 2-D planar quasicrystal having Penrose tiling structure in the form of Ni (or NiFe) disks embedded in Fe (or Co) matrix revealed the localization of the SW eigenfrequencies resulting from the quasiperiodicity of the magnetic structure [161]. Bhat and Grundler showed the MQCs comprising of Py interconnected nanobars arranged in Penrose P2, P3, and Ammann tiling exhibit SW modes with eight and tenfold rotational symmetries with varying in-plane bias magnetic field orientations [162]. The same group later demonstrated that the tenfold rotational symmetry of aperiodic nanohole arrangements results in Conway worm like nanochannels [163]. Lisiecki *et al.* reported a remarkable dynamic coupling between propagating SWs through Py nanowires of two different widths arranged in a Fibonacci sequence [164]. Construction of numerous types of MQCs with different variants of Penrose tiling, oblique tiling, Kite and Dart tiling [165], and Ammann-Beenker tiling [166, 167] offer unprecedented tunability of the SW dynamics and magnonic band structure.

1.2.1.4. Bicomponent and Binary Magnonic Crystals

In bicomponent magnonic crystals (BMCs), one ferromagnetic element is embedded into a matrix of another ferromagnetic material [168], where the dipolar-exchange coupling becomes high at the interface of two ferromagnetic materials. As a consequence, SWs in BMCs can propagate with large group velocities providing additional tunability to the SW dynamics as well as magnonic band structures. Initial studies on 1D BMC in the form of laterally patterned periodic arrays of alternating Co and NiFe stripes with varying widths revealed [169-171] well-defined frequency bandgaps strongly dependent on their structural dimensions. Dual magnonic and phononic bandgaps in 1D BMCs in the form of linear periodic arrays of alternating Fe (or Ni) and NiFe nanostripes have been demonstrated [172], which revealed no magnon-phonon interaction in such structure. Soon after this, the investigation on 2D BMCs have been started and Co nanodisks embedded in Py antidots showed two channels of SWs, one through the Co nanodisk and another in between them [173]. In a parallel work on SW dispersion of 2D BMC consisting of Co square dots embedded in Py matrix showed larger frequency width of magnonic bands than the constituent antidots and a complicated magnonic band structure,

where the Co dots act as amplifiers of dipole coupling between the Py dots [174]. Several works on the spatial and field control of SW dynamics in BMCs formed by periodic Co nanodots introduced in a thin NiFe film have been reported [175-177]. Choudhury *et al.* achieved a strong signature of inter-element exchange interaction across the interface and ensuing enhancement of the SW propagation velocity in a Py-filled CoFe ADLs [178]. A very interesting investigation [179] on periodically nanostructured magnets in the form of NiFe nanodisks embedded into shallow-etched CoFeB matrix has been demonstrated as an omnidirectional grating coupler showing a giant enhancement of the amplitude of the short wavelength SWs with compared to a bare microwave antenna.

However, the improved functionalities of BMCs come at the expense of more complicated fabrication processes, such as multistep lithography and two-photon photolithography. Binary magnonic crystal (BNM) is another type of MC, which can provide more control parameters for tuning the magnonic band structure but can be fabricated employing simpler lithography processes by placing two structures of the same material next to each other forming the basis of the crystal. A Py/Co binary nanostructure fabricated by a simple self-aligned shadow deposition technique exhibited rich SW dynamics [180]. Observation of spectral narrowing and mode conversion in novel binary nanostructures has been reported where square shaped Py nanodots of two different sizes are diagonally connected to form a binary basis [181]. Excellent tunability of magnetization reversal mechanisms and magnetic anisotropy in specially engineered binary ADLs with alternating antidot diameter have also been explored [182]. The fabrication and direct mapping of magnetization states in anti-ring nanostructures forming a BNM have been reported, where a ferromagnetic nanodot is embedded in a non-magnetic hole [183]. Investigations of static and dynamic properties of such anti-ring structures and their potential application in in biosensing have been demonstrated [184, 185]. Porwal *et al.* reported SW mode conversion and mode hopping with bias magnetic field orientation in an annular antidote lattice forming a BNM [186].

1.2.1.5. Multilayerd Nanostructures

Multilayerd nanostructures can be considered as 3D MCs. The shifting of the data storage technology from the longitudinal to the perpendicular recording mode indicates that nanomagnet arrays fabricated on films with perpendicular magnetic anisotropy (PMA) can be considered as more effective data storage and recording media. A lot of fascinating physics are there to be explored in patterned magnetic nanostructures based on PMA-MLs. Few reports

exist on magnetization reversal and DW study with defects and edge corrugations [187], increase of coercive field [188] in antidots carved on [Co/Pd] MLs and DW pinning in antidots carved on [Co/Pt] MLs [189]. Small modifications of the layer thickness or deterioration of interface quality can lead to extrinsic defects in the PMA-MLs. Magnetization reversal in [Co/Pd] antidot lattices having defects and edge corrugations [187] demonstrated an increase in the Neel domain walls, as compared to Bloch walls, with the increase in the antidot diameters. Piramanayagam *et al.* investigated the magnetic properties of antidots fabricated on $[Co/Pd]_{10}/Ru/[Co/Pd]_3$ MLs with varying Co layer thickness and showed that the anitiferromagnetic coupling (AFC) to be responsible for the PMA in these structures [190]. It was also observed that the PMA near the rim of [Co/Pd] ML antidots, instead of being exactly perpendicular, gets slightly tilted. Theoretical study of patterned PMA-MLs revealed that magnetic inhomogeneity along the central axis splits the magnetostatic SWs into two bands, and the exchange SWs into a number of bands [191]. The magnetization reversal mechanisms in perpendicularly magnetized nanostructures has been observed to be highly dependent on the condition of the edges [192]. The first experimental study of SW dynamics such systems came up in 2014, when Pal *et al*. reported a decrease in SW frequency of [Co/Pd] ML ADLs to values well below the unpatterned ML with increasing antidot density [193] The experimental observations were modelled by assuming nanoscale rim-like shell regions with degraded PMA value surrounding the antidots created by the Ga^+ ion bombardment during fabrication using the FIB technique. The shape of the antidots was found to play important roles in the in-plane domain structure surrounding the antidots and the ensuing edge-localized SW spectra in the same system [194]. The formation of artificial skyrmions and antiskyrmions via localized ion irradiation of [Co/Pt] multilayers, to create localised circular regions with in-plane magnetization have also been reported [195].

Recently researchers have started to explore unconventional and new structures including, artificial spin ice structures [199, 197], and topological magnetic solitons [198]. More recently the expansion of MCs into third dimension [110, 199, 200] led to the emergence of unconventional and complex spin textures, where novel physical effects comprising geometry, topology, frustration and chirality can be explored. Consorted efforts from the nanomagnetism community are thus highly desirable in future for the construction of ultra-high density data storage and memory devices with more advanced functionalities.

1.3. Magnetization Dynamics in Magneto-Elastically Coupled Nanomagnets

The non-volatility and unprecedented energy efficiency of nanomagnetic logic and memory devices have spurred investigations of different types of magnetization switching schemes in nanomagnets. Unfortunately, the large dissipative losses occur when nanomagnets are switched with either magnetic field generated by a current [201] or by a spin polarized current exerting either a spin transfer torque [202] or causing DW motion [203]. 'Straintronic' or magnetoelastic switching has emerged as an extremely energy-efficient mechanism for magnetization switching of magnetostrictive nanomagnets [204-206]. Mechanical vibrations are found almost everywhere and most of them are often unwanted and the mechanical energy is wasted. To recover this kind of energy, magnetostrictive materials are used in transducers to transform unwanted mechanical vibrations into useful electric power. Magnetization of a magnetostrictive nanomagnet can be switched by mechanical strain via elastic coupling to the underlying piezoelectric substrates (eg. $LiNbO_3$, PMN-PT etc.), activated by electrical voltage utilizing the inverse magnetostrictive (Villari) effect [207]. When strain is produced in the piezoelectric substrate, it generates surface acoustic waves (SAW) that periodically contracts and expands the nanomagnet placed on the substrate and changes its magnetization owing to the Villari effect. Several groups have reported the control of magnetization in magnetostrictive films on piezoelectric substrates using voltage generated strain, demonstrating reversible control of nanomagnetic domains [208], and strain assisted reversal of perpendicular magnetization in Co/Ni multilayers [209]. Strain controlled magnetization dynamics in Ni nanostructures deposited on piezoelectric substrates has been reported [210-214]. Mondal *et al.* observed hybrid magnetodynamical modes having rich spin-wave textures associated with straintronic switching in a single semi-elliptical magnetostrictive Co nanomagnet deposited on a piezoelectric PMN-PT substrate using time-resolved magneto-optical Kerr effect (TR-MOKE) measurements [114]. There are also some experimental evidences of MTJs being switched in this fashion [215, 216]. Recently, design of extreme sub-wavelength magneto-elastic electromagnetic antenna with multiferroic nanomagnets has been proposed [217]. A SAW launched in the piezoelectric substrate causes the oscillations of the magnetizations of the nanomagnets, which emit EM waves at the applied SAW frequency. Such antennas allow drastic miniaturization of communication systems. Despite of having excellent energy efficiency, this technique has not been properly used in switching MRAM elements due to

certain drawbacks. First of all, the magnetization of nanomagnets cannot always be flipped by 180° using this method, which is essential for MRAM operation. Generally, the magnetostrictive nanomagnets are in the shape of an elliptical disk, where the in-plane anisotropy dominates over the surface anisotropy. A SAW launched in the substrate with an alternating electrical voltage produces a biaxial strain (compression in the direction of the major (easy) axis of the elliptical nanomagnet and tension along the minor (hard) axis, or vice versa). Thus, the magnetization of the magnetostrictive nanomagnet is rotated away from its stable orientation along the major axis toward the minor axis (90° rotation). In case of such 90° rotation, the probability of writing and storing of data is 50%. Also, at room temperature, geometrical defects in the nanostructures may cause failures in the switching [218].

1.4. Objectives of the Thesis

The skeleton of this thesis consist of experimental and numerical investigation of ultrafast spin dynamics in a variety of 2D ferromagnetic patterned nanostructures (including nanodots, antidots as well as multilayered nanostructures), synthetic antiferromagnetic (SAF) structures and SAW driven modulation of spin dynamics in strongly interacting multiferroic nanomagnets by time-resolved (time-resolved magneto-optical Kerr effect (TR-MOKE) microscope and magnetometer) and wavevector resolved (Brillouin light scattering (BLS)) techniques. The precise objectives of this research are to investigate the effects of geometrical structuring, the strength and orientation of external bias magnetic field, interlayer interactions, laser fluence and SAW on the ferromagnetic and antiferromagnetic systems. The investigated systems are as follows:

(1) Binary Magnonic Crystal as Diatomic Nanodot Array: Reconfigurable magnonic band structure in a binary magnonic crystal (BMN) comprised of $Ni_{80}Fe_{20}$ diatomic nanodot array (two different sized nanodots placed in close proximity to each other forming a complex double-dot unit cell) has been studied using Brillouin light scattering (BLS) technique. Excellent tunability of the magnonic band structure has been observed with the orientation of bias magnetic field along with the emergence of new interaction modes due to strong magnetostatic inter-dot interactions in the diatomic unit. A strong anisotropy in the SW dispersion is observed in this structure, which is also evident in the iso-frequency curves.

(2) Magnonic crystals with complex geometry: Ultrafast magnetization dynamics in ferromagnetic antidot arrays with complex geometry has been studied using TR-MOKE microscopy. The quasiperiodic octagonal lattice lacking translation symmetry, along with a

complex triangular antidot basis lacking reflection symmetry, exhibits a strong eight-fold anisotropy superposed with a weak three-fold anisotropy. On the contrary, the most primitive square lattice exhibits a strong four-fold anisotropy superposed with a weak three-fold anisotropy. The most densely packed hexagonal lattice shows a strong six-fold anisotropy encased with a weak three-fold anisotropy. The spatial profiles of SWs revealed the presence of both even and odd modes, due to the asymmetric potential energy landscapes. A SW mode conversion from extended to quantized ones and vice versa has been observed with the in-plane bias magnetic field orientation.

(3) Synthetic Antiferromagnets: The underlying mechanism of magnetic configuration driven ultrafast demagnetization in synthetic antiferromagnet (SAF) structures comprised of $[Co/Pt]_N$ MLs with PMA periodically separated by Ru and Ir spacers has been studied using TR-MOKE magnetometer, where the magnetization of adjacent ML stacks alternate owing to the antiferromagnetic interlayer exchange coupling (IEC). We concluded that the spin-transport of optically excited carriers can have a significant contribution to the ultrafast demagnetization, in addition to spin-flip scattering processes. An active control over the individual mechanisms has been achieved by specially designing the samples and altering the external magnetic field and excitation fluence.

(4) Multilayered Nanostructures: Anisotropic variation of SW dynamics in diamond shaped antidot lattices patterned on $[Co/Pd]_N$ multilayers with PMA has been studied using TR-MOKE microscopy, where in-plane domain structures are formed in narrow rim-like shell regions around the antidots because of the reduction of magnetic anisotropy due to the Ga+ ion irradiation during the focused ion beam (FIB) milling process of antidot fabrication. The modulation of the in-plane domain structures with the orientation of bias magnetic field leads to the stark anisotropic variation of the SW dynamics.

(5) Magneto-Elastic Coupling in Interacting Multiferroic Nanomagnets: The magnetoelastic coupling between surface acoustic waves and spin waves at GHz frequencies in densely packed elliptical Co nanomagnet array fabricated on piezoelectric $LiNbO_3$ substrate has been studied using TR-MOKE microscopy. Resonant amplification of intrinsic magnon modes and generation of new extrinsic modes have been observed in absence of any bias magnetic field opening new avenues towards bias-field free reconfigurable magnonics.

References

[1] A. J. Dekker, “Solid State Physics,” Macmillan Publishers India Ltd., New Delhi, India (1981).
[2] A. H. Morrish, “The Physical Principles of Magnetism,” IEEE Press, New York, United States (2001).
[3] P. Weiss, J. Phys. Theor. Appl. **6**, 661 (1907).
[4] L. Landau, and E. Lifshitz, Phys. Z. Sowjet. **8**, 153 (1935).
[5] T. Gilbert, IEEE. Trans. Magn. **40**, 3443 (2004).
[6] L. Neel, Annales de Physique. **12**, 137 (1948).
[7] H. A. Kramers, Physica. **1**, 182 (1934).
[8] P. W. Anderson, Phys. Rev. **79**, 350 (1950).
[9] C. Zener, Phys. Rev. **82**, 403 (1951).
[10] L. Neel, Comp.Rend.Acad.Sci.France, **255**, 1545 (1962).
[11] M. A. Ruderman, and C. Kittel, Phys. Rev. **96**, 99 (1954).
[12] T. Kasuya, Progress of Theoretical Physics. **16**, 45 (1956).
[13] J. Finley, and L. Liu, Appl. Phys. Lett. **116**, 110501 (2020).
[14] S. Tehrani, E. Chen, M. Durlam, M. DeHerrera, J. M. Slaughter, J. Shi, and G. Kerszykowski, J. Appl. Phys. **85**, 5822 (1999).
[15] J. Åkerman, Science **308**, 508 (2005).
[16] T. Thomson, G. Hu, and B. D. Terris, Phys. Rev. Lett. **96**, 257204 (2006).
[17] B. D. Terris, T. Thomson, and G. Hu, Microsyst. Technol. **13**, 189 (2007).
[18] O. Hellwig, A. Berger, T. Thomson, E. Dobisz, Z. Z. Bandic, H. Yang, D. S. Kercher, and E. E. Fullerton, Appl. Phys. Lett. **90**, 162516 (2007).
[19] J. R. Childress, and R. E. Fontana Jr, C. R. Physique, **6**, 997 (2005).
[20] S. H. Chung, A. Hoffmann, S. D. Bader, C. Liu, B. Kay, L. Makowski, and L. Chen, Appl. Phys. Lett. **85**, 2971 (2004).
[21] M. Arruebo, R. Fernández-Pacheco, M. R. Ibarra, and J. Santamaría, Nano Today **2**, 22 (2007).
[22] A. K. Gupta, and M. Gupta, Biomaterials **26**, 3995 (2005).
[23] G. E. Moore. Electronics Magazine. Retrieved April 1, 2020 (1965-04-19).
[24] Re, Mark, "Tech Talk on HDD Areal Density" (PDF). Seagate (2015).
[25] B. D. Terris, and T. Thomson, J. Phys. D: Appl. Phys. **38**, R199 (2005).
[26] C. Chappert, and P. Bruno, J. Appl. Phys. **64**, 5736 (1988).
[27] J. E. Snyder, M. H. Kryder, and P. Wynblatt, J. Appl.Phys. **67**, 5172 (1990).
[28] D. Makarov, E. Bermúdez-Ureña, O. G. Schmidt, F. Liscio, M. Maret, C. Brombacher, S. Schulze, M. Hietschold, and M. Albrecht, Appl. Phys. Lett. **93**, 153112 (2008).
[29] K. Kobayashi, and G. Ishida, J. Appl. Phys. **52**, 2453 (1981).
[30] Q. Leng, M. Mao, C. Hiner, L. Miloslavsky, M. Miller, S. Tran, C. Qian, and H. C. Tong, IEEE Trans. Magn. **35**, 2553 (1999).
[31] T. Yogi, T.A. Nguyen, S.E. Lambert, G.L. Gorman, and G. Castillo, IEEE Trans. Magn. **26**, 1578 (1990).
[32] H. Hata, T. Hyohno, T. Fukuichi, K. Yabushita, M. Umesaki, and H. Shibata, IEEE Trans. Magn. **26**, 2709 (1990).
[33] Camley, R. E. & Stamps, R. L. J. Phys.: Condens. Matter. **5**, 3727 (1993).
[34] M. N. Baibich, J. M. Broto, A. Fert, F. Nguyen Van Dau, and F. Petroff, Phys. Rev. Lett. **61**, 2472 (1988).
[35] G. Binasch, P. Grünberg, F. Saurenbach, and W. Zinn, Phys. Rev. B **39**, 4828 (1989).
[36] D. C. Ralph, and M. D. Stiles, J. Magn. Magn. Mater. **320**, 1190 (2008).

[37] E. E. Fullerton, D. T. Margulies, M. E. Schabes, M. Carey, B. Gurney, A. Moser, M. Best, G. Zeltzer, K. Rubin, H. Rosen, and M. Doerner, Appl. Phys. Lett. **77**, 3806 (2000).
[38] S. I. Iwasaki, IEEE Trans. Magn. **1**, 71, (1980).
[39] P. F. Carcia, A. D. Meinhaldt, and A. Suna, Appl. Phys. Lett. **47**, 178 (1985).
[40] X. M. Liu , P. Ho , J. S. Chen and A. O. Adeyeye , J. Appl. Phys., 2012, 112 , 073902
[41] S. N. Piramanayagam, J. Appl. Phys. **102**, 011301 (2007).
[42] O. Hellwig, T. Hauet, T. Thomson, E. Dobisz, J. D. Risner-Jamtgaard, D. Yaney, B. D. Terris, and E. E. Fullerton, Appl. Phys. Lett. **95**, 232505 (2009).
[43] O. Hellwig, S. Maat, J. B. Kortright, and E. E. Fullerton, Phys. Rev. B **65**, 144418 (2002).
[44] L. You, R. C. Sousa, S. Bandiera, B. Rodmacq, and B. Dieny, Appl. Phys. Lett, **100**, 172411 (2012).
[45] N. Nakajima, T. Koide, T. Shidara, H. Miyauchi, H. Fukutani, A. Fujimori, K. Iio, T. Katayama, M. Nývlt, and Y. Suzuki, Phys. Rev. Lett. **81**, 5229 (1998).
[46] F. J. A. den Broeder, W. Hoving, and P. J. H. Bloemen, J. Magn. Magn. Mater. **93**, 562 (1991).
[47] N. Amos, R. Fernandez, R. Ikkawi, B. Lee, A. Lavrenov, A. Krichevsky, D. Litvinov, and S. Khizroev, J. Appl. Phys. **103**, 07E732 (2008).
[48] J. Yoon, S.-Y. Park, Y. Jo, M.-H. Jung, C.-Y. You, T. Kim, J. R. Rhee, and Y. K. Kim, Curr. Appl. Phys. **9**, 688 (2009).
[49] M. Hehn, S. Padovani, K. Ounadjela, and J. P. Bucher, Phys. Rev. B **54**, 3428 (1996).
[50] D. Wu, T. Jin, Y. Lou, and F. Wei, Appl. Surf. Sci. **346**, 567 (2015).
[51] M. Coïsson, F. Vinai, P. Tiberto, and F. Celegato, J. Magn. Magn. Mater. **321**, 806 (2009).
[52] F. Luo, F. Zheng, G. Yin, D. Wu, and F. Wei, Appl. Phys. Express **6**, 073003 (2013).
[53] N. Vukadinovic, H. L. Gall, J. B. Y. V. Gehanno, A. Marty, Y. Samson, and B. Gilles, Eur. Phys. J. B **13**, 445 (2000).
[54] C. Banerjee, P. Gruszecki, J. W. Klos, O. Hellwig, M. Krawczyk, and A. Barman, Phys. Rev. B **96**, 024421 (2017).
[55] C. H. Back, and H. C. Siegmann, J. Magn. Magn. Mater. **200**, 774 (1999).
[56] V. Kambersky, Czech J. Phys., Sect. B **26**, 1366 (1976).
[57] P. Bruno, Ferienkurse des Forschungszentrums Zürich, Zürich, (1993).
[58] S. Mizukami, E. P. Sajitha, D. Watanabe, F. Wu, T. Miyazaki, H. Naganuma, M. Oogane, and Y. Ando, Appl. Phys. Lett. **96**, 152502 (2010).
[59] G. Malinowski, F. Dalla Longa, J. H. H. Rietjens, P. V. Paluskar, R. Huijink, H. J. M. Swagten, and B. Koopmans, Nat. Phys. **4**, 855 (2008).
[60] S. Bandiera, R. C. Sousa, S. Auffret, B. Rodmacq, and B. Dieny, Appl. Phys. Lett. **101**, 072410 (2012).
[61] A. Moser, K. Takano, D. T. Margulies, M. Albrecht, Y. Sonobe, Y. Ikeda, S. Sun, E. E. Fullerton, J. Phys. D: Appl. Phys. **35**, R157 (2002).
[62] Z. Liu, P. Huang, S. Hernandez, G. Ju, T. Rausch, IEEE Trans. Magn. **54**, 1 (2018).
[63] L. Neel, Science **174**, 985 (1971).
[64] R. A. Duine, K. J. Lee, S. S. P. Parkin, and M. D. Stiles, Nat. Phys. **14**, 217 (2018).
[65] K. Yakushiji, A. Sugihara, A. Fukushima, H. Kubota, and S. Yuasa, Appl. Phys. Lett. **110**, 092406 (2017).
[66] L. Cuchet, B. Rodmacq, S. Auffret, R. C. Sousa, I. L. Prejbeanu, and B. Dieny, Sci. Rep. **6**, 21246 (2016).
[67] B. N. Engel, J. Åkerman, B. Butcher, R. W. Dave, M. DeHerrera, M. Durlam, G. Grynkewich, J. Janesky, S. V. Pietambaram, N. D. Rizzo, J. M. Slaughter, K. Smith, J. J. Sun, and S. Tehrani. IEEE Trans. Magn. **41**, 132 (2005).
[68] Hayakawa, J., Ikeda, S., Lee, Y. M., Sasaki, R., Meguro, T., Matsukura, F., Takahashi, H. & Ohno, H., Jpn. J. Appl. Phys. **45**, L1057 (2006).

[69] A. Bergman, B. Skubic, J. Hellsvik, L. Nordstrom, A. Delin, and O. Eriksson, Phys. Rev. B **83**, 224429 (2011).
[70] D. Houssameddine, J. F. Sierra, D. Gusakova, B. Delaet, U. Ebels, L. D. Buda-Prejbeanu, M. C. Cyrille, B. Dieny, B. Ocker, J. Langer, and W. Maas, Appl. Phys. Lett. **96**, 072511 (2010).
[71] T. Shiino, S.-H. Oh, P. M. Haney, S.-W. Lee, G. Go, B. G. Park, and K.-J. Lee, Phys. Rev. Lett. **117**, 087203 (2016)
[72] S.-H. Yang, K.-S. Ryu, and S. S. P. Parkin, Nat. Nanotechnol. **10**, 221 (2015).
[73] A. Fernandez-Pacheco, N. J. Steinke, D. Mahendru, A. Welbourne, R. Mansell, S. L. Chin, D. Petit, J. H. Lee, R. Dalgliesh, S. Langridge, and R. P. Cowburn, Adv. Mater. Interf. **3**, 1600097 (2016).
[74] Saarikoski, H., Kohno, H., Marrows, C. H. & Tatara, G. Phys. Rev. B **90**, 094411 (2014).
[75] S. Mizukami, F. Wu, A. Sakuma, J. Walowski, D. Watanabe, T. Kubota, X. Zhang, H. Naganuma, M. Oogane, Y. Ando, and T. Miyazaki, Phys. Rev. Lett. **106**, 117201 (2011).
[76] S. Mizukami, A. Sugihara, S. Iihama, Y. Sasaki, K. Z. Suzuki, and T. Miyazaki, Appl. Phys. Lett. **108**, 012404 (2016).
[77] S. Lenne, Y.-C. Lau, A. Jha, G. Y. P. Atcheson, R. E. Troncoso, A. Brataas, J. M. D. Coey, P. Stamenov, and K. Rode, arXiv preprint arXiv:1903.04432
[78] A. Barman, V. V. Kruglyak, R. J. Hicken, J. Scott, A. Kundrotaite, and M. Rahman, J. Appl. Phys. **95**, 6998 (2004).
[79] R. Skomski, J. P. Liu, and D. J. Sellmyer, Phys. Rev. B **60**, 7359 (1999).
[80] S. Tehrani, E. Chen, M. Durlam, M. DeHerrera, J. M. Slaughter, J. Shi, and G. Kerszykowski, J. Appl. Phys. **85**, 5822 (1999).
[81] J.-S. Lee, J. Mater. Chem. **21**, 14097 (2011).
[82] R. C. Sousa and I. L. Prejbeanu, C. R. Physique **6**, 1013 (2005).
[83] T. Thomson, G. Hu, and B. D. Terris, Phys. Rev. Lett. **96**, 257204 (2006).
[84] B. D. Terris, T. Thomson, and G. Hu, Microsyst. Technol. **13**, 189 (2007).
[85] O. Hellwig, A. Berger, T. Thomson, E. Dobisz, Z. Z. Bandic, H. Yang, D. S. Kercher, and E. E. Fullerton, Appl. Phys. Lett. **90**, 162516 (2007).
[86] J. R. Childress, and R. E. Fontana Jr, C. R. Physique **6**, 997 (2005).
[87] D. A. Allwood, G. Xiong, C. C. Faulkner, D. Atkinson, D. Petit, and R. P. Cowburn, Science **309**, 1688 (2005).
[88] A. V. Chumak, A. A. Serga, and B. Hillebrands, Nat. Commun. **5**, 4700 (2014).
[89] S. K. Kim, K. S. Lee, and D. S. Han, Appl. Phys. Lett. **95**, 082507 (2009).
[90] Y. Au, M. Dvornik, O. Dmytriiev and V.V. Kruglyak, Appl. Phys. Lett. **100**, 172408 (2012).
[91] K. Vogt, F. Y. Fradin, J. E. Pearson, T. Sebastian, S. D. Bader, B. Hillebrands, A. Hoffmann and H. Schultheiss, Nat. Commun. **5**, 3727 (2014).
[92] K. S. Lee and S. K. Kim, J. Appl. Phys. **104**, 053909 (2008).
[93] V. E. Demidov, S. Urazhdin, H. Ulrichs, V. Tiberkevich, A. Slavin, D. Baither, G. Schmitz, and S. O. Demokritov, Nat. Mater. **11**, 1028 (2012).
[94] S. Kaka, M. R. Pufall, W. H. Rippard, T. J. Silva, S. E. Russek, and J. A. Katine, Nature **437**, 389 (2005).
[95] A V Chumak, A A Serga, and B Hillebrands, J. Phys. D: Appl. Phys. **50**, 244001 (2017).
[96] B. Lenk, H. Ulrichs, F. Garbs, M. Münzenberg, Phys. Rep. **507**, 107 (2011).
[97] S. Lequeux, J. Sampaio, V. Cros, K. Yakushiji, A. Fukushima, R. Matsumoto, H. Kubota, S. Yuasa, and J. Grollier, Sci. Rep. **6**, 31510 (2016).
[98] S. H. Chung, A. Hoffmann, S. D. Bader, C. Liu, B. Kay, L. Makowski, and L. Chen, Appl. Phys. Lett. **85**, 2971 (2004).

[99] M. Arruebo, R. Fernández-Pacheco, M. R. Ibarra, and J. Santamaría, Nano Today **2**, 22 (2007).
[100] F. Bloch, "Zur theorie des ferromagnetismus," Z. Phys. **61**, 206 (1930).
[101] A. V. Chumak, V. I. Vasyuchka, A. A. Serga and B. Hillebrands, Nat. Phys. **11**, 453 (2015).
[102] P. Graczyk and M. Krawczyk, Phys. Rev. B **96**, 024407 (2017).
[103] W. Yu, T. Yu, and G. E. W. Bauer, Phys. Rev. B **102**, 064416 (2020).
[104] Y. V. Gulyaev, and S. A. Nikitov, Dokl. Physics **46**, 687 (2001).
[105] M. Kostylev, P. Schrader, R. L. Stamps, G. Gubbiotti, G. Carlotti, A. O. Adeyeye, S. Goolaup, and N. Singh, Appl. Phys. Lett. **92**, 132504 (2008).
[106] Z. K. Wang, V. L. Zhang, H. S. Lim, S. C. Ng, M. H. Kuok, S. Jain, A. O. Adeyeye, ACS Nano **4**, 643 (2010).
[107] V. V. Kruglyak, A. Barman, R. J. Hicken, J. Appl. Phys. **97**, 10A706 (2005).
[108] B. Rana, D. Kumar, S. Barman, S. Pal, Y. Fukuma, Y. Otani, and A. Barman, ACS Nano **5**, 9559 (2011).
[109] J. R. Vivas, S. Mamica, M. Krawczyk, and V. V. Kruglyak, Phys. Rev. B **86**, 144417 (2012).
[110] S. Sahoo, S. Mondal, G. Williams, A. May, S. Ladak, and A. Barman, Nanoscale, **10**, 9981 (2018).
[111] N. I. Polushkin, S. A. Michalski, L. Yue, R. D. Kirby, Phys. Rev. Lett. **97**, 256401 (2006).
[112] B. Obry, P. Pirro, T. Bracher, A. V. Chumak, J. Osten, F. Ciubotaru, A. A. Serga, J. Fassbender, and B. Hillebrands, Appl. Phys. Lett. **102**, 202403 (2013).
[113] A. De, S. Mondal, S. Sahoo, S. Barman, Y. Otani, R. K. Mitra and A. Barman, Beilstein J. Nanotechnol. **9**, 1123 (2018).
[114] S. Mondal, M. A. Abeed, K. Dutta, A. De, S. Sahoo, A. Barman, and S. Bandyopadhyay, ACS Appl. Mater. Interf. **10**, 43970 (2018).
[115] R. L. Stamps and R. E. Camley, J. Magn. Magn. Mater. **813**, 177 (1998).
[116] R. L. Stamps and R. E. Camley, Phys. Rev. B **60**, 12264 (1999).
[117] S. Jung, B. Watkins, L. DeLong, J. B. Ketterson, and V. Chandrasekhar, Phys. Rev. B **66**, 132401 (2002).
[118] G. Gubbiotti, G. Carlotti, T. Okuno, T. Shinjo, F. Nizzoli, and R. Zivieri, Phys. Rev. B **68**, 184409 (2003).
[119] G. N. Kakazei, P. E. Wigen, K. Y. Guslienko, V. Novosad, A. N. Slavin, V. O. Golub, N. A. Lesnik, and Y. Otani, Appl. Phys. Lett. **85**, 443 (2004).
[120] 117V. V. Kruglyak, A. Barman, R. J. Hicken, J. R. Childress, and J. A. Katine, J. Appl. Phys. **97**, 10A706 (2005).
[121] V. V. Kruglyak, P. S. Keatley, R. J. Hicken, J. R. Childress, and J. A. Katine, Phys. Rev. B **75**, 024407 (2007).
[122] P. S. Keatley, V. V. Kruglyak, A. Neudert, E. A. Galaktionov, R. J. Hicken, J. R. Childress, and J. A. Katine, Phys. Rev. B **78**, 214412 (2008).
[123] J. M. Shaw, T. J. Silva, M. L. Schneider, and R. D. McMichael, Phys. Rev. B **79**, 184404 (2009).
[124] V. V. Kruglyak, P. S. Keatley, A. Neudert, R. J. Hicken, J. R. Childress, and J. A. Katine, Phys. Rev. Lett. **104**, 027201 (2010).
[125] B. Rana, S. Pal, S. Barman, Y. Fukuma, Y. Otani, and A. Barman, Appl. Phys. Express **4**, 113003 (2011).
[126] P. V. Bondarenko, A. Y. Galkin, B. A. Ivanov, and C. E. Zaspel, Phys. Rev. B **81**, 224415 (2010).
[127] S. Saha, R. Mandal, S. Barman, D. Kumar, B. Rana, Y. Fukuma, S. Sugimoto, Y. Otani, and A. Barman, Adv. Funct. Mater. **23**, 2378 (2013).

[128] S. Mondal, S. Barman, S. Choudhury, Y. Otani, and A. Barman, J. Mag. Mag. Mat. **458**, 95 (2018).
[129] B. K. Mahato, B. Rana, D. Kumar, S. Barman, S. Sugimoto, Y. Otani, and A. Barman, Appl. Phys. Lett. **105**, 012406 (2014).
[130] K. Adhikari, S. Choudhury, R. Mandal, S. Barman, Y. Otani, and A. Barman, J. Appl. Phys. **121**, 043909 (2017).
[131] K. Adhikari, S. Sahoo, A. K. Mondal, Y. Otani, and A. Barman, Phys. Rev. B **101**, 054406 (2020).
[132] O. N. Martyanov, V. F. Yudanov, R. N. Lee, S. A. Nepijko, H. J. Elmers, R. Hertel, C. M. Schneider, and G. Schönhense, Phys. Rev. B **75**, 174429 (2007).
[133] S. Tacchi, M. Madami, G. Gubbiotti, G. Carlotti, A. O. Adeyeye, S. Neusser, B. Botters, and D. Grundler, IEEE Trans. Magn. **46**, 172 (2010).
[134] H. Ulrichs, B. Lenk, and M. Münzenberg, Appl. Phys. Lett. **97**, 092506 (2010).
[135] S. Neusser, G. Duerr, H. G. Bauer, S. Tacchi, M. Madami, G. Woltersdorf, G. Gubbiotti, C. H. Back, and D. Grundler, Phys. Rev. Lett. **105**, 067208 (2010).
[136] T. Schwarze, R. Huber, G. Duerr, and D. Grundler, Phys. Rev. B **85**, 134448 (2012).
[137] R. Bali, M. Kostylev, D. Tripathy, A. O. Adeyeye, and S. Samarin, Phys. Rev. B **85**, 104414 (2012).
[138] S. Tacchi, M. Madami, G. Gubbiotti, G. Carlotti, H. Tanigawa, T. Ono, and M. P. Kostylev, Phys. Rev. B **82**, 024401 (2010).
[139] S. Neusser, B. Botters, M. Becherer, D. Schmitt-Landsiedel and D. Grundler, Appl. Phys. Lett. **93**, 122501 (2008).
[140] K. Adhikari, S. Barman, R. Mandal, Y. Otani and A. Barman, Phys. Rev. Appl. **10**, 044010 (2018).
[141] S. Choudhury, S. Majumder, S. Barman, Y. Otani and A. Barman, Phys. Rev. Appl. **10**, 064044 (2018).
[142] F. Montoncello, L. Giovannini and M. Krawczyk, J. Appl. Phys. **112**, 033911 (2012).
[143] S. Neusser, G. Duerr, S. Tacchi, M. Madami, M. L. Sokolovskyy, G. Gubbiotti, M. Krawczyk and D. Grundler, Phys. Rev. B **84**, 094454 (2011).
[144] R. Mandal, P. Laha, K. Das, S. Saha, S. Barman, A. K. Raychaudhuri and A. Barman, Appl. Phys. Lett. **103**, 262410 (2013).
[145] R. Mandal, S. Saha, D. Kumar, S. Barman, S. Pal, K. Das, A. K. Raychaudhuri, Y. Fukuma, Y. Otani and A. Barman, ACS Nano **6**, 3397 (2012).
[146] R. Mandal, S. Barman, S. Saha, Y. Otani and A. Barman, J. Appl. Phys. **118**, 053910 (2015).
[147] S. Pal, J. W. Klos, K. Das, O. Hellwig, P. Gruszecki, M. Krawczyk and A. Barman, Appl. Phys. Lett. **105**, 162408 (2014).
[148] S. Mallick, S. Mondal, T. Seki, S. Sahoo, T. Forrest, F. Maccherozzi, Z. Wen, S. Barman, A. Barman, K. Takanashi and S. Bedanta, Phys. Rev. Appl. **12**, 014043 (2019).
[149] A. De, S. Mondal, S. Choudhury, S. Sahoo, S. Majumder, S. Barman, Y. Otani, and A. Barman, J. Mag. Mag. Mat. **487**, 165263 (2019).
[150] A. Manzin, G. Barrera, F. Celegato, M. Coïsson, and P. Tiberto, Sci. Rep. **6**, 22004 (2016).
[151] G. Venkat, N. Kumar, and A. Prabhakar, IEEE Trans. Mag., **50**, 11 (2014).
[152] S. Choudhury, S. Barman, Y. Otani, and A. Barman, ACS Nano **11**, 8814 (2017).
[153] S. Choudhury, S. Barman, Y. Otani, and A. Barman, J. Magn. Magn. Mater. **489**, 165408 (2019).
[154] A. De, K. Dutta, S. Mondal, S. Barman, Y. Otani, and A. Barman, Phys. Rev. B, **103**, 064402 (2021).
[155] D. Levine, and P. J. Steinhardt, Phys. Rev. B **34**, 596 (1986).

[156] C. H. Chen, R. Z. Qiu, C. H. Chang, and W. J. Hsueh, AIP Adv. **4**, 087102 (2014).
[157] C. H. O. Costa, M. S. Vasconcelos, P. H. R. Barbosa, and F. F. Barbosa Filho, J. Magn. Magn. Mater. **324**, 2315 (2012).
[158] C. H. O. Costa, M. S. Vasconcelos, and E. L. Albuquerque, J. Appl. Phys. **109**, 07D319 (2011).
[159] S. V. Grishin, E. N. Beginin, M. A. Morozova, Y. P. Sharaevskii, and S. A. Nikitov, J. Appl. Phys. **115**, 053908 (2014).
[160] W. J. Hsueh, C. H. Chen, and R. Z. Qiu, Phys. Lett. A **377**, 1378 (2013).
[161] J. Rychły, S. Mieszczak, and J. W. Kłos, J. Magn. Magn. Mater. 450, 18 (2018).
[162] V. S. Bhat and D. Grundler, Phys. Rev. B **98**, 174408 (2018).
[163] S. Watanabe, V. S. Bhat, K. Baumgaert, and D. Grundler, Adv. Funct. Mater. **30**, 2001388 (2020).
[164] F. Lisiecki, J. Rychły, P. Kuswik, H. Głowinski, J. W. Kłos, F. Groß, N. Träger, I. Bykova, M. Weigand, M. Zelent, E. J. Goering, G. Schütz, M. Krawczyk, F. Stobiecki, J. Dubowik, and J. Grafe, Phys. Rev. Appl. **11**, 054061 (2019).
[165] B. Farmer, V. S. Bhat, A. Balk, E. Teipel, N. Smith, J. Unguris, D. J. Keavney, J. T. Hastings, and L. E. De Long, Phys. Rev. B **93**, 134428 (2016).
[166] M. Senechal, Quasicrystals and Geometry (Cambridge University Press, Cambridge, 1996).
[167] M. Gardner, Penrose Tiles to Trapdoor Ciphers: And the Return of Dr Matrix, MAA Spectrum, Mathematical Association of America, Spectrum Series (Cambridge University Press, Cambridge, 1997), p. 41.
[168] S. Tacchi, G. Duerr, J. W. Klos, M. Madami, S. Neusser, G. Gubbiotti, G. Carlotti, M. Krawczyk, and D. Grundler, Phys. Rev. Lett. **109**, 137202 (2012).
[169] Z. K. Wang, V. L. Zhang, H. S. Lim, S. C. Ng, M. H. Kuok, S. Jain, and A. O. Adeyeye, Appl. Phys. Lett. **94**, 083112 (2009).
[170] Z. K. Wang, V. L. Zhang, H. S. Lim, S. C. Ng, M. H. Kuok, S. Jain, and A. O. Adeyeye, ACS Nano **4**, 643 (2010).
[171] C. S. Lin, H. S. Lim, Z. K. Wang, S. C. Ng, and M. H. Kuok, Appl. Phys. Lett. **98**, 022504 (2011).
[172] V. L. Zhang, H. S. Lim, C. S. Lin, Z. K. Wang, S. C. Ng, M. H. Kuok, S. Jain, A. O. Adeyeye, and M. G. Cottam, Appl. Phys. Lett. **99**, 143118 (2011).
[173] G. Duerr, M. Madami, S. Neusser, S. Tacchi, G. Gubbiotti, G. Carlotti, and D. Grundler, Appl. Phys. Lett. **99**, 202502 (2011).
[174] G. Gubbiotti, S. Tacchi, M. Madami, G. Carlotti, S. Jain, A. O. Adeyeye, and M. P. Kostylev, Appl. Phys. Lett. **100**, 162407 (2012).
[175] G. Duerr, M. Madami, S. Neusser, S. Tacchi, G. Gubbiotti, G. Carlotti, and D. Grundler, Appl. Phys. Lett. **99**, 202502 (2011).
[176] G. Duerr, S. Tacchi, G. Gubbiotti, and D. Grundler, J. Phys. D: Appl. Phys. **47**, 325001 (2014).
[177] M. Krawczyk, S. Mamica, M. Mruczkiewicz, J. W. Klos, S. Tacchi, M. Madami, G. Gubbiotti, G. Duerr, and D. Grundler, J. Phys. D: Appl. Phys. **46**, 495003 (2013).
[178] S. Choudhury, S. Saha, R. Mandal, S. Barman, Y. Otani, and A. Barman, ACS Appl. Mater. Interf. **8**, 18339 (2016).
[179] H. Yu, G. Duerr, R. Huber, M. Bahr, T. Schwarze, F. Brandl, and D. Grundler, Nat Commun **4**, 2702 (2013).
[180] S. Saha, S. Barman, J. Ding, A. O. Adeyeye, and A. Barman, Appl. Phys. Lett. **102**, 242409 (2013).
[181] N. Porwal, K. Dutta, S. Mondal, S. Choudhury, J. Sinha, A. Barman, and P. K. Datta, J. Magn. Magn. Mater. **501**, 166378 (2020).

[182] N. Tahir, M. Zelent, R. Gieniusz, M. Krawczyk, A. Maziewski, T. Wojciechowski, J. Ding, and A. O. Adeyeye, J. Phys. D: Appl. Phys. **50**, 025004 (2017).
[183] N. Singh, C. C. Wang, and A. O. Adeyeye, J. Magn. Magn. Mater. **320**, 113 (2008).
[184] J. Ding, N. Singh, M. Kostylev, and A. O. Adeyeye, Phys. Rev. B **88**, 014301 (2013).
[185] M. Sushruth, J. Ding, J. Duczynski, R. C. Woodward, R. A. Begley, H. Fangohr, R. O. Fuller, A. O. Adeyeye, M. Kostylev, and P. J. Metaxas, Phys. Rev. Appl. **6**, 044005 (2016).
[186] N. Porwal, A. De, S. Mondal, K. Dutta, S. Choudhury, J. Sinha, A. Barman, and P. K. Datta, Sci. Rep. **9**, 12138 (2019).
[187] M. Krupinski, P. Sobieszczyk, P. Zieliński, and M. Marszałek, Sci. Rep. **9**, 13276 (2019).
[188] D. Tripathy and A. O. Adeyeye, New J. Phys **13**, 023035 (2011).
[189] M. T. Rahman, N. N. Shams, C. H. Lai, J. Fidler, and D. Suess, Phys. Rev. B **81**, 014418 (2010).
[190] S. N. Piramanayagam, M. Ranjbar, H. K. Tan, W. C. Allen Poh, R. Sbiaa, and T. C. Chong, J. Appl. Phys. **111**, 07B916 (2012).
[191] M. Krawczyk, S. Mamica, J. W. Kłos, J. Romero-Vivas, M. Mruczkiewicz, and A. Barman, J. Appl. Phys. **109**, 113903 (2011).
[192] J. M. Shaw, S. E. Russek, T. Thomson, M. J. Donahue, B. D. Terris, O. Hellwig, E. Dobisz, and M. L. Schneider, Phys. Rev. B **78**, 024414 (2008).
[193] S. Pal, J. W. Klos, K. Das, O. Hellwig, P. Gruszecki, M. Krawczyk, and A. Barman, Appl. Phys. Lett. **105**, 162408 (2014).
[194] S. Pan, S. Mondal, M. Zelent, R. Szwierz, S. Pal, O. Hellwig, M. Krawczyk, and A. Barman, Phys. Rev. B **101**, 014403 (2019).
[195] S. Zhang, A. K. Petford-Long, and C. Phatak, Sci. Rep. **6**, 31248 (2016).
[196] Y. Li, G. Gubbiotti, F. Casoli, F. J. T. Gonçalves, S. A. Morley, M. C. Rosamond, E. H. Linfield, C. H. Marrows, S. McVitie, and R. L. Stamps, J. Phys. D Appl. Phys. **50**, 015003 (2017).
[197] S. Mamica, X. Zhou, A. Adeyeye, M. Krawczyk, and G. Gubbiotti, Phys. Rev. B **98**, 054405 (2018).
[198] S. Woo, K. M. Song, H.-S. Han, M.-S. Jung, M.-Y. Im, K.-S. Lee, K. S. Song, P. Fischer, J.-I. Hong, J. W. Choi, B.-C. Min, H. C. Koo, and J. Chang, Nat. Commun. **8**, 15573 (2017).
[199] S. Mamica, M. Krawczyk, M. L. Sokolovskyy, and J. Romero-Vivas, Phys. Rev. B **86**, 144402 (2012).
[200] A. Fernández-Pacheco, R. Streubel, O. Fruchart, R. Hertel, P. Fischer, and R. P. Cowburn, Nat. Commun. **8**, 15756 (2017).
[201] M. T. Alam, M. J. Siddiq, G. H. Bernstein, M. T. Niemier, W. Porod, and X. S. Hu, IEEE Trans. Nanotechnol. **9**, 348 (2010).
[202] D. C. Ralph and M. D. Stiles, J. Magn. Magn. Mater. **320**, 1190 (2008).
[203] M. Yamanouchi, D. Chiba, F. Matsukura, and H. Ohno, Nature, **428**, 539 (2004).
[204] K. Roy, S. Bandyopadhyay, J. Atulasimha, Appl. Phys. Lett. 99, 063108 (2011).
[205] N. D'Souza, M. Salehi-Fashami, S. Bandyopadhyay, J. Atulasimha, Nano Lett. 16, 1069 (2016).
[206] N. D'Souza, A. Biswas, H. Ahmad, M. Salehi-Fashami, M. M. Al-Rashid, V. Sampath, D. Bhattacharya, M. A. Abeed, J. Atulasimha, S. Bandyopadhyay, Nanotechnology, 29, 442001 (2018).
[207] X. Zhaoa, and D. G. Lord, J. Appl. Phys. **99**, 08M703 (2006).
[208] H. Zhou, S. Shi, D. Nian, S. Cui, J. Luo, Y. Qiu, H. Yang, M. Zhu, and G. Yu, Nanoscale, **27** (2020).
[209] D. B. Gopman, C. L. Dennis, P. J. Chen, Y. L. Iunin, P. Finkel, M. Staruch, and R. D. Shull, Sci. Rep. **6**, 27774 (2016).

[210] I. Gilbert, A. C. Chavez, D. T. Pierce, J. Unguris, W.-Y. Sun, C.-Y. Liang, and G. P. Carman Appl. Phys. Lett. **109**, 162404 (2016).
[211] C. Berk, M. Jaris, W. Yang, S. Dhuey, S. Cabrini, H. Schmidt, Nat. Commun.**10**, 2652 (2019).
[212] Z. Xiao, R. Lo Conte, M. Goiriena-Goikoetxea, R. V. Chopdekar, C.-H. A. Lambert, X. Li, A. T. N'Diaye, P. Shafer, S. Tiwari, A. Barra, A. Chavez, K. P. Mohanchandra, G. P. Carman, K. L. Wang, S. Salahuddin, E. Arenholz, J. Bokor, R. N. Candler, ACS Appl. Mater. Interfaces **12**, 6752 (2020).
[213] Y. Yahagi, B. Harteneck, S. Cabrini, H. Schmidt, Phys. Rev. B **90**, 140405 (R) (2014).
[214] W. Edrington, U. Singh, M. A. Dominguez, J. R. Alexander, R. Nepal, S. Adenwalla, Appl. Phys. Lett. **112**, 052402 (2018).
[215] L. M. Loong, X. Qiu, Z. P. Neo, P. Deorani, Y. Wu, C. S. Bhatia, M. Saeys, and H. Yang, Sci. Rep. **4**, 6505 (2014).
[216] N. Roschewsky, S. Schafer, F. Hellman, and V. Nikitin, Appl. Phys. Lett. **112**, 232401 (2018).
[217] J. L. Drobitch, A. De, K. Dutta, P. K. Pal, A. Adhikari, A. Barman, and S. Bandyopadhyay, Adv. Mater. Technol. 2000316 (2020).
[218] M. A. Abeed, J. Atulasimha, and S. Bandyopadhyay, J. Phys. Condens. Matter. **30**, 394001 (2018).

Chapter 2

2. Theoretical Framework

The era of basic magnetism was initiated with the discovery of magnetic poles by P. Peregrines, who wrote the first extant treatise describing the properties of magnets. Since then, the theoretical contents have been enriched by the rigours and consistent efforts of researchers and various fundamental theories have been proposed to understand the origin of magnetization in different magnetic materials which can be classified into five broad groups: diamagnet, paramagnet, ferromagnet, ferrimagnet and antiferromagnet. Among these, the ferromagnets are found to possess most challenging and interesting properties to be explored by the ultrafast optical microscopy including characteristic demagnetization times in femtosecond range, magnetization relaxation times in low picoseconds range, precession frequency varying over a broad range, domain-wall width and spin-wave wavelengths in the nanometer range. The modern research deals with nanoscale ferromagnetic systems, which are indispensable for the development of future spintronic devices. Apart from technological importance, ferromagnetic nanostructures are also interesting from fundamental point of view because of the non-trivial static and dynamic behavior of the magnetization in such small confined geometries. Several characteristic magnetic properties of nanoscale ferromagnetic media display a strong dependence on the particle shape and size. Hence, understanding the theory behind the strong impact of nanopatterning on the magnetic properties of ferromagnets is of utmost importance, for which, the quantum mechanical concept of 'spin' degrees of freedom becomes imperative than the classical ones.

This chapter provides the fundamental framework and basic theories of various properties of ferromagnetic systems, which form the basis of our investigation. The chapter starts with an overview of the various energies that play a role in the dynamics of a ferromagnetic system. Next, we focus on the magnetization dynamics followed by the illustration of different aspects of spin waves. Finally, the basic theories of synthetic antiferromagnets and magnetoelastic coupling and the underlying physics of magneto-optical Kerr effect have been presented.

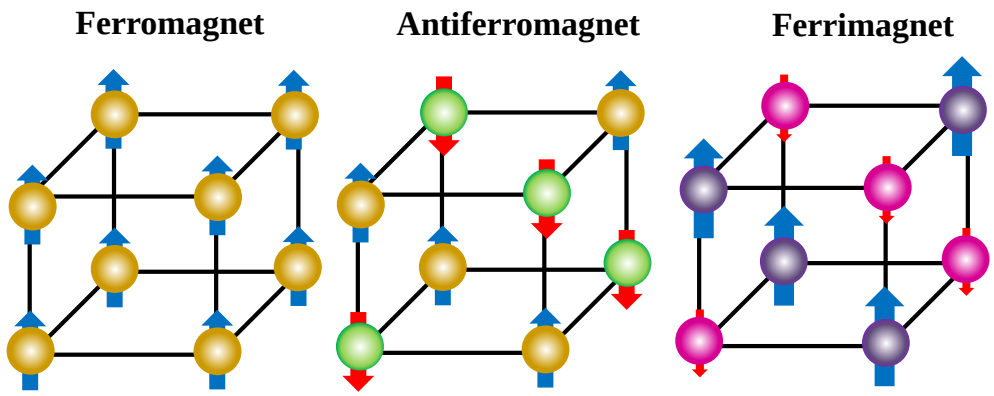

Fig. 2.1: Spin orientations in ferromagnet, antiferromagnet and ferrimagnet.

2.1. Magnetic Energy

The total energy of a ferromagnetic material consists of several energy terms such as Zeeman energy (arises in response to an external magnetic field), exchange energy, magnetostatic self-energy (also known as demagnetizing energy), and magnetic anisotropy energy.

$$E_{total} = E_Z + E_{ex} + E_d + E_K \quad (2.1)$$

where, E_Z is the Zeeman energy, E_{ex} is the exchange energy, E_d is the demagnetizing energy and E_K is the anisotropy energy. In equilibrium, the system is in a local minimum of the total free energy. A brief outline of some of the vital energy factors are as follows:

2.1.1. Zeeman Energy

The Zeeman energy describes the interaction of the magnetization M with an external magnetic field H_0. The energy is given by:

$$E_Z = -\mu_0 \int_V M.H_0 d\tau \quad (2.2)$$

where V is the volume occupied by the magnetic structure and dτ the volume element. This equation states that in presence of an external magnetic field, the magnetization tends to align along H_0 for the energy minimization.

2.1.2. Exchange Energy

The exchange interaction [1] between the neighbouring magnetic moments, forces the moments into parallel or antiparallel alignment. It stems from the Coulomb interaction energy

and Pauli Exclusion Principle. The expression of Heisenberg Hamiltonian for exchange energy is:

$$E_{ex} = -\sum_{i,j} J_{ij}\, S_i . S_j \quad (2.3)$$

where J_{ij} is the exchange integral and S_i and S_j is the spin operator of i^{th} and j^{th} spin.

J_{ij} = +1 for parallel arrangement of the spin, i.e., for ferromagnetic arrangement.

J_{ij} = -1 for antiparallel arrangement of the spin, i.e., for antiferromagnet arrangement.

Considering the continuum model, E_{ex} can be expressed as:

$$E_{ex} = A \int_V (\nabla m)^2 \, d^3r \quad (2.4)$$

where, $m = M/M_s$ is the ratio of magnetization to the saturation magnetization. The summation in Eq. 2.3 is replaced by Eq. 2.4 considering m as a continuously defined vector quantity and A is the exchange stiffness coefficient given by:

$$A = \frac{2JS^2}{a} \quad (2.5)$$

where, a is the lattice constant. The value of A for Ni, Co, Fe and Py are 9×10^{-12} J/m, 30×10^{-12} J/m, 21×10^{-12} J/m, and 13×10^{-12} J/m, respectively.

The aforementioned exchange is also known as the direct exchange interaction, in which the electrons of magnetic atoms interact with its nearest neighbours. The exchange energy is a short range interaction and depends upon the nearest neighbours. Exchange can also occur in indirect ways, which couples magnetic moments over relatively larger distances. Examples of various types of indirect exchange are: (i) RKKY (Ruderman–Kittel–Kasuya–Yosida) exchange, where the localized inner d- or f-shell electron spins in a metal are coupled with the conduction electrons; (ii) super-exchange, where the exchange is mediated via different non-magnetic ion; (iii) antisymmetric exchange (also known as Dzyaloshinskii-Moriya interaction (DMI)), where the spin orbit interaction (SOI) plays major role and often leads to canting of spins by small angle.

2.1.2.1. RKKY Exchange

The RKKY interaction is a long range exchange interaction between localized inner d-electrons and conduction electrons of a metal. It was originally proposed by Malvin Ruderman and Charles Kittel [2] to explain unusually broad nuclear spin resonance lines in metallic Ag. A second-order perturbation theory was used to describe the indirect exchange coupling in which the nuclear spin of one atom interacts with itinerant electrons through the hyperfine interaction. Later, Tadao Kasuya [3] proposed a similar indirect exchange coupling, which could be applied

to the inner d-electron (localized) spins that interact with the itinerant electrons. This theory was further expanded by Kei Yosida. The RKKY exchange interaction takes the following form:

$$H(R_{ij}) = \frac{S_i.S_j}{4} \frac{|\Delta|^2 m^*}{(2\pi)^3 R_{ij}^4 \hbar^2} \left[2k_F R_{ij} cos(2k_F R_{ij}) - sin(2k_F R_{ij})\right] \quad (2.6)$$

Where, H represents the Hamiltonian, R_{ij} is the distance between the nuclei i and j, S_i is the nuclear spin of atom i, m^* is the effective mass of the electrons in the crystal, k_F is the Fermi momentum and Δ is a matrix element that represents the strength of the hyperfine interaction. An interesting property of the RKKY exchange is that it experiences oscillations with the period π/k_F as a function of distance between localized spins. These are known as Friedel oscillations which play an important role in giant magnetoresistance (GMR) and spin glasses.

2.1.2.2. Superexchange

The direct exchange is unable to explain the antiferromagnetism of most transition-metal compounds. Most antiferromagnetic insulators are transition-metal oxides, so that the transition-metal cations are separated by large oxygen anions and consequently, direct hopping between the *d*-orbitals is unlikely to occur. Superexchange, also known as Kramers–Anderson superexchange, is a kind of indirect magnetic interaction, which is the strong antiferromagnetic coupling between two next-to-nearest neighbour cations via a non-magnetic anion. It was originally proposed by Hendrik Kramers in 1934 [4] when he observed that in crystals like MnO, the Mn atoms interact with one another despite having nonmagnetic oxygen atoms between them. Later, Phillip Anderson [5] refined the Kramers' model. The coupling between the cations through the non-magnetic anions can be either ferro- or antiferromagnetic determined by the Goodenough-Kanamori-Anderson (GKA) [6, 7] rules. Superexchange is short ranged interaction as compared to other types of magnetic interaction based on direct exchange.

2.1.2.3. Anisotropic Exchange

The spin-orbit interaction (SOI) results in an anisotropic contribution to the exchange Hamiltonian of two electrons. The anisotropic exchange interaction exists in structures that exhibit broken inversion symmetry. The interaction has both symmetric and antisymmetric parts with respect to permutation of spin components. Antisymmetric exchange, also known as the Dzyaloshinskii–Moriya interaction (DMI) [8, 9], is a contribution to the total magnetic

exchange interaction between two neighbouring magnetic spins S_i and S_j. DMI arises from the inversion symmetry breaking at the interfaces between a ferromagnetic (FM) and a non-magnetic heavy metal (HM) layer, having strong SOI. The Hamiltonian for DMI can be written as:

$$H_{DM} = D_{ij} . (S_i \times S_j) \quad (2.7)$$

The DMI at the interface between ferromagnetic (FM) and non-magnetic heavy metals (HMs) plays a pivotal role for the stabilization of chiral spin textures, such as magnetic skyrmions [10] and skyrmion bubbles.

2.1.3. Interlayer Exchange Coupling Energy

While stacking two ferromagnetic (FM) layers separated by a non-magnetic (NM) spacer layer to form a synthetic antiferromagnet (SAF) [11], the magnetizations of the two magnetic layers interact via interlayer exchange coupling (IEC). Such coupling originates from the scattering of electrons at the interfaces between the FM layers and the NM spacers. The IEC energy per unit area is given by [12]:

$$E_{IEC} = -J_1 \frac{M_1.M_2}{M_{S1}M_{S2}} - J_2 \left(\frac{M_1.M_2}{M_{S1}M_{S2}}\right)^2 \quad (2.8)$$

where J_1 and J_2 are, respectively, the bilinear and biquadratic coupling constants, which have units of erg/cm^2. They are associated to effective exchange fields $H_{ex1}^{(i)} = J_1/M_i d_i$ and $H_{ex2}^{(i)} = J_2/M_i d_i$, M_1 and M_2 are the magnetizations of the two ferromagnetic layers, with M_{s1} and M_{s2} corresponding to the saturation values. $J_1 > 0$ and $J_1 < 0$ correspond, respectively, to ferromagnetic and antiferromagnetic couplings. In the case of biquadratic coupling, $J_2 > 0$ tends to make the magnetizations in the two films to lie at 90° to one another, whereas, if $J_{1,2} > 0$, a parallel alignment between the two ferromagnetic states is favoured.

2.1.4. Magnetostatic Self Energy or Demagnetizing Energy

Magnetostatic self energy in a ferromagnetic material originates due to the interaction between the magnetic dipoles. This is also known as demagnetizing energy and is expressed as:

$$E_d = -\frac{1}{2} H_d . M \quad (2.9)$$

where, H_d is the demagnetizing field.

$$H_d = -N_d . M \quad (2.10)$$

where, N_d is the demagnetizing factor.

In continuum limit, the demagnetizing energy is expressed as:

$$E_d = -\frac{1}{2}\,\mu_0 \int_{sample} M.H_d\, d^3r \qquad (2.11)$$

The demagnetizing energy depends upon the entire sample, i.e., it is a long range interaction.

2.1.5. Magnetic Anisotropy

Magnetic anisotropy [13] describes how the magnetic properties of a material depend on the direction. Generally, it is noticed that the magnetization is oriented along some preferred direction in space (easy axes of magnetization) along which a magnetic system is easier to magnetize than the other. Deviation from these directions imposes an energy loss, known as the anisotropy energy [14, 15].

2.1.5.1. Magnetocrystalline Anisotropy

It is an intrinsic property of the material caused by the spin-orbit interaction (SOI). The spatial arrangement of the orbital electrons is strongly associated with the crystallographic structure. Consequently, the interaction between the electrons and spins leads to the alignment of the spins along well defined crystallographic axes [16].

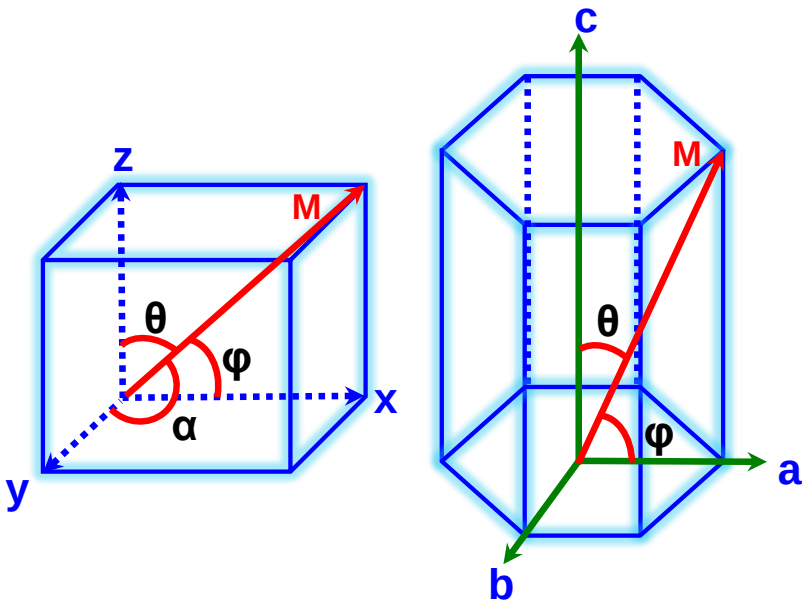

Fig. 2.2: Coordinate system for (a) uniaxial hexagonal closed packed system and (b) cubic system.

The anisotropic energy in cubic structure can be expressed as:

$$E_{cryst} = K_0 + K_1\left(\alpha_x^2\alpha_y^2 + \alpha_y^2\alpha_z^2 + \alpha_z^2\alpha_x^2\right) + K_2\alpha_x^2\alpha_y^2\alpha_z^2 + \ldots. \quad (2.12)$$

The anisotropic energy in hcp structure can be expressed as:

$$E_{cryst} = K_0 + K_1(sin^2\theta) + K_2(sin^4\theta) + (K_3 + K_3'cos6\varphi)sin^6\theta \quad (2.13)$$

Here K_0, K_1, K_2, K_3, and K'_3 are anisotropy constants. α_1, α_2 and α_3 are the three components of magnetization direction. θ (φ) is the angle between a (c) axes with magnetization vector in hcp structure. However, as an hcp structure has lower symmetry than a cubic structure, the magnitude of magnetocrystalline anisotropy is higher in hcp structures than the cubic structures.

2.1.5.2. Shape Anisotropy

Another very common origin of magnetic anisotropy is the shape of the element. The anisotropic dipolar interaction of free magnetic poles (stray and demagnetization fields) comes into play when the geometry of micrometer or submicrometer sized magnetic element is asymmetric. A magnetic system with finite boundaries exhibits poles at its surfaces which lead to stray field outside the sample as well as demagnetizing field inside the sample. The energy corresponding to the stray field is given by:

$$E_{dem} = -\frac{1}{2}\int \mu_0 M.H_{dem}dV \quad (2.14)$$

In case of a homogeneously magnetized ellipsoid,

$$H_{dem} = -NM \quad (2.15)$$

Thus, the stray field energy (demagnetizing energy) reduces to:

$$E_{dem} = \frac{1}{2}\mu_0\int MNMdV \quad (2.16)$$

$$E_{dem} = \frac{1}{2}V\mu_0MNM \quad (2.17)$$

Here V is the volume of the sample and N strongly depends on the shape and geometry of the element. Finally, the preferred orientation of magnetization lies along which E_{dem} is minimum.

2.1.5.3. Surface and Interface Anisotropy

The broken symmetry at surfaces and interfaces of magnetic thin films and multilayers often induces some anisotropy. This results in the effective anisotropy (K_{eff}) constant, which can be divided into two parts:

$$K^{eff} = K_V^{eff} + \frac{2K_S^{eff}}{d} \quad (2.18)$$

K_V^{eff} is the effective volume anisotropy constant involving the magnetocrystalline terms as well as the demagnetizing term, K_S^{eff} is the effective surface or interface anisotropy constant and *d* is the thickness. The competition between volume and surface (or interface) anisotropy gives rise to a dependence of the magnetization direction on the film thickness and below a critical film thickness; the interface anisotropy orients the magnetization of the sample towards perpendicular-to-plane or out-of-plane (OOP) direction.

2.1.5.4. Strain Induced Anisotropy

A magnetic system under strain acquires some anisotropy energy due to the change in the magnetoelastic (ME) energy [17-20]. Magnetostriction is a phenomenon in which the shape of a ferromagnetic material is changed during the process of magnetization. However, if the magnetization is changed upon application of mechanical stress – then it is known as inverse magnetostriction or the Villari effect. It was first discovered by E. Villari in the year 1865 [21]. Ferromagnets (e.g. Ni) that shrink during magnetization (have negative magnetostriction) lose some of their magnetic qualities when stretched (negative Villari effect). On the other hand, the stretching of ferromagnets with positive magnetostriction (e.g. NiFe alloy) leads to an increase in their magnetic properties (positive Villari effect).

The strain generated in terms of length elongation or contraction is [22]:

$$\frac{\delta l}{l} = \frac{3}{2}\lambda_s \left(cos^2\theta - \frac{1}{3}\right) \quad (2.19)$$

where λ_s is the isotropic magnetostriction and θ is the angle between the magnetization and the axis of stress. If σ is the applied stress, then energy expression becomes:

$$E_\sigma = -\frac{3}{2}\lambda_s \sigma\, cos^2\theta \quad (2.20)$$

2.1.5.5. Perpendicular Magnetic Anisotropy

The preferred magnetic moment orientation in ultrathin magnetic films and multilayers can differ significantly from their bulk counterparts. The preferred orientation of magnetization (*M*) of a ferromagnetic film generally lies in-plane (IP), because the magnetic energy is smaller in the IP direction due to the demagnetization field. However, at an interface, the electron orbital is substantially deformed towards the interface, resulting in an enhancement of the spin-

orbit interaction (SOI), due to which, the electron at the interface experiences an additional magnetic energy. As a result, the OOP direction of *M* becomes energetically favourable.

There is no effect of SOI when *M* is in IP direction, because the orbital is not deformed along this direction. Hence the effective magnetic field is:

$$H_{eff} = H_{intrinsic} \quad (2.21)$$

The magnetic energy in the IP direction is:

$$E_{IP} = - H_{intrinsic} \, . \, M \quad (2.22)$$

However, when *M* lies in OOP direction, there is an additional magnetic field of the SOI (H_{SO}), due to the orbital deformation in this direction. Thus, the effective magnetic field (H_{eff}) becomes:

$$H_{eff} = H_{intrinsic} + H_{SO} \quad (2.23)$$

Hence, the magnetic energy in the OOP direction becomes:

$$E_{OOP} = - (H_{intrinsic} + H_{SO}) \, . \, M \quad (2.24)$$

Since the absolute value of the negative magnetic energy is larger in the OOP direction of *M*, the direction of the easy axis of magnetization becomes perpendicular to the sample plane.

Generally, strong PMA is observed at the interfaces between 3d transition metal FMs (e.g. Co) and heavy nonmagnetic (NM) metals (e.g. W, Au, Pt, Pd) [23]. However, PMA is also observed at the interfaces between 3d transition FMs (e.g. Co, Fe and their alloys like CoFeB) and MO_x (M = Mg, Al, Ta, Ru). The heterostructures made from CoFeB and MgO have drawn particular attention due to lower damping constant of CoFeB and high tunnelling magnetoresistance (TMR) ratio at room temperature [24, 25].

2.2. Timescales of Magnetization Dynamics

The term magnetization dynamics covers a broad range of phenomena occurring at different timescales starting from few femtoseconds (fs) to microseconds (μs). The fastest dynamics include fundamental exchange interaction (~ 10 fs), spin transfer torque (~10 fs – 1 ps) and laser induced ultrafast demagnetization (~hundreds of fs). The relatively slower phenomena are magnetization precession (~ 10 – 100 ps), damping (~ 100 ps to few ns), precessional switching (~ few ps – few hundred ps) and vortex core switching (few tens of ps – several ns). Finally, the slowest one is the domain wall (DW) dynamics which occurs between few ns to few μs.

When a very short (few tens of fs) high energy laser pulse falls on a magnetized ferromagnetic sample, it causes an ultrafast demagnetization (sub-100 to few hundred fs). As soon as the laser

pulse is withdrawn, the system tries to get back its equilibrium condition via remagnetization process. This initially occurs via fast relaxation (within ~ 5 ps) due to the exchange of energy from hot electrons and spins to the lattice. Subsequently, there is a slow relaxation (within hundred ps) via the diffusion of lattice heat to the surroundings. In the course of the slow relaxation process, the system also undergoes a precessional motion about the effective magnetic field, which eventually damps out within few ns.

2.2.1. Ultrafast Demagnetization

The phenomenon of ultrafast demagnetization was first experimentally observed [26] in 1996 by Baurepiare *et al*. A sharp drop in the Kerr signal within few hundred fs after the absorption of a 60 fs pump pulse in Ni thin film using magneto-optical pump-probe technique was reported. The results were explained by the thermalization of the electron, spin and lattice baths within the three temperature model (3TM). This was a real milestone in the research of magnetization dynamics because of the unprecedented short timescale. Thereafter, a lot of efforts were made to investigate this so-called 'ultrafast demagnetization' both experimentally and theoretically. Despite of extensive research, the underlying mechanisms of this phenomenon is still a subject of intense debate till date.

2.2.1.1. Three Temperature Model

In the Three temperature model (3TM), it is assumed that the system consists of three thermalized reservoirs for exchanging energy, namely, the electron, lattice and spin systems at temperatures T_e, T_l and T_s respectively. The absorbed energy creates hot electrons within the system. During this transient hot electron regime, spin dependent scattering (SDS) modifies the spin population. This induces a spin dynamics associated with T_s (different from T_e and T_l) and leads to the ultrafast demagnetization. Later, the dissipation of energy from electron and spin baths to lattice bath gives rise to the fast remagnetization. The temporal evolution of the system can be described by three coupled differential equations:

$$C_e(T_e)\frac{dT_e}{dt} = -G_{ef}(T_e - T_l) - G_{es}(T_e - T_s) + P(t) \quad (2.25)$$

$$C_s(T_s)\frac{dT_s}{dt} = -G_{es}(T_s - T_e) - G_{sl}(T_s - T_l) \quad (2.26)$$

$$C_l(T_l)\frac{dT_l}{dt} = -G_{el}(T_l - T_e) - G_{sl}(T_l - T_s) \quad (2.27)$$

By time-resolved second harmonic generation (SHG), Hohlfeld *et al.* [27] observed that the magnetic response is faster as compared to the electron thermalization and the transient

magnetization reaches minimum (~ 50 fs) before the electron thermalization is completed. Subsequently, Ju *et al.* [28] studied nonequilibrium spin dynamics following fs photoexcitation and confirmed the existence of a transient spin polarized hot electron gas thereby suggesting that the thermalized spins contribute to a transient magnetization effect. A large enhancement to the transient Kerr effect in the exchange biased NiFe/NiO bilayers was reported as opposed to the ‘‘bare’’ epitaxial NiFe thin films [29]. An important report came up in 2000, where Koopmans *et al.* [30] provided clear evidence for nonmagnetic contributions (not directly scaling with the true demagnetization) to the femtosecond magneto-optic response in ferromagnetic nickel and concluded that the spin relaxation (~ 0.5–1 ps) may be explained by spin-lattice relaxation, whereas, on a slower timescale (~ 100 ps) optically induced spin precession is observed.

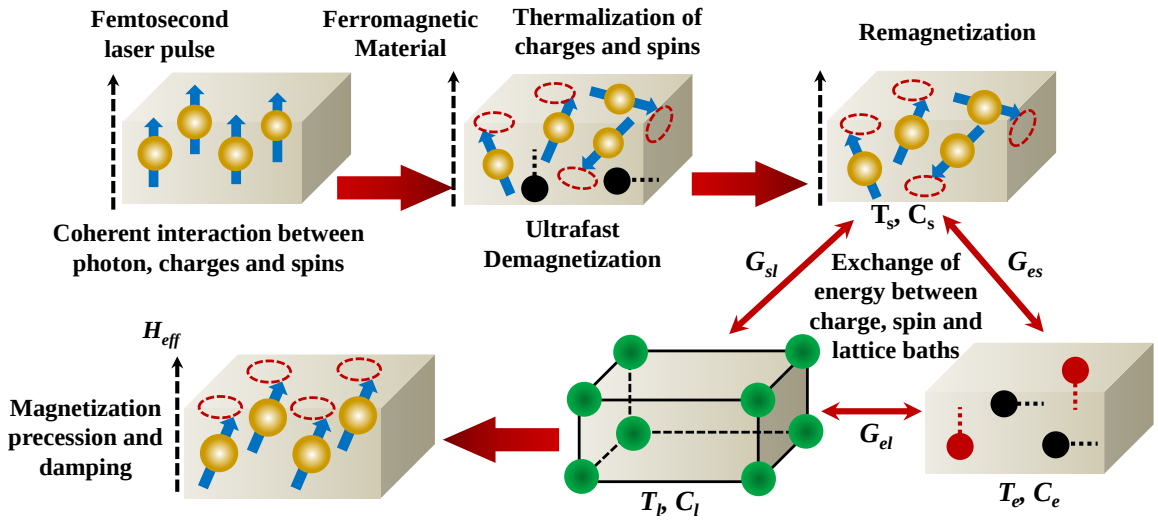

Fig. 2.3: Schematic representation of ultrafast magnetization dynamics based upon three temperature model.

2.2.1.2. Spin-Orbit Coupling

Zhang and Hübner explained the ultrafast demagnetization process in terms of exchange interaction and spin-orbit coupling (SOC) [31]. From theoretical calculations, they showed that the intrinsic spin dynamics in Ni occurs within ~10 fs, while extrinsic effects such as laser pulse duration and spectral width can slow down the observed dynamics. The relaxation time can also be modified by tuning the exchange strength. They predicted that in total four different relaxation processes occur during ultrafast demagnetization: (i) electronic equilibration (within 1 fs, due to electron-electron interaction); (ii) electron-spin relaxation (within few fs, due to

exchange interaction or SOC); (iii) electron-lattice thermalization (within 1 ps, due to electron-photon coupling); (iv) spin-lattice relaxation (within 100 ps, due to SOC as well as anisotropic crystal-field fluctuations). Later, the same authors demonstrated that the ultrafast demagnetization is a cooperative effect of external laser field and intrinsic SOC field [32].

2.2.1.3. Elliot-Yafet Electron-Phonon Spin-Flip Scattering

An often discussed explanation of ultrafast demagnetization is the spin-flip electron-phonon scattering via the Elliott-Yafet (EY) mechanism [33, 34] which leads to the transfer of angular momentum from $<S_e>$ to $<L_l>$. In 2005, Koopmans *et al.* tried to establish a correlation between ultrafast demagnetization and Gilbert damping and proposed that, phonon-mediated spin-flip scattering during ultrafast demagnetization is responsible for the spin angular momentum transfer to the lattice [35]. By extending the phenomenological 3TM with EY-like spin-flip channel, Koopmans named it a microscopic three-temperature model (M3TM) [36]. Ab initio calculations for ultrafast demagnetization due to the EY electron-phonon spin-flip scattering were reported for transition-metal ferromagnets bcc Fe, fcc Co, and fcc Ni [37-39]. Researchers have also tried to find the reason behind the fast demagnetization of transition metals (TM) and slow demagnetization of rare earth (RE) metals [40]. A compact differential equation based on EY scattering describing the ultrafast magnetization dynamics is as follows:

$$\frac{dm}{dt} = Rm\,\frac{T_p}{T_c}\left[1 - \coth\left(\frac{mT_c}{T_e}\right)\right] \tag{2.28}$$

$$R \propto a_{sf}\frac{T_c^2}{\mu_{atomic}} \tag{2.29}$$

where a_{sf} is the spin-flip probability and if it increases then demagnetization will be faster (e.g. a_{sf} is larger for Co and Ni but smaller for Gd). R is a material-specific scaling factor for the demagnetization rate.

2.2.1.4. Electron-Electron Scattering Mediated by Coulomb Interaction

In 2009, Krauss *et al.* [41] made model calculations with electron-electron scattering in systems with large SOC and concluded that electron-electron scattering mediated by Coulomb interaction could be the reason for ultrafast demagnetization. This scattering mechanism is not (quasi)elastic, thus the available phase space for transitions from minority to majority bands is much larger than for electron-phonon scattering. The majority and the minority energy dispersions are spin split and hence a nonzero magnetization exists in equilibrium. The ultrafast

optical excitation creates nonequilibrium electronic distributions in bands accessible by the pump photon energy, and the electrons undergo intraband as well as interband Coulomb scattering processes. The fast remagnetization occurs due to the transfer of energy to the lattice bath. Mueller *et al*. [42] also made model calculations including both electron-electron and electron-phonon scattering and concluded that the former is essential for the ultrafast demagnetization.

2.2.1.5. Electron-Magnon Scattering

In a system with large SOC, it is possible to reduce the spin angular momentum $<S_e>$ via electron-magnon interaction. In 2008, Carpene *et al.* [43] proposed a spin-flip mechanism similar to the EY scattering, but with magnons acting as the reservoir for $<S_e>$. Through the LS coupling, the creation of magnons leads to a decrease in $<S_e>$ and to a subsequent increase in $<L_l>$. The latter is rapidly quenched by the crystal field. Therefore, in the proposed scenario the laser-induced ultrafast demagnetization can be explained in terms of electron-magnon interaction.

2.2.1.6. Relativistic Spin Flip Scattering

A theory of ultrafast demagnetization based on the direct, relativistic spin-photon interaction was proposed by Bigot *et al.* [44]. According to this theory, the ultrarelativistic terms stemming from Dirac Hamiltonian provide a coupling between the electromagnetic field of the pump laser pulse and the spins of electrons in the material. A full ab initio investigation of the influence of the relativistic spin-photon interaction on the magnetization and magneto-optical response was carried out by Mandal *et al.* [45], where the relativistic terms that are involved in coupling of the spin and photon fields were analyzed.

2.2.1.7. Laser Induced Spin Flip

A theory came up on the direct action of the laser on electron's spin, causing a direct, laser-induced spin flip [46]. Zhang *et al.* searched the answer to a fundamental question of what does TR-MOKE actually probe, a simple optical excitation artefact (charge origin) or a genuine magnetic excitation (spin origin)? By constructing a phase-sensitive polarization versus magnetization plot, they found that the magnetic signals are delayed by 10 fs with respect to the optical signals for short pulses, while, for longer pulses, the delay shortens and the behavior approaches the continuous-wave response.

2.2.1.8. Phonon-Phonon Interaction: The Einstein-de Haas Effect

The Einstein-de Haas effect was originally observed in a landmark experiment [47] demonstrating that the angular momentum associated with the aligned spins in a ferromagnet can be converted to mechanical angular momentum by reversing the direction of magnetization using an external magnetic field. The same effect was discussed [48] in the context of ultrafast demagnetization by raising the question that, whether the ultrafast reduction of the spin angular momentum $<S_e>$ could result in a net rotation of the irradiated area of the sample. Using femtosecond time-resolved x-ray diffraction, Dornes *et al.* [49] demonstrated that the loss of angular momentum from the spin system upon laser-induced demagnetization of ferromagnetic iron is transferred to the lattice on sub-picosecond timescales, thus launches a transverse strain wave that propagates from the surface into the bulk. They concluded that the interaction with the lattice has an important role in the phenomenon of ultrafast demagnetization.

2.2.1.9. Phonon-Magnon Interaction

Scattering of phonons with magnons are much slower (on a 100-ps time scale) [50] and it is generally believed that phonon-magnon scattering is too slow for the ultrafast demagnetization in fcc Ni and fcc Co, but possibly it is relevant for the demagnetization in Gd and Tb [51, 52].

2.2.1.10. THz Emission during Ultrafast Demagnetization

In 2003, Beaurepaire *et al.* [53] showed that the laser induced ultrafast demagnetization in ferromagnetic films has intimate relation with the emission of a terahertz electromagnetic pulse. The radiated electric field $E(t)$ was explained in terms of Maxwell equations (radiation from a time dependent magnetic dipole) and was expected to be proportional to the second time derivative of the magnetization d^2M/dt^2. When the sample is optically excited by the pump pulse, the spin-flip events occurring via SOC, could not give rise to a complete demagnetization. Simultaneously, the relaxation of electrons (spins) between the majority and minority sub-bands, assisted by the emission of a THz photon occurs, which contributes to the total demagnetization process.

2.2.1.11. Superdiffusive Spin Transport

Malinowski *et al.* [54] first observed that excited hot electron spin transport enhances and speeds up the demagnetization in a synthetic antiferromagnetic (SAF) structure. Thereafter, a

semiclassical model was proposed by Battiato *et al.* [55, 56] demonstrating that the laser induced ultrafast demagnetization can be explained without any spin-flip channel, but with a superdiffusive spin transport where the majority electrons diffuse faster into the substrate as opposed to the minority electrons. Standard diffusive processes are governed by Brownian motion and are characterized by the variance of the displacement of a particle distribution function σ^2 which grows linearly with time: $\sigma^2(t) \infty t^\gamma$, with γ = 1, whereas, the Ballistic diffusion is characterized by γ = 2 [57]. In this theory, the electron motion was described by superdiffusive processes with the fact that γ is time dependent and goes from a ballistic regime γ = 2 for small times to diffusive regime γ = 1 for long times. After the absorption of a photon, an electron gets excited from a d band to the sp-like bands above the Fermi level. The mobility of sp-like electrons is much larger than that of d electrons. Superdiffusive transport gives rise to demagnetization, because, the laser-excited electrons in the sp bands have higher velocities and the excited spin majority and minority electrons have different lifetimes [58]. The newly excited electrons will have enough energy to contribute to the demagnetization. In this process, the total 'first generation flux' in presence of distributed source of excited electrons is:

$$\Phi(z,t) = \int_{-\infty}^{\infty} dz_0 \int_{-\infty}^{t} dt_0 S^{ext}(z_0.t_0)\varphi(z,t;z_0,t_0) \quad (2.30)$$

S^{ext} is the electron source term.

After obtaining the density of second and third generation electrons, the entire process can be summed up and a coupled transport equation can be derived as:

$$\frac{dn^{tot}}{dt} + \frac{n^{tot}}{\tau} = \left(-\frac{\partial}{\partial z}\,\hat{\varphi} + \hat{I}\right)\left(\hat{S}n^{tot} + S^{ext}\right) \quad (2.31)$$

n^{tot} is the electron density and τ is the lifetime. The main idea behind the superdiffusive spin transport mechanism is the passive demagnetization due to spatial transport of spins experiencing multiple electronic collisions. Many experiments were carried out to physically prove the existence of superdiffusive spin transport [59, 60]. The theory of superdiffusive spin transport can successfully explain the striking difference between magnetic metals and magnetic dielectrics. As this process is inhibited in insulators, it is not a dominant effect in ferromagnetic films on insulating substrate [61].

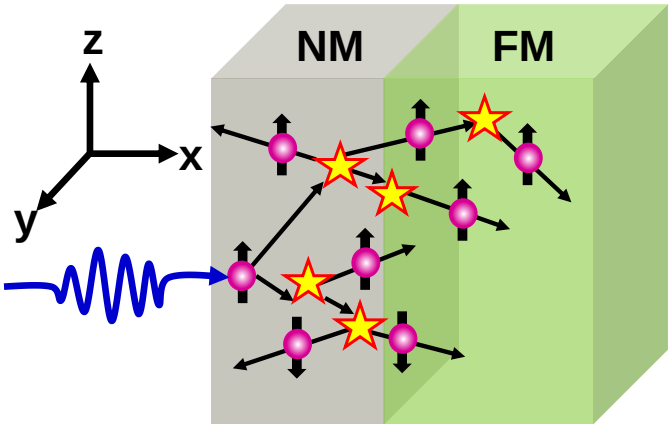

Fig. 2.4: Schematic of the superdiffusive processes caused by laser excitation.

2.2.1.12. Competition between Spin Flip Scattering and Spin Transport

Proposed mechanisms for ultrafast demagnetization generally fall into two broad categories: spin-flip scattering and spin-transport mechanisms. The former explains the demagnetization process as a sudden increase in scattering processes, resulting in a decrease of spin order. These scattering processes can include electron–electron, electron–phonon, electron–magnon and even direct spin–light interactions. Such scatterings must involve a transfer of angular momentum from the electronic spins to other subsystems. The second category relies on the idea that laser excitation causes a rapid transport of majority spins away from the excited region. Transport is considerably less efficient for minority spins, thus leaving behind a region of reduced magnetization density. Several studies have discussed the importance of spin-flip scattering of thermalized electrons and superdiffusive spin transport of hot, nonequilibrium electrons, in ultrafast magnetization dynamics. Experiments on layered structures have demonstrated the importance of spin transport, while demagnetization of metallic films on insulators was ascribed to spin flips, leading to an emerging consensus that both processes play a role. Wieczorek *et al.* [62] reported that laser-excited spin dynamics in Co/Cu(001) films are dominated by by spin-dependent transport effects (~100 fs) when the electronic system is not yet thermalized, while after hot electron thermalization (>200 fs) local spin-flip processes dominate. Simultaneous presence and of both spin flip scattering and spin transport have been observed to influence the ultrafast demagnetization mechanism in ferromagnetic multilayers [63, 64].

2.2.1.13. Optically Induced Spin Transport Effect

Most recently, a previously unknown scheme known as optically induced spin transport (OISTR) effect has been proposed [65, 66] for the ultrafast manipulation of spins, which showed that optical excitation can directly, coherently, and efficiently redistribute spins between different magnetic sublattices in a multicomponent magnetic material without altering the total magnetization of the system. Dewhurst *et al.* [67] showed that the initial spin dynamics within 20 fs in ferromagnetic/nonmagnetic (FM/NM) interfaces is driven almost entirely by OISTR effect with majority spin transferred to the NM and minority spin to the FM, and at later times, the FM is further demagnetized by spin-orbit-induced spin flips.

2.2.2. Precessional Magnetization Dynamics

The magnetic moments of a magnetic material experience a torque in presence of an external magnetic field which induces a precessional motion along the magnetic field direction. Additionally, the moments try to align themselves along the external magnetic field in order to minimize the Zeeman energy. Effectively, they execute a damped spiral motion about the magnetic field direction which is referred to as precessional magnetization dynamics. The behavior of magnetization precession is phenomenologically illustrated by the Landau-Lifshitz-Gilbert (LLG) equation, which was first introduced by Lev Landau and Evgeny Lifshitz in 1935 as Landau-Lifshitz (LL) equation [68] and later, modified by Gilbert by inserting a Gilbert damping term [69]. The formulation is briefly described as follows:

When a magnetic moment μ_m is placed in an effective magnetic field H_{eff}, it experiences a torque given as:

$$\tau = \mu_m \times H_{eff} \tag{2.32}$$

From a semiclassical approach, the magnetic moment (μ_m) can be related to the angular momentum L of electrons as follows:

$$\mu_m = -\gamma L \tag{2.33}$$

where $\gamma = \frac{g\mu_B}{\hbar}$ is the gyromagnetic ratio, g is the Lande-factor (g ≈ 2), μ_B is the Bohr magnetron and $\hbar$ is the reduced Planck constant [70-73]. By applying the momentum theorem one can express Eq. 2.28 as the rate of change of angular momentum L:

$$\frac{dL}{dt} = \mu_m \times H_{eff} \tag{2.34}$$

Using Eq. 2.29 the above expression becomes:

$$\frac{d\mu}{dt} = -\gamma\mu \times H_{eff} \tag{2.35}$$

Here, the effective magnetic field H_{eff} is a sum of all external and internal magnetic fields and is expressed by the following:

$$H_{eff} = H_0 + h(t) + H_{ex} + H_{dem} + H_{ani} \quad (2.36)$$

H_0 is the applied magnetic field, $h(t)$ is the dynamic component, H_{ex} is the exchange field and H_{dem} represents the demagnetization field created by the dipolar interaction of magnetic surface and volume charges and the H_{ani} includes all kinds of anisotropic fields described above.

In the continuum limit, the atomic magnetic moment (μ) can be replaced by the macroscopic magnetization (M) resulting in the equation of motion, i.e., the Landau-Lifshitz (LL) equation:

$$\frac{dM}{dt} = -\gamma M \times H_{eff} \quad (2.37)$$

The above equation features a continuum precession i.e., the system is non-dissipative. To avoid this impractical situation, Landau and Lifshitz proposed the damping term as:

$$-\lambda m \times (m \times H_{eff}) \quad (2.38)$$

Later, Gilbert introduced another damping term into the LL equation which resulted in the so called Landau-Lifshitz-Gilbert (LLG) equation, written as:

$$\frac{dM}{dt} = -\gamma M \times H_{eff} + \frac{\alpha}{M_S}\left(M \times \frac{dM}{dt}\right) \quad (2.39)$$

Here α is the dimensionless Gilbert damping parameter and M_s is the saturation magnetization of the magnetic material.

2.2.2.1. Macrospin Model of Ferromagnetic Resonance: Kittel Formula

In macrospin model, the magnetization of a ferromagnetic element is considered uniform throughout the element. Hence, the magnetic moment of the whole element can be represented by a giant magnetic moment (macrospin). Under the influence of a stable bias magnetic field, all the spins of the ferromagnetic material will be aligned. If an alternating magnetic field with a frequency equal to the inherent precessional frequency of the system is applied perpendicular to the bias magnetic field, then the entire system will start precessing coherently by absorbing power from the oscillating field, which is known as the resonance condition. J. H. E. Griffiths first experimentally reported the ferromagnetic resonance (FMR) phenomenon in 1946 [74]. Griffiths observed that the ferromagnetic resonance occurs at a much higher frequency than the Larmor precession frequency. In 1947, Charles Kittel first derived the expression for ferromagnetic resonance considering the shape of the specimen [75].

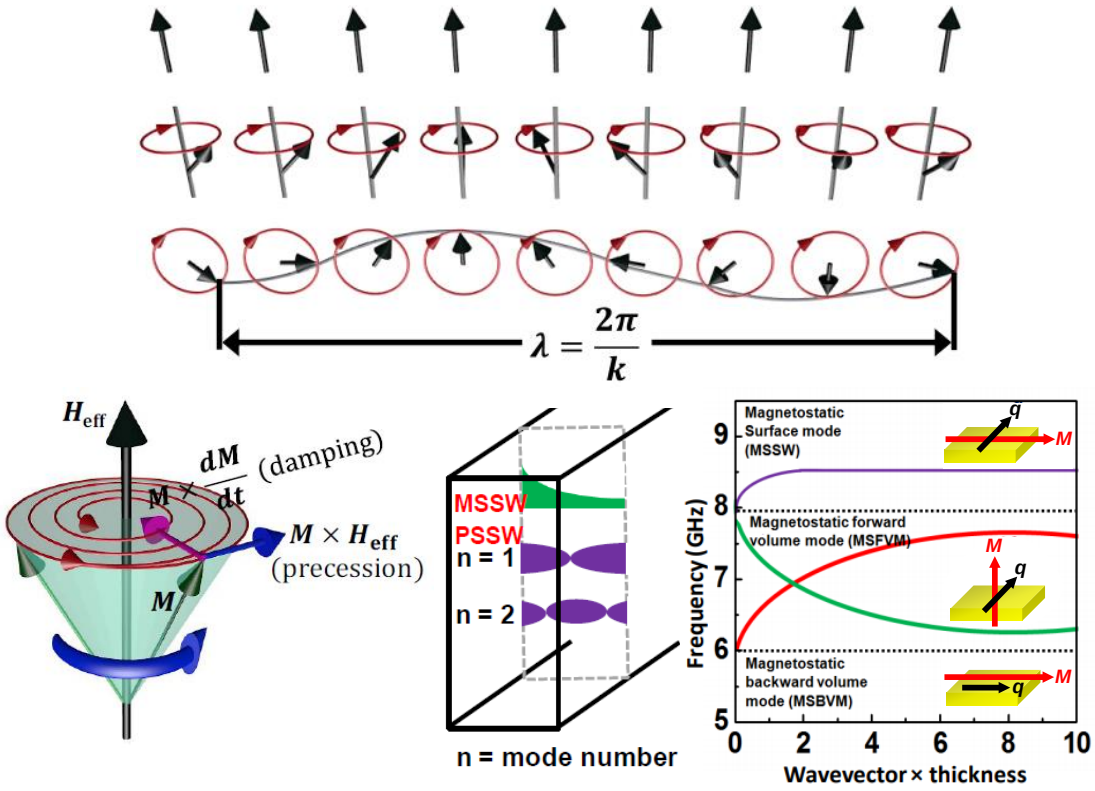

Fig. 2.5: (a) Semiclassical representation of spin wave (SW) in a ferromagnet: the ground state, chain of precessing magnetic moments and the SW (top view). (b) Motion of the magnetization around the effective magnetic field. Schematics of (c) perpendicular standing SW mode (PSSW) and magnetostatic surface SW mode (MSSW) within ferromagnetic thin film. (d) The dispersion relation for different types of magnetostatic SWs modes.

For uniform precession, Eq. 2.35 reduces to:

$$\frac{dM}{dt} = -\gamma M \times H_{eff} \tag{2.40}$$

This Eq. 2.36 will take the following form

$$\frac{dM_x}{dt} = \gamma\left(M_y H_z^{eff} - H_y^{eff} M_z\right) \tag{2.41}$$

$$\frac{dM_y}{dt} = \gamma\left(M_z H_x^{eff} - H_z^{eff} M_x\right) \tag{2.42}$$

$$\frac{dM_z}{dt} = \gamma\left(M_x H_y^{eff} - H_x^{eff} M_y\right) \tag{2.43}$$

The demagnetizing factors along x, y and z directions for a general ellipsoid are N_x, N_y and N_z, respectively. H_z is the static magnetic field which is applied along the z axis and H_x is the alternating field applied along the x axis. Therefore, the effective magnetic field along x, y and z directions are:

$$H_x^{eff} = H_x - N_x M_x \tag{2.44}$$

$$H_y^{eff} = -N_y M_y \tag{2.45}$$

$$H_z^{eff} = H_z - N_z M_z \quad (2.46)$$

Substituting Eqs. 2.40, 2.41, and 2.42 into Eqs. 2.37, 2.38, and 2.39 we obtain,

$$\frac{dM_x}{dt} = \gamma \left[H_z + \left(N_y - N_z\right)M_z\right]M_y \quad (2.47)$$

$$\frac{dM_y}{dt} = \gamma \left[M_z H_x - \left(N_x - N_z\right)M_z M_x - M_x H_z\right] \quad (2.48)$$

$$\frac{dM_z}{dt} = 0 \quad (2.49)$$

These three equations can be solved considering $M = me^{j\omega t}$

Solving these equations, the expression for the ferromagnetic resonance (FMR) frequency can be obtained as:

$$\omega_0 = \gamma \left[\left\{H_z + \left(N_y - N_z\right)M_z\right\}\left\{H_z + \left(N_x - N_z\right)M_z\right\}\right]^{\frac{1}{2}} \quad (2.50)$$

2.2.3. Spin Waves

If an array of spins is disturbed locally by some external perturbation, then the disturbance generated by collective phase coherent precession of magnetization or spins in the ferromagnetic medium, propagates as a wave, known as spin wave (SW). The concept of SWs was introduced by F. Bloch [76] in the year 1930. Magnons are the quanta of SWs. As the SWs have much smaller wavelength than the electromagnetic wave at the same frequency, the usage of SWs as information carriers is more advantageous in miniaturized devices.

Depending on the wavelength and range of interaction, SWs can be categorized in exchange dominated, dipole-exchange dominated or dipole dominated SWs. In the long wavelength regime, the phase difference between consecutive spins is small, the SWs are primarily dominated by dipolar energy and are known as dipole dominated or magnetostatic SWs. On the other hand, in the short wavelength regime, the SWs are governed by exchange interaction and are known as exchange SWs.

2.2.3.1. Magnetostatic Spin Waves

The characteristics of magnetostatic SWs were first reported by Damon and Eshbach [77] in 1961. As the dipolar interaction is anisotropic, the frequency, amplitude and propagation properties of magnetostatic modes strongly depend on the geometry of propagation direction with respect to the applied magnetic field and the film plane. When both the applied magnetic field and the SW wave vector lie in the film plane and are perpendicular (parallel) to each other, a magnetostatic surface wave mode (backward volume magnetostatic mode) is obtained. On

the contrary, if the magnetic field is applied perpendicular to the film plane and SW propagates parallel to the surface, it is known as forward volume magnetostatic mode.

The magnetostatic surface wave (MSSW) mode is also known as Damon and Eshbach (DE) mode. It shows a positive dispersion starting from the Kittel mode at zero wave vector (q = 0), and is further characterized by the localization of SW amplitude in the vicinity of the top and bottom surfaces along with its nonreciprocal behavior. In absence of magnetic anisotropy and exchange interaction, the dispersion relation of the DE mode [78] is described as:

$$f_{DE} = \gamma\,[H_0(H_0 + 4\pi M_S) + (2\pi M_s)^2(1 - e^{-2qd})]^{\frac{1}{2}} \quad (2.51)$$

At q = 0, the dispersion relation becomes:

$$(f_{DE})_{q=0} = \gamma\,[H_0\,(H_0 + 4\pi M_S)]^{\frac{1}{2}} \quad (2.52)$$

The above frequency is same as the frequency of Kittel mode or uniform mode.

The backward volume magnetostatic mode (BWVMS) possesses a negative dispersion (group and phase velocities are in opposite directions). Considering negligible anisotropy the dispersion relation of the lowest order BWVMS mode is given by:

$$f_{\mathrm{BWVMS}} = \gamma\left[H_0\left(H_0 + 4\pi M_S\frac{1-e^{-2qd}}{qd}\right)\right]^{\frac{1}{2}} \quad (2.53)$$

In the long wavelength limit, the dispersion relation of the FWVMS mode can be expressed after neglecting anisotropy as:

$$f_{\mathrm{FWVMS}} = \gamma\left[(H_0 + 4\pi M_S)\left(H_0 - 4\pi M_S\left(\frac{1-e^{-qd}}{qd}\right)\right)\right]^{\frac{1}{2}} \quad (2.54)$$

2.2.3.2. Exchange Spin Waves

The exchange interaction comes into play when the wave vector of SW is increased (wavelength is decreased). Basically, the exchange interaction becomes dominant when the wavelength of SW is of the order of the exchange length which is given by:

$$l_{ex}(r) = \sqrt{\frac{2A}{\mu_0 M_S^2}} \quad (2.55)$$

where A is the exchange constant. It is worth mentioning here that the Heisenberg exchange dominated SW mode does not depend on the relative orientation of the wave vector and magnetic field. The SW dispersion relation with dipolar-exchange interactions is given by [79]:

$$f_{dip-ex} = \frac{\gamma}{2\pi}\left[\left(H_0 + 2\pi M_S qd\sin^2\varphi + \frac{2A}{M_S}q^2\right)\left(H_0 + 4\pi M_S - 2\pi M_S qd + \frac{2A}{M_S}q^2\right)\right]^{\frac{1}{2}} \quad (2.56)$$

where φ is the angle between applied field H_0 and q.

It is also possible to excite SWs propagating perpendicular to the plane of the film to form perpendicular standing spin wave (PSSW) modes. PSSW modes are exchange dominated modes and the dispersion relation for the PSSW mode without considering the contribution of in-plane wave vector is given by [80]:

$$f_{PSSW} = \frac{\gamma}{2\pi}\left[\left(H_0 + \frac{2A}{M_S}\,q^2\right)\left(H_0 + 4\pi M_{eff} + \frac{2A}{M_S}q^2\right)\right]^{\frac{1}{2}} \quad (2.57)$$

where M_{eff} is the effective magnetization of the system, d is the film thickness and q is the wave vector of PSSW mode

$$q = \frac{n\pi}{d} \quad (2.58)$$

where n is the quantum number of the SWs.

2.2.3.3. Confined Spin-Wave Modes in Magnetic Structures

In the discussion above, we have dealt with the SWs in infinite thin film. However, the SW spectra are substantially modified in confined magnetic structures due to the boundary conditions imposed by the lateral dimensions [81]. The SWs form standing waves [82] in the distribution of 'potential wells' defined by the geometry of the structure. The formation of standing waves leads to localized or quantized modes (with multiple quantization numbers) when the feature dimensions are of the order of the wavelength of the SW. Overall, the number of SW modes increases whose properties are strongly dependent on the geometry of the system as well as the orientation of the magnetic field. The geometrical confinement also affects the dispersion relation, which results in a number of allowed and forbidden bands in case of periodically patterned magnonic crystal (MC) [83]. The band structure of MCs comprised of several Brillouin Zones (BZs) [84] provides excellent control over the SW properties by manipulating external structuring.

2.3. Synthetic Antiferromagnets

The free energy of a synthetic antiferromagnet (SAF) multilayer [85] with an interlayer coupling J_{ij} between consecutive ferromagnetic layers indexed by i and j having equal thicknesses t_m and bulk saturation magnetization M_S is given by:

$$E = -\frac{1}{2}\sum_{ij} J_{ij}\cos\left(\theta_i - \theta_j\right) - M_S t_m H \sum_i \cos\theta_i + E_{anis} \quad (2.59)$$

The angles θ are referenced with respect to the applied magnetic field. The first term of Eq. 2.55 is the usual bilinear exchange, the second term is the Zeeman term, and E_{anis} is the

anisotropy contribution. Considering only the Zeeman and exchange contributions dominate, if we assume that all layers are identical and coupling mainly occurs between neighboring layers, and $\theta_{i-1} = \theta_{i+1} = -\theta_i = -\theta$, Eq. 2.55 can be simplified as:

$$E = -(N-1)J\cos 2\theta - NM_S\, t_m\, H\, cos\theta \quad (2.60)$$

However, the above expression fails to correctly describe the shape of magnetization curves of SAF multilayers, as the hysteresis loops have a non-negligible remanence and curvature. Such hysteresis loops can be fitted by a model including a biquadratic interlayer exchange, which was initially proposed by Ruhrig *et al.* [86]. Thus, the free energy expression becomes:

$$E = Nt_m M_S\, H\, cos\theta - (N-1)(J\cos 2\theta + Bcos^2\, 2\theta) \quad (2.61)$$

The term B ($B < 0$) takes into account the biquadratic coupling, which leads to perpendicular zero-field configurations of the spins ($\varphi_i = \theta_i - \theta_{i+1} = 2\theta = 90^{\circ}$), as compared to the bilinear coupling which causes antiparallel configurations ($\varphi_i = \theta_i - \theta_{i+1} = 2\theta = 180^{\circ}$). Several origins have been proposed for the biquadratic term, either as an intrinsic effect related to the interlayer coupling mechanism or due to extrinsic effects related to the morphology of the multilayer. Slonczewski proposed that the presence of atomic steps in the spacer layer could cause an apparent biquadratic coupling [87]. If there is an atomic step in the spacer layer, the sign of the interlayer coupling will change from positive (ferromagnetic) to negative (antiferromagnetic). A periodic array of steps will thus induce fluctuations of IEC. If the size of the steps is smaller than some critical length, Slonczewski's model predicts a behavior of the magnetization curves which can be fitted by the biquadratic IEC. Several authors [88, 89] have reported that the hysteresis curves can be fitted by considering energy expressions which involve biquadratic terms.

2.4. Strain Induced Magnetization Dynamics

When a nanomagnet is fabricated on a piezoelectric substrate, the strain generated in the nanomagnet can be expressed by the Hooke's law:

$$\sigma = Y\,.\,\varepsilon \quad (2.62)$$

where Y is the Young's modulus of the nanomagnet, σ is the stress and ε is the strain generated by SAW. The SAW will induce periodic strain anisotropy in the nanomagnet via inverse magnetostriction or Villari effect. The applied stress can change the magnetization due to magnetoelastic (ME) interaction. The velocity of the SAW can be written as:

$$v = \lambda f \quad (2.63)$$

where λ is the wavelength and it depends on the distance between pinning points (lattice constants) for periodically patterned nanomagnet arrays.

The elastic energy per unit volume can be expressed as [90]:

$$E_{el} = \frac{1}{2}\,\varepsilon\,.\,\sigma = \frac{1}{2}\,\varepsilon\,.\,(Y\,.\,\varepsilon) \tag{2.64}$$

In magnetostrictive materials, due to the ME coupling, the total strain has a magnetic component in addition to the elastic one,

$$\varepsilon = \varepsilon_{el} + \varepsilon_{me} \tag{2.65}$$

Therefore Eq. 2.64 can be written as:

$$E_{el} = \frac{1}{2}\,(\varepsilon - \varepsilon_{me})\,.\,Y\,(\varepsilon - \varepsilon_{me}) \tag{2.66}$$

The magnetoelastic contribution to the effective field can be written as [91]:

$$H_{me} = \frac{1}{\mu_0 M_S}\left(\frac{\partial E_{el}}{\partial m}\right) \tag{2.67}$$

$$H_{me} = \frac{1}{\mu_0 M_S}\,\sigma\,\left(\frac{\partial \varepsilon_{me}}{\partial m}\right) \tag{2.68}$$

2.5. Magneto Optical Kerr Effect (MOKE)

Magneto-optical effect was first invented by Michael Faraday in 1845, in a piece of glass placed in between two magnetic pole pieces. He observed that the plane of polarization of a linearly polarized light gets rotated when the light is transmitted through the magnetized material. Later, in 1877, John Kerr observed a similar rotation of polarization in the reflected light as well [92]. Kundt observed that this effect is enhanced in the presence of a ferromagnetic surface [93]. Upon reflection from a magnetized sample, a plane polarized light is converted to an elliptically polarized light, which is known as magneto-optical Kerr effect (MOKE). The corresponding rotation of the plane of polarization (i.e. rotation of the major axis of the ellipse) is called the Kerr rotation. If *r* and *k* denote the parallel and perpendicular electric field vector components of the reflected light with respect to the incident light, then Kerr rotation (θ_K) and ellipticity (ε_K), which are proportional to the magnetization of the sample, can be written as,

$$\theta_K + i\varepsilon\mathrm{K} = \frac{k}{r}\ \text{, where k << r} \tag{2.69}$$

2.5.1. MOKE Geometries

There are three types of MOKE geometries namely polar, longitudinal and transverse, depending upon the orientation of magnetization vector with respect to the sample surface and the plane of incidence.

When the magnetization lies perpendicular to the sample surface but parallel to the plane of incidence of light, then the effect is known to occur in polar geometry. Since the plane of polarization of both s-polarized light (polarization perpendicular to the plane of incidence) and p-polarized light (polarization parallel to the plane of incidence) is always perpendicular to the magnetization, irrespective of the angle of incidence, a Lorentz force always exists resulting in a Kerr rotation in polar geometry. The polar configuration is generally used to study thin films, which exhibit perpendicular magnetic anisotropy (PMA).

If the magnetization lies in sample plane and also parallel to the plane of incidence of light, then the geometry is known as longitudinal geometry. The longitudinal Kerr effect depends upon the angle of incidence of light and in case of normal incidence, the Kerr effect vanishes because either the Lorentz force vanishes for p-polarized light or points along the direction of the light for s-polarized light. In longitudinal MOKE, the measurements are performed by keeping the angle of incidence in between 5° and 60°.

If the magnetization lies in the plane of sample but perpendicular to the plane of incidence of light, then the geometry is known as transverse geometry. In this geometry also Kerr effect is absent for the normal incidence of light. In case of oblique incidence, the polarization does not change, since either the Lorentz force is absent for s-polarized light or the direction of polarization of the induced component remains same as the incident polarization for p-polarized light. However, the transverse effect is associated with a change in the intensity of

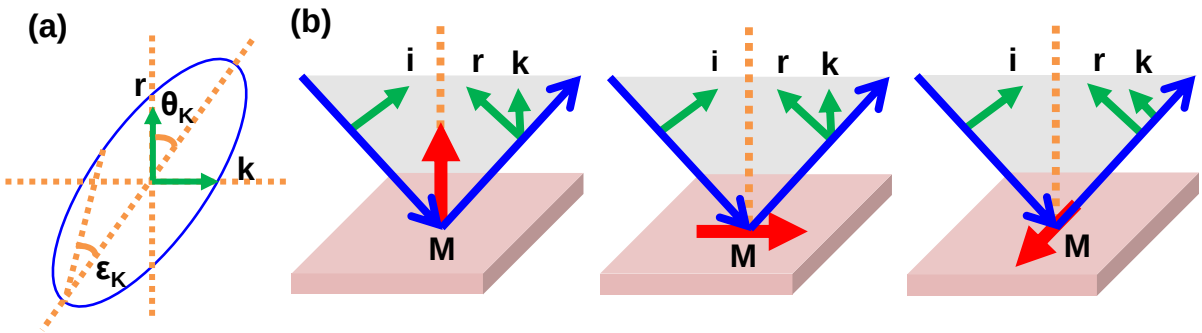

Fig. 2.6: (a) Geometry of the Kerr rotation (θ_K) and Kerr ellipticity (ε_K). (b) Schematics of polar, longitudinal and transverse MOKE geometries are shown.

the reflected light when the orientation of magnetization is changed. The change in the intensity depends on the component of magnetization perpendicular to the plane of incidence.

2.5.2. Physical Origin of MOKE

The origin of MOKE can be explained by either macroscopic dielectric theory or microscopic quantum theory. Macroscopically, magneto-optic effects arise from the antisymmetric, off-diagonal elements in the dielectric tensor. When light propagates through a medium, the movement of its electrons follows the electrical field of the light. Thus, for a linearly polarized light, the response of the electrons can be considered as a combination of left and right circular motions, with the radii of the circles being equal. The electric dipole moment proportional to the radius of the circular orbit will be same for the left and right circularly polarized light (LCP or RCP). Consequently, there will be no Faraday rotation. In presence of a magnetic field, an additional Lorentz force will act on the left and right circular motions of electrons in the opposite ways, pointing them towards or away from the centre of the circle. Thus, depending on the direction of magnetic field, the radius for left circular motion will be reduced and that for right circular motion will expand or vice versa. The difference between the radii of LCP and RCP light will give a finite difference in dielectric constants leading towards the magneto-optical Kerr effect (MOKE).

However, the quantum mechanical approach, stresses on the spin-orbit interaction (SOI) coupling the spin of the electron to its orbital motion, gives rise to Kerr effect in a ferromagnet. The movement of electrons under the influence of the electric field vector of light affects the SOI, which may be considered as an effective magnetic vector potential (A) given by: $A \sim s \times \nabla V$, s and ∇V being the electron spin and the electric field respectively, acting on the motion of the electron. This effect is not so prominent in non-magnets, because of the presence of equal amount of up and down spins cancels the effect. This effect is barefaced in ferromagnets, due to the unbalanced population of electron spins.

References

[1] A. H. Morrish, IEEE Press, New York, United States, (2001).
[2] M. A. Ruderman, C. Kittel, Phys. Rev. **96**, 99 (1954).
[3] T. Kasuya, P. Th. Phys. **16**, 45 (1956).
[4] H. A. Kramers, Physica. **1**, 182 (1934).
[5] P. W. Anderson, Phys. Rev. **79**, 350 (1950).
[6] J. B. Goodenough, Phys. Rev. **100**, 564 (1955).
[7] J. Kanamori, J. Phys. Chem. Solids. **10**, 87 (1959).
[8] I. E. Dzyaloshinskii, Sov. Phys. JETP **5**, 1259 (1957).
[9] T. Moriya, Phys. Rev. **120**, 91 (1960).
[10] A. Fert, V. Cros, and J. Sampaio, Nat. Nanotechnol. **8**, 152 (2013).
[11] R. A. Duine, K.-J. Lee, S. S. P. Parkin, and M. D. Stiles, Nat. Phys. **14**, 217 (2018).
[12] S. M. Rezende, C. Chesman, M. A. Lucena, A. Azevedo, F. M. de Aguiar, and S. S. P. Parkin, J. Appl. Phys. **84**, 958 (1998).
[13] P. Bruno, Physical Origins and Theoretical Models of Magnetic Anisotropy, Jürich, (1993).
[14] M. McCaig, Permanent magnets in theory and practice (Pentech Press, 1977).
[15] T. Thomson, Metallic Films for Electronic, Optical and Magnetic Applications, edited by K. Barmak, and K. Coffey, p. 454 (Woodhead Publishing, 2014).
[16] P. Bruno and J.-P. Renard, Appl. Phys. A **49**, 499 (1989).
[17] R. C. O'Handley, and S. W. Sun, J. Magn. Magn. Mater. **104**, 1717 (1992).
[18] L. Ranno, A. Llobet, R. Tiron, and E. Favre-Nicolin, Appl. Surf. Sci. 188, 170 (2002).
[19] E. R. Callen, and H. B. Callen, Phys. Rev. **129**, 578 (1963).
[20] W. F. Brown, C. Truesdell, Magnetoelastic Interactions, Springer Tracts in Natural Philosophy, Vol. 9 (1966).
[21] E. Villari, Annu. Rev. Phys. Chem. **126**, 87 (1865).
[22] S. Chikazumi, Physics of Ferromagnetism, the International Series of Monographs on Physics, **94** (1997).
[23] S. Pal, B. Rana, O. Hellwig, T. Thomson, and A. Barman, Appl. Phys. Lett. **98**, 082501 (2011).
[24] S. Ikeda, J. Hayakawa, Y. Ashizawa, Y. M. Lee, K. Miura, H. Hasegawa, M. Tsunoda, F. Matsukura, and H. Ohno, Appl. Phys. Lett. **93**, 082508 (2008).
[25] C. Duan, J. P. Velev, R. F. Sabirianov, Z. Zhu, J. Chu, S. S. Jaswal, and E. Y. Tsymbal, Phys. Rev. Lett. **101**, 137201 (2008).
[26] E. Beaurepaire, J. C. Merle, A. Daunois, and J. Y. Bigot, Phys. Rev. Lett. **76**, 4250 (1996).
[27] J. Hohlfeld, E. Matthias, R. Knorren, and K. H. Bennemann, Phys. Rev. Lett. **78**, 4861 (1997).
[28] G. Ju, A. Vertikov, A. V. Nurmikko, C. Canady, G. Xiao, R. F. C. Farrow, and A. Cebollada, Phys. Rev. B **57**, R700 (1998).
[29] G. Ju, A. V. Nurmikko, R. F. C. Farrow, R. F. Marks, M. J. Carey, and B. A. Gurney, Phys. Rev. Lett. **82**, 3705 (1999).
[30] B. Koopmans, M. van Kampen, J. T. Kohlhepp, and W. J. M. de Jonge, Phys. Rev. Lett. **85**, 844 (2000).
[31] W. Hubner, and G. P. Zhang, Phys. Rev. B **58**, R5920 (1998).
[32] G. P. Zhang, and W. Hubner, Phys. Rev. Lett. **85**, 3025 (2000).
[33] R. J. Elliott, Phys. Rev. **96**, 266 (1954).
[34] Y. Yafet, in Solid State Physics, Vol. 14, edited by F. Seitz and D. Turnbull (Academic, New York, 1963), p. 1.

[35] B. Koopmans, J. J. M. Ruigrok, F. Dalla Longa, and W. J. M. de Jonge, Phys. Rev. Lett. **95**, 267207 (2005).
[36] B. Koopmans, H.H.J.E. Kicken, M. van Kampen, and W.J.M. de Jonge, J. Mag, Mag. Mat. **286,** 271 (2005).
[37] K. Carva, M. Battiato, and P. M. Oppeneer, Phys. Rev. Lett. **107**, 207201 (2011).
[38] S. Essert, and H. C. Schneider, Phys. Rev. B **84**, 224405 (2011).
[39] K. Carva, M. Battiato, D. Legut, and P. M. Oppeneer, Phys. Rev. B **87**, 184425 (2013).
[40] B. Koopmans, G. Malinowski, F. Dalla Longa, M. Aeschlimann, Nat. Mat. **9**, 259 (2009).
[41] M. Krauss, T. Roth, S. Alebrand, D. Steil, M. Cinchetti, M. Aeschlimann, and H. C. Schneider, Phys. Rev. B **80**, 180407(R) (2009).
[42] B. Y. Mueller, T. Roth, M. Cinchetti, M. Aeschlimann, and B. Rethfeld, New J. Phys. **13**, 123010 (2011).
[43] E. Carpene, E. Mancini, C. Dallera, M. Brenna, E. Puppin, and S. De Silvestri, Phys. Rev. B **78**, 174422 (2008).
[44] J.-Y. Bigot, M. Vomir, and E. Beaurepaire, Nat. Phys. **5**, 515 (2009).
[45] R. Mandal, M. Berritta, K. Carva, and P. M. Oppeneer, Phys. Rev. B **91**, 174415 (2015).
[46] G. P. Zhang, W. Hubner, G. Lefkidis, Y. Bai, and T. F. George, Nat. Phys. 5, 499 (2009).
[47] A. Einstein and W. J. de Haas, Verhandl. Deuts. Phys. Ges. **17**, 152 (1915).
[48] B. Koopmans, M. van Kampen, and W. J. M. de Jonge, J. Phys.: Condens. Matter **15**, S723 (2003).
[49] C. Dornes, Y. Acremann, M. Savoini, M. Kubli, M. J. Neugebauer, E. Abreu, L. Huber, G. Lantz, C. A. F. Vaz, H. Lemke, E. M. Bothschafter, M. Porer, V. Esposito, L. Rettig, M. Buzzi, A. Alberca, Y. W. Windsor, P. Beaud, U. Staub, Diling Zhu, Sanghoon Song, J. M. Glownia, and S. L. Johnson, Nat. Lett. **565**, 209 (2019).
[50] J. Stohr, and H. C. Siegmann, From Fundamentals to Nanoscale Dynamics, 1st ed. (Springer, Berlin, 2006).
[51] W. Hubner, and K. H. Bennemann, Phys. Rev. B **53**, 3422 (1996).
[52] M. Wietstruk, A. Melnikov, C. Stamm, T. Kachel, N. Pontius, M. Sultan, C. Gahl, M. Weinelt, H. A. Durr, and U. Bovensiepen, Phys. Rev. Lett. **106**, 127401 (2011).
[53] E. Beaurepaire, G. M. Turner, S. M. Harrel, M. C. Beard, J.-Y. Bigot, and C. A. Schmuttenmaer, Appl. Phys. Lett. **84**, 3465 (2004).
[54] G. Malinowski, F. Dalla Longa, J. H. H. Rietjens, P. V. Paluskar, R. Huijink, H. J. M. Swagten, and B. Koopmans, Nat. Phys. **4**, 855 (2008).
[55] M. Battiato, K. Carva, and P. M. Oppeneer, Phys. Rev. Lett. **105**, 027203 (2010).
[56] M. Battiato, K. Carva, and P. M. Oppeneer, Phys. Rev. B **86**, 024404 (2012).
[57] R. Metzler, and J. Klafter, Phys. Rep. **339**, 1 (2000).
[58] N. Moisan, G. Malinowski, J. Mauchain, M. Hehn, B. Vodungbo, J. Luning, S. Mangin, E. E. Fullerton, and A. Thiaville, Sci. Rep. **4**, 4658 (2014).
[59] A. Eschenlohr, M. Battiato, P. Maldonado, N. Pontius, T. Kachel, K. Holldack, R. Mitzner, A. Fohlisch, P. M. Oppeneer, and C. Stamm, Nat. Mater. **12**, 332 (2013).
[60] D. Rudolf, C. L. Vorakiat, M. Battiato, R. Adam, J. M. Shaw, E. Turgut, P. Maldonado, S. Mathias, P. Grychtol, H. T. Nembach, T. J. Silva, M. Aeschlimann, H. C. Kapteyn, M. M. Murnane, C. M. Schneider, and P. M. Oppeneer, Nat. Commun. **3**, 1037 (2012).
[61] A. J. Schellekens, W. Verhoeven, T. N. Vader, and B. Koopmans, Appl. Phys. Lett. **102**, 252408 (2013).
[62] J. Wieczorek, A. Eschenlohr, B. Weidtmann, M. Rosner, N. Bergeard, A. Tarasevitch, T. O. Wehling, and U. Bovensiepen, Phys. Rev. B **92**, 174410 (2015).
[63] E. Turgut, C. La-o-vorakiat, J. M. Shaw, P. Grychtol, H. T. Nembach, D. Rudolf, R. Adam, M. Aeschlimann, C. M. Schneider, T. J. Silva, M. M. Murnane, H. C. Kapteyn, and S. Mathias, Phys. Rev. Lett. **110**, 197201 (2013).

[64] S. Pan, O. Hellwig, and A. Barman, Phys. Rev. B **98**, 214436 (2018).
[65] P. Tengdin, C. Gentry, A. Blonsky, D. Zusin, M. Gerrity, L. Hellbruck, M. Hofherr, J. Shaw, Y. Kvashnin, E. K. Delczegczirjak, M. Arora, H. Nembach, T. J. Silva, S. Mathias, M. Aeschlimann, H. C. Kapteyn, D. Thonig, K. Koumpouras, O. Eriksson, and M. M. Murnane, Sci. Adv. **6**, eaaz1100 (2020).
[66] M. Hofherr, S. Hauser, J. K. Dewhurst, P. Tengdin, S. Sakshath, H. T. Nembach, S. T. Weber, J. M. Shaw, T. J. Silva, H. C. Kapteyn, M. Cinchetti, B. Rethfeld, M. M. Murnane, D. Steil, B. Stadtmuller, S. Sharma, M. Aeschlimann, and S. Mathias, Sci. Adv. **6**, eaay8717 (2020).
[67] J. K. Dewhurst, P. Elliott, S. Shallcross, E. K. U. Gross, S. Sharma, Nano Lett. **18**, 1842 (2018).
[68] L. Landau and E. Lifshitz, Phys. Z. Sowjet. 8, 153 (1935).
[69] T. Gilbert, IEEE. Trans. Magn. **40**, 3443 (2004).
[70] J. A. Weil, J. R. Bolton, Electron Paramagnetic Resonance: Elementary Theory and Practical Applications (Wiley, 2007).
[71] B. Odom, D. Hanneke, B. D'Urso, G. Gabrielse, Phys. Rev. Lett. **97**, 030801 (2006).
[72] J. L. Heilbron, T. S. Kuhn, Hist. Stud. Phys. Sci. 1 (1969).
[73] R. Shankar, Principles of Quantum Mechanics (Springer US, 1995).
[74] J. H. E. Griffiths, Nature **158**, 670 (1946).
[75] C. Kittel, Phys. Rev. **73**, 155 (1948).
[76] F. Bloch, "Zur theorie des ferromagnetismus," Z. Phys. **61**, 206 (1930).
[77] R. W. Damon and J. R. Eshbach, J. Phys. Chem. Solids. **19**, 308 (1961).
[78] S. O. Demokritov, B. Hillebrands, and A. N. Slavin, Phys. Rep. **348**, 441 (2001).
[79] R. Arias, and D. L. Mills, Phys. Rev. B. **60**, 7395 (1999).
[80] M. Cottam, and D. Lockwood, Wiley, New York, (1986).
[81] K. Y. Guslienko, and A. N. Slavin, Phys. Rev. B **72**, 014463 (2005).
[82] C. Yu, M. J. Pechan, W. A. Burgei, and G. J. Mankey, J. Appl. Phys. **95**, 6648 (2004).
[83] Z. K. Wang, V. L. Zhang, H. S. Lim, S. C. Ng, M. H. Kuok, S. Jain, and A. O. Adeyeye, ACS Nano. **4**, 643 (2010).
[84] M. Krawczyk, S. Mamica, M. Mruczkiewicz, J. W. Klos, S. Tacchi, M. Madami, G. Gubbiotti, G. Duerr, and D. Grundler, J. Phys. D: Appl. Phys. **46**, 495003 (2013).
[85] J. F. Bobo, H. Kikuchi, O. Redon, E. Snoeck, M. Piecuch, and R. L. White, Phys. Rev. B **60**, 4131 (1999).
[86] M. Ruhrig, R. Schafer, A. Hub ert, R. Mosler, J. A. Wolf, S. Demokritov, and P. Grunberg, Phys. Status Solidi A **125**, 635 (1991).
[87] J. C. Slonczewski, Phys. Rev. Lett. **67**, 3172 (1991).
[88] H. Fujiwara, and M. R. Parker, J. Magn. Magn. Mater. **135**, L23 (1994);
[89] H. Fujiwara, W. D. Doyle, A. Matsuzono, and M. R. Parker, ibid. **140**, 519 (1995).
[90] J. J. Krebs, G. A. Prinz, M. E. Filipkowski, and C. J. Gutierrez, J. Appl. Phys. **79**, 4525 (1996).
[91] D. Castilla, R. Yanes, M. Sinusía, G. Fuentes, J. Grandal, M. Maicas, T. E. G. Alvarez-Arenas, M. Muñoz, L. Torres, L. López and J. L. Prieto, Sci. Rep. **10**, 9413 (2020).
[92] C.-Y. Liang, S. M. Keller, A. E. Sepulveda, A. Bur, W.-Y. Sun, K. Wetzlar, and G. P. Carman. Nanotechnology **25**, 435701 (2014).
[93] J. Kerr, Philos. Mag. Series **3**, 321 (1877).
[94] A. Kundt, Philos. Mag. Ser. **5**, 308 (1884).

Chapter 3

3. Experimental Techniques

Fabrication of the nanostructures with high-quality lateral features, surface, and interface with dimensions down to almost atomic range involves massive effort by the experts in the field of nanoscience and technology. The continuous hunt for miniaturized devices has urged the scientists to push the boundary beyond atomic limits. High-quality samples can be grown by bottom-up and top-down approaches [1]. The former relies on the chemical synthesis and mesoscopic pattern formation. Thus, nanoparticles, nanowires, micro-organisms etc. are synthesized. Some well used methods following this approach are electrochemical deposition through porous templates, plasma arcing, sol-gel synthesis, hydrothermal synthesis, molecular self-assembly, etc [2-4]. However, using bottom-up approach, it is often difficult to obtain highly ordered and mono dispersed structures. Top-down approach is therefore required to fabricate a range of highly controlled and ordered structures such as nanodot array, antidot array, nanostripes, quasicrystals, bicomponent nanostructures, binary nanostructures, and several other micro- and nanostructures by pattering magnetic thin films and multilayers. Some of the lithographic methods that follow this approach are photolithography, electron beam lithography, ion-beam lithography, deep ultraviolet lithography, scanning lithography, scanning probe lithography, nanosphere lithography, etc. [5-7]. Several other methods under this category are shadow masking, ion-beam irradiation, ion implantation, laser machining etc. Optimization of the fabrication procedure is extremely important to achieve high quality interfaces while involving different kinds of materials and to get very sharp edges while fabricating narrow sized elements avoiding structural distortions. In this chapter, the working principles of magnetron sputtering, electron beam evaporation and electron beam lithography will be discussed which have been used to grow high quality ferromagnetic thin films, multilayers and nanostructures studied in this thesis.

Several electrical, optical, electro-optical, and atomic interaction-based characterization techniques have been developed relentlessly over several decades to probe the magnetic properties of the thin films and nanostructures. The topographical and elemental quality of the samples under investigation have been characterized by using scanning electron microscopy (SEM), energy dispersive x-ray spectroscopy (EDX) atomic force microscopy (AFM). The spin textures, magnetization and stray field distribution have been investigated by using

magnetic force microscope (MFM), vibrating sample magnetometry (VSM) and static MOKE magnetometry. We have further used the time-resolved magneto optical Kerr effect (TR-MOKE) magnetometry and Brillouin light scattering (BLS) to investigate the magnetization dynamics. Both these techniques rely on magneto-optical interactions, which are different from electrical methods (like ferromagnetic resonance or FMR) which does not conventionally allow for a space resolution on the microscale. In this chapter, we briefly discuss the principles and advantages of the aforementioned techniques.

3.1. Fabrication Techniques

3.1.1. Sputtering

This is a plasma vapor deposition technique which is used to deposit good quality thin films and multilayers [8]. It is a multiple collision process where the positive ions in the plasma of an inert gas are accelerated and used to dislodge and eject atoms from source (target) material. These eroded or cluster of atoms then condense over a substrate to form a thin film of desired parameters. The sputtering process is schematically shown in Fig. 3.1.

Initially, an inert gas (generally Ar) is introduced into a pre-pumped vacuum chamber. Subsequently, gaseous plasma is created and sustained inside the chamber using a high energy source (ranging from a few hundred to a few thousand electron volts). The plasma is described as the fourth state of matter where neutral gas atoms, ions, electrons and photons exist in a nearly balanced state simultaneously. The cathode (target) is composed of the material or alloy to be deposited, whereas, the substrate serves as the anode. Depending on whether the target material is conductive or non-conductive, a direct current (DC) or radio frequency (RF) power supply can be used. As soon as the power supply is on, the free electrons in the plasma accelerate away from the cathode. The accelerated electrons collide with the neutral gas atoms in their path and leave the positively charged ions. The positively charged ions are then accelerated, strike the target surface and eject neutral atoms and electrons out of it. These ejected atoms then travel in a typical line-of-sight cosine path and get subsequently deposited on the substrate which is kept in proximity with the target. This whole process is performed under high vacuum of around 10^{-7} Torr or better.

The two major problems of the conventional sputtering technique are slow deposition rate and overheating of the target due to extensive electron bombardment. One way to address these problems is to use magnetron sputtering, in which magnets are used behind the cathode to trap

the free electrons in a cyclic path just above the cathode. In this way the velocity of electrons near the target decreases, and as a consequence, it is possible to deposit layered structures in lesser time and with lower substrate temperature.

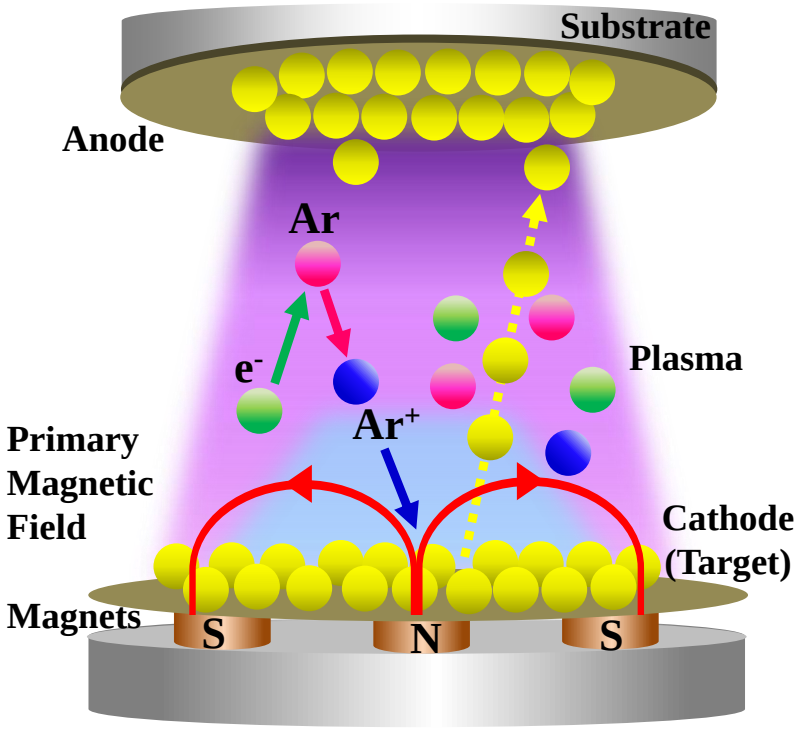

Fig. 3.1: Schematic diagram of the sputtering technique.

3.1.2. Electron Beam Evaporation

The electron beam evaporation (EBE) is a physical vapor deposition technique [9], where an intense beam of electrons is generated from a filament via thermionic emission and is steered towards the source material by the electric and magnetic fields. The collision with electron beam causes heating of the source material and it vaporizes after reaching the boiling point within a vacuum environment. The surface atoms having sufficient energy traverse the vacuum chamber and are used to coat a substrate placed above the evaporating material. The pressure in the chamber is maintained such that the mean free path remains lesser than the distance between the electron beam source and the substrate. The "line of sight" arrival of material is required when masking is employed to generate a pattern in the substrate. The low arrival energy is also advantageous for sensitive substrates. The EBE process is schematically shown in Fig. 3.2.

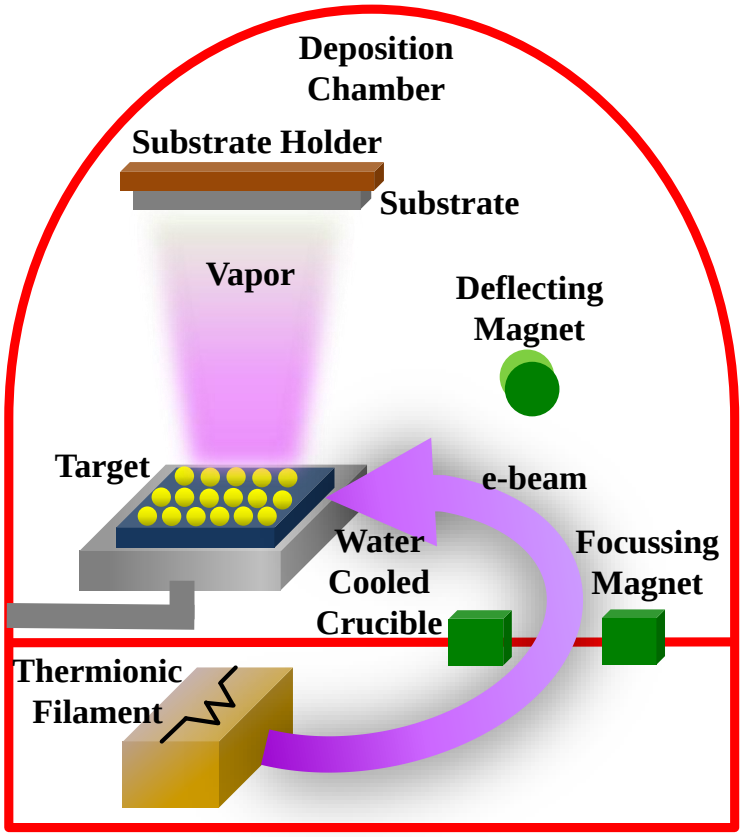

Fig. 3.2: Schematic diagram of the EBE technique.

3.1.3. Electron Beam Lithography

The electron beam lithography (EBL) technique is used to fabricate two dimensional arrays with submicron features, much smaller than that can be visualized by the naked eye or even optical microscope [10]. This technique is composed of the following fundamental steps:

(1) A pre-cleaned substrate is spin-coated with bilayer polymethyl methacrylate (PMMA 495K and 950K) positive tone e-beam resist. The two layer coating helps in achieving an undercut edge profile of the resist after development of the pattern onto it.

(2) The resist is exposed to focused electron beams inside a scanning electron microscope (SEM) connected with a computer. In this step the desired structure is drawn using commercially available design software (Auto CAD).

(3) After writing, the resist is developed in methyl isobutyl ketone (MIBK) and isopropyl alcohol (IPA), MIBK:IPA :: 1:3, solution, followed by rinsing in water.

(4) In the next step, the desired material is deposited on top of the developed resist.

(5) Finally, the lift off is done in acetone using ultrasonic agitation to remove the unexposed resist along with the film deposited on it.

The EBL process is schematically shown in Fig. 3.3.

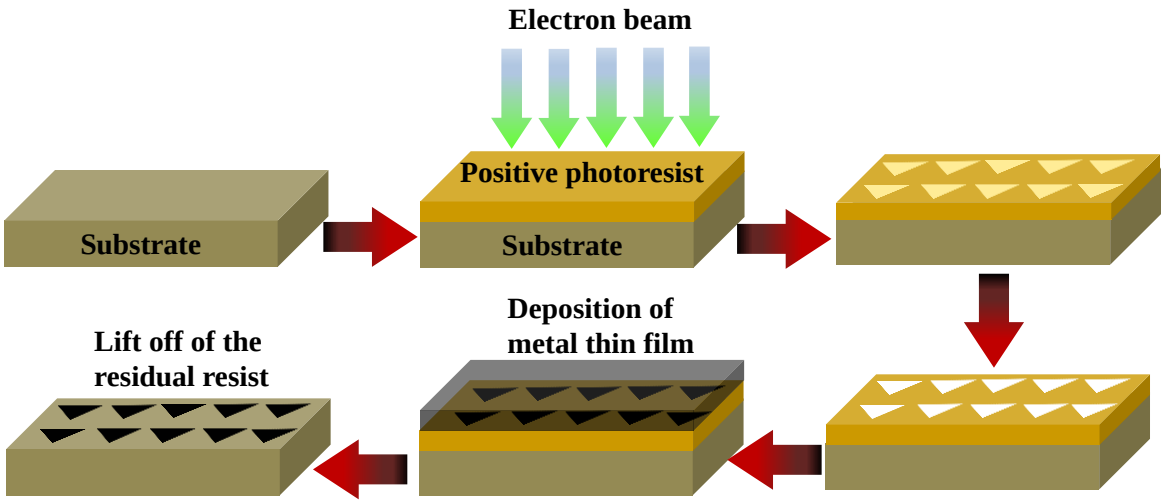

Fig. 3.3: Schematic diagram of the EBL process.

3.2. Measurement Techniques

3.2.1. Scanning Electron Microscopy

The scanning electron microscope (SEM) produces images of a sample by scanning the surface with a high-energy beam of electrons [11]. The electron microscope was developed when the wavelength became the limiting factor in light microscopes. Electrons have much shorter wavelengths, enabling better resolution. The schematic of a SEM is shown in Fig. 3.4. In a typical SEM, an electron beam is generated from a cathode by phenomenon of thermionic emission or an electric field. The beam is then focused by one or two electromagnetic condenser lenses.

Subsequently, the beam passes through pair of scanning coils or pair of deflector plates, which can deflect the beam in a two-dimensional rectangular region of the sample surface so that it scans in a raster fashion. Finally the electron beam is focused onto the sample by an objective lens. As the highly energetic electron beam interacts with the sample, they produce secondary electrons, backscattered electrons, and Auger electrons. Energy is also emitted in the form of characteristic x-rays and visible light (cathodo-luminescence). The secondary electrons which are produced by inelastic scattering of incident electrons with the atoms of the sample are collected by a detector to form images which are then displayed on the computer screen. Due

to a very narrow electron beam, SEM images have large depth of field with the capability to produce three-dimensional images, which are quite important for investigating the morphology of the sample surface. The samples are generally fixed on a metal stub by a sticky carbon tape. There is a possibility of charge accumulation at the sample surface which may affect the quality of the image. Hence, to avoid charge accumulation, the samples should be electrically conductive at the surface as well as grounded. We have used "FEI QUANTA 200" and "FEI Helios NanoLab 600" SEMs to characterize our samples.

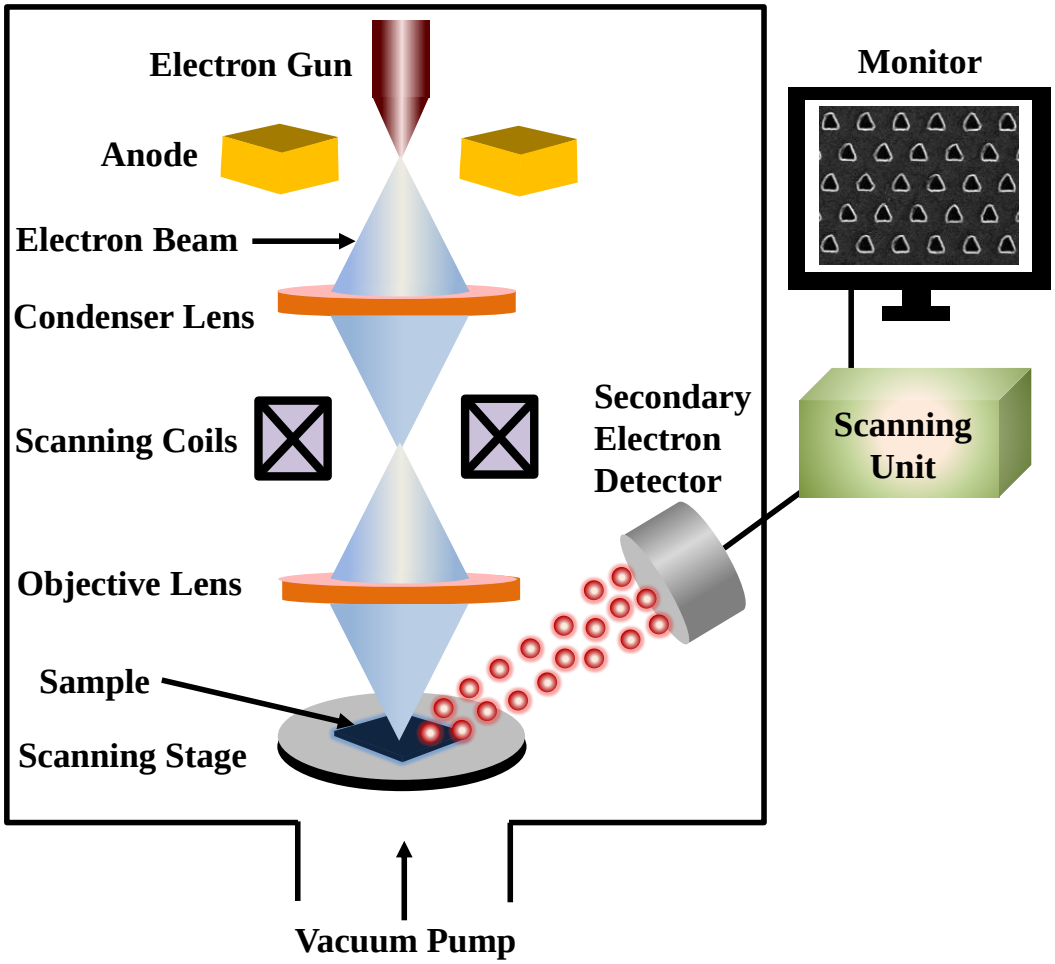

Fig. 3.4: Schematic diagram of SEM technique.

3.2.2. Energy-Dispersive X-ray Spectroscopy

The energy dispersive x-ray spectroscopy (EDX) technique is used for the elemental analysis or for investigating the chemical purity of a sample. The schematic of an EDX spectrometer is shown Fig. 3.5. Every atom at the ground state contains a number of electrons moving around the nuclei and arranged in different characteristic shells. Whenever a high energy beam of charged particles, like electrons, protons or sometimes x-rays hits the sample it ejects out electrons from an inner shell and creates a hole. Subsequently, the electrons from outer shells jump to the inner shells to fill the hole. The energy difference between these two shells is then radiated in the form of an x-ray. The energy of the emitted x-ray is basically the characteristics of an element's atomic structure. Since the atomic structure of each element is unique, the energy of the emitted x-ray is also unique in nature. A Si (Li) detector is used as an energy dispersive spectrometer to measure the energy and number of the emitted x-rays. The elements are identified from the peak energy values of the emitted x-rays and the atomic percentage of the elements in the sample are obtained from the relative heights of the peaks. Generally, the EDX spectrometer is attached to the SEM. We have used an EDX spectrometer from EDAX attached with "FEI QUANTA 200" SEM.

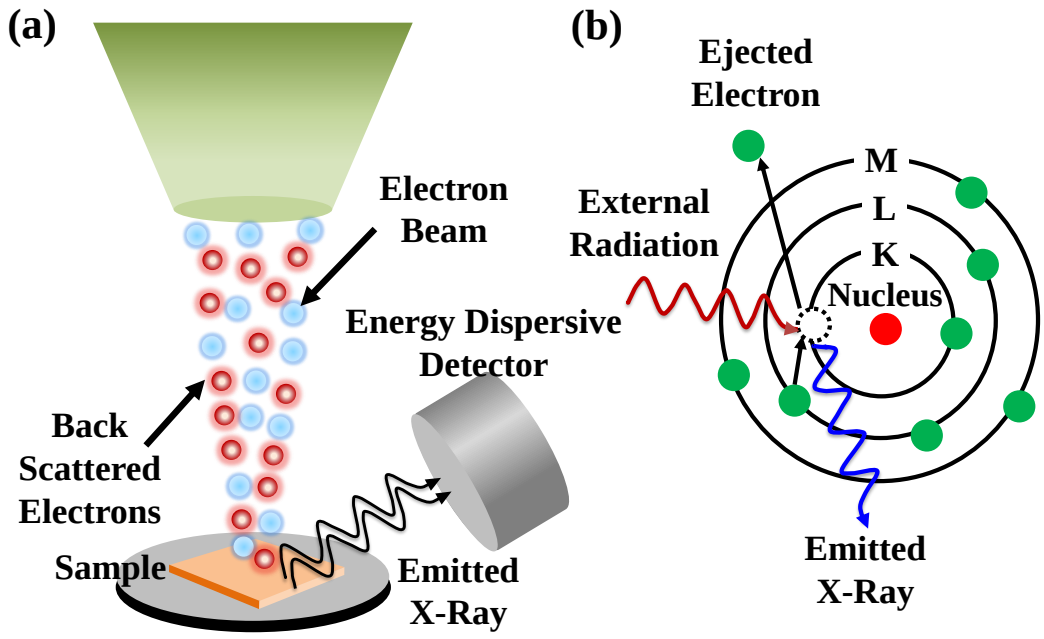

Fig. 3.5: (a) Schematic diagram of EDX spectrometer. (b) Schematic of interaction of accelerated electrons with sample and emission of X-rays from the designated orbit.

3.2.3. Atomic Force Microscopy

Atomic force microscopy (AFM) is a high resolution (down to tens of nm) scanning probe microscopy which was developed by Gerd Binnig, Calvin Quate and Christoph Gerber [12]. AFM is used to image the surface topography, roughness etc. for a variety of materials, such as, thin films, nanostructures, biological membranes, polymers, semiconductors, ceramics, composites, glasses etc. A typical AFM consists of a very tiny sharp probing tip (radius of curvature of few nanometers) at the end of a cantilever, which is scanned very closely across the sample surface (Fig. 3.6) The distance between the tip and the sample surface is so small that atomic-range forces such as Van der Waals forces, capillary and adhesive forces, chemical bonding and electrostatic forces act between them. The force acting on the tip is obtained by detecting the deflection of the cantilever, measured by a laser spot reflected from the top surface of the cantilever, which is captured by a four-quadrant photodetector. The differences between the signals from different quadrants of photodetector give the estimate of the deflections of the cantilever. The sample is placed on a piezoelectric controller which helps in performing the raster scan. Additionally, there is a feedback mechanism that enables the piezoelectric scanner to keep the tip at a constant force while obtaining the information of height or at constant height for obtaining the information of force.

Primarily, there are three modes of operation in AFM: contact mode, non-contact mode and tapping mode.

(i) Contact mode: Contact mode is a so-called static operating mode where the tip scans the sample in close contact with its surface. A constant repulsive Van der Waals force is maintained always between the tip and the sample surface. In this mode to prevent any damage or scratch over the sample surface, cantilevers with low stiffness and longer length are used in order to achieve a large enough deflection signal while keeping the interaction force low. However, the contact mode yields very low resolution

(ii) Non-contact mode: The non-contact mode is used in situations where tip contact may cause any degradation of the sample. In this mode, the tip experiences an attractive Van der Waals force. The cantilever oscillates/vibrates at its resonant frequency, where the vibration amplitude is few nanometers (< 10 nm). The Van der Waals forces, which are strongest in this range, act to decrease the resonance frequency of the cantilever. This decrease in resonant frequency combined with the feedback loop system maintains a constant amplitude or frequency of vibration by adjusting the average tip-to-sample distance. The topographic image of the sample surface is obtained by measuring the tip-to-sample distance, i.e. the tip height at

each point. In non-contact mode, the lengths of the cantilevers are smaller than those used in contact mode.

(iii) Tapping mode: The tapping mode is the most commonly used mode in AFM. In this mode the cantilever vibrates at or near its resonant frequency using a piezoelectric crystal mounted in the AFM tip holder similar to non-contact mode. However, the vibration amplitude is greater than 10 nm, typically 100 to 200 nm. Several interacting forces such as Van der Waals forces, dipole-dipole interactions, electrostatic forces, etc. acts on the cantilever when the tip comes close to the sample surface and causes the vibration amplitude to decrease or phase to be changed. The tip height above the sample surface is controlled by the piezoelectric actuator to maintain a fixed vibration amplitude or phase of the cantilever during scanning. In this mode the tip can touch the sample surface only at its lowest position. Hence, it is called intermittent contact mode.

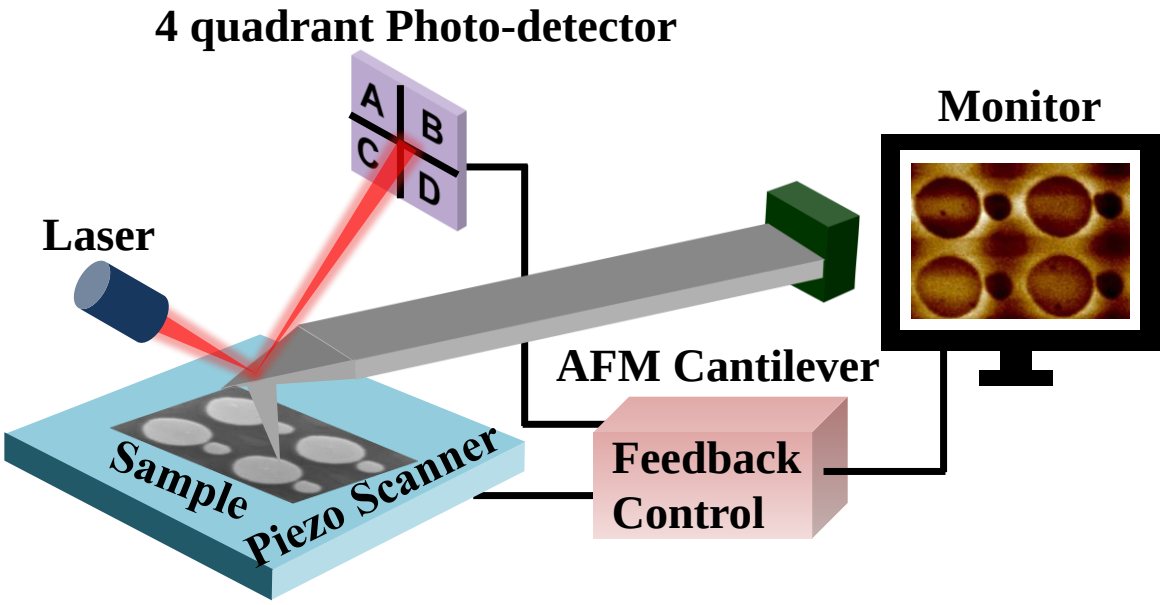

Fig. 3.6: Schematic diagram of AFM technique.

3.2.4. Magnetic Force Microscopy

In magnetic force microscopy (MFM) the magnetic texture formed within a magnetic sample can be studied by the magnetic interactions between the tip and the sample. It is mostly associated with the AFM set-up. MFM tips are coated with a thin magnetic layer having high coercivity so that magnetization state of the tip does not change during imaging. Consequently, the radius of curvature of MFM tips is greater than the AFM tips. As the tip is brought close to the sample, it senses the magnetic forces along with the atomic and electrostatic forces due to

the interaction with the components of stray fields from the magnetic sample. To increase the magnetic contrast of the image, the AFM image is taken first. Then the tip is lifted up further away and scanned again over the sample at that particular height to extract the magnetic signal. This is known as 'dual scan' method of MFM imaging. The magnetic signal thus obtained is extracted and processed by the software to provide information about magnetic texture of the sample.

3.2.5. Vibrating Sample Magnetometry

The vibrating sample magnetometry (VSM) technique is employed to measure the magnetic properties of a sample including the magnetic moment, its behavior as a function of applied magnetic field (*H*) and temperature (*T*). Simon Foner invented VSM technique in 1955 and reported it in 1959 [13]. It operates on the Faraday's law of induction, which states that a changing magnetic flux through a coil gives rise to an electric field induced in the coil. Mathematically,

$$E_{in} = -n_w A \frac{dB}{dt} \tag{3.1}$$

where E_{in} is the induced electric field, *A* is the area of the coil with number of turns n_w.

Using $B = \mu_0 (H + M)$, for constant magnetic field we get,

$$E_{in} = -n_w A \frac{dM}{dt} \tag{3.2}$$

Since the magnetization (*M*) depends on the total magnetic moment (*m*), the above equation finally reduces to,

$$E_{in} = -mwzy_0 n_w n_c G cos(wt) \tag{3.3}$$

where *w* and *z* are frequency and amplitude of vibration, respectively, y_0 is the distance to the pickup coils, n_c is the number of pickup coils and *G* is geometric factor of the sample. This electric field can be used to examine the magnetic moment of a sample.

The schematic of the set up is shown in Fig. 3.7. During measurement, the sample is first placed in a constant magnetic field. The magnetic dipole moment of the sample then creates a stray magnetic field around the sample. The sample is attached to a piezoelectric transducer assembly, which converts sinusoidal electric signal (generated by an oscillator/amplifier) into a sinusoidal vibration of the sample rod which creates a sinusoidal oscillation of the sample. The resulting oscillation in the magnetic moment of the sample induces a voltage in the pickup coil (located close to the sample), which is independent of the applied magnetic field. This technique thus converts the dipole field of the sample into an ac electrical signal, which can be

amplified and measured using a lock-in amplifier where the output of the piezoelectric signal serves as the reference signal. Any change in the applied magnetic field or temperature causes a change in the magnetic dipole moment of the sample, which gives the *M-H* or *M-T* curves of a ferromagnetic material.

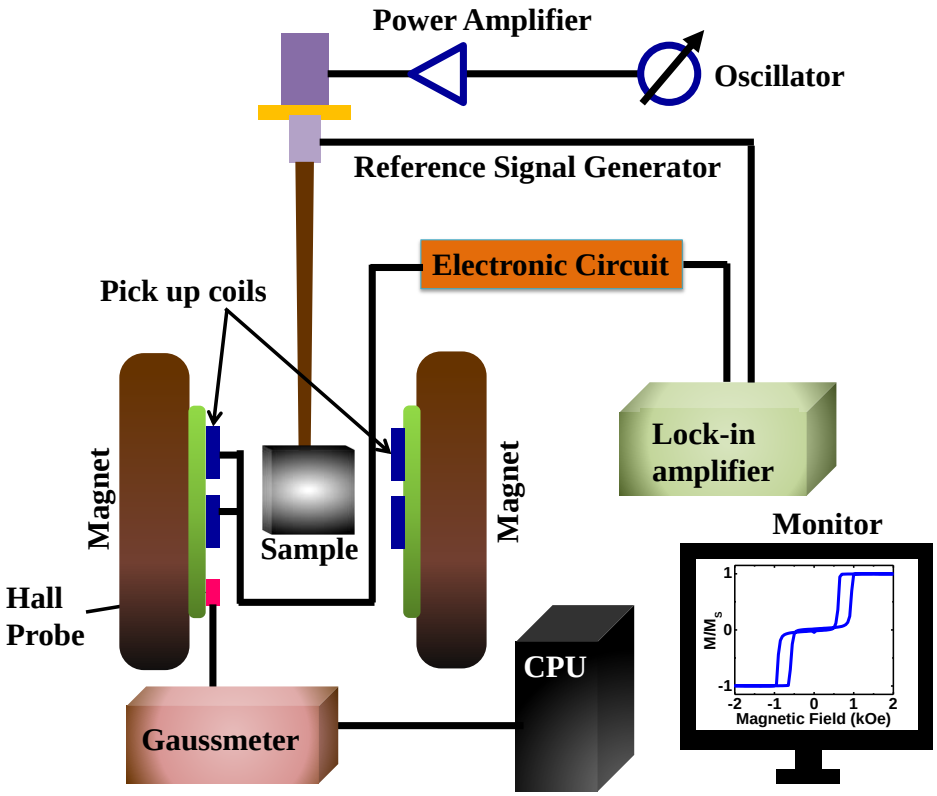

Fig. 3.7: Schematic diagram of VSM technique.

3.2.6. Static Magneto Optical Kerr Effect Magnetometry

The static magneto-optical Kerr effect (SMOKE) magnetometer is used to measure the magnetic hysteresis loops of continuous and patterned ferromagnetic thin films [1, 14]. The schematic diagram of the home built SMOKE set up in our laboratory is shown in Fig. 3.8.

A plane polarized continuous wave He-Ne laser (wavelength = 632 nm, power ≈ 30 mW) is used for this measurement. The laser beam passes through a Glan-Thompson (GT) polarizer and becomes fully polarized with s-polarization. This polarized beam is then chopped at 2 kHz frequency by a mechanical chopper, which is controlled by a controller unit. The chopped beam is then guided by a pair of mirrors (M1 and M2) to a lens (L1) which focuses the beam onto the sample. The sample is mounted on a high precision rotating mount between the pole pieces

of an electromagnet and the measurement is performed in longitudinal geometry, where the plane of incidence is parallel to the direction of the magnetic field.

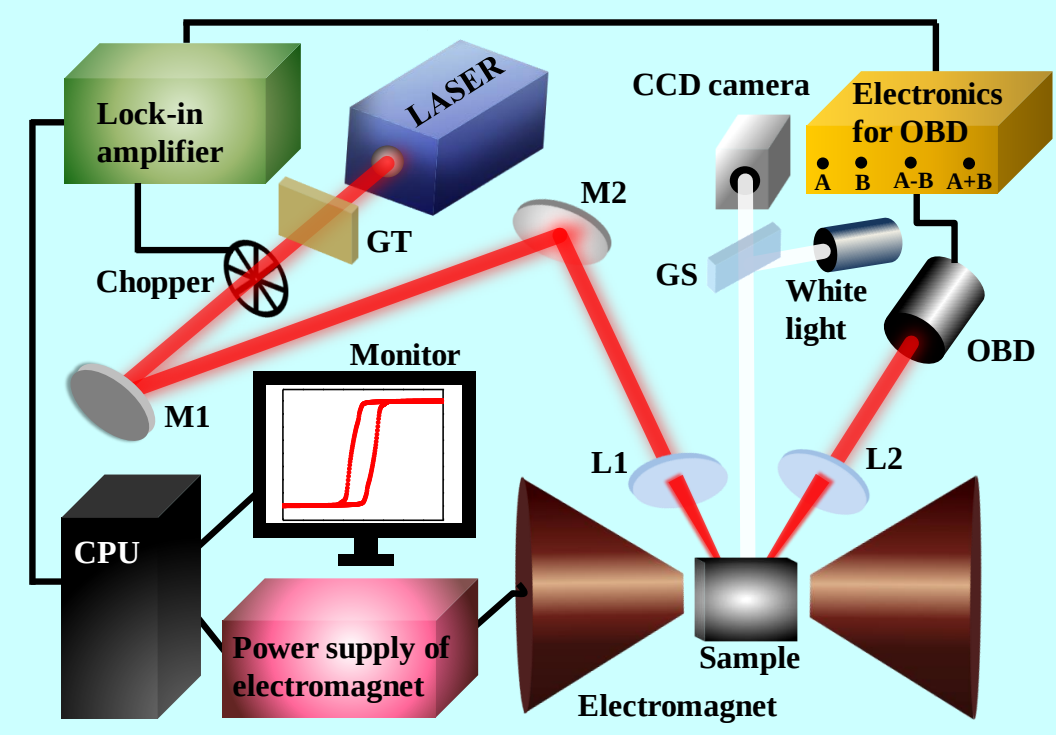

Fig. 3.8: Schematic diagram of static MOKE magnetometer in longitudinal geometry.

The electromagnet provides a variable bipolar in-plane magnetic field. A white light is also used for viewing purpose, which is divided into two parts using a glass slide (GS). One fraction is incident on the sample and the other fraction is sent to a CCD camera to locate the laser spot onto the sample. The magnetic moment of the sample rotates the plane of polarization of the reflected beam from its initial direction owing to the Kerr rotation. Finally, the reflected beam from the sample is collected by another lens (L2) and directed towards an optical bridge detector (OBD). The OBD consists of a polarizing beam splitter (PBS), which splits the beam in two perpendicularly polarized components. Then two Si-photodiode detectors A and B adopt those components and convert them into electrical signals. In absence of any magnetic field, the OBD is brought to its balanced condition (A = B) by rotating the axis of the PBS. As the magnetic field is applied, the polarization of the beam is changed and the OBD no longer remains in the balanced condition ($A \neq B$). The difference signal (A – B), which is proportional to the magnetization of the sample, is measured in a phase sensitive manner by a lock-in amplifier as a function of the external magnetic field to obtain the hysteresis loop. The

frequency of the chopper is fed to the lock-in amplifier as a reference signal. The OBD signal is further converted to Kerr rotation by rotating the PBS 1° away from its balanced condition and recording the equivalent voltage, which is subsequently used as the calibration factor. To obtain hysteresis loop, the magnetic field is varied from positive to negative direction and the change in magnetization is recorded using a homemade Labview software. The hysteresis loop obtained from SMOKE technique provides information like saturation field, coercive field, remanence, anisotropy, Kerr rotation/ellipticity which are very useful for the characterization of a sample.

3.2.7. Time-Resolved Magneto Optical Kerr Effect Technique

The time-resolved MOKE (TR-MOKE) magnetometry is employed to study ultrafast magnetization dynamics from femtosecond to nanosecond time scale, in which a series of phenomena, *viz.*, ultrafast demagnetization, fast and slow remagnetzations, magnetization precession and damping occur [1, 14]. This technique relies upon both the excitation and detection of the magnetization dynamics in optical manner, i.e. an all-optical technique. This state-of-the-art system has several advantages such as:

1. This technique offers the highest temporal resolution down to sub -100 fs.
2. Sample fabrication procedure is straight forward. No additional waveguide structures are required as that in case of ferromagnetic resonance technique.
3. This is a local measurement technique where the spatial resolution can go down to sub-μm regime.
4. This is a reliable and non–invasive measurement technique.

The working principle of the TRMOKE set up used during the works demonstrated in this thesis is based upon the two-color pump-probe (both collinear and non-collinear) geometry where the magnetic response is recorded in a stroboscopic fashion. In this section we have provided an overview of the two different variants of TR-MOKE techniques based on fs oscillator and amplified laser systems.

3.2.7.1. TR-MOKE Microscopy in Collinear Geometry

The generation of ultrashort laser pulses of required wavelength involves a composite laser system consisting of the following laser units: diode laser, diode pumped solid state laser

(DPSS: Millennia) and Titanium (Ti): sapphire (Al_2O_3) laser (Tsunami). The CW output from an array of diode lasers is used to pump the DPSS system. The DPSS with maximum power 10 W (variable) and wavelength $\lambda = 532$ nm is used to pump the Ti: sapphire laser, which uses regenerative acousto-optic mode locking mechanism to produce fs laser pulse (wavelength (λ) ~ 800 nm, repetition rate ~ 80 MHz and pulse width ~ 80 fs). The fundamental beam is divided into two parts. The intense part is fed to a second harmonic generator (SHG) to produce the second harmonic beam (λ ~ 400 nm), which is used to pump or excite the magnetization dynamics of the sample, while the time-delayed fundamental beam (λ ~ 800 nm) is used to probe the magnetization dynamics. A brief discussion of different laser units is as follows.

Millennia

First, an array of diode lasers is used to pump a solid state laser. The CW output of the diode laser bars, after being collimated by a cylindrical micro-lens, is coupled to an optical fibre bundle by the *FCbar* technology, which efficiently directs the beam towards the DPSS system. This DPSS unit uses Nd^{3+} ions doped in a Yttrium Vanadate crystalline matrix ($Nd:YVO_4$) to serve as the gain medium. The monochromatic output of the diode laser overlaps with the absorption spectra of the Nd^{3+} ion. The Nd^{3+} is a four level system which primarily emits photons of wavelength 1064 nm due to the transition of electron from $4F_{3/2}$ level to $4I_{3/2}$ level. However, there are also transitions at other wavelengths, which have lower gain along with a higher threshold value than the 1064 nm transition at room temperature and the wavelength selection optics limit the oscillation to 1064 nm. Subsequently, a lithium triborate (LBO: $LiBi_3O_5$) nonlinear crystal is used to double its frequency in order to convert the output wavelength to $\lambda = 532$ nm. As the efficiency of the LBO crystal is sensitive to temperature and humidity of the surrounding environment, it is important to maintain the crystal at the appropriate phase-matching temperature and a prescribed humidity value to optimize its efficiency and to keep the output fixed at $\lambda = 532$ nm. This is achieved by using a temperature regulating oven while it is constantly purged by dry N_2. As the crystal itself keeps the fundamental and the second harmonic beams collinear (noncritically phase-matched), a rigorous alignment of the Millennia cavity is not required. Additionally, a large acceptance angle makes it insensitive to any slight misalignment within the Millennia. A mechanical shutter is also attached to the cavity to block the output beam when required.

Tsunami

The output of DPSS finally pumps a Ti-sapphire oscillator (Tsunami), which delivers tunable output of near-IR wavelengths ranging from 690 nm to 1080 nm with pulse width of about 80 fs [15]. Here, the lasing medium is titanium ions (Ti^{3+}) doped sapphire (Al_2O_3) crystal. Tsunami laser head contains the Ti:sapphire rod and the optics, such as, input coupler (IC), rod focusing mirrors, guiding mirrors, beam folding mirrors, a high reflector (HR), an output coupler (OC), dispersion control elements and tuning elements that form the resonator cavity. A ten-fold mirror cavity, longer than that in a CW laser is necessary for the modelocked laser in order to allow it to run at the convenient repetition rate (near 80 MHz). The problem of astigmatism in the Tsunami output beam is eliminated by accurately aligning the angles of the cavity focus mirrors and the rod length at Brewster's angle. An acousto-optic modulator (AOM) is used for active mode locking in Tsunami, which is driven by a rf signal. The main disadvantage of active mode locking is the mismatch between cavity length and the external driving frequency. Therefore, the mode locking becomes unstable quiet often. To overcome this, the AOM is driven by a rf signal, which is again driven by a feedback from the laser cavity. If the laser cavity length is slightly changed, the drive signal to the modulator is changed accordingly. This is known as regenerative mode locking, which allows the laser to operate for extended periods without shutdowns.

However, the generation of a shorter pulse comes with a greater frequency distribution within a pulse, because of the Heisenberg uncertainty principle (time-bandwidth product of a Gaussian pulse is 0.441). As, the refractive index (η) of any material is a function of frequency (f), therefore, each f in a pulse experiences a slightly different η and hence a slightly different velocity (v). The variation is called as the group velocity dispersion (GVD). In Tsunami, the intracavity GVD, the working frequency and corresponding bandwidth of the output laser can be controllably tuned using a four prism and slit arrangement. During the experiment, we keep the wavelength (λ) of the output beam constant at ~ 800 nm because our Si-based photo detectors are most sensitive near this wavelength.

Second Harmonic Generator

The second harmonic generator (SHG, Model 3980) is used for doubling the frequency of the fundamental beam from the Ti-sapphire laser [16]. Inside the SHG cavity, a nonlinear crystal of barium beta borate (β-BaB_2O_4 or BBO) is used for the frequency doubling. This crystal is also capable of generating third, and higher harmonics of laser. Hence, the near-IR input light

comes out as near-UV light. The conversion efficiency of BBO is higher as compared to LBO crystal. As the efficiency is inversely proportional to the cross-sectional area of the beam, the beam waist is reduced before incidence on the crystal by a telescopic arrangement constructed using a couple of plano-convex lenses. To minimize the pulse width broadening due to GVD of the fundamental pulse, it is necessary to use a thin SHG crystal to obtain short output pulses without employing another compensating crystal. This crystal is hygroscopic, and thus, kept inside a sealed cylinder with AR-coated windows and filled with an index-matching fluid. The orientation of the crystal can be tuned externally. Traversing through the crystal, the diverging residual fundamental beam and its frequency doubled counterpart travel collinearly. A prism separates the second harmonic from the residual fundamental beam. The fundamental beam, however, cannot pass through because of the high reflective coating on the prism at infrared wavelength. The fundamental beam is vertically polarized whereas the second harmonic is horizontally polarized. The second harmonic is then guided to the output end by a pair of Littrow prisms which make the beam roughly parallel to the fundamental beam and compensate the beam ellipticity. These prisms also have antireflection (AR) coating at second harmonic wavelength to minimize any reflection losses from the prism surfaces. Finally, the residual fundamental beam and its second harmonic exit through two different output windows.

Description of the Two-Color Pump-Probe Set-Up in Collinear Geometry

The fundamental beam (λ = 800 nm) from the Ti-sapphire pulsed laser source is divided into two parts by a 70:30 beam splitter. The intense part passes through the second harmonic generator (SHG) to produce the pump beam (λ = 400 nm), which is guided towards the sample by a set of steering mirrors. The fundamental beam is attenuated as per requirement and is guided to the retro-reflector (RR) fixed on an automated variable delay stage. By moving the RR back and forth it is possible to introduce the desired optical path difference between pump and probe beams, which actually corresponds to the time delay in this experiment. After the optical alignment of the probe beam before the RR, a couple of mirrors are used to guide the beam towards the microscope objective (40X MO) having a numerical aperture (N.A.) of 0.65. In this path of the probe beam, the collimation is retrieved, and beam diameter is slightly expanded with a telescopic arrangement using two lenses (focal lengths of 75 mm and 200 mm respectively). A Glan-Thompson (GT) polarizer confirms the polarization of the probe beam and finally another mirror steers the beam towards the beam combiner. The pump beam is

chopped at a frequency of about 2 kHz by a mechanical chopper. Both the pump and probe beams are spatially overlapped using a beam combiner and are collinearly focused onto the sample using the same MO. The sample is mounted on a computer controlled piezoelectric scanning x-y-z stage. Using the MO and the z-travel of the piezoelectric stage, the probe beam is tightly focused to a diffraction limited spot size of ~ 800 nm at the sample. The pump beam is slightly defocused with a spot size of ~1 μm due to the chromatic aberration.

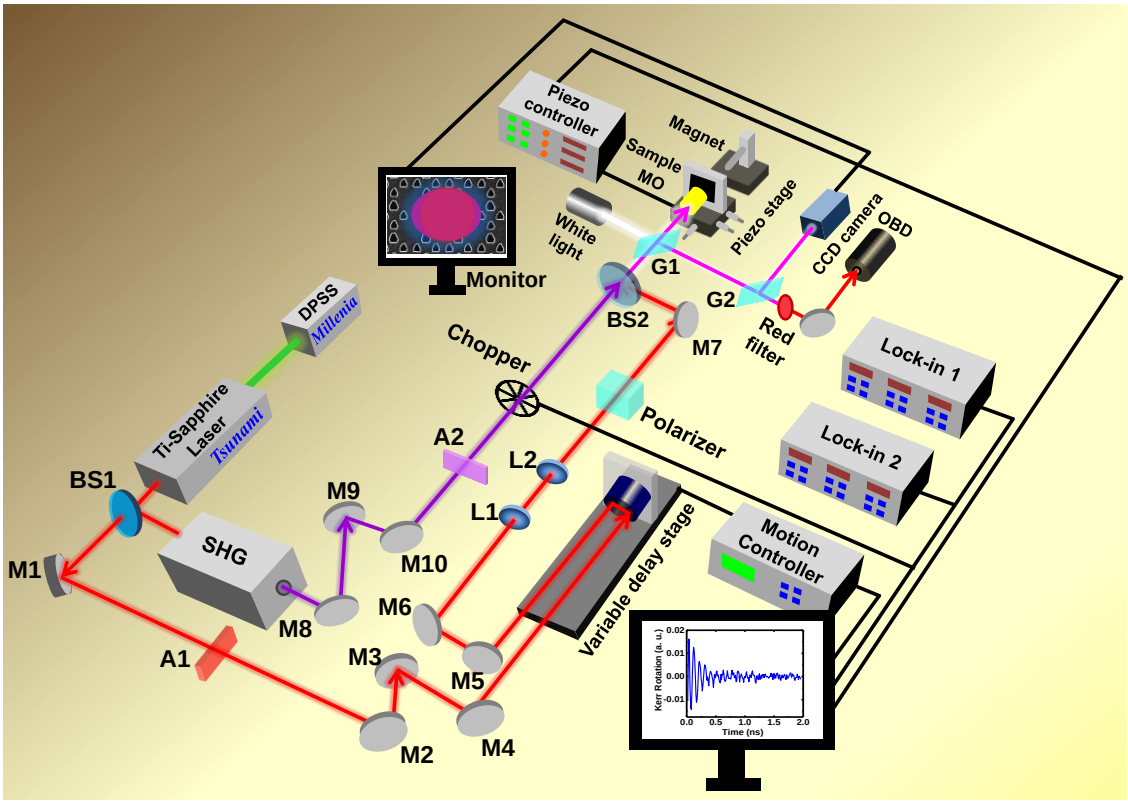

Fig. 3.9: Schematic diagram of custom-build TR-MOKE microscope set-up with collinear pump and probe geometry. M-mirror, BS-beam splitter, L-lens, OBD-optical bridge detector, F-filter, A-attenuator, G-glass slide.

A viewing arrangement is made using a white light focussed on the sample by the same MO. A CCD camera is used to visualize the sample and the position of pump-probe on the sample. After incidence, the beams are reflected back through the same MO. A filter then blocks the pump beam and allows the probe beam to be incident on the optical bridge detector (OBD), the operation of which is described earlier in the static-MOKE section. The pump beam perturbs the equilibrium magnetization of the sample, thereby inducing the dynamics. This affects the Kerr rotation of the reflected probe beam, which is dependent on the time delay between pump and probe pulses. By changing the RR position on the delay stage by small steps, the time

evolution of the magnetization dynamics (along with the reflectivity signal) is measured by the OBD in a phase-sensitive manner. The difference signal (A – B) from the OBD gives the Kerr rotation, whereas, the sum (A + B) gives the total reflectivity signal showing the dynamics of the electronic state of the sample as well as the acoustic modes. The schematic diagram of the set-up is shown in Fig. 3.9 and the photograph of the set-up is shown in Fig. 3.10.

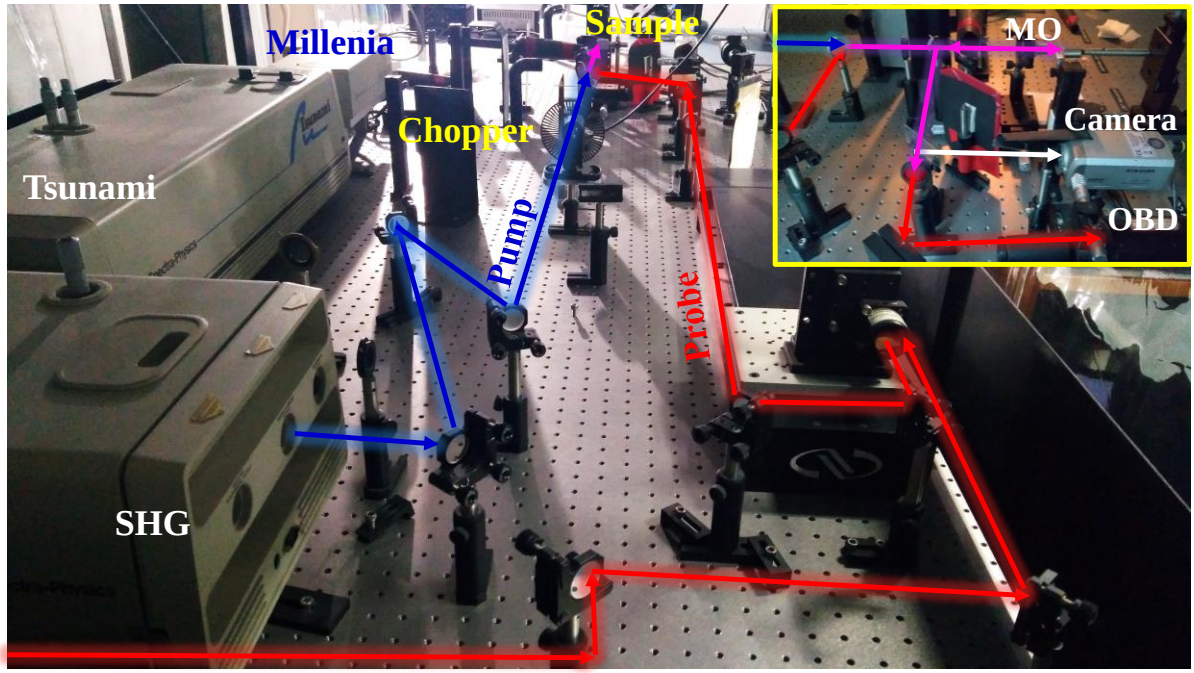

Fig. 3.10: A photograph of the TR-MOKE microscopy set-up in the laboratory of Prof. Anjan Barman at the S. N. Bose National Centre for Basic Sciences, Kolkata, India.

3.2.7.2. TR-MOKE Magnetometry in Non-Collinear Geometry

In this setup, an amplified femtosecond laser system generates the fundamental beam with wavelength of 800 nm and pulse width of about 40 fs by regenerative amplification method. One part of this fundamental laser beam is used as the probe beam, and another part is frequency doubled using a second harmonic generator (SHG) and is used as the pump beam to excite the magnetization dynamics of the sample. Both the pump and probe beams are incident non-collinearly on the sample surface using wavelength specific lens and mirrors. The pump beam is incident at an oblique incidence while the probe beam is incident at a normal incidence on the sample plane. The back-reflected probe beam is used to detect the time-resolved Kerr rotation in the polar geometry in addition to the simultaneous detection of time-resolved reflectivity signal.

The procedure of generation of amplified femtosecond laser pulse is quite complicated. The entire amplifier system (Libra, Coherent) consists of the following units: ultrafast oscillator (Vitesse), diode-pumped solid state pump laser (DPSS, Evolution), regenerative cavity, stretcher and compressor grating arrangements, synchronization and delay generator etc. In the following subsections we will discuss those units briefly.

Vitesse

The Vitesse laser is a compact Verdi (DPSS)-pumped ultrafast laser that produces modelocked, sub-100 femtosecond pulses at an 80 MHz repetition rate with an output power greater than 200 mW average power at 800 nm [17]. The Vitesse laser head includes (1) the laser diode system, (2) Verdi and, (3) Verdi Pumped Ultra-Fast (VPUF) laser head and some steering mirrors allowing exact positioning of the exit beam.

(1) Laser diode system

Light generated by laser diode system is transported by fibre array package (FAP) and is used to pump the gain medium of Verdi. The main component of diode laser system is FAP I and FAP II, each of which contains a laser diode bar capable of efficiently converting the electrical energy to optical energy. The wavelength of the emitted light is temperature dependent. Proper heat sink and cooling fans are there to maintain the optimum temperature.

(2) Verdi

The Verdi laser head includes neodymium-doped Yttrium Vanadate (Nd:YVO_4) as the gain medium, LBO (Lithium Triborate, LiB_3O_5) as the frequency doubling crystal, an etalon as the single-frequency optic, an optical diode, astigmatic compensator, two pump mirrors, and two end mirrors. It uses unidirectional single-frequency ring cavity with the facility of intra-cavity second harmonic generation (SHG) to produce multi-watt green (532 nm) output. Intra-cavity etalon enables the single frequency selectivity. Verdi absorbs energy from 808 nm input and produces strong single line emission of 1064 nm, which is later frequency doubled. It is important to maintain the temperature of Nd:YVO_4 to minimize the astigmatism. The LBO crystal can act as an output coupler and the tower temperature for this crystal is maintained at 150°C in order to have 90° phase matching between the fundamental beam (1064 nm) and its second harmonic (532 nm). After exiting the resonator, the 532-nm-beam is steered by a mirror towards the VPUF. A Piezoelectric transducer driven lever controls the tilt for maintaining optimum pump beam alignment into VPUF, and hence, this system is known as power track mirror arrangement.

(3) Verdi pumped ultra-fast (VPUF) laser

The VPUF is an ultrafast laser that uses Ti:Sapphire as the gain medium. Multiple negative dispersion mirrors (NDM) provide the total negative dispersion compensation that is required to produce sub-100 femtosecond pulses. Modelocking is achieved using Kerr-Lens Modelocking (KLM) technique with an automatic starter, which triggers the initiation of modelocking. The GVD may introduce reshaping of pulse or spectral chirp (either positive or negative). Also, due to KLM, frequency components of a pulse get phase-shifted differently. This is known as self-phase modulation (SPM) which causes temporal chirping leading towards pulse broadening. To compensate these GVD and chirping, multiple NDMs (which are basically Fabry-Perot etalons) are used to bring the net GVD down to zero.

Evolution

The Evolution-30 is a diode-pumped Q-switched laser capable of producing average energy more than 20 mJ for 527-nm-beam having 1 kHz repetition rate [18]. The heart of the Evolution-30 system is a neodymium-doped lithium yttrium fluoride (Nd:YLF) laser rod, acting as gain medium, pumped by three sets of four AlGaAs diode laser arrays. The laser light produced by the Nd:YLF laser rod is frequency-doubled to green light and emitted as energetic Q-switched pulses.

The components are:

(1) Power supply and laser diode

A laser diode is employed to pump the laser gain medium.

(2) Nd:YLF gain medium

Nd:YLF is used because of long upper-state lifetime (470 microsecond). It provides efficient energy storage for high-pulse energy operation at low repetition rates and its low thermal lensing and natural birefringence avoid loss of beam quality. As a birefringent material, Nd:YLF lases at two principle wavelengths: the 1047 nm (extraordinary) or the 1053 nm (ordinary) transition. The output beam of Evolution-30 is frequency doubled part of 1053 nm laser. The 1053 nm transition is used because of the higher absorption of the pump light by this transition, resulting in lower heat generation and lower thermal lensing.

(3) Acousto-optic Q-switching

An acousto-optic modulator (AOM) is a block of fused silica that acts as an optical phase grating when vibrated by an ultrasonic wave. If the fused silica block is subjected to ultrasonic vibration, the photo-elastic effect couples the strain field of ultrasonic wave to the refractive

index of the block. The resultant optical grating has a period and amplitude set by the acoustic (ultrasonic) wavelength. When a laser beam is incident upon this grating, a portion of the intensity is diffracted out of the beam. This energy loss is sufficient to destroy the "Q" of the cavity and prevent lasing. Generally a piezo electric transducer (PZT) is used in the AOM to convert electrical signal into ultrasonic sound. The laser can be returned to its high "Q" state after switching off the voltage applied of the PZT. If the ultrasonic vibration is stopped, then fused silica block emits "Q-switched" laser pulse. In the Evolution-30, two synchronized AOMs are used.

(4) Frequency doubling LBO crystal

A nonlinear LBO crystal is used as output coupler to frequency double the Q switched beam. The small birefringence of LBO allows non-critical phase matching and provides a larger acceptance angle for high efficiency frequency conversion. Non-critical phase matching relies on the temperature dependence of the dispersion of the crystal. A heater maintains the tower temperature usually at 327.5°F (164°C). This crystal can also efficiently work in the temperature range between 157°C and 171°C. The Nd:YLF-generated 1053 nm light gets frequency doubled by passing through this LBO crystal and finally a green output at 527 nm is emitted.

Working Principle of Libra

The physical phenomena associated with the regenerative amplification of femtosecond laser within Libra [19] are as follows:

(1) Chirped pulse amplification (CPA)

Chirped pulse amplification (CPA) is a technique for amplifying an ultrashort laser pulse up to the petawatt level with the laser pulse being stretched out temporally and spectrally prior to amplification. CPA for lasers was introduced by Donna Strickland and Gérard Mourou at the University of Rochester in the mid-1980s, work for which they received the Nobel Prize in Physics in 2018. Sometimes highly intense laser beam can lose its energy within a very short path length due to unwanted self-focusing. CPA can avoid this obstacle. Typically, a device called '*stretcher*' introduces positive chirp (GVD) and thus provides for a long chirped pulse suitable for amplification. The pulse is then amplified without any self-focusing. After amplification, a negative chirp provided by a '*compressor*' compensates for the positive chirp introduced by a stretcher and the pulse is restored to near its original duration. Ti:Sapphire is

an ideal material for CPA lasers. Libra employs CPA to stretch a weak pulse by 10,000 times with the help of a grating and amplifies it by a factor of 10^6 by using Ti:Sapphire crystal.

(2) Pulse stretching and compressing

A diffraction grating which reflects different wavelengths of a beam at different angles can introduce varying delay for varying wavelengths. This stretches or compresses the pulse temporally. Stretchers and compressors are characterized by their dispersion. With negative dispersion, light with higher frequencies (shorter wavelengths) takes less time to travel through the device than light with lower frequencies (longer wavelengths). With positive dispersion, it is the other way around. In a stretcher grating, the blue side of the spectrum has to travel far and are time delayed with respect to red side. The pulse thus has a positive GVD due to this stretching and is known as a positively chirped pulse. In a compressor grating the scenario is just opposite. The bluer frequency components travel faster in order to compensate the delay with respect to the redder part and thus the pulse achieves its desired temporal width again.

(3) Regenerative amplification (RGA)

The absorption transition of a Ti:Sapphire crystal occurs between 400-600 nm and the short wavelength side of the fluroscence spectrum merges with this transition wavelength. Thus, the actual range of lasing becomes limited in the IR range. The large gain bandwidth of this Ti:Sapphire crystal is exploited for pulse amplification. In the RGA cavity of Libra, Ti:Sapphire crystal rod is used to amplify a single nJ pulse (selected from mode-locked train of seed laser emitted from Vitesse) to mJ pulse. This amplification for single pass within the crystal is very small. RGA cavity offers a multipass travel to the seed laser so that a very high overall gain can be achieved.

The operation of several optical components involved during the amplification process is described below:

(1) Stretching operation – The entire path traversed by the beam starting from Vitesse output up to RGA cavity is as follows (See Fig. 3.10 for the beam path):

SM1 - SBS - FI - SM2 - SG - SM3 - SM4 - SM3 - SG - SM5 - SM6 - SG - SM3 - SM4 - SM3 - SG - SM7 - SM8 - SM9 - SM10 - RGA cavity

(2) RGA operation – RGA cavity employs a “Z-fold configuration” as follows:

RM1 - PC1 - RWP - RI1 - RM2 - RTS - RM3 - RP - RI2 - PC2 - RM4.

Here, RM2 and RM3 transmit the pump beam (green) but reflect the seed laser. RP reflects and transmits the beam depending upon the polarization. The repetition rate of the amplified laser is generally much lower than that of the seed laser. The output of Vitesse is an 'S' polarized pulse. RTS (the crystal) and RP transmit only 'P' polarized light. It allows the pump beam to pass. The quarter wave plate RWP is employed with an end-pumped mirror to double pass the beam making it 'S' to 'P' polarized or vice-versa.

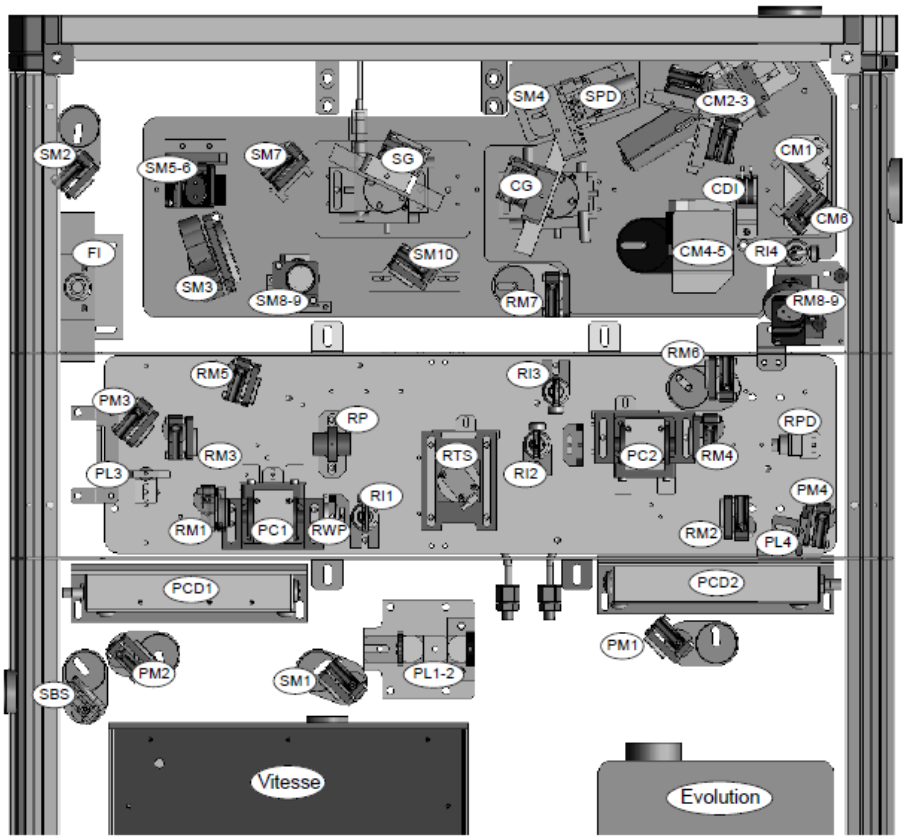

Fig. 3.10: Schematic diagram of top view of Libra having separate stages: CPA unit including seed laser, RGA with pump laser and compressor unit. [Reference: Operator's Manual, Libra-Ultrafast Amplifier Laser System, (Coherent, USA).]

Pockels cells - Pockels cells (PCs) rely on the linear electro-optic effect and produces birefringence in an optical medium in application of the electric field. The Pockels effect occurs in crystals that lack inversion symmetry, such as lithium niobate ($LiNbO_3$). PCs act as a *voltage-controlled waveplate* and are the basic components of electro-optic modulators (EOM). In the RGA cavity, there are two PCs (PC1 and PC2). When voltage is applied to PC, it acts as a quarter wave plate and then the double-pass mechanism is used to rotate the polarization of the beam by 90°.

(3) Compressing operation – The beam path in the compressor part is as follows:
CM1 – CDI – CG - CM2 - CM3 – CG - CM4 - CM5 – CG - CM3 - CM2 – CG – CDI – Output.

Optimization of the amplified pulse

Efficient amplification depends on precise coordination of timing of seed source, pump source of the amplifier and the PCs. Synchronization and delay generator (SDG Elite) [20] provides digital control of the timing signal and required voltages to operate the RGA cavity. It accepts input from the seed and pump laser and supplies a trigger signal for each PC at an adjustable delay. Additional delay signals can also be provided as per requirement. The delays can operate pump laser frequency or an integral divisor.

Seeding the RGA cavity with the beam having insufficient bandwidth may cause permanent optical damage. Hence, the bandwidth of the seed laser is extremely important parameter to monitor. Strong signal from a pair of photodiodes located at the stretcher compartment indicates that the seed laser has sufficient bandwidth. SDG monitors these parameters and shows error message whenever any fault occurs. Once an amplified pulse is generated efficiently, the pulse width of the beam can be optimized externally by fine tuning of the compressor delay stage using remote control. For drastic change in pulse width, angle of both the gratings have be tuned manually.

Second Harmonic Generator

The SHG is used with the amplified laser system (Model: Harmonic, HGS-T) to generate the pump beam of 400 nm wavelength for our pump-probe experiment. The working principle is similar to SHG (model: 3980) used in the oscillator laser system used in the TR-MOKE microscopy set up. This model can also generate the third harmonic with wavelength in deep UV regime, from the fundamental beam.

Description of the Two-Color Pump-Probe Set-Up in Non-Collinear Geometry

The S-polarized fundamental laser beam from the amplifier (Libra) laser is guided by a set of five mirrors before being split into two equal parts using a 50:50 beam splitter. A part of this fundamental laser beam is fed into the SHG and after frequency doubling (λ = 400 nm) we obtain the pump beam. The other part of the fundamental laser beam (λ = 800 nm) is attenuated

and used as the probe beam. This probe beam is steered by a number of mirrors to a RR placed on a motorized delay stage for the introduction of a variable time delay.

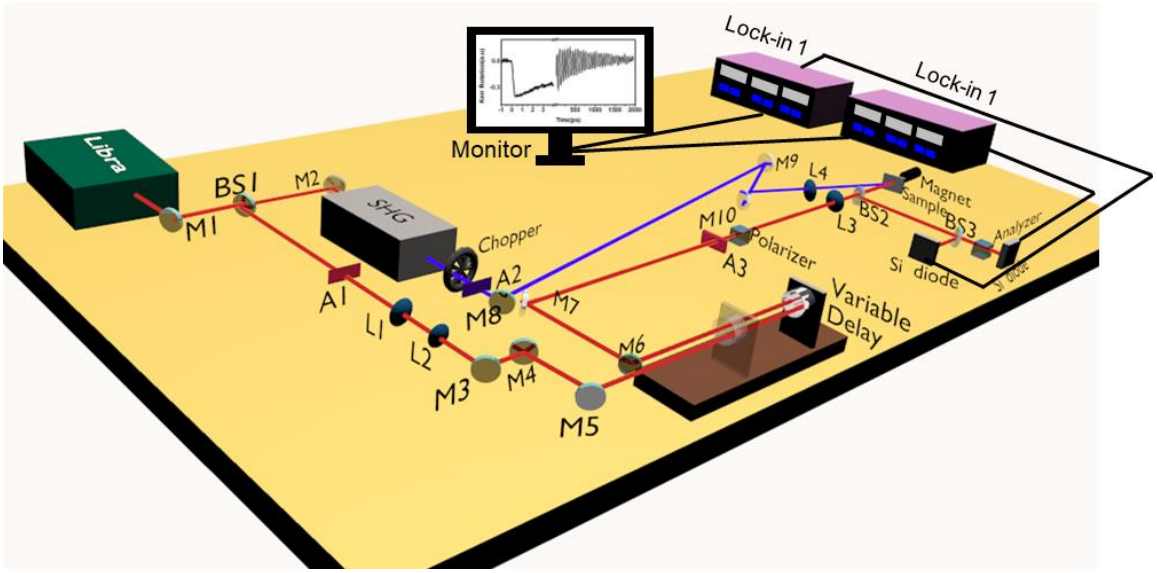

Fig. 3.11: Schematic diagram of the optical pump-probe set-up (non-collinear geometry) with amplified fs laser unit. M-mirror, BS-beam splitter, L-lens, A-attenuator.

The probe beam coming out from the RR is guided by a few mirrors and is focused on to the sample by using a plano-convex lens of focal length. A GT polarizer (GTH5M, Thorlabs) with extinction ratio of 100000:1, is placed in the path of the probe beam to ensure high degree of polarization of the incident probe beam. The pump beam is guided on to the sample by using a set of five steering mirrors which are adjusted to compensate the optical path length with respect to the probe beam. Variable attenuators are kept in the pump and probe paths for adjusting the power falling on to the sample. The pump and probe beams are made to incident non-collinearly on to the sample surface. The pump beam falls on the sample in an oblique incidence, whereas, the probe beam is incident normally. The pump beam is kept slightly defocused on the sample to avoid any damage of the sample by the high irradiation by the power, whereas, the probe beam is tightly focused on the sample and placed carefully at the centre of the pump beam. The pump and probe beams have spot sizes of ~ 200 μm and ~ 100 μm respectively. The pump beam is blocked after reflection from the sample. The reflected probe beam is split into two parts with a beam splitter. One part is fed directly into a Si photodetector which measures the total reflectivity. The other part is fed to another Si photodetector through a GT polarizer, which measures the Kerr rotation. The pump beam is the chopped by using an optical chopper (Thorlabs, MC2000B) and the detector signals for

measuring reflectivity and Kerr rotation are measured by two lock-in amplifiers (SR830, Stanford Research System) in a phase sensitive manner using reference beam from the optical chopper output. The bias magnetic field is applied by using permanent magnets as per requirement. The schematic diagram of the TR-MOKE setup in non-collinear geometry is shown in Fig. 3.11 and the photograph of the set up is shown in Fig. 3.12.

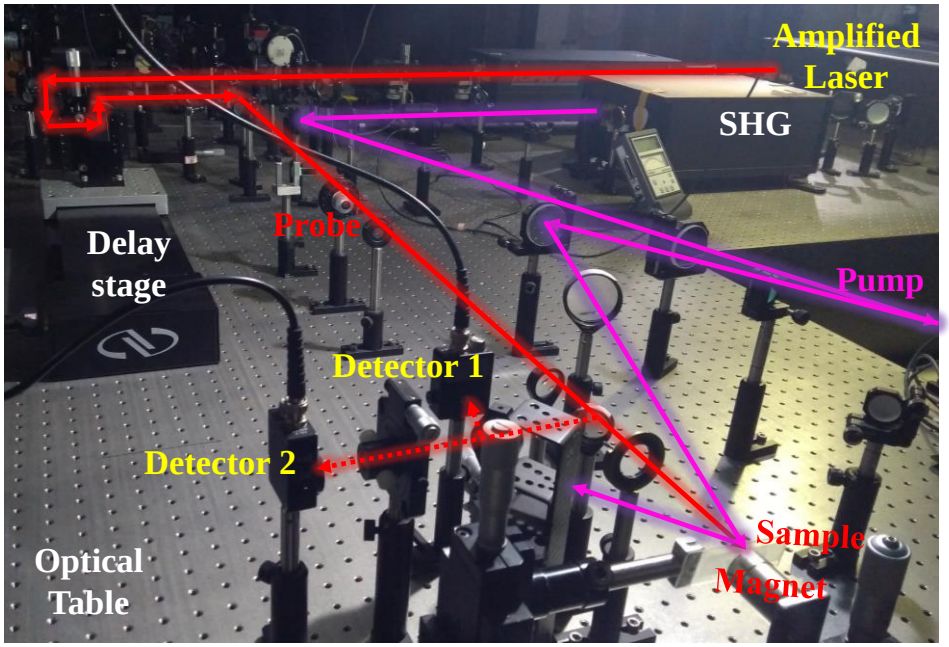

Fig. 3.12: Photograph of the optical pump-probe set-up (non-collinear geometry) based on an amplified fs laser system in the laboratory of Prof. Anjan Barman at the S. N. Bose National Centre for Basic Sciences, Kolkata, India.

Comparison of important features of the lasers optimized for the two TR-MOKE systems

Specification	Oscillator-based laser	Amplifier-based laser
Wavelength	~ 800 nm	~ 800 nm
FWHM of power spectra	~ 12 nm	~ 30 nm
Pulse Width	~ 80 fs	~ 40 fs
Repetition rate	~ 80 MHz	~ 1kHz
Pulse width	25 nJ	4 mJ
Average output power	~ 2 W	~ 4 W

Measurement of Time-Resolved Dynamics

A typical time-resolved Kerr rotation data obtained from a 20-nm-thick $Ni_{80}Fe_{20}$ film has been demonstrated in Figure 3.13 (a) where the different temporal regions are indicated. The region I ($t < 0$) is also known as negative delay region where the sample is probed before the arrival of pump pulse and the equilibrium magnetization under external bias field is obtained. Region II contains a sharp demagnetization within hundreds of fs followed by a fast relaxation (Region III) within few ps. In Region IV, a slower relaxation is observed together with a precession of magnetization around its new equilibrium position. Figure 3.13 (b) shows the precessional dynamics after removing the negative delay and ultrafast demagnetization and subtracting a bi-exponential background. The corresponding fast Fourier transform (FFT) spectrum obtained from the precessional oscillation data is presented in Figure 3.13 (c) which gives the precession frequency.

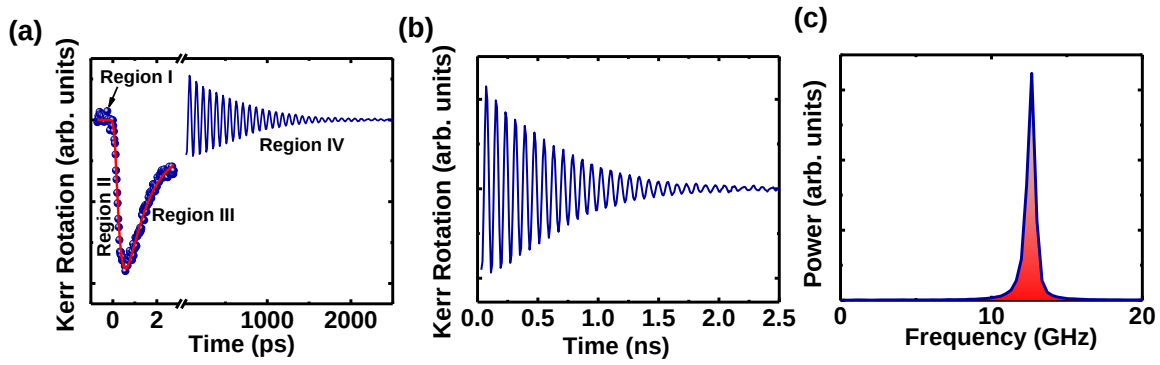

Fig. 3.13: (a) Typical time-resolved Kerr rotation data taken from a $Ni_{80}Fe_{20}$ sample of 20 nm thickness with an in-plane bias field (H) of 1.3 kOe. (b) Precessional oscillation part of the time-resolved data and (c) the corresponding precessional frequency after performing fast Fourier transformation.

3.2.8. Brillouin Light Scattering Technique

The Brillouin light scattering (BLS) is a spectroscopic technique developed [21] to be a very powerful and versatile tool in magnetic research because of its wide flexibility in terms of measuring samples, frequency-, phase-, time-resolution, and localized spatial resolution. The other advantages include (i) the ability to measure the thermal excitations (in the absence of any external stimulation), (ii) investigation of SW response over a broad frequency range upto 500 GHz, with a resolution of 50 MHz. (iii) the potential to investigate dispersion of SWs with different absolute values and orientations of their wave vectors. Furthermore, one can extract rich information about the magnetic properties of magnetic layers, such as saturation magnetization, magnetic anisotropy and coupling parameter between different magnetic layers.

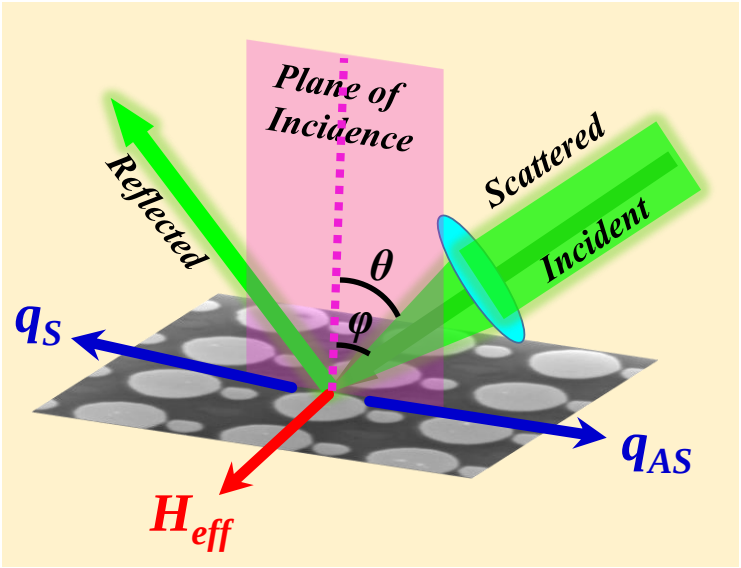

Fig. 3.14: The scattering geometry showing the incident, reflected and scattered beams, the direction of magnon wave vectors for Stokes and anti Stokes process in BLS. The measurement geometry shown is DE geometry.

Principles

In this technique a monochromatic laser beam is incident on the sample surface. The scattering geometry depicting the incident and scattered beam, the incidence angle and the direction of wave vectors is shown in Fig. 3.14. Maximum portion of the incident light is reflected or absorbed, and a small fraction is scattered from the thermally excited SWs, which can be divided into two main categories: the elastic and inelastic scattering. In the elastic scattering (like Rayleigh scattering), the photon's energy or frequency is unchanged. However, in the

inelastic scattering, a shift in the angular frequency occurs, which forms the basis of the spin wave detection in this technique. The scattered light is collected using the same lens as that used for incident beam, within a solid angle in the direction 180° from the incident light, which is known as the 180°-backscattering geometry. This backscattered light is then frequency analyzed using a multi-pass tandem Fabry-Perot (FP) interferometer to extract the information about the surface and bulk magnons.

The inelastic scattering mechanism can be defined as a photon-magnon collision from a quantum mechanical viewpoint, i.e. in terms of the creation (Stokes process) and annihilation (anti-Stokes process) of a magnon of angular frequency (ω) and wave vector which is shown in Fig. 3.15. The conservation of energy (frequency) and momentum (wave vector) between the magnon and the incident (*i*) and scattered (*s*) photons yields

$$\hbar\omega_s = \hbar\omega_i \pm \hbar\omega \tag{3.1}$$

$$\hbar k_s = \hbar k_i \pm \hbar q \tag{3.2}$$

where '+'('-') sign stands for the anti-Stokes (Stokes) shift and ω_i, k_i, ω_s, k_s are the angular frequencies and wave vectors of the incident and scattered light, respectively. The above equations are only valid for the wave vector (q) component parallel to the film plane, as during the scattering of light from thin films the perpendicular component of the wave is not conserved due to the breaking of translational symmetry.

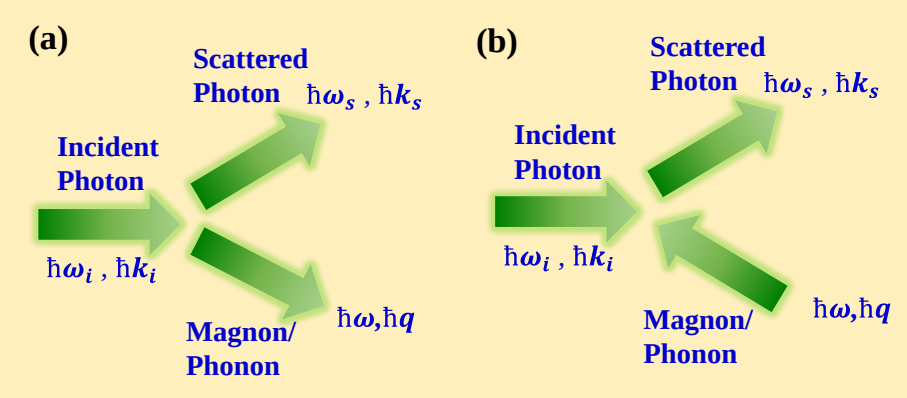

Fig. 3.15: Schematic of the (a) Stokes and (b) anti Stokes Scattering processes occurring in BLS.

From the conservation of momemtum, we can determine the wave vector of SWs during scattering. A very small amount of energy of incident light is exchanged with the system during the scattering. The visible photon energy is about few eV, whereas the magnon energy in BLS is about ~ 10^{-4} eV. Consequently, the magnitude of k_s should be very close to k_i. The scattering profile of a photon by a bulk magnon is shown in Fig. 3.16 (a). Here, k_s must lie on the dashed

circle line, whose radius is equal to the magnitude of k_i and the cone represents the collection angle of the scattered beam, whose central axis aligns with k_i. Assuming that k_i and k_s are collinear (k_s = -k_i), i.e. in the backscattered geometry, the wave vector magnitude of the emitted or absorbed bulk magnon $|q|$ is always equal to $2|k_i|$.

The scattering of a photon by a surface magnon is shown in Fig. 3.16 (b). Here, the conserved component of the incident beam is equal to $|k_i|sin\theta$, where θ is the angle between k_i and sample surface normal. Hence, the wave vector of the magnon is,

$$|\bar{q}| = \left|\bar{k}_i \sin\theta - \bar{k}_s sin\theta\right| = 2|k_i|sin\theta \quad (3.3)$$

Therefore, by varying the incident angle, no new information can be obtained about the bulk magnons, whereas the surface magnon reveals the important frequency-wave vector dispersion relation. Eq. 3.3 is known as the Bragg's condition and provides an approximation for most of the light scattering experiments.

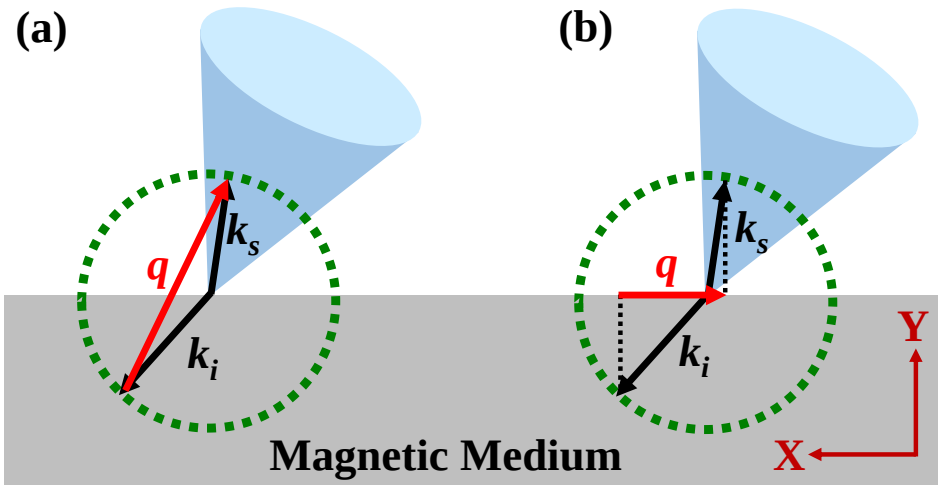

Fig. 3.16: Scattering of laser beam by (a) bulk magnon and (b) surface magnon. The direction of q corresponds to the anti Stokes process.

Instrumentation

Laser

A 300 mW solid state CW laser together with a controller unit (Excelsior, Spectra Physics) is used in the experiment. A diode laser is used to pump the Nd^{3+} ions doped in the crystal of yttrium vanadate (Nd: YVO4), which emits photons at 1064 nm. This infrared output is converted to visible light by sending it through a non-linear crystal of lithium triborate (LBO)

for frequency doubling (wavelength 532 nm). The emitted laser beam has a diameter of about 670 μm with a beam divergence of about 1.03 mrad.

The Pinhole and Light Modulator

The light modulator is a double shutter system situated right behind the entrance pinhole of the TFP. The shutters SH1 and SH2 are alternately opened in the TFPI operation, thereby controlling the light intensity reaching the photon detector. Since the detector is a single photon counter, strong elastic light can cause damage to the detector. Thus, to protect it, this device operates in synchronization with the scanning stage.

Tandem Fabry-Pérot Interferometer

The frequency analysis of SWs in BLS spectroscopy is challenging. The frequencies of magnons can be up to 300 GHz (~ 10 cm^{-1}), which is ~ 10^{-5} times smaller than that of a typical excitation frequency of laser light. Additionally, the inelastic scattering crosssection is very small as compared to the elastic scattering. Hence, an efficient detection of the fractional amount of incident laser power with high signal to noise ratio is required. These conditions are satisfied by the implementation of a triple-pass Tandem Fabry-Pérot Interferometer (TPFI), which consists of two single Fabry-Pérot Interferometers (FPI) connected in series and the light passes each FPI three times.

The Fabry-Pérot Interferometer

A typical FPI [22] consists of two plain, partially reflecting mirrors mounted parallel to each other at a distance (L). The light entering the FPI, undergoes multiple back and forth reflections and transmissions. The transmitted beams constructively interfere with each other in the condition:

$$L = \frac{n\lambda_0}{2} \tag{3.4}$$

where n = 1, 2, 3…. is an integer (transmission order) and λ is the wavelength of the light. Therefore, the consecutive interference orders are separated by a frequency gap Δf (free spectral range (FSR)) as,

$$\Delta f = \frac{c}{2L} = \frac{150}{L}\, GHz.\, mm^{-1} \tag{3.5}$$

where c is the velocity of light. The finesse of the interferometer can be written as,

$$F = \frac{\Delta f_{FSR}}{\Delta f_{FWHM}} \tag{3.6}$$

where, Δf_{FWHM} is the full with at half maximum of the transmission curve. The transmitted intensity of the FPI is written as,

$$I_t = \frac{I_0}{1+\left({}^{4F^2}/_{\pi^2}\right)sin^2\left({}^{2\pi L}/_{\lambda_0}\right)} \quad (3.7)$$

where I_0 is the intensity of the incident light.

The finesse, which is regarded as the quality of the instrument is written as, $F = \frac{\pi\sqrt{R}}{(1-R)}$, whereas, the contrast is written as, $C = 1 + \frac{4R}{(1-R)^2}$

The contrast for an *n*-pass interferometer is the n^{th} power of that of a single-pass one.

Tandem Configuration

The periodicity of transmitted intensity as a function of the mirror spacing can become a major problem of FPI. For a fixed mirror spacing *L*, if two wavelengths (λ_1 and λ_2) are present in the light beam, such that,

$$2L = m_1\lambda_1,\ 2L = m_2\lambda_2 \quad (3.8)$$

The transmission condition is satisfied for both the wavelengths at different orders. As the reference beam determines the order of transmission spectrum, the order of the second wavelength that does not match with the reference beam remains unaccessed. Moreover, it is difficult to identify whether a peak signal belongs to the Stokes side of a specific transmission order or it is the anti-Stokes signal of the previous order. To address these shortcomings, the interferometer is used in a tandem configuration (developed by Dr. J. R. Sandercock) [23],

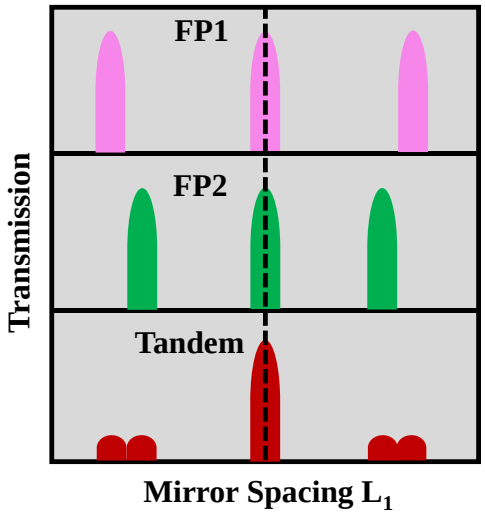

Fig. 3.17: Transmission Spectra of FP1 and FP2 and in tandem operation.

where the light passes consecutively through two interferometers, mounted under an angle α, as shown in Fig. 3.17. The right mirror of each FPI sits on the translation stages, and the other on a separate angular orientation device. The scanning stage can move the right mirror of each pair along the optical axis of FP1. A displacement (d) of the translation stage leads to a change of the mirror distance in FP1 by $\Delta L_1 = d$, while the change for FP2 is: $\Delta L_2 = \Delta L_2 \cos(\alpha)$, which also satisfies the synchronization condition as,

$$\frac{\delta L_1}{\delta L_2} = \frac{L_1}{L_2} \tag{3.9}$$

This can be used to suppress the intermixing of different orders. For that, each FPI is adjusted to transmit separately before scanning the linear stage. Although their transmission orders are different, they together provide a central transmission order which can be adjusted by varying the mirror spacing of FP2. The other orders are suppressed because the free spectral range (FSR) of the two FPIs becomes different. When the stage is moved, the change in the mirror spacing is given by the following:

$$l_1 = L_{10} + d \tag{3.10}$$

$$l_1 = (L_{10} + d)\cos\alpha \tag{3.11}$$

where, l_1 and l_2 are the changes in mirror spacing for FP1 and FP2, respectively while, L_{10} is the initial mirror spacings of FP1 (at $d = 0$). After the six passes through the FPIs, the light is directed to a photomultiplier tube which counts the number of transmitted photons as a function of the mirror spacing. To achieve this, the scanning stage constantly sweeps the distance corresponding to the required frequency window and the data is recorded for long time to attain sufficient statistics. In this way, the obtained BLS intensity is proportional to the spin wave intensity at a given frequency.

Description of the Experimental BLS Set-Up

The inelastically scattered light carries information about the frequency and wave vector of the involved spin wave mode and the intensity of the scattered light is proportional to the intensity of studied spin wave. the BLS technique offers two different measurement geometries: (i) Forward scattering geometry, where the scattered beam is collected after transmission of the probing beam through a transparent sample, and (ii) Backscattered geometry, where the beams that are backscattered from the surface of opaque sample are investigated. Fig. 3.18 represents the schematics of the optical beam path used for conventional BLS experimental arrangement.

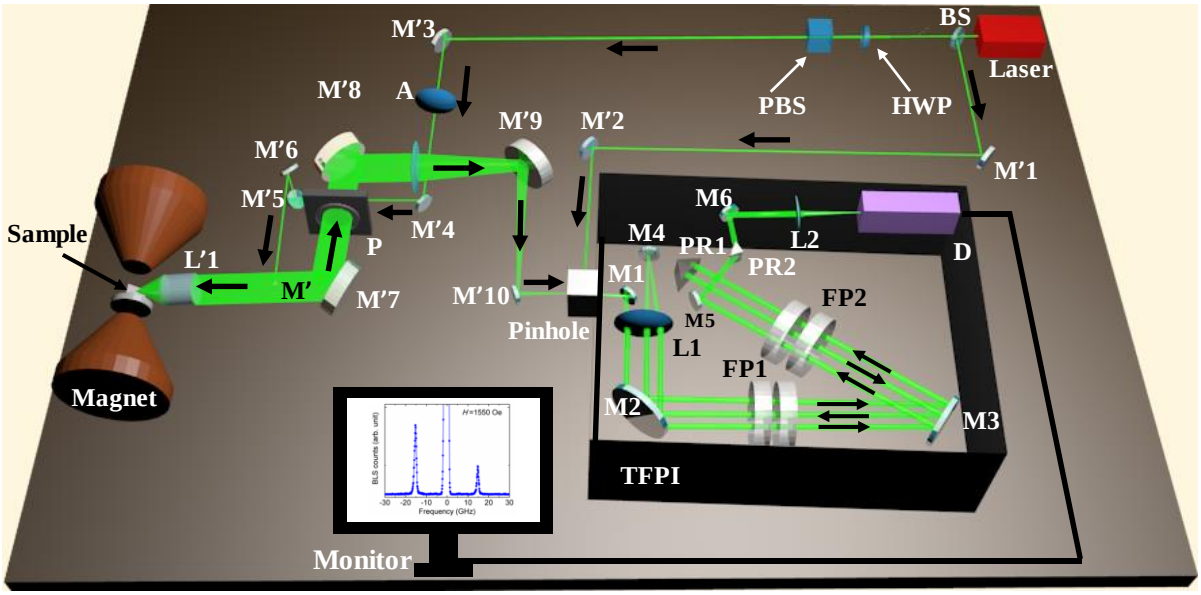

Fig. 3.18: The set-up and optical pathway for conventional BLS set-up. BS-Beam Splitter, PBS-Polarizing Beam Splitter, HWP-Half Wave Plate, M-Mirror, L-Lens, TFPI-Tandem Fabry Perot Interferometer.

A laser light emitted by a diode-pumped, frequency-doubled, single mode solid-state laser of wavelength (λ) 532 nm is used (the power of the emitted light is 300 mW) for the measurement of thermally excited magnons. The light is then split into two beams using a 10:90 beam splitter (BS). The smaller part of the deflected beam is directed straight to the TFPI using two mirrors, which serves as a reference beam. The purpose of this reference beam is:

(1) It is used to stabilize the mirror spacing of the Fabry-Perot etalons.

(2) It generates the central elastic peak in BLS spectrum, which helps to determine the frequency shift of the scattered beam with respect to the incident beam.

(3) It is used to estimate the transmission order of the FP etalon, which is again used to deduce the frequencies present in the scattered light.

The other part of the beam is sent through a half wave plate (HWP) and a polarized beam splitter (PBS), in order to eliminate the small in-plane polarized component from the partially polarized beam of the laser. The beam, perpendicularly polarized to the optical table, is then guided by a set of mirrors towards the sample which is lying between the electromagnets. Finally M′ acts as a tiny prism mirror to minimize the blocking of the backscattered beam by itself and the beam is focused onto the sample using an achromatic doublet lens. The sample is mounted on a rotation stage, where the change in the rotation angle changes the angle of incidence, thereby addressing different transferred SW wave vector. A magnetic field is applied

perpendicular to the transferred wave vector direction, i.e. in the Damon-Eshbach (DE) geometry. The scattered beam is collected by the same lens and continues its way towards the entrance pinhole of a JRS Scientific Instrument (3+3)-pass TFPI for frequency analysis. A crossed polarizer P is inserted in the path of the scattered light to suppress the elastically scattered beam as well as the beam containing the signal from phonons. Inside the TFPI, the beam hits mirror M1 and then reaches FP1 via lens L1 and mirror M2. After passing through FP1, the beam undergoes its first pass (beam 1) until it is reflected from M3 (beam 2) and passes through FP2. Then the beam is reflected from PR1 and traces back its path via FP2 (beam 3) and FP1 (beam 4) and reaches M4. The beam is once again reflected at M4, and thus it gets redirected, passes through FP1 and FP2 for the third time (beam 5 and beam 6 respectively) to finally arrive at the single-photon counter (D). The resulting light has very low intensity which is detected by the photon detector and the signals are sent to a computer for storage and analysis. A photograph of the BLS set-up is shown in Fig. 3.19.

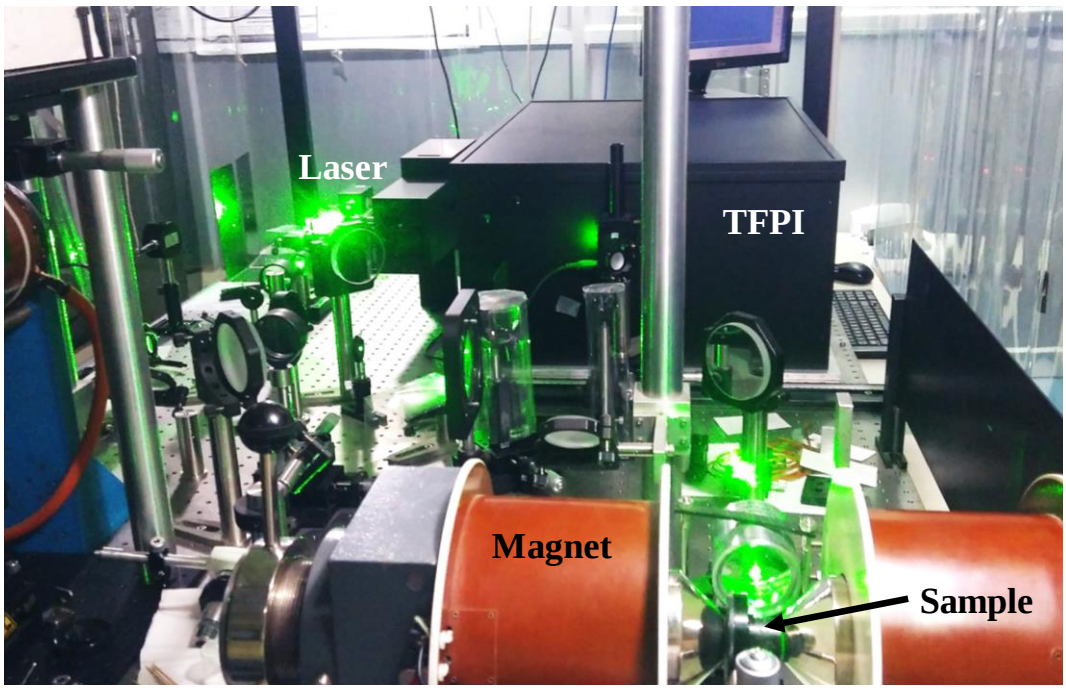

Fig. 3.19: Photograph of the BLS set-up in the laboratory of Prof. Anjan Barman at the S. N. Bose National Centre for Basic Sciences, Kolkata, India.

References

[1] A. Barman and A. Haldar, Solid State Phys, vol 65. (Elsevier Inc., Burlington, 2014).
[2] B. W. Zingsem, T. Feggeler, A. Terwey, S. Ghaisari, D. Spoddig, D. Faivre, R. Meckenstock, M. Farle, and M. Winklhofer, Nat. Commun. **10**, 4345 (2019).
[3] T. Preller, D. Menzel, S. Knickmeier, J. Cedric Porsiel, B. Temel and G. Garnweitner, Nanomaterials, **8**, 297 (2018).
[4] S. Ge, X. Shi, K. Sun, C. Li, C. Uher, J. R. Baker, M. M. Banaszak Holl, and B. G. Orr, J. Phys. Chem. C **113**, 13593 (2009).
[5] 33J. Aizenberg, J. A. Rogers, K. E. Paul, and G. M. Whitesides, Appl. Phys. Lett. **71**, 3773 (1997).
[6] P. B. Fischer and S. Y. Chou, Appl. Phys. Lett. **62**, 2989 (1993).
[7] F. Rousseaux, D. Decanini, F. Carcenac, E. Cambril, M. F. Ravet, C. Chappert, N. Bardou, B. Bartenlian, and P. Veillet, J. Vac. Sci. Technol. B **13**, 2787 (1995).
[8] Sputtering by Particle Bombardment, Springer, (2007).
[9] Electron Beam Evaporation, Vacuum Deposition onto Webs, Films and Foils (Second Edition), Elsevier (2011).
[10] G. R. Sune, Electron beam lithography for nanofabrication, PhD thesis, Universitat Autònoma de Barcelona (2008).
[11] D. Mcmullan, Scanning Electron Microscopy 1928–1965, Scanning. **17**, 175 (1995).
[12] G. Binnig, C. F. Quate, and C. Gerber, Phys. Rev. Lett. **56**, 930 (1986).
[13] S. Foner, Rev. Sci. Instrum. **30**, 548 (1959).
[14] A. Barman and J. Sinha, Spin Dynamics and Damping in Ferromagnetic Thin Films and Nanostructures (Springer Publishing AG, Switzerland, 2017).
[15] User's Manual, Tsunami: Mode-locked Ti:Sapphire Laser, (Spectra-Physics, California, USA, 2002).
[16] User's Manual, Model 3980: Frequency Doubler and Pulse Selector, (Spectra-Physics, California, USA, 2002).
[17] Operator's Manual, Vitesse-Diode Pumped Modelocked Ti:Sapphire Laser, (Coherent, USA).
[18] Operator's Manual, Evolution-15/30 High Energy High Average Power Q Switched Laser System, (Coherent, USA).
[19] Operator's Manual, Libra-Ultrafast Amplifier Laser System, (Coherent, USA).
[20] Operator's Manual, SDG Elite-Synchronization and Delay Generator, (Coherent, USA).
[21] L. Brillouin, Ann. Phys. **17**, 88 (1922).
[22] J. R. Sandercock, "Operator Manual for the Tandem Fabry-Perot Interferometer," (1999).
[23] J. R. Sandercook, "Operator manual of Tandem Fabry-Perot interferometer TFP-1," (2010).

Chapter 4

4. Numerical Techniques

The magnetization dynamics of ferromagnetic thin films with uniform magnetization throughout the sample can be determined under the macrospin formalism, in which the non-linear ordinary differential LLG equation is solved by linearizing it under small angle approximation to calculate the SW frequency and other parameters. However, in confined magnetic structures (e.g. multilayered and/or patterned structures), the demagnetizing field arising from the unsaturated magnetic dipoles at the finite boundaries play a crucial role in controlling the static magnetic texture and the magnetization dynamics, and hence, the calculations are not straight forward. The situation becomes more complex with the samples having non-ellipsoidal geometries when analytical solution becomes more complicated. Moreover, experiments face severe challenges due to various limitations in the fabrication techniques and measurement conditions. As a consequence, theory faces stern challenges to reproduce (or predict) the real situation due to the lack of appropriate approximations and boundary conditions for nanoscale magnetic systems. Thus various micromagnetic modelling and computer-based numerical techniques have been developed to determine the local demagnetizing field profile and to calculate the consequent SW properties of non-uniformly magnetized samples. One of the most popular methods is micromagnetic simulations, where the magnetization is considered to be a continuous function of position, the sample is divided into large number of cells and the dynamic motion of each cell is considered as a macrospin interacting with the neighboring cells by short-range exchange and long-range dipolar interactions due to the effect of magnetocrystalline anisotropy and external magnetic fields. There also exist other theoretical models, which, under certain assumptions, calculate the magnetic properties. In this thesis, we have employed both micromagnetic simulations (using object oriented micromagnetic framework (OOMMF) and LLG micromagnetic simulator) and a combination of analytical and numerical technique (using plane wave method) to analyze the characteristics of the dynamic magnetization of the studied systems.

4.1. Micromagnetic Simulations

This is an efficient tool for studying a wide variety of magnetic phenomena including magnetization reversal and dynamics. There are two popular approaches to compute such approximations and to solve LLG equation in micromagnetics: finite difference method (FDM) and finite element method (FEM). In FDM, the system space is discretized into a number (N) of regular cubic cells known as 'finite differences'. Subsequently, each cell is assigned with a magnetization vector and their relative interactions are taken into account by the minimization of total energy. A few examples of FDM simulators are OOMMF [1], LLG Micromagnetic Simulator [2], MicroMagus [3], Mumax^3 [4] etc. However, FDM simulations are not applicable for complicated geometry like curved boundary or irregular microstructures. These problems can be addressed by using FEM, in which the system is discretized into finite elements in two dimensions (like triangles, squares, or rectangles) or three dimension (like tetrahedrons, cubes, or hexahedra) depending on the shape and dimension of the system. Despite reproducing complex geometries easily, FEM is much slower as compared to the FDM due to the requirement of much more computational resource (or memory). Examples of FEM simulators include NMAG [5] MAGPAR [6], MicroMagnum [7], TetraMag [8] etc. In the following sections an overview of the simulators used in this thesis mentioning their features and functionalities are provided.

4.1.1. Object Oriented Micromagnetic Framework

OOMMF is a public domain micromagnetics program developed at the National Institute of Standards and Technology (NIST) by M. J. Donahue and D. G. Porter [1]. The code is written in C++ and Tcl/Tk language. In OOMMF, the sample or space is discretized into small cuboidal cells (known as 'finite differences') of equal size. It utilizes an ODE solver to relax 3D spins on a 2D mesh of square cells while using fast Fourier transform (FFT) to compute the self-magnetostatic field. All the required parameters like bulk saturation magnetization, Zeeman field, magnetocrystalline anisotropy, exchange stiffness constant, damping, gyromagnetic ratio, sample structure and dimensions, and the magnetic field geometry are provided at the beginning of the simulation through an input file called 'MIF' file. An initial state of magnetization is also provided at the starting point of simulation. As the simulation starts, the evolvers (controlled by drivers) update the magnetization configuration from one step to the next. There are mainly two types of evolvers, time evolvers (track the LLG dynamics) and minimization evolvers (locate the local minima in the energy surface through direct minimization techniques). The

evolvers are mainly controlled by their compatible drivers (i.e. time and minimization drivers), which determine when a simulation stage (or run) is completed using specified stopping criterion in the input MIF file. The convergence criterion in the simulation is created by setting the stopping value of *dm/dt* or time, which is set in such a way that the maximum torque, $m \times H$ (where $m = M/M_S$) goes well below 10^{-6} A/m. At the stopping time, the maximum value of *dm/dt* across all spins drops below the set value. The finial magnetization state obtained as the 'ground state' is then specified as the initial magnetization in the dynamic simulation file. By providing an external perturbation in terms of additional magnetic field, the dynamic magnetization is simulated. In OOMMF, we can set a periodic boundary condition (PBC) in different dimensions to simulate realistic systems with finite and smaller sample geometry. The demagnetizing field can be computed very efficiently by this method. However, being FDM software, it has less flexibility than the FEM software in replicating exact geometries for the objects with curved surface and all the calculations in OOMMF are performed at T = 0 K.

4.1.2. DotMag

The spatial mapping of the power and phase profiles of the resonant modes inside a nanostructure provides an explicit idea about comparison between relative spin precession amplitudes and phases of different SW modes and helps to visualize their spatial variation throughout the system. Our research group have developed a post-processing code, DotMag, to investigate these features [9], which works with output files of various micromagnetic solvers, including OOMMF and Mumax3. After simulating the magnetization dynamics using the above-mentioned simulator, one can obtain the output files in terms of time varying magnetization ($m(x, y, z, t)$). The FFT of such time-resolved spatially averaged magnetization curve gives the frequency spectrum, which shows several well resolved resonant modes. DotMag performs a discrete Fourier transform of the time dependent magnetization by fixing one of the spatial co-ordinates with respect to time. Generally, the simulations performed without discretizing the z dimension, considering an average demagnetizing effect and all other possible effects in the entire cell. The fixed value of the z-coordinate can be chosen to any point from the top to bottom surface of the system. Finally, the program plots the (x, y) spatial distribution of the power and phase profiles of the SW modes according to the following relations:

Power: $$p^{z_m f_n}(x, y) = 20 \log_{10} FFT\left[\tilde{M}^{z_m}(f_n, x, y)\right] \quad (4.1)$$

Phase: $$\emptyset^{z_m f_n}(x, y) = \tan^{-1}\left(\frac{Im\,(\tilde{M}^{z_m}(f_n,x,y))}{Re\,(\tilde{M}^{z_m}(f_n,x,y))}\right) \quad (4.2)$$

where f_n is the frequency of a resonant mode. The power is presented in terms of dB and phase in radian. MATLAB is used to run and control this code. The frequency resolution depends upon the total simulation time and the spatial resolution of the power and phase maps depends upon the discretization of sample (or number of cells) during micromagnetic simulation.

4.1.3. LLG Micromagnetic Simulator

M. R. Scheinfein is the designer and licensor of this commercial simulator [2]. In this simulator, the LLG equation is solved by FDM like in OOMMF. However, the LLG simulator has some extra features, which are not available in OOMMF. The temperature effect can be introduced here by providing an equivalent random magnetic field. Additionally, there is provision to trigger the magnetization dynamics by spin polarized current, which is an essential requirement for spin valve like structures. Another important feature is that the magnetostatic interaction among magnetic nanoelements can be visualized better by colored contour plots. Finally, in the LLG simulator, it is easier to control the input magnetic parameters in a multilayered nanostructure, as compared to that in OOMMF.

There are three modules of functionality in LLG micromagnetic simulator as described below:

Input phase: This is the control interface which helps to define the parameters and designing customized simulation. Since the program solves the LLG equations using finite differences for exchange energies and fields, as well as boundary elements for magnetostatic self-energies and fields, the object must be defined as a grid. This simulator uses rectangular pixels on a Cartesian grid. Once the environment is set, LLG initializes all of the arrays to start computing the demagnetization field coupling tensors. As the simulation phase begins the user is prompted to store the simulation parameters in several files.

Simulation phase: In this phase the simulation is performed based on the solution of the differential equations (LLG Simulation Sheet).

Review phase: In this phase, the user can review the results by re-playing them through a graphically animated movie (LLG Movie Viewer) or the user can view a domain or field file in the viewer control.

LLG supports four integrators to solve ODE. The most primitive one is an ‘Euler Cartesian’ method, which is the fastest but least accurate. The ‘Rotation Matrices’ method is chosen for solutions where damping is greater than 0.5. This is used to study the magnetic ground state configurations. The ‘Cartesian Predictor-Corrector integrator’ is the most accurate and also faster when damping is about 0.01. The ‘Gauss-Seidel Stable’ method is a semi-implicit first-order integration scheme, in which the integration time steps can be much larger on fine grids.

4.2. Plane Wave Method

The plane wave method (PWM) is extensively used to calculate the band structure for a periodic geometry, e.g. in photonic, phononic or magnonic crystals [10-13]. The method provides full-spectra of eigen excitations for any type of lattice, any shape of scattering centres and for various dimensions of the periodicity. In magnonic crystals (MCs), the inhomogeneity of the internal magnetic field is considered in the form of the superposition of plane waves, that eventually converts the LLG equation to an eigenvalue problem, which is subsequently solved using standard numerical routines to find out the eigenvalues (SW frequencies) and eigen vectors (amplitude of the dynamical component of the magnetization vector).

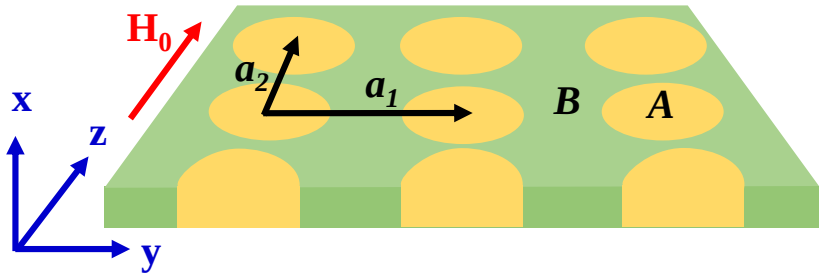

Fig. 4.1: A rectangular MC formed by circular ferromagnetic elements *A* embedded in matrix *B*.

We assume the MC to be composed of an array of scattering centres of finite thickness made of ferromagnetic material embedded in an infinite ferromagnetic matrix. The schematic of a MC with circular scattering centers arranged in a rectangular array along with the co-ordinate axes is depicted in Fig. 4.1. We have assumed the x-axis to be perpendicular to the sample plane and the external bias field H_0 is applied in the sample plane along the z-axis. We solve the LL equation, i.e., the equation of motion of the magnetization vector M(r, t) in space and time,

$$\frac{\partial M(r,t)}{\partial t} = -\gamma\mu_0 M(r,t) \times H_{eff}(r,t) \qquad (4.3)$$

where γ and μ_0 are the gyromagnetic ratio and the permeability of vacuum, respectively and H_{eff} denotes the effective magnetic field acting on the magnetization.

In the linear approximation, the component of the magnetization vector parallel to the static magnetic field (i.e. in z direction) is constant in time (t), and its magnitude is larger as compared to the dynamic perpendicular components $m(r,t)$, i.e. $|m(r,t)| \ll M_z(r)$, where $M_z \sim M_S$ and $M(r,t) = M_z(r)\hat{z} + m(r,t)$. For monochromatic SWs, we can write $m(r,t) = m(r)e^{i\omega t}$, where ω is the angular frequency of the SWs. We further consider that H_{eff} consists of the uniform and constant external magnetic field H_0 (strong enough to enforce parallel alignment

of all the magnetic moments), the exchange field H_{ex} and the magnetostatic field H_{ms}, while neglect the contribution of the anisotropy field for the sake of simplicity.

In the classical limit, we can write the time and space dependent exchange field in terms of the exchange length l_{ex} as [14]:

$$H_{ex}(r,t) = \left(\nabla . l_{ex}^2(r)\nabla m(r,t)\right) \tag{4.4}$$

where, $l_{ex}(r) = \sqrt{\frac{2A(r)}{\mu_0 M_S^2(r)}}$ and $A(r)$ is the exchange stiffness constant.

The magnetostatic field can be divided into a static and a dynamic component, $H_{ms}(r)$ and $h_{ms}(r)$, $H_{ms}(r,t) = H_{ms,z}\hat{Z} + h_{ms}(r)e^{i\omega t}$. Finally, H_{eff} can be written as:

$$H_{eff}(r,t) = H_0\hat{z} + (\nabla . l_{ex}^2(r)\nabla)m(r,t) + H_{ms,z}\hat{z} + h_{ms}(r)e^{i\omega t} \tag{4.5}$$

The respective components of $M(r,t)$ and $H_{eff}(r,t)$ in different coordinate axes are used to calculate the vector product on the right hand side of the aforementioned LL equation. Equating this with the corresponding left hand side, the expressions for the dynamic magnetization components $m_x(r)$ and $m_y(r)$ as obtained follows:

$$m_x(r) = \frac{\mu_0\gamma}{i\omega}\left(m_y(r)(H_0 + H_{ms}) - M_s h_{ms,y} - M_s\nabla . l_{ex}^2(r)\nabla m_y(r)\right) \tag{4.6}$$

$$m_y(r) = \frac{\mu_0\gamma}{i\omega}\left(M_s h_{ms,y} + M_s\nabla . l_{ex}^2(r)\nabla m_y(r) - m_x(r)(H_0 + H_{ms})\right) \tag{4.7}$$

Subsequently, all the periodic functions (both in time and space) are mapped onto the Fourier space. The material parameters M_S, A and l_{ex}^2 have the periodicity of the lattice constant, i.e.

$$M_S(\vec{r} + \vec{a}) = M_S(\vec{r}) \tag{4.8}$$

$$A(\vec{r} + \vec{a}) = A(\vec{r}) \tag{4.9}$$

$$l_{ex}^2(\vec{r} + \vec{a}) = l_{ex}^2(\vec{r}) \tag{4.10}$$

where $\vec{a}$ is a general lattice vector in the direction of periodicity. We perform the Fourier transformation to map the periodic functions M_S and l_{ex}^2 to the reciprocal space. The Fourier transformation formulas are:

$$M_S(r_\parallel) = \sum_G M_S(G)e^{iG.r_\parallel}\ ,\ l_{ex}^2(r_\parallel) = \sum_G l_{ex}^2(G)e^{iG.r_\parallel} \tag{4.11}$$

where $G = (G_y, G_z)$ denotes the reciprocal lattice vector of the periodic structure. The dynamic components of $M(r,t)$ and $H_{ms}(r,t)$ can be converted by using the Bloch's theorem as,

$$m(r_\parallel) = e^{iqr_\parallel}\sum_G m_q(G)e^{iG.r_\parallel},\ h_{ms}(r_\parallel) = e^{iqr_\parallel}\sum_G h_{ms,q}(G)e^{iG.r_\parallel} \tag{4.12}$$

The formulas for the static and dynamic magnetostatic fields, $H_{ms,z}(r_\parallel, x)$, $H_{ms,x}(r_\parallel, x)$, $H_{ms,y}(r_\parallel, x)$ can be derived by solving the Maxwell's equations with proper electromagnetic boundary conditions at both surfaces of the slab of 2D MC. The analytical solutions in the form of a Fourier series can be obtained for both the static and dynamic magnetostatic fields:

$$H_{ms,z}(r_{\parallel},x) = -\sum_G \frac{M_S(G)}{G^2} G_z^2 \times \left(1 - cosh(|G|x)e^{-|G|d/2}\right)e^{iG.r_{\parallel}} \quad (4.13)$$

$$H_{ms,y}(r_{\parallel},x) = -\sum_G \frac{m_y(G)}{|q+G|^2} \left(q_y + G_y\right)^2 \times \left(1 - cosh(|q+G|x)e^{-|q+G|d/2}\right) e^{i(q+G).r_{\parallel}} \quad (4.14)$$

$$H_{ms,x}(r_{\parallel},x) = -\sum_G m_x(G)\, cosh(|q+G|x) \times e^{-|q+G|d/2} e^{i(q+G).r_{\parallel}} \quad (4.15)$$

where *d* is the thickness of the slab. In the works presented in this thesis, the above expressions are calculated at *x=d/2*, i.e., at the surface of the film.

The substitution of equations (4.8) to (4.15) in the aforementioned LL equation leads to the algebraic eigenvalue problem with eigenvalues $\frac{i2\pi f}{\gamma \mu_0 H_0}$ and eigen vectors $m_{x,q}(G)$ and $m_{y,q}(G)$, which can be structured in a matrix form as follows:

$$\widehat{M} m_q = \frac{i2\pi f}{\gamma \mu_0 H_0}\, m_q \quad (4.16)$$

With eigen vector defined as $m_q^T = \left[m_{x,q}(G_1) \ldots\ldots m_{x,q}(G_N), m_{y,q}(G_1) \ldots\ldots m_{y,q}(G_N)\right]$. The matrix $\widehat{M}$ can be written in a block-matrix form:

$$\widehat{M} = \begin{pmatrix} \widehat{M}^{xx} & \widehat{M}^{xy} \\ \widehat{M}^{yx} & \widehat{M}^{yy} \end{pmatrix} \quad (4.17)$$

The submatrices are defined as follows:

$$\widehat{M}^{xx} = \widehat{M}^{yy} = 0 \quad (4.18)$$

$$\begin{aligned} \widehat{M}_{ij}^{xy} = \delta_{ij} &+ \sum_l \frac{\left(q + G_j\right).\left(q + G_l\right)}{H_0} l_{ex}^2\left(G_l - G_j\right) M_s(G_i - G_l) \\ &+ \frac{\left(q_y + G_{y,j}\right)^2}{H_0 \left|q + G_j\right|^2} \left(1 - C\left(q + G_j, x\right)\right) M_s\left(G_i - G_j\right) \\ &- \frac{1}{H_0} \frac{\left(G_{z,i} - G_{z,j}\right)^2}{\left|G_i - G_j\right|^2} M_s\left(G_i - G_j\right) \left(1 - C\left(G_i - G_j, x\right)\right) \\ \widehat{M}_{ij}^{yx} = -\delta_{ij} &- \sum_l \frac{\left(q + G_j\right).\left(q + G_l\right)}{H_0} l_{ex}^2\left(G_l - G_j\right) M_s(G_i - G_l) \\ &- \frac{1}{H_0} C\left(q + G_j, x\right) M_s\left(G_i - G_j\right) \\ &+ \frac{1}{H_0} \frac{\left(G_{z,i} - G_{z,j}\right)^2}{\left|G_i - G_j\right|^2} M_s\left(G_i - G_j\right) \left(1 - C\left(G_i - G_j, x\right)\right) \end{aligned} \quad (4.19)$$

where reciprocal lattice vector indices *i*, *j*, and *l* are integers in the range <1, N>. The additional function used in the equations above is defined as follows:

$$C(q,x) = cosh(|q|x)e^{-|q|d/2} \quad (4.20)$$

The above system of equations can be solved for different SW wave vector by standard numerical routines to find the corresponding eigenvalues (the SW frequency *f*) and eigen vectors (m_q). It is required to estimate the square of the modulus of the fundamental harmonics of magnetization to tally the calculated dispersion with the experimentally obtained band structure via BLS spectroscopy.

$$I_{BLS} \infty \left| m_q(G = 0) \right|^2 \tag{4.21}$$

The spatial mode profiles can also be calculated for a given wave vector and frequency, by determining the modulus of the dynamic magnetization ($m_x(r)$) for each spatial point. It is worth mentioning that the PWM calculations stand upon the consideration that both the matrix and the scattering centres consist of ferromagnetic materials. In case of patterned dot or antidot array, where either the scattering centres or the matrix are made up of non-magnet, we should assign a very small value to the material parameters in order to avoid any unphysical solutions.

References

[1] M. Donahue, D. G. Porter, OOMMF User's Guide, Version 1.0, NIST Interagency Report No. 6376 1999) (https://math.nist.gov/oommf/).
[2] M. R. Scheinfein, E. A. Price, 2003, LLG User Manual v2.50, (http://llgmicro.home.mindspring.com/).
[3] MicroMagus, (http://www.micromagus.de/).
[4] A. Vansteenkiste, J. Leliaert, M. Dvornik, M. Helsen, F. Garcia-Sanchez, and B. Van Waeyenberge, AIP Advances. **4**, 107133 (2014). (https://mumax.github.io/).
[5] H. Fangohr, M. Albert, M. Franchin, IEEE, Nmag micromagnetic simulation tool - software engineering lessons learned (IEEE, New York, 2016), Proceedings of 2016 Ieee/Acm International Workshop on Software Engineering for Science (http://nmag.soton.ac.uk/nmag/).
[6] Magpar, (http://www.magpar.net/).
[7] B. Krüger, G. Selke, A. Drews, D. Pfannkuche, IEEE Trans. Magn. **49**, 4749 (2013).
[8] A. Kakay, E. Westphal, R. Hertel, IEEE Trans. Magn. **46**, 2303 (2010).
[9] D. Kumar, O. Dmytriiev, S. Ponraj, and A. Barman, J. Phys. D: Appl. Phys. **45**, 015001 (2012).
[10] V. Laude, M. Wilm, S. Benchabane, A. Khelif, Phys. Rev. E. **71**, 036607 (2005).
[11] J. O. Vasseur, P. A. Deymier, B. Djafari-Rouhani, Y. Pennec, and A-C. Hladky-Hennion, Phys. Rev. B. **77**, 085415 (2008).
[12] M. Krawczyk and H. Puszkarski, Phys. Rev. B. **77**, 054437 (2008).
[13] M Krawczyk, S Mamica, M Mruczkiewicz, J W Klos, S Tacchi, M Madami, G Gubbiotti, G Duerr, and D Grundler, J. Phys. D: Appl. Phys. **46**, 495003 (2013).
[14] M. Krawczyk, M. L. Sokolovskyy, J. W. Klos, and S. Mamica, Adv. Condens. Matter Phys. 764783 (2012).

Chapter 5

5. Investigation of Magnetization Dynamics in Two-Dimensional $Ni_{80}Fe_{20}$ Diatomic Nanodot Arrays

5.1. Introduction

Ordered arrays of magnetic nanoelements have the potential to serve as magnetic storage [1], memory [2], logic [3], and spin-torque nano-oscillator [4] devices as well as magnonic crystals [5–7]. For the first two applications, the magnetostatic interaction (cross-talks) between the individual elements (bits) must be negligible, whereas strong interactions between the elements are a pre-requisite for the next three applications, as mentioned above. In the latter case, the nanoelement array may act as a medium of propagation of magnetic excitations in the form of collective long-wavelength spin waves (SWs), when the individual magnetic elements are strongly magnetostatically coupled. Magnonic crystals (MCs) are artificial crystals made up of periodically patterned arrays of ferromagnetic materials, which can be considered as carriers of SWs. In such systems, interesting properties of magnetization dynamics and SWs can be tuned by changing the material and geometric parameters of the nanostructures, as well as by changing the strength and orientation of the bias magnetic field. MCs find potential application in magnonic waveguides [8], filters [9], interferometers [10], phase shifters [11], spin-wave emitters [5], and magnonic logic devices [12, 13]. Magnetization dynamics in ferromagnetic nanodot arrays have been investigated extensively over the last decade by various experimental techniques, which can be distinguished by a time-domain technique (optical and field-pumped time-resolved magneto-optical Kerr effect (TR-MOKE)) [14–16], frequency-domain technique (ferromagnetic resonance) [17], and wave vector-domain technique (Brillouin light scattering (BLS)) [18–20], as well as by numerical techniques such as the plane-wave method [21], micromagnetic simulations [22], and analytical technique [23–25]. These studies were mainly focussed on collective magnetization dynamics in ferromagnetic nanodot arrays by varying the material, shape, size, lattice spacing, lattice symmetry of the array, as well as the strength and orientation of the external bias magnetic field. For example, Kruglyak *et. al* reported an interesting size-dependent cross-over between different precessional modes by using TR-

MOKE measurements [26]. The transition between different collective modes by the variation of lattice constant and bias magnetic field as a consequence of the modification of inter-element interaction has also been reported [27, 28]. Variation of the shape of the nanodots as well as lattice symmetry showed a large change in the internal magnetic field as well as the inter-dot interaction field giving rise to a large change in the spin-wave modes and the dynamical configurational anisotropy in ferromagnetic nanodots [29–31]. Dipolarly coupled magnetic elements of different types have been reported in the literature. Studies have shown the tunability of magnonic band structures in a dense array of dipolarly coupled nanostripes of alternating width, depending on the magnetic ordering of neighbouring wires, i.e. parallel and antiparallel alignment [32, 33].

Bicomponent magnonic crystals (BMCs) have the potential to tune the collective magnetization dynamics more efficiently due to the rich inter-element exchange and dipolar coupling and several attempts have been made so far to develop BMCs in the form of embedded ferromagnetic nanostructures in another ferromagnetic matrix [34], nanodots with two different materials [35], antidots with different size, etc. However, more possibilities of developing new types of BMCs need to be explored for further advancement of this emerging research field. Here, we have used $Ni_{80}Fe_{20}$ (Py) nanodots with two different sizes but the same thickness placed in close proximity as the diatomic (double dots connected by magnetostatic interaction) basis structure, which is arranged in a square lattice in an attempt to develop a new type of BMC, which has not been reported in the literature before. We have studied the collective magnetization dynamics in such diatomic magnetic nanodots by using the BLS technique. We specifically investigated the thermal SWs with wave vector $k \approx 0$ in the diatomic nanodots for different values and orientations of the in-plane bias magnetic field and different lattice constants. The micromagnetic simulations are also performed to investigate the mode profiles of the SWs and also to understand the evolution of the magnetization dynamics from single dots to the large array via the diatomic unit. Our results have opened a pathway to tailor the magnonic properties in this type of system.

5.2. Methods

500 μm × 500 μm arrays of circular-shaped diatomic Py nanodots with 30 nm thickness were fabricated on self-oxidized Si [100] substrate by a combination of electron-beam lithography and electron-beam evaporation. The beam current used during the lithography is 500 pA for a dose time of 1.0 μs. The base pressure of the deposition chamber was 2×10^{-8} Torr for the

deposition of Py by electron-beam evaporation. Figs 5.1 (a) and (b) show the scanning electron microscopy (SEM) images of the two samples S1 and S2. The diameter of the larger (d1) and smaller (d2) dot of a diatomic unit is 700 and 280nm, respectively, the inter-dot (intra-unit) separation (s1) is about 35nm, while the inter-unit separation (s2) is about 170nm (lattice constant 1185nm) for S1 and 300nm (lattice constant 1315nm) for S2. The diameter of the dots shows maximum ±5% deviation, while the edge-to-edge separation between the dots of a diatomic unit shows maximum ±10% deviation within different lattices. The inter-dot separation of a diatomic unit is chosen to be very small, so that the dots are strongly magnetostatically coupled and show strong collective modes of precession. The dots are chosen to be of circular shape, so that the individual dots do not possess any configurational anisotropy due to their shape, although fabrication related deformations in the real sample may induce some shape anisotropy.

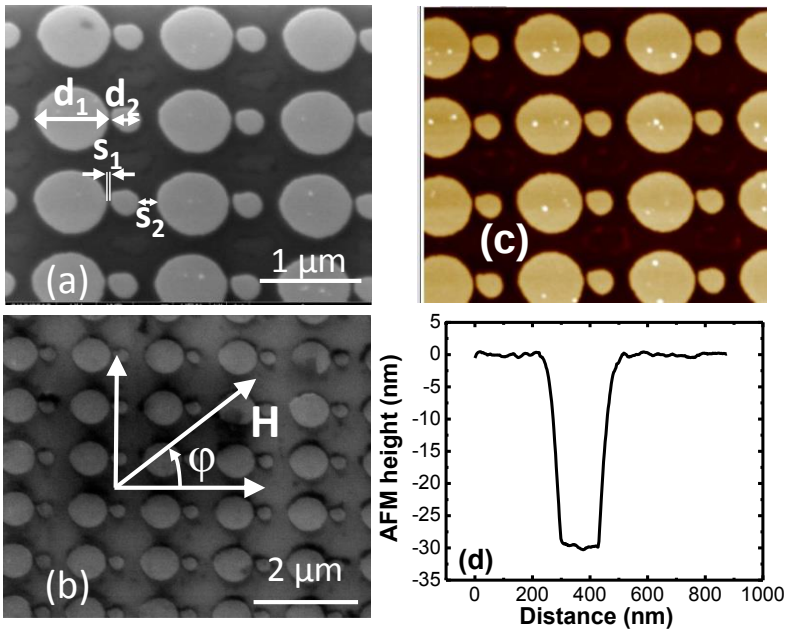

Fig. 5.1: SEM images of Py diatomic nanodot arrays with two different inter-unit separations of (a) 170 nm (S1) and (b) 300nm (S2). (c) AFM image of S1. (d) AFM height profile of S1 showing that the thickness of sample is ~30 nm.

We have performed BLS measurements in backscattered geometry to study the thermal SWs in these samples and the measurement geometry is shown schematically in Fig. 5.2 (c). A continuous-wave single-mode diode-pumped solid-state laser of wavelength λ = 532nm and power of 130 mW was focused onto the sample to a spot size ~ 40 µm and the inelastically scattered light from the sample due to the interaction between incident photons and magnons was analysed to determine the spin-wave frequencies by using a Sandercock type six-pass

tandem Fabry–Perot interferometer. The laser light impinges parallel to normal of the sample plane, which enables the measurement for the k ≈ 0 wave vector. Here, the frequency shift of the scattered beam from the incident laser frequency corresponds to the thermally excited spin-wave frequency. In our experiment, an in-plane bias magnetic field *H*, applied parallel to the sample surface and perpendicular to the plane of incidence of light (the measurement geometry in our experiment is shown schematically in Fig. 5.2 (c)), is varied from 0.3–1.5 kOe. The observed frequency shift of the spectra is strongly related to the applied bias field, showing its magnetic origin. The BLS spectra are measured for the k ≈ 0 wave vector for two different bias field orientations (φ = 0° and 90°), as shown in Fig. 5.3. Further details of the BLS setup are described elsewhere [36]. Fig. 5.2 (d) shows the Gaussian fit to a typical elastic peak of the BLS spectra to get an estimate of instrumental linewidth [37]. From the fit, a linewidth of ~0.3 GHz is obtained, which gives the measure of the lower limit of the linewidth in our BLS spectra.

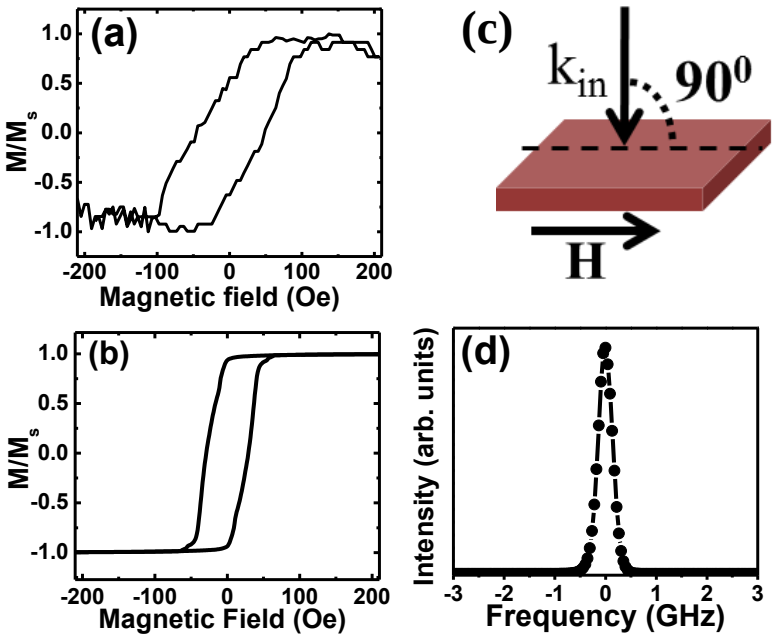

Fig. 5.2: (a) Magnetic hysteresis loop of S1 measured by Static Magneto Optical Kerr Effect Microscopy. (b) Simulated magnetic hysteresis loop of the same using OOMMF software. (c) Measurement geometry for BLS experiment in our study. Here k_{in} is the incident wave-vector and *H* is the in-plane bias magnetic field. (d) Gaussian fit to a typical elastic peak of the BLS spectra to obtain an estimate of the instrumental linewidth of our experiment setup.

In order to understand the observed SW spectra and their variation with various parameters, we have performed micromagnetic simulations using OOMMF software [38]. We have also simulated the spin-wave mode profiles (power and phase of individual resonant mode) by using a home-grown Matlab based code named DotMag [39]. We have simulated single nanodots of

two different sizes, a diatomic basis structure, and arrays of the diatomic nanodots to reproduce our experimental data and also to understand the evolution of the collective magnetization dynamics from single dot via diatomic basis to the large array. The frequencies and spatial profiles of the modes of the individual elements are found to be significantly modified in the diatomic unit and further in the 2D arrays, and additional modes also appeared. Furthermore, the simulated mode profiles are found to be different for two different orientations of the bias field. The simulations are performed on the nanodot arrays after applying a 2D periodic boundary condition (2D-PBC). We simulated both the ideal structures without any edge deformation and the real sample structures to understand the effects of edge deformation on the spin-wave spectra and mode profiles in the real sample. The simulation results with the introduction of the actual edge deformations are given in the Appendix I. The real sample geometry for simulation was derived from the SEM images. The calculations were done by dividing the samples into arrays of cuboidal cells of dimensions 4 × 4 × 30 nm^3, while the material parameters for Py were used as gyromagnetic ratio γ = 17.6 MHz/Oe, anisotropy field H_k = 0, saturation magnetization M_s = 800 emu/cc, and exchange stiffness constant A = 1.3 × 10^{-6} erg/cm. The lateral dimensions of the cells are below the exchange length, $l_{ex} = \sqrt{\frac{2A}{\mu_0 M_s^2}}$ (~5.7 nm or 5.7 × 10^{-7} cm) of Py. The material parameters were obtained by measuring the variation of precessional frequency (f) with bias field for a Py thin film and by fitting them using the Kittel formula,

$$f = \frac{\gamma}{2\pi}\sqrt{(H + H_k)(H + H_k + 4\pi M_s)} \qquad (5.1)$$

The exchange stiffness constant A is obtained from the literature [40]. In OOMMF simulation, at first to obtain the static magnetic configuration, a large magnetic field was applied to saturate the sample magnetization and then the magnetic field was reduced to the bias field value. The system was then allowed to reach the equilibrium. A pulsed magnetic field was applied to simulate the magnetization dynamics. The spatial maps of magnetization were calculated at time steps of 10 ps for a total duration of 4 ns.

5.3. Results and Discussion

The surface topography of the diatomic nanodot arrays has been measured by atomic force microscopy (AFM) and the AFM image of S1 is shown in Fig. 5.1 (c). The height profile obtained from AFM is shown in Fig. 5.1 (d), which confirms that the thickness of the sample is ~30nm. Fig. 5.2 (a) shows the magnetic hysteresis loop of S1 measured using a static magneto-

optical Kerr effect (SMOKE) microscope and Fig. 5.2 (b) shows the simulated hysteresis loop of the same. The value of saturation magnetic field obtained from SMOKE measurement (~120 Oe) is slightly greater than that obtained from the simulated hysteresis loop (~80 Oe). Nevertheless, in BLS measurements the strength of applied in-plane bias field has always been kept greater than the saturation field values.

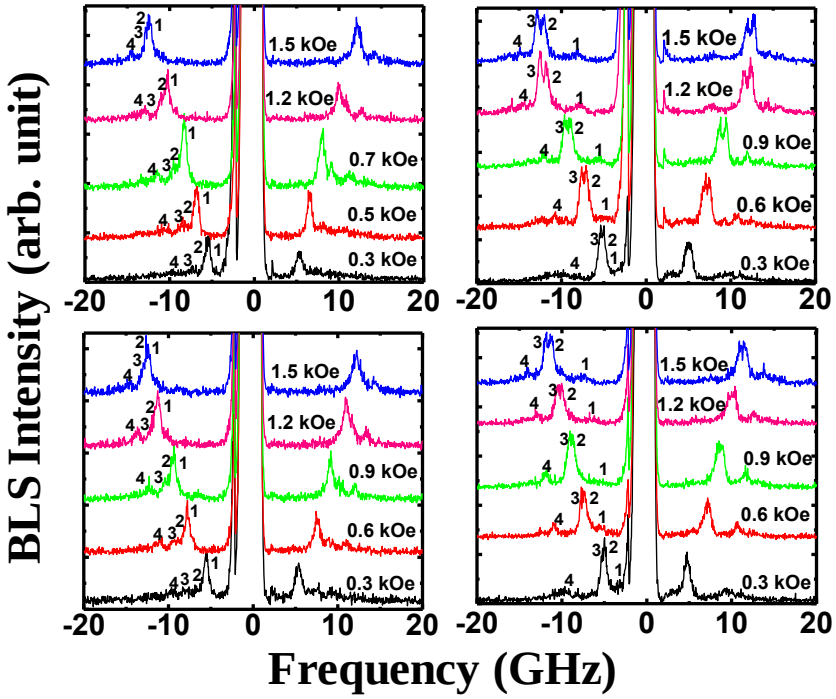

Fig. 5.3: BLS spectra of the two Py diatomic nanodot arrays (S1 and S2) at different in-plane bias magnetic fields. Field values and mode numbers are mentioned for corresponding spectra. Spin-wave spectra from S1 for (a) $\varphi = 0°$ and (b) $\varphi = 90°$. Spin-wave spectra from S2 for (c) $\varphi = 0°$ and (d) $\varphi = 90°$.

In Fig. 5.3, we present the measured BLS spectra at different bias magnetic field strengths and two different bias field orientations for the two different diatomic nanodot arrays. In both orientations, a number of modes have been observed and frequencies of all the modes increase with the increase in applied bias field, i.e. all the modes show dispersion with the applied bias field. However, the powers of the spin-wave modes are different in the two different bias field orientations. The powers of the modes decrease with increase of frequency in $\varphi = 0°$ orientation, whereas the lowest and highest frequency modes have lesser power compared to the two central modes, which have nearly equal power in the $\varphi = 90°$orientation of the bias field. Interestingly, in the $\varphi = 0°$ orientation of the bias field, the separation between mode 2 and 3 decreases as H increases and finally almost merges at $H = 1.5$ kOe, whereas in the $\varphi = 90°$ orientation of the

bias field, the opposite phenomenon occurs, i.e. the separation between mode 2 and 3 increases as H increases. Also, the frequencies of the modes are different in the two different orientations for a particular value of *H*. We have separately plotted magnified views of the spectra at H = 1 kOe for the two arrays at two different orientations (except for S2 at φ= 0°, where instead of 1 kOe, the spectrum has been taken at 0.9 kOe) in Fig. 5.4 (a). The frequency axis is rotated by 180° here for the sake of clarity.

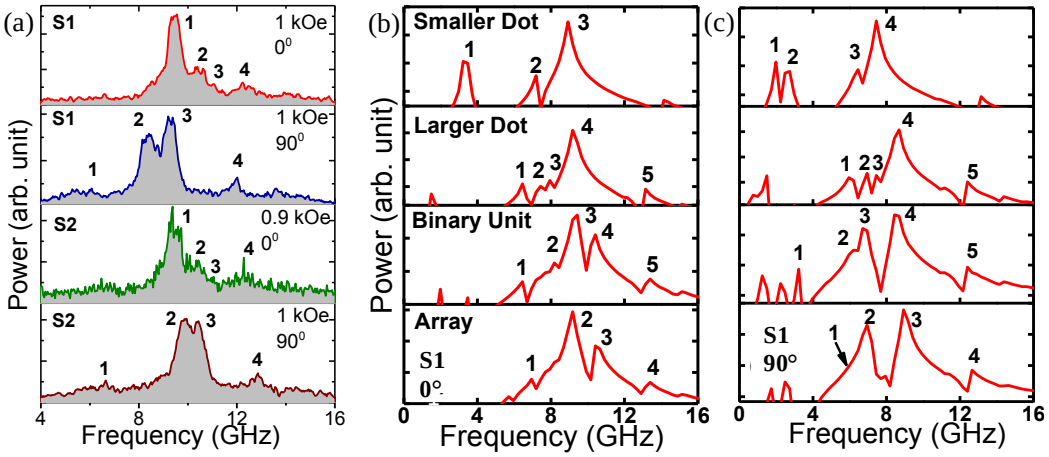

Fig. 5.4: (a) Magnified views of the spin-wave spectra for S1 and S2 at φ = 0° and 90°. The corresponding bias field is shown in the respective spectrum (b) FFT power spectra of the simulated time-domain magnetization of S1at φ = 0°and (c) φ = 90°. Each column contains four panels corresponding to the simulated spectra of smaller dot, larger dot, a diatomic unit and an array with periodic boundary condition.

Figs. 5.4 (b) and (c) show the FFT power spectra of the simulated time-domain magnetization. The power and phase profiles of the simulated modes for the two different orientations (φ = 0° and 90°) of the in-plane bias field are shown in Figs. 5.5 and 5.6, respectively. The simulated FFT spectra of the smaller dot of diameter 280 nm and thickness 30 nm (Fig. 5.4(b)) show two distinct high-power modes at 3.3 GHz (mode 1) and 9.2 GHz (mode 3), which are the edge mode (EM) and centre mode (CM) of the dot. In addition, a lower-power mode is observed at 7.2 GHz (mode 2), which is found to be a standing wave mode of backward volume (BV) magnetostatic SW in origin. Interestingly, when the bias field is rotated by 90° (Figs 5.4 (c) and 6) the lowest frequency mode splits into two asymmetric EMs at 2.1 GHz (mode 1) and 2.7 GHz (mode 2), in addition to a low-power BV mode at 6.4 GHz (mode 3) and a CM at 7.5 GHz (mode 4). The FFT spectra of the larger dot of diameter 700 nm and thickness 30 nm show (Figs. 5.4 (b) and 5.5) one dominant CM at 9.2 GHz (mode 4) having two low-power shoulders and a distinct mode with BV-like characteristics at 8.0 GHz (mode 3 with quantization number

n = 11), 7.5 GHz (mode 2 with n = 9), and 6.4 GHz (mode 1 with n = 5), and a complex high-frequency mode at 13.2 GHz (mode 5) with mixed BV and Damon–Eshbach (DE) character (n = 23, m = 2). When the bias field is rotated to φ = 90° (Figs. 5.4 (c) and 6) the main dominant mode retains its spatial character of CM but gets slightly red shifted compared to the one at φ = 0° and appears at 8.6 GHz (mode 4). The other modes with lower power appear at 7.4 GHz (mode 3), 7.0 GHz (mode 2), and 5.9 GHz (mode 1) (all BV-like modes with n = 9, 7, and 5, respectively), and 12.5 GHz (mode 5, which is a complex mode with mixed BV-DE character, n = 23, m = 2).

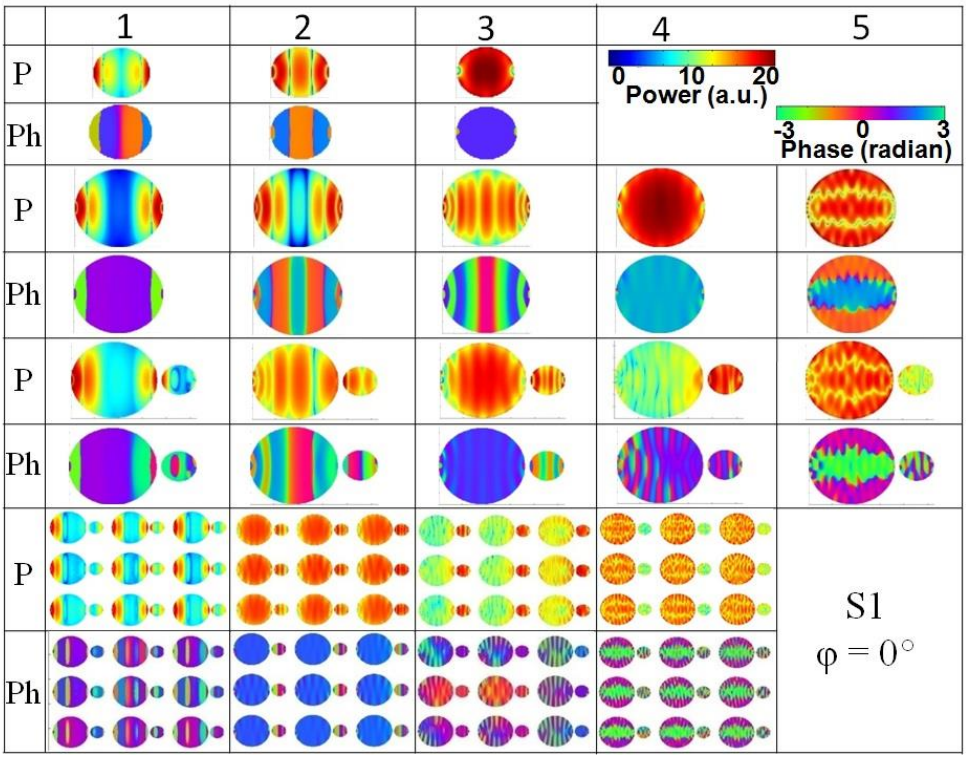

Fig. 5.5: The power and phase maps for different spin-wave modes of individual nanodots, diatomic unit and array (S1) for H = 1 kOe applied at φ = 0° showing the evolution of the modes from individual nanodots to the array via a diatomic unit. The color maps for the power (in arbitrary units) and phase (in radians) distributions are shown at the top. Sizes of the dots are not in scale.

However, the mode characteristics are significantly modified when the larger and the smaller dots are placed next to each other with a gap of about 35 nm between their nearest edges. In the first orientation of the applied bias field, i.e. for φ = 0° (Figs. 5.4 (b) and 5.5) the two lowest-frequency modes at 2.0 and 3.4 GHz are not analysed, as they appeared neither in the simulated nor in the experimental array of diatomic nanodots. Here, mode 1 (6.4 GHz) corresponds to a BV-like mode with n = 5 in both the dots, while mode 2 (8.2 GHz), 3 (9.4 GHz), and 4 (10.4

GHz) correspond to a BV-like mode with quantization number (large element, small element) as (9, 5), (16, 7), and (17, 8). The asymmetry in mode number and mode profile in the diatomic unit stems from the strong magnetostatic interaction between the dots at their nearest edges.

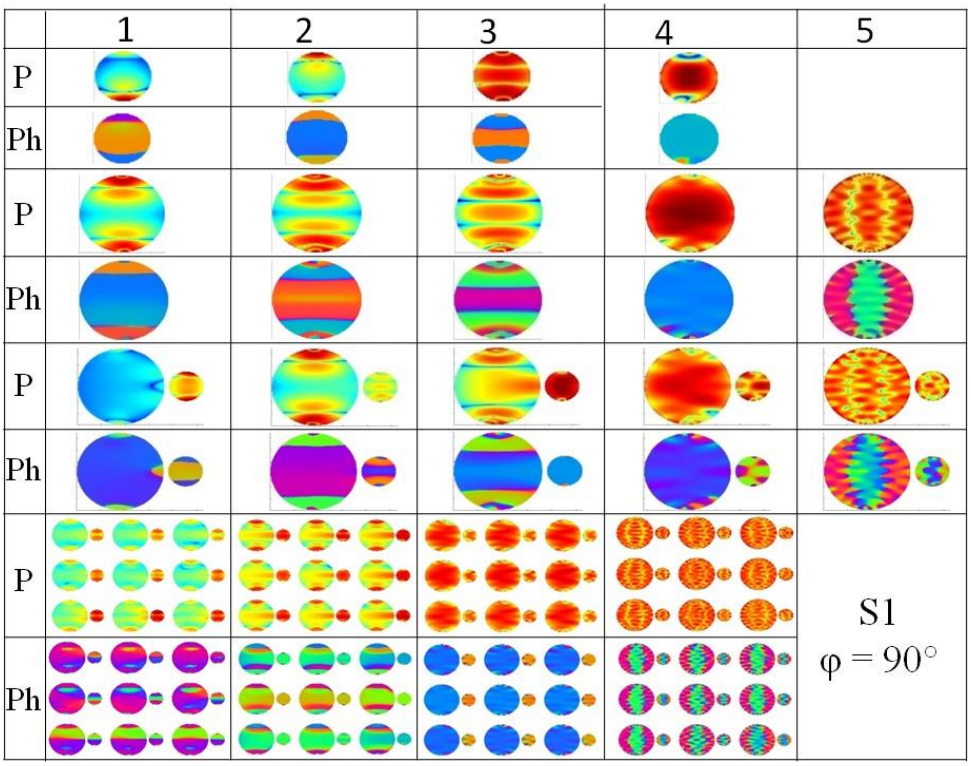

Fig. 5.6: The power and phase maps for different spin-wave modes individual nanodots, diatomic unit and array (S1) for H = 1 kOe applied at φ = 90° showing the evolution of the modes from individual nanodots to the array via a diatomic unit. The color maps for the power and phase distributions are as shown in Fig. 5.5. Sizes of the dots are not in scale.

Mode 5 (13.2 GHz) corresponds to the mixed BV-DE like mode (n = 25, m = 2) in the larger dot and a BV-like mode (n = 9) in the smaller dot. For φ = 90°, we again did not analyse the two lowest-frequency modes at 1.2 and 2.2 GHz, as they did not appear in the experimental spectra (Figs. 5.4 (c) and 5.6). Here, mode 1 (3.3 GHz) corresponds to the EM of both dots, which is a new collective mode as pure EM was not observed in the single larger dot. Mode 2 (6.1 GHz) corresponds to a BV-like mode with n = 5 in both the dots. Mode 3 (6.8 GHz) corresponds to a BV-like mode (n = 7) in the larger dot and CM in the smaller dot. Mode 4 (8.6 GHz) is a complex mode with a mixed BV-DE-like character in both the dots (n = 13, m = 2 in the larger one and n = 7, m = 2 in the smaller one). Mode 5 (12.5 GHz) is also a complex mode with a BV-DE-like character in both the dots (n = 25, m = 2 in the larger one and n = 11, m = 3 in the smaller one).

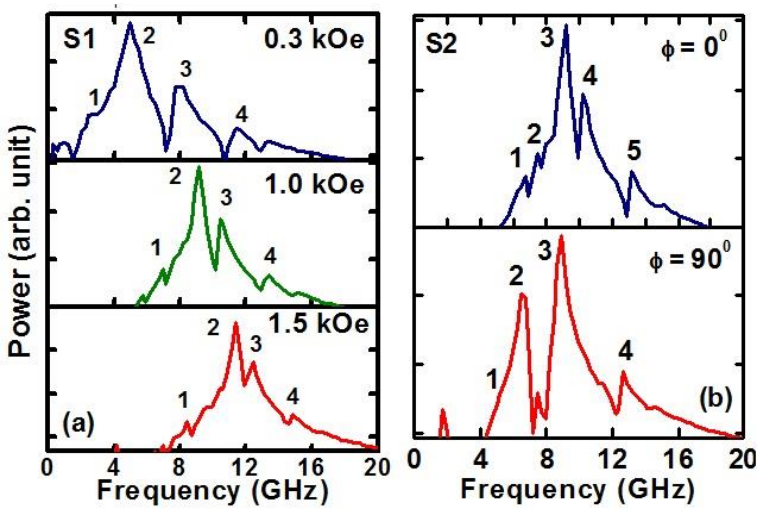

Fig. 5.7: (a) FFT power spectra of simulated time-domain magnetization for three different values of the in-plane bias magnetic field applied at φ = 0°for smooth edged array corresponding to S1. (b) FFT power spectra of simulated time-domain magnetization for the array S2 for H = 1 kOe applied at φ = 0° and 90°.

These modes are further modified in the arrays, as observed both from the experimental and simulated spectra from the array. For φ = 0°, the four modes observed in the experimental spectra at k ≈ 0 (Fig. 5.4(a)) are well reproduced by micromagnetic simulations, as shown in Figs. 5.4 (b) and 5.5, although the lowest-frequency mode at 6.8 GHz (present in the simulated spectra) is not prominent in the experimental spectra. The frequencies of these modes are almost the same as the diatomic unit, but the lower-frequency modes do not appear here. Here, mode 1 (6.8 GHz) is a collective BV-like mode in both the larger (n = 7) and smaller (n = 3) dots with different mode quantization number. Mode 2 (9.2 GHz) corresponds to a near uniform mode in the larger dot and BV-like mode (n = 5) in the smaller dot. Mode 3 (10.5 GHz) corresponds to a BV-like mode in both the larger (n = 17) and smaller (n = 8) dots, which is identical to mode 4 of the diatomic unit. Mode 4 (13.5 GHz) is also identical to mode 5 of the diatomic unit. Hence, the long-range magnetostatic interaction between the elements in the array strongly modifies only the lower-frequency modes, while the higher-frequency modes remain unaltered as these modes are dominated by exchange interaction as opposed to the purely dipolar-dominated lower frequency modes. In the other orientation (φ = 90°) of the bias field, three clear modes and a weaker shoulder-like mode appear in the simulated FFT spectra of the array (Fig. 5.4 (c)). Mode 1 (5.8 GHz) corresponds to a BV mode with n = 7 in the larger one and n = 5 in the smaller one. Whereas mode 2 (6.9 GHz), 3 (9.0 GHz), and 4 (12.5 GHz) correspond

to mode 3, 4, and 5 of the diatomic unit in this bias field configuration, showing very weak effects of long-range dipolar interaction on these modes in the array.

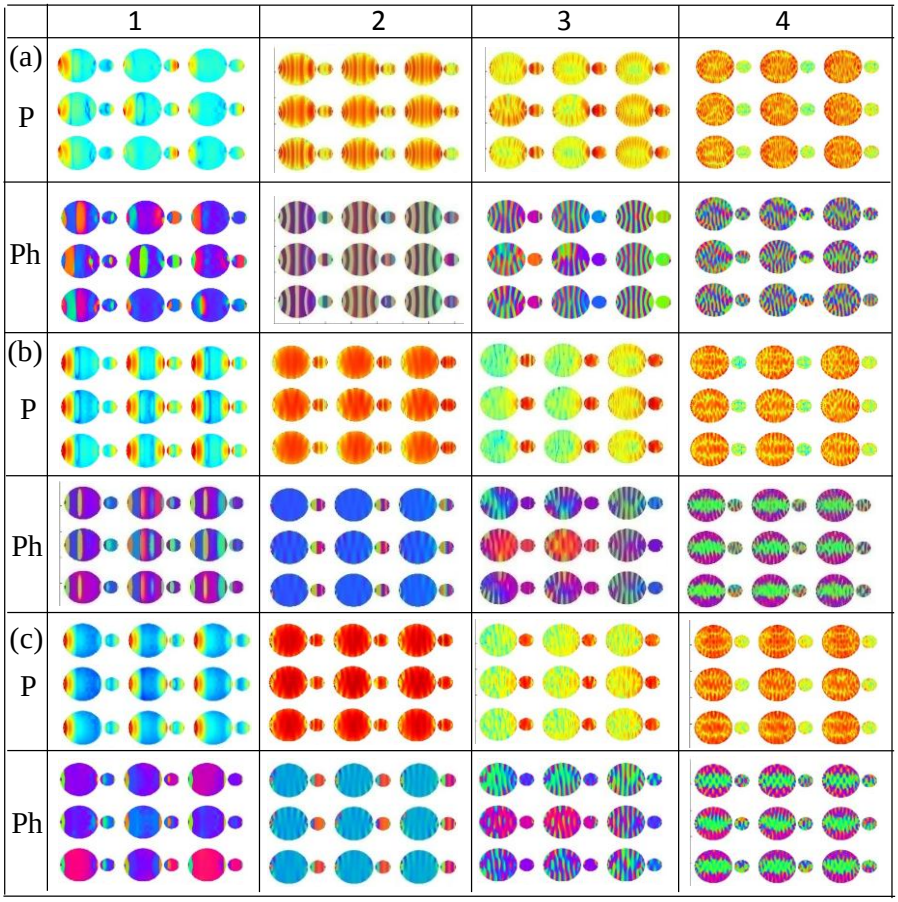

Fig. 5.8: The power and phase maps for different spin-wave modes of the array S1 for different values of the bias magnetic field of (a) H = 0.3 kOe, (b) H = 1.0 kOe and (c) H = 1.5 kOe applied at φ =0°. The color maps for the power and phase distributions are as shown in Fig. 5.5. Sizes of the dots are not in scale.

The introduction of edge deformation causes further modifications of the spin-wave modes, which gives a better match with the experimental spectra. As in this type of dipolarly coupled nanodots, the coupling strength depends on the unsaturated spins present in the dot edges. Hence, the lowest-frequency modes are mainly modified by the introduction of edge roughness. For the sake of clarity, we have presented the simulations with rough-edged samples in the Appendix I. The variation of bias magnetic field systematically varied the resonant mode frequencies as expected, but the number of modes remained unchanged. We further investigated the effects of the bias magnetic field on the mode profiles. Fig. 5.7 (a) shows the FFT spectra for the simulated time domain magnetization and Fig. 5.8 shows the power and phase maps at three different bias field values applied to S1 at φ = 0°. While all the quantized modes become

more prominent with the reduction of the bias field, the most dominant mode (mode 2) is most strongly affected. At high values of applied bias magnetic field the most intense peak corresponds to a spatially uniform CM. However, the most intense peak shows primarily BV-like nature with n = 11 when the applied bias magnetic field strength is reduced.

As we vary the inter-dot separation (lattice constant) of the array from 170 nm (1185 nm) to 300 nm (1315nm), while keeping the diatomic unit fixed, we do not observe any significant variation in the spin-wave spectra of the array in both bias field orientations apart from the fact that a new mode at 7.6 GHz appears in S2 for φ= 0° as opposed to S1, which is a BV-like mode with n = 9 in the larger dot and n = 5 in the smaller one. Simulated mode profiles (Figs. 5.7 (b) and 5.9) also reveal that the higher-frequency modes as observed in the experimental spectra remain unaltered, while the lowest frequency mode (mode 1) becomes more symmetric in S2 due to the reduction of inter-unit interaction in the array. For φ = 90°, the collective behavior was weak in S1 and hence, the reduction of lattice constant did not affect either the SW spectra or the mode profiles.

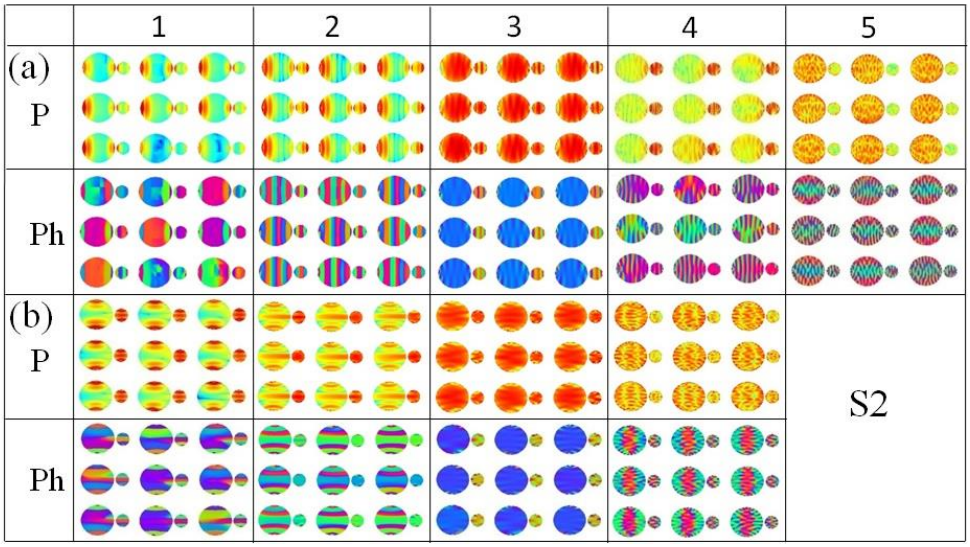

Fig. 5.9: The power and phase maps for different spin-wave modes of the array S2 for H = 1 kOe at (a) φ = 0° and (b) φ = 90°.The color maps for the power and phase distributions are as shown in Fig. 5.5. Sizes of the dots are not in scale.

The SW mode profiles already give some information about the origin of the differences in the spin-wave spectra in different lattices. To gain more insight into the dynamics, we have further simulated the magnetostatic field distribution of the diatomic nanodot arrays by using LLG micromagnetic simulator [41]. Figs. 5.10 (a) and (b) show the contour plots of the magnetostatic fields of S1 for the two different bias field orientations, and Fig. 5.10 (c) represents the contour

plot of the magnetostatic fields of S2 in φ = 0° orientation. The arrows represent the magnetization inside the dots. It is clear that the dipolar contribution from the magnetostatic stray field dominates for the two arrays in the two different orientations of the bias field, and the density of the inter-unit interacting field lines is much smaller than the intra-unit interaction field. Consequently, the interunit interacting fields are influenced by the change in lattice constant.

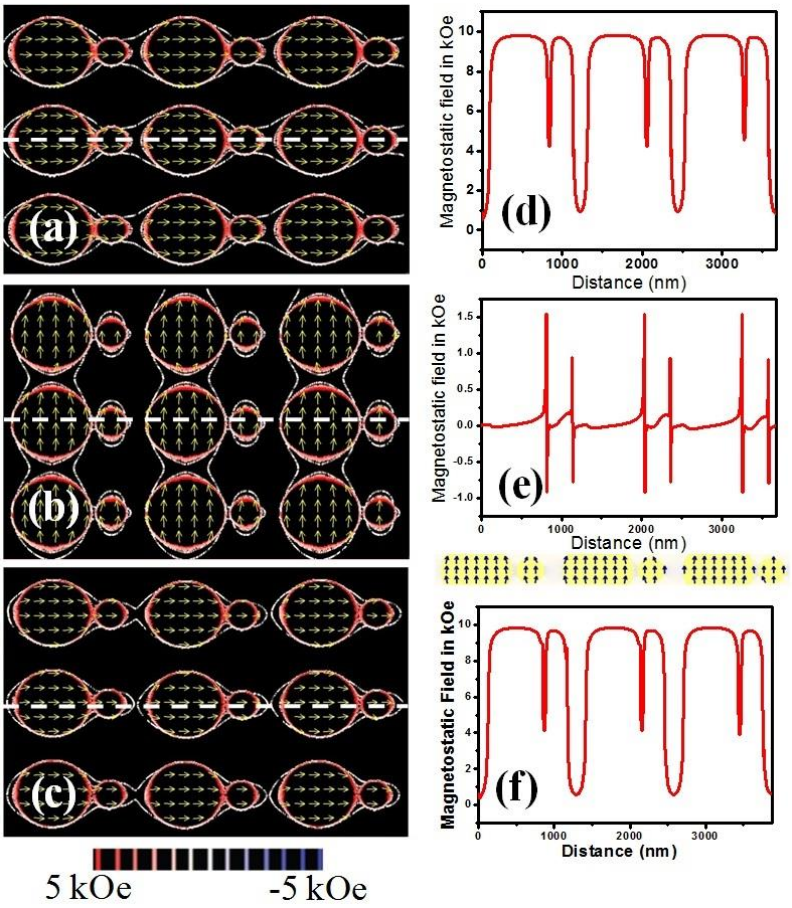

Fig. 5.10: The contour maps of simulated magnetostatic field distribution for the diatomic nanodot arrays (a) S1 at φ = 0°,(b) S1 at φ = 90° and (c) S2 at φ = 0°. (d) – (f) The corresponding line scans of simulated magnetostatic fields from the arrays obtained from the positions indicated by white dotted lines.

To quantify the intra-unit and inter-unit interaction, we have taken line scans of the simulated magnetostatic fields along the white dotted lines from S1 (φ = 0° and 90°) and S2 (φ = 0°), as shown in Figs. 5.10 (d)–(f). The magnitude of the inter-unit stray field in S1 is ~1.0 kOe, whereas in S2 it is ~0.6 kOe, indicating weaker dipolar interaction in S2 compared to S1. The intra-unit stray field of a diatomic unit is very large (~4.0 kOe) with similar values for both the arrays at φ = 0°. The total field inside the two dots of a diatomic unit is identical with a value of about 10 kOe in both S1 and S2 for φ = 0°. However, when the bias field is rotated to φ =

90°, the intra-unit and inter-unit field become 1.5 and 0.9 kOe, respectively, indicating that the interaction is very much reduced in the $\varphi = 90°$ orientation of the applied bias field leading to a weaker collective dynamical behavior, as observed in our experiment.

5.4. Conclusion

In conclusion, we have fabricated a 2D diatomic MC where Py nanodots of two different diameters are placed very close to each other to form the basis structure, which is arranged in the square lattice of two different lattice constants. A BLS study of the two different arrays for the $k \approx 0$ wave vector by varying the bias magnetic field strength and orientation reveal rich spin-wave spectra for these BMCs, which can be tuned by both the bias magnetic strength and orientation. We reproduced the observed spectra by micromagnetic simulations and interpreted the origin of the observed spectra by simulated spin-wave mode profiles. To this end, we simulated the individual nanodots, a diatomic basis unit, as well as the 2D arrays to understand how the modes evolve from the single element to the array via the diatomic unit. A number of quantized, localized, and extended modes are observed in the nanodots. New collective modes also appear in the diatomic unit and the large array, which indicates interaction among the larger and smaller dots within the diatomic unit. Variation of the bias magnetic field orientation further influenced the collective behavior of the modes. The new interacting mode in the diatomic unit and the array has either blue or red shifted for the two different orientations of the bias magnetic field. Further variation of bias magnetic field magnitude did not influence the observed spectra and mode profiles significantly, barring the fact that the most intense peak in the spectra corresponds to different spin-wave modes at different magnetic field values. It shows spatially uniform nature at high field strength. But in low field regime, the most intense peak shows BV-like nature due to the reduction in the internal magnetic field. Variation of lattice constant also did not affect the observed spectra and mode profile significantly apart from a lower-frequency mode, which becomes more prominent in the larger lattice constant and its mode profile becomes more symmetric due to the reduction in the inter-unit interaction field. This work may lead to the study of the detailed spin-wave dispersion phenomenon, with motivation of searching for tunable magnonic band structure and band gap, for understanding the functionality of such diatomic MC as an active element of future magnonic devices.

References

[1] O. Hellwig, A. Berger, T. Thomson, E. Dobisz, Z. Z. Bandic, H. Yang, and D. S. Kercher, Appl. Phys. Lett. **90**, 162516 (2007).
[2] S. Tehrani, E. Chen, M. Durlam, M. D. Herrera, J. M. Slaughter, J. Shi, and G. Kerszykowski, J. Appl. Phys. **85**, 5822 (1999).
[3] A. Haldar, D. Kumar, and A. O. Adeyeye, Nat. Nanotechnol. **11**, 437 (2016).
[4] S. Kaka, M. R. Pufall, W. H. Rippard, T. J. Silva, S. E. Russek, and J. A. Katine, Nature **437**, 389 (2005).
[5] B. Lenk, H. Ulrichs, F. Garbs, and M. Münzenberg, Phys. Rep. **507**, 107 (2011).
[6] M. Krawczyk, and D. Grundler, J. Phys.: Condens. Matter **26**, 123202 (2014).
[7] A. V. Chumak, V. I. Vasyuchka, A. A. Serga, and B. Hillebrands, Nat. Phys. **11**, 453 (2015).
[8] J. W. Klos, D. Kumar, M. Krawczyk, and A. Barman, Sci. Rep. **3**, 2444 (2013).
[9] S. K. Kim, K. S. Lee, and D. S. Han, Appl. Phys. Lett. **95**, 082507 (2009).
[10] N. Kanazawa, T. Goto, K. Sekiguchi, A. B. Granovsky, C. A. Ross, H. Takagi, Y. Nakamura, and M. Inoue, Sci. Rep. **6**, 30268 (2016).
[11] Y. Au, M. Dvornik, O. Dmytriiev, and V. V. Kruglyak, Appl. Phys. Lett. **100**, 172408 (2012).
[12] A. Khitun, E. Nikitov, and K. L. Wang, J. Appl. Phys. **106**, 123909 (2009).
[13] M. P. Kostylev, A. A. Serga, T. Schneider, B. Leven, and B. Hillebrands, Appl. Phys. Lett. **87**, 153501 (2005).
[14] B. Rana, S. Pal, S. Barman, Y. Fukuma, Y. Otani, and A. Barman, Appl. Phys. Exp. **4** 113003, (2011).
[15] V. V. Kruglyak, P. S. Keatley, A. Neudert, R. J. Hicken, J. R. Childress, and J. A. Katine, Phys. Rev. Lett. **104**, 027201 (2010)
[16] S. Saha, S. Barman, Y. Otani, and A. Barman, Nanoscale **7**, 18312 (2015).
[17] J. Ding, and A. O. Adeyeye Adv. Funct. Mater. **23**, 1684 (2012).
[18] R. Zivieri, F. Montoncello, L. Giovannini, F. Nizzoli, S. Tacchi, M. Madami, G. Gubbiotti, G. Carlotti, and A. O. Adeyeye Phys. Rev. B **83**, 054431 (2011).
[19] S. Tacchi, M. Madami, G. Gubbiotti, G. Carlotti, H. Tanigawa, T. Ono, and M. P. Kostylev, Phys. Rev. B **82**, 024401 (2010).
[20] G. Gubbiotti, G. Carlotti, T. Okuno, M. Grimsditch, L. Giovannini, F. Montoncello, and F. Nizzoli, Phys. Rev. B **72**, 184419 (2005).
[21] M. Krawczyk, and H. Puszkarski, Phys. Rev. B **77**, 054437 (2008).
[22] A. Barman, and S. Barman, Phys. Rev. B **79**, 144415 (2009).
[23] P. Chu, D. L. Mills, and R. Arias Phys. Rev. B **73**, 094405 (2006).
[24] P. V. Bondarenko, A. Y. Galkin, B. A. Ivanov, and C. E. Zaspel, Phys. Rev. B **81**, 224415 (2010).
[25] R. Verba, G. Melkov, V. Tiberkevich, and A. Slavin, Phys. Rev. B **85**, 014427 (2012).
[26] V. V. Kruglyak, A. Barman, R. J. Hicken, J. R. Childress, and J. A. Katine Phys. Rev. B **71**, 220409 (2005).
[27] B. Rana, D. Kumar, S. Barman, S. Pal, Y. Fukuma, Y. Otani, and A. Barman, ACS Nano **12**, 9559 (2011).
[28] S. Mondal, S. Choudhury, S. Barman, Y. Otani, and A. Barman, RSC Adv. **6**, 110393 (2016).
[29] B. K. Mahato, B. Rana, D. Kumar, S. Barman, S. Sugimoto, Y. Otani, and A. Barman Appl. Phys. Lett. **105**, 012406 (2014).
[30] S. Saha, R. Mandal, S. Barman, D. Kumar, B. Rana, Y. Fukuma, S. Sugimoto, Y. Otani, and A. Barman, Adv. Funct. Mater. **23**, 2378 (2013).

[31] C. Mathieu, C. Hartmann, M. Bauer, O. Buettner, S. Riedling, B. Roos, S.O. Demokritov, B. Hillebrands, B. Bartenlian, and C. Chappert, A. Müller, B. Hoffmann, and U. Hartmann, Appl. Phys. Lett. **70**, 291 (1997).
[32] S. Tacchi, M. Madami, G. Gubbiotti, G. Carlotti S. Goolaup, A. O. Adeyeye, N. Singh, and M. P. Kostylev, Phys. Rev. B **82**, 184408 (2010).
[33] J. Topp, D. Heitmann, M. P. Kostylev, and D. Grundler, Phys. Rev. Lett. **104**, 207205 (2010).
[34] S. Choudhury, S. Saha, R. Mandal, S. Barman, Y. Otani, and A. Barman, ACS Appl. Mater. Interfaces **8**, 18339 (2016).
[35] G. Gubbiotti, S. Tacchi, M. Madami, G. Carlotti, S. Jain, and A. O. Adeyeye, Appl. Phys. Lett. **100**, 162407 (2010).
[36] A. Haldar, C. Banerjee, P. Laha, and A. Barman, J. Appl. Phys. **115**, 133901 (2014).

Chapter 6

6. Anisotropic Spin-Wave Dispersion in Two-Dimensional $Ni_{80}Fe_{20}$ Diatomic Nanodot Array

6.1. Introduction

The rapid development in the emerging research field of 'magnonics' and 'magnon-spintronics' is connected to the possibility of using spin waves (SWs) as means for low power signal transmission and data processing. Recently, magnetic nanostructures have emerged as a promising candidate in the fields of spin-torque- (ST-) and spin-Hall nano oscillators (SHNO) [1,2] and magnonic crystals (MCs) [3,4], in addition to their conventional usage in magnetic storage, memory and sensor devices. The MCs represent the magnetic counterpart of photonic, phononic and plasmonic crystals offering unprecedented opportunity to design and exploit new generation GHz-frequency logic devices [5], filters [6], phase shifters [7], couplers [8], transistors [9] and highsensitivity magnetic sensors [10]. Magnonic devices offer better prospects for miniaturization as SWs operating at GHz or sub-THz frequencies have micrometric or nanometric wavelength. Knowledge of the nature of SW propagation and magnonic band structure of any MC is essential to any desired application. A range of theoretical and experimental studies have surged during last one decade, which continue to grow at a fast pace on the tailoring of magnonic spectra and band structure in one- [11, 12], pseudo-one [13], two- [14–17], and three-dimensional [18, 19] arrays of magnetic nanostructures. Recently, efficient control over the magnonic band structure in dense arrays of width-modulated Py nanowires have been reported [20]. Initial works on SW quantization and propagation in ferromagnetic nanodot arrays showed neither dispersive modes nor magnonic band gap formation [21,22]. The SW dynamics in those systems were mainly governed by the internal fields of the nanodots and dipolar interactions between the nanodots. Afterwards, a few experimental studies showed the evidence of dispersive nature and propagating character of SW modes in two-dimensional arrays of closely packed nanodots. Considerable anisotropy concerning the dynamical coupling and the existence of maxima and minima in the dispersion curves of the propagating SWs for different bias magnetic field orientations has been observed in some nanodot arrays of square and hexagonal symmetry [23–25]. More recently, Graczyk *et*

al. demonstrated the magnonic band structure and formation of hybridization and Bragg bandgap in a continuous Py film induced by vertical dynamic coupling with an array of Py/Pt nanodots [26]. Newer and more complex structures are nowadays being introduced for better functionalities and tunable properties. These include bicomponent magnonic crystals (BMCs) [27–30] and magnonic quasicrystals [31, 32] which provide more control parameters for tuning the magnonic bands. Nonetheless, the improved device operations necessitate more complex fabrication processes, including multistep lithography and two-photon photolithography. Binary magnonic crystal (BMN) is another type of complex magnonic crystal, which can be fabricated using simpler lithographic technique by placing two different structures of the same material next to each other forming a complex base. Hitherto, very few works have been reported on such structures. BMN in the form of anti-ring or annular antidot lattice, showed some new modes due to the interaction between the antidot and the central dot regions [33, 34]. Another new structure has been reported where two antidot sublattices of alternating diameters create non uniform demagnetizing field which significantly alters the field dependent SW mode transformation [35]. Recently, we have introduced a new type of BMN in the form of a diatomic nanodot lattice where two nanodots of different sizes are placed in close proximity to each other. We have reported the bias-fielddependent resonant modes and their spatial profiles at $q \approx 0$ wave vector and observed the effect of the double-dot unit cell in its field dependent SW spectra [36]. In the present study, we have investigated both experimentally and numerically how the complex double-dot unit cell engineers the SW dispersion with wave vector in two orthogonal orientations of the bias magnetic field. The calculated iso-frequency contours explain the origin of anisotropic propagation of some of the eigenmodes. Achievement of band tunability in such complex structure by simply changing the bias field orientation is useful for practical implementation.

6.2. Methods

A 30-nm-thick circular shaped $Ni_{80}Fe_{20}$ (Py) diatomic nanodot array of 500 μm x 500 μm area, characterized by a complex double-dot unit cell arranged on a rectangular lattice, has been fabricated on self-oxidized Si [1 0 0] substrate by means of electron beam lithography (EBL) and electron-beam evaporation (EBE). The deposition chamber was maintained at a base pressure of 2×10^{-8} Torr during the evaporation and the lithography was performed for a dose time of 1.0 μs at a beam current of 500 pA. The diameter of the larger and smaller dot of one unit is about 700 nm and 280 nm, respectively. The separation between larger and smaller dot

(intra-unit) is about 35 nm, while the inter-unit separation is about 170 nm. The corresponding lattice constants are a = 1185 nm and b = 850 nm, as shown in the inset of Fig. 6.1 (b). The diameter of the dots and the edge-to-edge separation between the dots show a maximum of ± 5% and ± 10% deviation, respectively.

Dispersion characteristics of thermal SWs in this Py diatomic dot array was recorded by Brillouin light scattering (BLS) technique. Due to the interaction between incident photons and magnons (quanta of SWs), light is scattered inelastically in BLS technique. The BLS spectra were measured and analyzed in the 180° backscattered geometry using a monochromatic solid state laser light (wavelength λ = 532 nm, power = 130 mW, spot size ≈ 40 μm) and a Sandercock-type (3 + 3) pass tandem Fabry-Perot interferometer (JRS Scientific Instruments). As a consequence of the conservation of momentum during the inelastic scattering, the in-plane transferred wave vector q depends on the incidence angle of light θ according to the equation: $q = (4\pi/\lambda)\sin\theta$. The incident and scattered beams were maintained in a cross polarized geometry during experiment to minimize the phonon contribution to the scattered light. The sample was subjected to an in-plane magnetic field, H = 1.0 kOe during the measurements, ensuring magnetic saturation of the sample, as can be inferred from magnetic hysteresis loop [36]. The BLS spectra were measured in the Damon-Eshbach geometry where the bias magnetic field and wave vector are mutually perpendicular, both being in the sample plane. The SW dispersion measurements have been done for two different values of φ, namely φ = 0° and 90°, as shown in Fig. 6.1 (a). We have recorded the spectra for up to two Brillouin Zones (BZs), i.e. q = 0.73 × 10^7 rad/m for φ = 0° and q = 0.53 × 10^7 rad/m for φ = 90°.

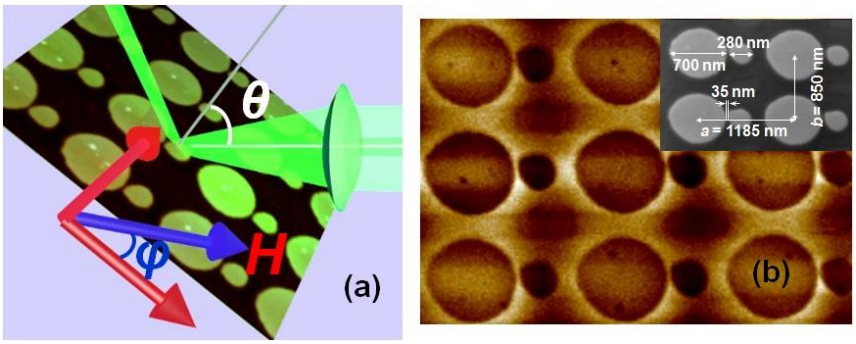

Fig. 6.1: (a) Schematic of the BLS measurement in backscattered geometry. The incident and scattered beams and the angle θ between them are shown. The in-plane orientation (φ) of the applied bias magnetic field H is also shown. (b) MFM image of the array. The inset shows the SEM image of the sample with the parameters.

We have calculated and interpreted the SW excitation spectra and dispersion of the diatomic dot lattice by plane wave method (PWM) [18, 27]. In this method the Landau-Lifshitz (LL) equation, i.e. the equation of motion of the magnetization vector $\boldsymbol{M}$ ($\boldsymbol{r}$,t) in space and time is solved under an effective magnetic field $\boldsymbol{H}_{eff}$:

$$\frac{\partial \boldsymbol{M}(\boldsymbol{r},t)}{\partial t} = -\gamma\mu_0 \boldsymbol{M}(\boldsymbol{r},t) \times \boldsymbol{H}_{\text{eff}}(\boldsymbol{r},t) \quad (6.1)$$

In general $\boldsymbol{H}_{\text{eff}}$ is the sum of several components and can be written as:

$\boldsymbol{H}_{eff} = \boldsymbol{H} + \boldsymbol{H}_{ex} + \boldsymbol{H}_{MS}$, where $\boldsymbol{H}$ is the uniform applied magnetic field, $H_{ex}(r,t) = (\nabla . l_{\text{ex}}^2(r)\nabla)m(r,t)$ is the exchange field with exchange length $l_{ex} = \sqrt{2A/\mu_0 M_s^2}$, $\boldsymbol{H}_{MS}$ is the magnetostatic field and A is the exchange stiffness constant. The exchange field and the magnetostatic field are space and time dependent. In the linear approximation, the component of the magnetization vector parallel to the static magnetic field is constant in time, and its magnitude is much greater than that of the perpendicular components. So, $|\boldsymbol{m}(\boldsymbol{r},t)| \ll M_{\text{s}}(\boldsymbol{r})$, where $\boldsymbol{M}(\boldsymbol{r},t) = M_S(\boldsymbol{r})\hat{z} + \boldsymbol{m}(\boldsymbol{r},t)$. In our calculations, we have assumed the static magnetic field to be oriented always along the z axis. Subsequently, all the periodic functions (both in time and space), including the static and dynamic parts of the magnetic fields and magnetization components, are mapped onto the Fourier space using Bloch's theorem [18]. Thus, the LL equation is converted to an algebraic eigenvalue problem, which is solved by standard numerical routines to find out the eigenvalues (SW frequencies) and eigenvectors (amplitude of the dynamical component of the magnetization vector) [18, 27].

The magnetostatic field is divided into a static ($\boldsymbol{H}_{MS}(\boldsymbol{r})$) and dynamic ($\boldsymbol{h}_{MS}(\boldsymbol{r},t)$) component. The dynamic component of the magnetization vector is dependent on both space and time and has the form: $\boldsymbol{m}(\boldsymbol{r},t) = \boldsymbol{m}(\boldsymbol{r})e^{i2\pi\nu t}$. The time dependence of the dynamic magnetostatic field has the same form as that of the dynamic component of the magnetization vector, i.e. $\boldsymbol{h}_{\text{MS}}(\boldsymbol{r},t) = \boldsymbol{h}_{\text{MS}}(\boldsymbol{r})\, e^{i2\pi\nu t}$. In the reciprocal space to express the dynamic components of the magnetization and magnetostatic field we use Bloch's theorem, which asserts that a solution of a differential equation with periodic coefficients can be represented as the product of a plane wave with the wave vector $\boldsymbol{q}$ = (q_y, q_z) from the first BZ and a periodic function, which can be expanded into Fourier series:

$$m(r) = \sum_G m_q(G) e^{i(q+G).r} \quad (6.2)$$

Where $\boldsymbol{G}$ = (G_y, G_z) denotes a reciprocal lattice vector of the periodic structure. The saturation magnetization (M_s) and the squared exchange length l_{ex}^2 are periodic functions of position in MC and hence they can also be mapped onto the reciprocal space using the Fourier transformation formulas:

$$M_s(r) = \sum_G M_s(G) e^{iG.r}$$
$$l_{ex}^2(r) = \sum_G l_{ex}^2(G) e^{iG.r} \quad (6.3)$$

Where the Fourier coefficients $M_s(G)$ and $l_{ex}^2(G)$ are determined analytically. The material parameters used were saturation magnetization M_s = 800 emu/cm^3, anisotropy field H_k = 0, Lande g-factor g = 2 and exchange stiffness constant $A = 1.3 \times 10^{-6}$ erg/cm. The value of A was taken from the literature [37], whereas the other parameters were obtained from ref. 36. To avoid any nonphysical frequency values, small but finite values of M_s and A are used for the air gap in between the magnetic materials. We have taken 450 plane waves to ensure a satisfactory convergence of the eigenvalue problem. The square of the modulus of the fundamental harmonics of magnetization determines the intensities calculated from PWM, which is compared with the experimentally measured peak intensities by BLS.

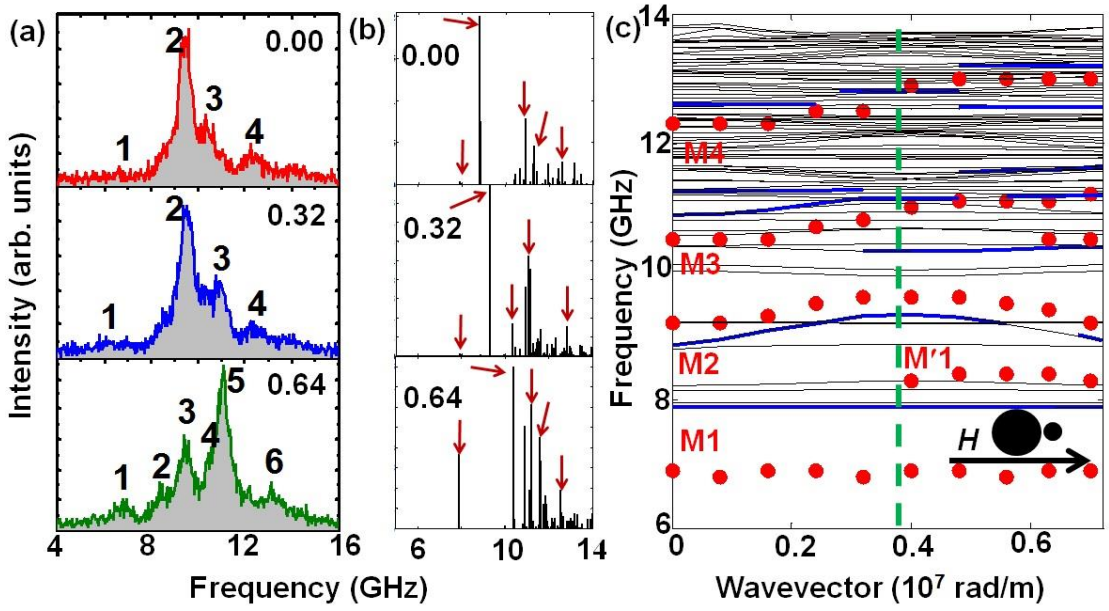

Fig. 6.2: (a) The Stokes side of BLS spectra taken at different values of the in-plane transferred wave vector q (denoted in units of 10^7 rad/m) for $\varphi = 0°$. The spectra are horizontally flipped for convenience. Mode numbers are mentioned for corresponding spectra. (b) Relative values of BLS intensities calculated by PWM for different values of q as shown here. (c) Magnonic band structure for φ = 0°. Thin lines are PWM results. Bold lines emphasize intense excitations as predicted by PWM. Solid circles represent the peaks in the BLS spectra. The dashed vertical line is the boundary of first BZ.

To provide an illustrative demonstration of how the SW propagation occurs in the diatomic nanodot array, we have simulated the SW response to local microwave excitation for two different orientations of the in-plane bias magnetic field using OOMMF software [38]. The micromagnetic simulations have been performed on a 3×3 dots matrix after application of a periodic boundary condition. During the simulations the sample is divided into cuboidal cells

of dimensions $4 \times 4 \times 30$ nm^3 where the lateral cell size is below the exchange length of Py (≈ 5.2 nm) to include the exchange interaction effect. The material parameters used in micromagnetic simulations are same as those used in PWM calculation. Initially the static magnetic configuration is obtained by applying a large enough magnetic field to saturate the sample magnetization followed by the reduction of the magnetic field to the bias field value. Then the system was allowed to reach the equilibrium. After we obtain the static magnetic configuration, we apply a time-varying field of "*sinc*" profile (frequency cut-off of 30 GHz) to launch SWs at the centre of the said array. The excitation is applied over a square region of 50 nm width.

6.3. Results and Discussion

Fig. 6.1 (a) schematically depicts the experimental BLS set up in conventional backscattered geometry. To study the magnonic band structure of 2D MCs, we need to change the SW wave vector, as well as its direction on the sample surface. The angle θ is varied by rotating the sample in the vertical plane, thus ensuring the variation of the magnon wave vector q and measurement of SW dispersion along the principal directions of the BZs of 2D MCs. On the other hand, by varying φ, one can study the effect of changing the angle between the applied in-plane magnetic field direction (assumed to be along the average sample magnetization) and the reference axis of the sample. In our experiment, we have studied the wave vector dispersion of the SWs in two different orientations of the in-plane bias magnetic field by varying θ, while fixing φ at 0° or 90°. Fig. 6.1 (b) shows the magnetic force microscopy (MFM) image of the sample measured at remanence. A clear magnetic contrast is observed in the larger dot showing prominent edge demagnetized regions, but no such contrast is observed in the smaller dot.

In Fig. 6.2 (a), we present few representative BLS spectra at varying wave vector for $\varphi = 0°$ configuration (H = 1 kOe) showing the evolution of the SW modes with wave vector. The calculated SW spectra for the corresponding wave vectors and the full SW dispersion for this sample at the same bias field configuration are shown in Fig. 6.2 (b) and (c), respectively. In the dispersion presented in Fig. 6.2 (c), the black lines represent the magnonic bands calculated from PWM, wherein the blue bold lines indicate the magnonic bands with large PWM intensity. The experimentally measured BLS intensities are superimposed on the calculated dispersion by red solid circles. The boundary of the first BZ is indicated by the green dotted vertical line. For $\varphi = 0°$, the experimentally obtained BLS spectra are characterized by four well defined modes as illustrated in Fig. 6.2 (a). The experimental dispersion within the first BZ show four distinct

modes, which are qualitatively reproduced by the PWM calculation. However, the frequency of mode 1 in the experiment does not agree well with theory. At the boundary of the first BZ, another mode M'1 becomes visible in the experiment, whose frequency lies close to the lowest frequency mode with significant intensity in PWM calculation. In addition, another mode gains significant intensity in PWM calculation at the boundary of the first BZ between M2 and M3, which is reproduced in the experiment only near the boundary of the second BZ. Other modes are in good agreement with theory for the whole range of wave vectors. The first mode (M1) is dispersionless, while M2 shows a significant dispersion with mirror symmetry with respect to the first BZ boundary presumably due to zone-folding. On the contrary, M3 and M4 show rather asymmetric dispersion with respect to the first BZ boundary. We will attempt to understand these behaviors by analyzing the SW mode profiles later in this article.

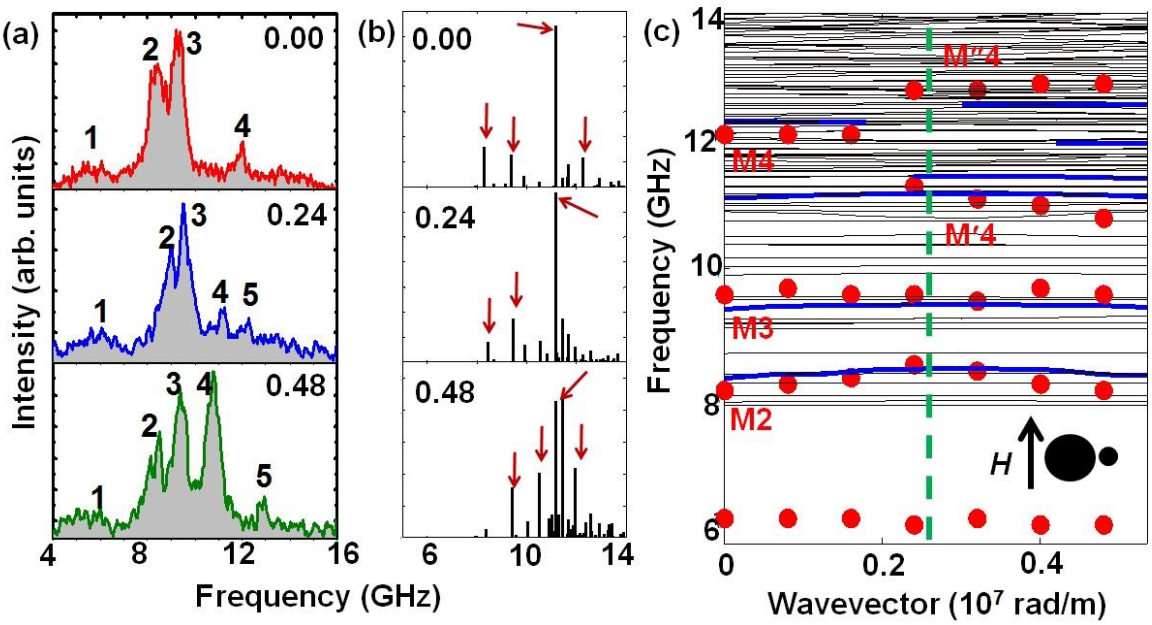

Fig. 6.3: (a) The Stokes side of BLS spectra taken at different values of the in-plane transferred wave vector q (denoted in units of 10^7 rad/m) for φ = 90°. The spectra are horizontally flipped for convenience. Mode numbers are mentioned for corresponding spectra. (b) Relative values of BLS intensities calculated by PWM for different values of q as shown here. (c) Magnonic band structure for φ = 90°. Thin lines are PWM results. Bold lines emphasize intense excitations as predicted by PWM. Solid circles represent the peaks in the BLS spectra. The dashed vertical line is the boundary of first BZ.

The experimental and theoretical SW spectra along with the SW dispersion for up to two BZs in φ = 90° orientation of the applied magnetic field are shown in Figs. 6.3 (a)–(c). Experimentally four modes are observed in this orientation. However, the lowest frequency mode (M1) is not theoretically obtained in this orientation. The mode M2 again shows a dispersive nature with mirror symmetry with respect to the boundary of the first BZ but its curvature reduces presumably due to the reduced group velocity of this SW mode in this orientation. The mode M3 is almost dispersionless both in theory and calculation. M4 is also dispersionless within the first BZ both in theory and experiment, while another high intensity mode was visible in PWM calculation between M3 and M4 within the first BZ, which was not resolved experimentally. Interestingly M4 in experiment splits at the boundary of the 1st BZ into two modes (M′4 and M″4) in the second BZ. These two modes are now well reproduced in PWM calculation. Two additional modes gain significant intensity in PWM calculation between M′4 and M″4, which are not resolved in the experiment.

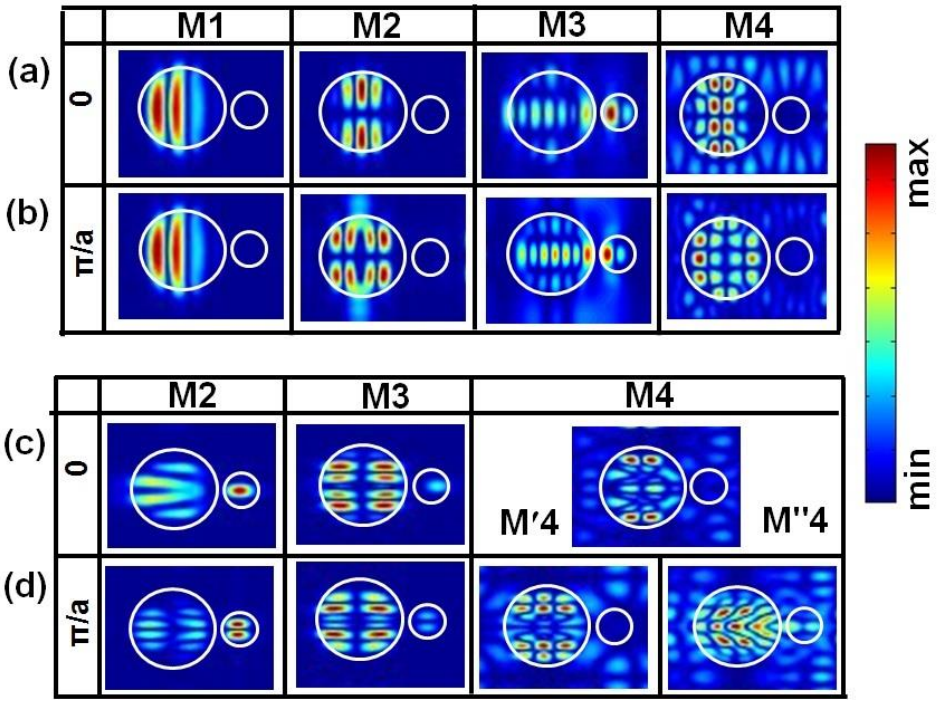

Fig. 6.4: Spatial profiles of the selected modes for (a) q = 0, (b) q = π/a at φ = 0° and (c) q = 0, (d) q = π/a at φ = 90°.

Deeper insight into the SW dynamics is obtained by calculating the SW mode profiles using the PWM, which correspond to the modulus of amplitude of the x-component of the dynamic magnetization, of the relevant experimental modes. Fig. 6.4 (a) and (b) depict the spatial profiles of the SW modes at q = 0 (centre of BZ) and q = π/a (boundary of the 1st BZ) for φ = 0° and

Fig. 6.4 (c) and (d) depict the same for $\varphi = 90°$. For $\varphi = 0°$, the calculated mode profile of M1 at $q = 0$ shows a backward volume (BV) magnetostatic SW mode with $m = 3$ with the power distributed over the larger dots in the array in slightly asymmetric manner within each dot. Previously, it was observed that the frequency of M1 is more accurately reproduced in micromagnetic simulations only after incorporation of the edge deformation [36], which could not be done in the PWM calculation. Hence, precise agreements between the experimental and theoretical mode frequencies are not obtained for this mode. We do not observe any substantial changes in the spatial profiles of M1 at $q = \pi/a$. The mode M2 at $q = 0$ again shows a mixed (n)- backward volume and (m)-Damon Eshbach (BV-DE) character in the larger dot with (m, n) as (5, 2). At $q = \pi/a$, this mode transforms to (4, 2). For M3, the mode profile in the larger dot for both $q = 0$ and π/a have mixed BV-DE character with mode numbers (7, 3) but the overall power distribution on different lobes changes. On the other hand, in the smaller dot the mode shows simple BV character with $m = 2$ at both $q = 0$ and π/a. For mode M4, the BV-DE mode transforms from (6, 4) to (4, 5) as q changes from 0 to π/a. For $\varphi = 90°$, the magnetic field is directed perpendicular to the diatomic unit and the edge effects become negligible compared to the former orientation, $\varphi = 0°$. Hence, the lowest frequency mode M1 is not obtained in the simulation. For M2, we observe BV-like mode with $m = 4$ and 1, in the larger and smaller dot, respectively at $q = 0$. Here, power is equally distributed in both dots. However, at $q = \pi/a$, the mode transforms to BV-DE nature in the larger dot with mode numbers (6, 2) and purely BV nature in the smaller dot with $m = 2$. In this case the power is concentrated primarily in the smaller dot. For M3, at $q = 0$, the mode shows a BV-DE character with mode numbers (7, 2) in the larger dots and a BV-like character with $m = 1$ in the smaller dot. It transforms to BV-DE mode with (6, 2) in the larger dot and BV-like mode with $m = 2$ in the smaller dot at $q = \pi/a$. In M3, the power is distributed primarily in the larger dot at both wave vectors. The mode M4 at $q = 0$, shows a mixed BV-DE nature with $m = 9$, $n = 4$. The power is mainly concentrated in the larger dot with comparatively more power at the edges compared to the central regions of the dot. This mode splits into two modes at the boundary of the 1st BZ and the power is again concentrated in the larger dot for both the modes. The lower frequency band M′4 shows mixed BV-DE characteristics ($m = 8$ and $n = 3$). The higher frequency branch M″4 exhibits more complex nature with mixed BV-DE characteristics ($m = 7$, $n = 5$). In the DE geometry, the spatial distribution shows an asymmetric nature presumably due to an interaction with the smaller dot; the latter shows weak power with mode numbers, $m = 1$, $n = 2$.

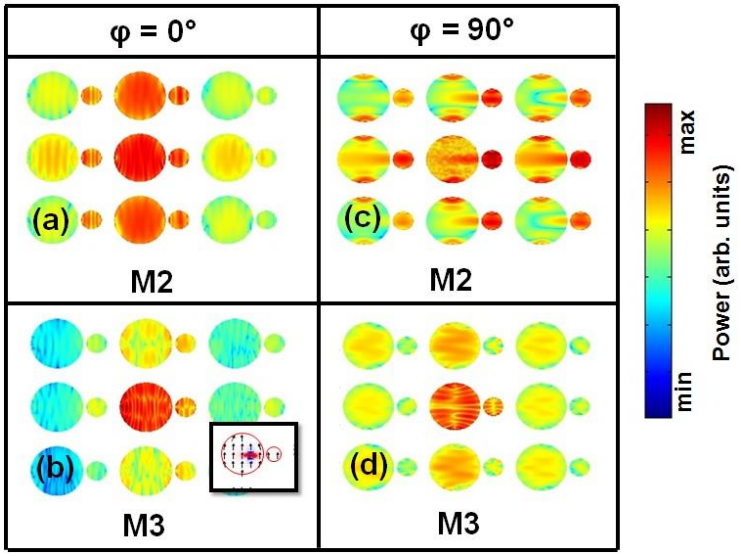

Fig. 6.5: Power profiles of different SW bands, after application of a local excitation at the central region of the array: (a) M2 at $\varphi = 0°$, (b) M3 at $\varphi = 0°$, (c) M2 at $\varphi = 90°$, (d) M3 at $\varphi = 90°$.

The usual band diagram representation and the corresponding SW mode profile are not sufficient to provide a deep insight into the propagating nature of the system under investigation. To this end, we have investigated the propagation of the SWs under local excitation for two mutually perpendicular orientations of the applied bias magnetic field. Since the lowest frequency mode, which is strongly affected by the rough edges of the dots, is not well reproduced in the PWM calculations and the highest frequency modes exhibit a complex nature, we mainly focus on the uniform mode (M2 for $\varphi = 0°$, M3 for $\varphi = 90°$) and the interacting mode (M3 for $\varphi = 0°$, M2 for $\varphi = 90°$) for this study. The experimental and simulated angular dispersion (Appendix II) of the frequency of the uniform mode and the interacting mode shows a nearly constant frequency of the uniform mode with negligible angular dispersion but a sudden transition in the frequency of the interacting mode for $\varphi > 30°$. Consequently, the frequency of the interacting mode is greater than the uniform mode for $\varphi < 30°$ and less than the uniform mode for $\varphi > 30°$. Also, the weaker coupling between the elements flattens the SW dispersion with the wave vector for M3. Fig. 6.5 shows exemplary simulation results of the SW propagation of the uniform and the interacting modes under local excitation for $\varphi = 0°$ and 90°. For this the SW response to microwave excitation, applied at the centre of a 3 × 3 array using a time-varying field of 'sinc' profile, has been simulated (Fig. 6.5 (a) and (b) for $\varphi = 0°$ and 6.5 (c) and (d) for $\varphi = 90°$). Fig. 6.5 (a) reveals that M2 (frequency ≈ 9.0 GHz) propagates almost uniaxially in the DE geometry. The mode M3 (frequency ≈ 10.5 GHz) exhibits a weak but similar propagation nature in the DE geometry (Fig. 6.5 (b)). This affirms the anisotropic

propagation of SWs (in the DE geometry) through the diatomic dot array for φ = 0°. On the contrary, for φ = 90° the dispersion of M2 (frequency ≈ 8.5 GHz) is isotropic throughout the whole lattice (Fig. 6.5 (c)). However, due to its flatter dispersion the energy transfer is less compared to the φ = 0° case. For M3 (frequency ≈ 9.0 GHz) negligible energy gets transferred due to its almost dispersionless behavior.

To obtain further insight into the origin of the anisotropy of SW propagation for different bias-field orientations, we have further computed the iso-frequency contours for the uniform mode and the interacting mode. The iso-frequency contours, i.e. the curves of the constant frequency in the wave vector space are wave counterparts of the Fermi surfaces [39]. Important indications regarding the preferential directions of SW propagation are provided by the group velocity, i.e. normal direction to the iso-frequency contour, which defines the direction of energy flow within the structure. At a given frequency, the lattice under investigation may behave in a dispersive fashion along certain directions, while being non-dispersive in others. A single iso-frequency contour is obtained by fixing the frequency at a fixed value and then scanning q_x from $-\pi$/a to $+\pi$/a and q_y from $-\pi$/b to $+\pi$/b. The dispersion relations of the diatomic dot lattice in the form of iso-frequency contours for the M2 and M3 bands in φ = 0° configuration are presented in Fig. 6.6 (a) and (b). The three-dimensional surface plot of the said magnonic bands, depicting the steepness of dispersion has also been shown in Fig. 6.6 (c) and (d).

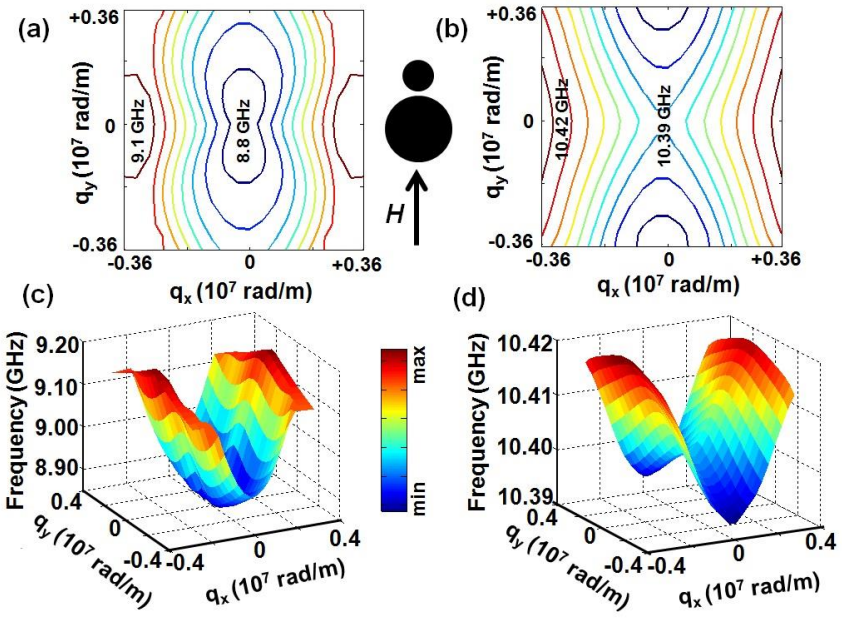

Fig. 6.6: Iso-frequency contours for (a) M2 and (b) M3 bands and the three-dimensional surface plot of (c) M2 and (d) M3 bands in φ = 0° configuration.

The dispersion contours of constant frequency corresponding to both M2 and M3 magnonic bands exhibit anisotropic behavior in φ = 0° configuration. In M2, a central minima surrounded by hyperbolic contours are observed, whereas in M3 a 'saddle point' is observed at the centre of the dispersion surrounded again by hyperbolic contours. The surface plots of these two bands, as shown in Fig. 6.6 (c) and (d), confirm that M2 undergoes a steeper dispersion (from 8.8 GHz to 9.1 GHz) as opposed to the mode M3 (from 10.39 GHz to 10.42 GHz). On the other hand, Fig. 6.7 depicts the iso-frequency contours and surface plots for M2 and M3 bands in φ = 90° configuration. In this case, the dispersion of M2 band is found to be almost isotropic in nature. But the steepness of dispersion is lowered as opposed to φ = 0° orientation, as observed from the surface plot depicted in Fig. 6.7 (c) (from 8.34 GHz to 8.44 GHz). On the other hand, the iso-frequency contour and the surface plots of M3 band for φ = 90°, as shown in Fig. 6.7 (b) and (d), reveals a very shallow dispersion in the magnonic band. Hence, from the iso-frequency contours, we conclude that SW propagation is anisotropic for φ = 0° but becomes nearly isotropic for φ = 90°.

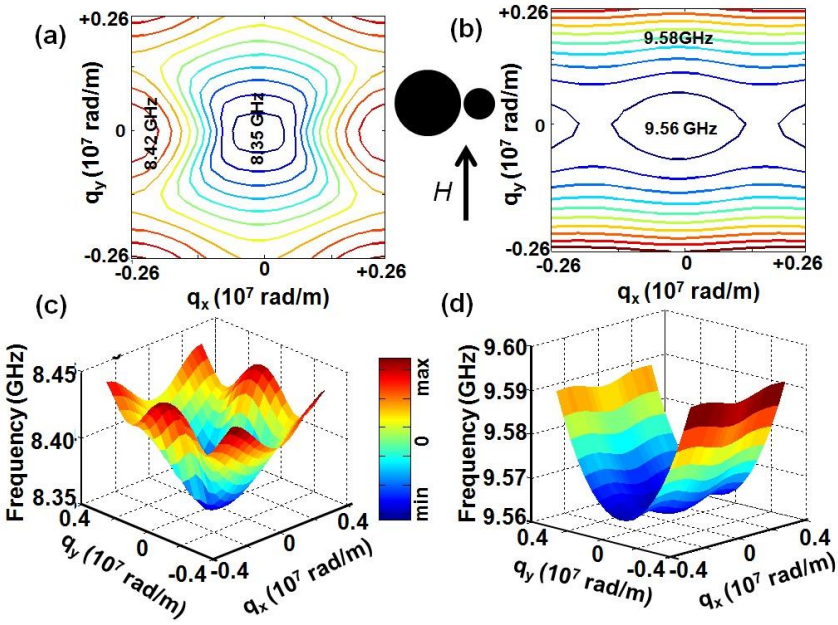

Fig. 6.7: Iso-frequency contours for the (a) M2 and (b) M3 bands and the three-dimensional surface plot of the (c) M2 and (d) M3 bands in φ = 90° configuration.

6.4. Conclusion

In conclusion, we have performed a combined experimental and numerical study of magnonic band structure and iso-frequency contours in magnetostatically coupled diatomic nanodot arrays with a complex double-dot unit cell. Frequency evolution of several spin eigenmodes as a function of wave vector in two different orientations of the applied in-plane magnetic field (φ = 0° and 90°) has been studied. A steeper dispersion of the uniform mode compared to the interacting mode, whose frequency is blue shifted with respect to the uniform mode, is found in φ = 0° configuration. Due to weaker interaction among the dots, the dispersion weakens and the nature is reversed for φ = 90°. Here, the red shifted interactive mode is found to be more dispersive than the uniform mode. A detailed micromagnetic investigation using local excitation and the calculated iso-frequency contours from plane-wave method further reveal the anisotropic properties of the SW eigenmodes and its origin. It has been observed that the SW propagation is anisotropic for φ = 0° but becomes nearly isotropic for φ = 90°. The dynamic dipolar coupling between the larger and smaller dots can play a crucial role by affecting the SW dispersion with wave vector for different orientations of the in-plane magnetic field. This work may lead towards the design and understanding of new type of reprogrammable binary magnonic crystal.

References

[1] S. Kaka, M. R. Pufall, W. H. Rippard, T. J. Silva, S. E. Russek, and J. A. Katine, Nature **437**, 389 (2005).
[2] L. Liu, C. F. Pai, D. C. Ralph, and R. A. Buhrman, Phys. Rev. Lett. **109**, 186602 (2012).
[3] Y. V. Gulyaev, S. A. Nikitov, L. V. Zhivotovskii, A. A. Klimov, P. Tailhades, L. Presmanes, C. Bonningue, C. S. Tsai, S. L. Vysotskii, Y. A. Filimonov, J. Expt. Th. Phys. Lett. **77**, 567 (2003).
[4] B. Lenk, H. Ulrichs, F. Garbs, and M. Munzenberg, Phys. Rep. **507**, 107 (2011).
[5] D. A. Allwood, G. Xiong, C. C. Faulkner, D. Atkinson, D. Petit and R. P. Cowburn, Science **309**, 1688 (2005).
[6] S. K. Kim, S. K. Lee, and D. S. Han, Appl. Phys. Lett. **95**, 082507 (2009).
[7] S. Louis, I. Lisenkov, S. Nikitov, V. Tyberkevych, and A. Slavin, AIP Adv. **6**, 065103 (2016).
[8] Q. Wang, P. Pirro, R. Verba, A. Slavin, B. Hillebrands, and A. V. Chumak, Sci. Adv. **4**, e1701517 (2018).
[9] A. V. Chumak, A. A. Serga and B. Hillebrands, Nat. Commun. **5**, 4700 (2014).
[10] M. Inoue, A. Baryshev, H.Takagi, P. B. Lim, K. Hatafuku, J. Noda, and K. Togo, Appl. Phys. Lett. **98**, 132511 (2011).
[11] Z. K. Wang, V. L. Zhang, H. S. Lim, S. C. Ng, M. H. Kuok, S. Jain, and A. O. Adeyeye, ACS Nano **4**, 643 (2010).
[12] S. Saha, S. Barman, Y. Otani, and A. Barman, Nanoscale **7**, 18312 (2015).
[13] C. Banerjee, S. Choudhury, J. Sinha, and A. Barman, Phys. Rev. Appl. 8, 014036 (2017).
[14] V. V. Kruglyak, A. Barman, R. J. Hicken, J. R. Childress and J. A. Katine, Phys. Rev. B **71**, 220409 (2005).
[15] S. Neusser, B. Botters, and D. Grundler, Phys. Rev. B **78**, 054406 (2008).
[16] A. Barman, and A. Haldar, Solid State Physics **65**, 1 (2014).
[17] S. Tacchi, B. Botters, M. Madami, J.W. Kłos, M. L. Sokolovskyy, M. Krawczyk, G. Gubbiotti, G. Carlotti, A. O. Adeyeye, S. Neusser, and D. Grundler, Phys. Rev. B **86**, 014417 (2012).
[18] M. Krawczyk and H. Puszkarski, Phys. Rev. B **77**, 054437 (2008).
[19] S. Sahoo, S. Mondal, G. Williams, A. May, S. Ladak, and A. Barman, Nanoscale **10**, 9981 (2018).
[20] G. Gubbiotti, L. L. Xiong, F. Montoncello, L. Giovannini, and A. O. Adeyeye, J. Appl. Phys. **124**, 083903 (2018).
[21] G. Gubbiotti, G. Carlotti, T. Okuno, T. Shinjo, F. Nizzoli and R. Zivieri, Phys. Rev. B **68**, 184409 (2003).
[22] G. Gubbiotti, G. Carlotti, T. Okuno, M. Grimsditch, L. Giovannini, F. Montoncello, and F. Nizzoli, Phys. Rev. B **72**, 184419 (2005).
[23] S. Tacchi, M. Madami, G. Gubbiotti, G. Carlotti, H. Tanigawa, T. Ono, and M. P. Kostylev, Phys. Rev. B **82**, 024401 (2010).
[24] S. Tacchi, F. Montoncello, M. Madami, G. Gubbiotti, G. Carlotti, L. Giovannini, R. Zivieri, F. Nizzoli, S. Jain, A. O. Adeyeye, and N. Singh, Phys. Rev. Lett. **107**, 127204 (2011).
[25] F. Montoncello, S. Tacchi, L. Giovannini, M. Madami, G. Gubbiotti, G. Carlotti, E. Sirotkin, E. Ahmad, F. Y. Ogrin, and V. V. Kruglyak, Appl. Phys. Lett. **102**, 202411 (2013).
[26] P. Graczyk, M. Krawczyk, S. Dhuey, W. G. Yang, H. Schmidt, and G. Gubbiotti, Phys. Rev. B **98**, 174420 (2018).
[27] M Krawczyk, S Mamica, M Mruczkiewicz, J W Klos, S Tacchi, M Madami, G Gubbiotti, G Duerr and D Grundler, J. Phys. D: Appl. Phys. **46**, 495003 (2013).

[28] G. Gubbiotti, S. Tacchi, M. Madami, G. Carlotti, Z. Yang, J. Ding, A. O. Adeyeye and M. Kostylev, Phys. Rev. B **93**, 184411 (2016).
[29] S. Saha, S. Barman, J. Ding, A. O. Adeyeye, and A. Barman, Appl. Phys. Lett. **102**, 242409 (2013).
[30] S. Choudhury, S. Saha, R. Mandal, S. Barman, Y. Otani, and A. Barman, ACS Appl. Mater. Interf. **8**, 18339 (2016).
[31] V. S. Bhat and D. Grundler, Phys. Rev. B **98**, 174408 (2018).
[32] S. Choudhury, S. Barman, Y. Otani, and A. Barman, ACS Nano **11**, 8894 (2017).
[33] N. Porwal, S. Mondal, S. Choudhury, A. De, J. Sinha, A. Barman, and P. K. Datta, J. Phys. D: Appl. Phys. **51**, 055004 (2018).
[34] J. Ding, N. Singh, M. Kostylev, and A. O. Adeyeye, Phys. Rev. B **88**, 014301 (2013).
[35] D. Tripathy, P. Vavassori, J. M. Porro, A. O. Adeyeye, and N. Singh, Appl. Phys. Lett. **97**, 042512 (2010).
[36] A. De, S. Mondal, C. Banerjee, A. K Chaurasiya, R. Mandal, Y. Otani, R. K Mitra, and A Barman, J. Phys. D: Appl. Phys. **50**, 385002 (2017).
[37] K. H. J. Buschow, Handbook of Magnetic Materials 18 (Amsterdam: Elsevier), 168 (2009).
[38] M. Donahue and D. G. Porter 1999 OOMMF User's Guide Version 1.0 Interagency Report NISTIR 6376 (Gaithersburg, MD: National Institute of Standard and Technology) (http://math.nist.gov/oommf).
[39] D. Kumar, J. W. Kłos, M. Krawczyk, and A. Barman, J. Appl. Phys. **115**, 043917 (2014).

Chapter 7

7. Field-Controlled Ultrafast Magnetization Dynamics in Two-Dimensional Nanoscale Ferromagnetic Antidot Arrays

7.1. Introduction

Recent advances in nanofabrication techniques have resulted in artificially patterned magnetic metamaterials, known as magnonic crystals (MCs), which have great potential for technological applications and fundamental research [1,2]. Investigation and tailoring of the magnetization dynamics in ferromagnetic nanodots [3,4], nanowires [5] and antidots [6-8] have fuelled considerable research on reconfigurable MCs, which act as a media for standing and propagating spin waves (SWs) in the GHz frequency regime. Ferromagnetic antidot lattices (magnetic thin films with periodic non-magnetic inclusions or embedded holes) have emerged as one of the strongest candidates for reconfigurable, effective media for SW propagation due to the larger propagation velocity (steeper dispersion) than nanodot lattices. They find potential applications in magneto-photonic crystals [9], ultrahigh density data storage media [10], frequency-based magnetic nanoparticle detectors [11], waveguides for SWs [12,13], spin-wave filters [14], spin-logic [15] and reprogrammable magnonic devices [16]. The edges of the antidots lead to quantization of SW modes due to lateral confinement as well as the generation of a periodically modulated internal magnetic field due to the demagnetization effect. A number of parameters can be varied to tune the magnonic spectra and magnetization dynamics in ferromagnetic antidot lattices. Several studies have been focused on the engineering of the coercive field, magnetoresistance and anisotropy properties on domain formation and the magnetization reversal mechanism with the change of shape, size and density of antidots [17, 18]. Extensive research on the dynamics of standing and propagating SWs in antidot lattices has shown pattern induced splitting [19], confinement, localization and propagation of SWs, depending upon the lattice and antidot geometry, base material and strength and orientation of the bias field [6-8,19-26]. Intrinsic configurational magnetic anisotropy arising due to the internal field variation can be tuned effectively by varying the antidot lattice symmetry [21,24]. The shape of the antidots is found to control the SW mode structures as well as the anisotropy

in the frequency spectra [25]. Quantized SW modes have been found to be transformed to propagating ones and vice versa in rhombic antidot lattices with the variation of the in-plane orientation of the bias magnetic field [26]. A particular study showed the hysteresis and anisotropy properties of $Ni_{80}Fe_{20}$ (Py) antidot lattices with hexagonal symmetry by the influence of the hole size, lattice packing fraction and scale factor via micromagnetic numerical approach [27]. Bi-component or filled antidot lattices can tune the SW properties and magnonic band structure more efficiently due to the strong inter element exchange and dipolar coupling [28, 29]. A remarkable difference in magnetic anisotropies and magnetization reversal mechanisms has been observed in systematically engineered square and binary antidot lattices [30]. Hexagonally arranged antidot lattices are interesting because they offer the highest packing density features among all Bravais and non-Bravais lattices. In contrast to other lattice symmetries, the hexagonal lattice structure exhibits six-fold anisotropy with an easy axis that alternates at every 60° and it does not obey the nearest-neighbour rule as the easy axes are oriented along the edges of the hexagonal unit cell [26, 31, 32]. All of those studies were performed on antidots of circular shape, and very rarely, antidot lattices with triangular-shaped holes, which may suffer from edge effects due to the sharp triangular edges of the holes, have been explored [25]. Unlike the circular or square-shaped antidots, the demagnetized regions around the sharp edges of the triangular-shaped antidots are asymmetric. These may lead to interesting properties of SW quantization in the regions between the antidots. Here, we have focused on the detailed and systematic investigation of the magnetization dynamics in two-dimensional Py antidot lattices where nanostructured triangular holes are arranged in a hexagonal lattice using an all-optical time-resolved magneto-optical Kerr microscope. We have investigated the variation in the nature of the extended and quantized SW modes in such systems by changing the strength and orientation of the in-plane bias-magnetic field and the lattice constant of the array. Micromagnetic simulations have also been performed to understand and interpret the experimental results, which helped to unravel the transformation of extended SW modes to quantized ones with the angular variation of the in-plane magnetic field and change in lattice constant. The opening and closing of channels for spin-wave extension and localization for a large number of bias field angles (in the full range of 0° to 90°) for this type of complex magnonic crystal have not been studied earlier. Also the sharp corners of the triangular holes of the high density antidot lattice and the complicated lattice structure create inhomogeneous internal magnetic fields due to the effective pinning centres for SWs created by the asymmetric demagnetized regions between the neighbouring triangular holes, which may give rise to some new and interesting physics of opening and closing of new

channels for spin-wave extension and/or localization at particular edges of the triangular holes. Finally we have extensively studied the variation in the internal magnetic field profiles and demagnetizing regions for different angular orientation of the applied bias magnetic field and lattice constant for deeper understanding of the origin of the observed SW modes in such complex magnonic crystal, which was not done previously.

7.2. Methods

25×25 μm^2 arrays of two-dimensional Py antidot arrays with triangular holes arranged in hexagonal lattice symmetry have been fabricated by a combination of electron-beam lithography electron-beam evaporation and ion milling [20]. The 20 nm-thick Py film was deposited on a commercially available self-oxidized Si(100) substrate and a 60-nm-thick protective layer of Al_2O_3 was deposited on top of the Py film in an ultrahigh vacuum chamber at a base pressure of 2×10^{-8} Torr. The Al_2O_3 capping layer was deposited on the Py film to protect the samples from external contamination of the environment, degradation with time, and also from direct irradiation of laser light. A PMMA/MMA bilayer resist was used for electron-beam lithography to prepare the resist pattern on the Py thin film followed by argon ion milling at a base pressure of 1×10^{-4} Torr with a beam current of 60 mA for 6 min for etching out the Py film from everywhere except the unexposed resist pattern to create the triangular antidots.

A custom-built all-optical time-resolved magneto-optical Kerr effect (TR-MOKE) microscope based on a two-color collinear optical pump–probe geometry has been employed to measure the ultrafast magnetization dynamics of the antidot lattices [33, 34]. In this technique, the second harmonic (λ = 400 nm, fluence = 20 mJ/cm^2, pulse width ≈100 fs, spot size = 1 μm) of the fundamental laser beam is generated by a second harmonic generator (SHG) from a mode-locked Ti:sapphire laser (Tsunami, Spectra Physics) to pump or excite the dynamics. The fundamental beam (λ = 800 nm, fluence = 5 mJ/cm^2, pulse width ≈80 fs, spot size = 800 nm) placed at the centre of the pump beam is used to probe the dynamics of the sample by measuring the time-varying polar Kerr rotation from the sample. The magneto-optical Kerr rotation is measured by an optical bridge detector as a function of the time delay between the pump and probe beams. The pump and probe beams are spatially overlapped and focused together on the antidot lattice in a collinear fashion by using a single microscope objective (N.A. = 0.65). The sample is scanned by an x–y–z piezoelectric scanning stage, which gives high stability to the sample in the presence of feedback loops.

The pump beam was chopped at 2 kHz frequency, and the phase-sensitive detection of the Kerr rotation and reflectivity were performed using lock-in amplifiers and an optical bridge detector at room temperature. A variable magnetic field is applied at a small angle (10°) to the sample

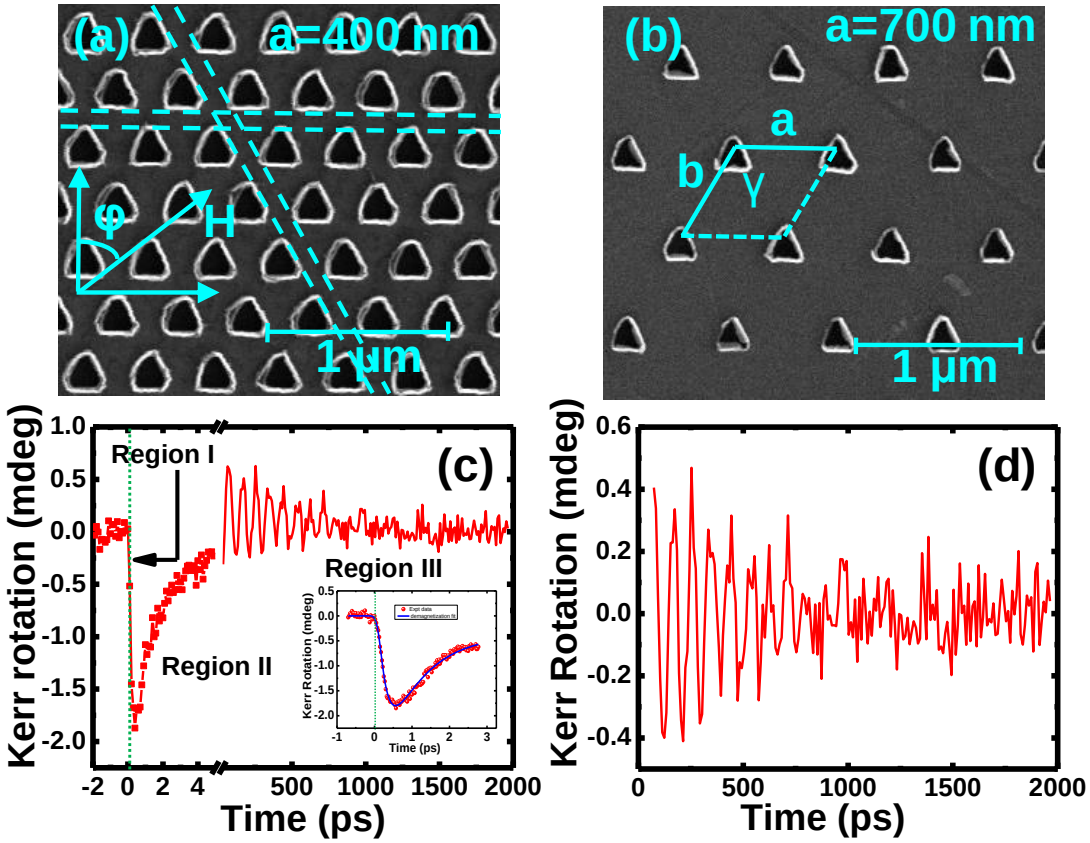

Fig. 7.1: Scanning electron micrographs of the Py antidot arrays with triangular holes of edge length = 200 nm, thickness = 20 nm, arranged in hexagonal lattice with varying lattice constants, (a) a = 400 nm, b = 360 nm and (b) a = 700 nm, b = 560 nm. The lattice constants of the lattices are shown in the micrographs along with the length scales. The unit cell is marked inside the lattice. The horizontal and diagonal channels for spin-wave propagation are marked by dotted lines and the applied bias field geometry is shown in (a). (c) Typical time-resolved Kerr rotation data for the array with a = 700 nm for H = 1.3 kOe. The inset shows the time-resolved Kerr rotation data for shorter time window obtained with a higher temporal resolution (symbols) and fit with three-temperature model (solid line) for extraction of the ultrafast demagnetization and fast relaxation time. The zero delay is shown by the vertical dotted line. (d) Background subtracted time-resolved Kerr rotation data showing the precessional oscillation of magnetizaton.

plane and its in-plane component is defined as the bias magnetic field H. In the experiment, we effectively vary the azimuthal angle (φ) of H between 0° and 90° at intervals of 15° for the hexagonal antidot lattice by rotating the samples using a high-precision rotary stage while keeping the microscope objective and H constant. The pump and the probe beams are made to incident on the same region of the array for each value of φ.

7.3. Results and Discussion

Fig. 7.1 (a) and (b) shows the scanning electron micrographs (SEMs) of the two hexagonal antidot arrays, S1 and S2. The edge length of the triangular holes is about 200 nm and the separation between the nearest edges for the two samples is about 200 nm and 500 nm, respectively (lattice constants (*a*) are 400 nm and 700 nm, respectively). About ±5% deviation in the edge length of antidots and lattice constant is observed. The SEM images show that the triangular antidots have rounded corners and they suffer from small asymmetry in their shapes. The above deviations and asymmetry in the shape of the antidots have been included in the micromagnetic simulations. The lattice parameters a and b are varied while the angle γ is kept constant at 120° for the hexagonal lattice as shown in Fig. 7.1 (b). The unit cell is also marked in Fig. 7.1 (b). The values of *a* and *b* (in nm) as obtained from the SEM images are 400 and 360 and 700 and 560, respectively, for the two lattices. The value of γ is obtained as 120 ± 2°.

Fig. 7.1 (c) shows representative time-resolved Kerr rotation data from the array with a = 700 nm with in-plane bias field of 1.3 kOe at φ = 0°. The graph reveals three important temporal regimes, namely, the ultrafast demagnetization (region I), fast relaxation (region II), and precessional motion superposed on a slow relaxation (region III). We have further performed precise measurements of the time-resolved Kerr rotation for about 3 ps from the zero delay with higher temporal resolution of 25 fs (Fig. 7.1 (c) inset) and fitted the data with the three temperature model using the analytical expression [35] given in Eq. 7.1.

$$-\frac{\Delta M}{M} = \left\{\left[\frac{A_1}{(1+t/\tau_0)^{1/2}} - \frac{A_2\tau_E - A_1\tau_M}{\tau_E - \tau_M}e^{-t/\tau_M} - \frac{\tau_E(A_1-A_2)}{\tau_E-\tau_M}e^{-t/\tau_E}\right]H(t) + A_3\delta(t)\right\}\otimes G(t) \qquad (7.1)$$

Here the time resolution for the laser profile is accounted by a Gaussian function G(t), and it is convoluted with the fit function, which contains two exponentials with time constants t_m and t_e representing the demagnetization and the fast relaxation time, respectively. H(t) and δ(t) represent the Heaviside step function and the Dirac delta function, respectively. A1, A2, and A3 are constants. From the fit we have obtained the ultrafast demagnetization time as 204 ± 3 fs and the fast relaxation as 1.0 ± 0.01 ps. This is followed by the slower relaxation process which occurs within 400 ± 7 ps, while the precessional oscillation is found to be superposed on the slower relaxation process. Fig. 7.1 (d) shows the precessional dynamics after removing the negative delay and ultrafast demagnetization and subtracting a bi-exponential background. Fast Fourier transform (FFT) is performed over this background-subtracted oscillatory Kerr rotation data to obtain the power vs frequency plot.

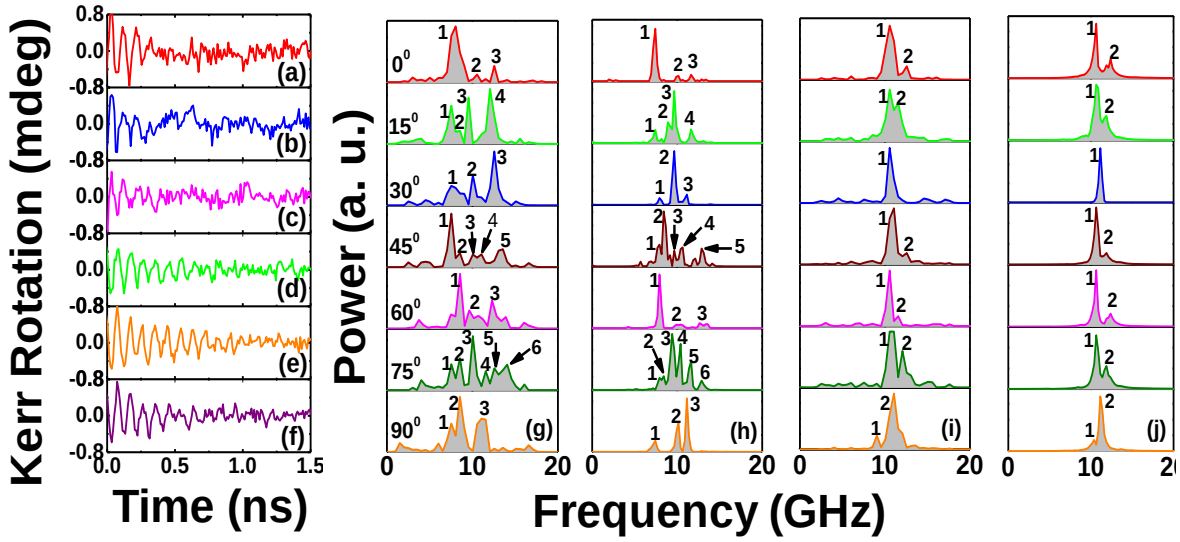

Fig. 7.2: (a) – (f) Experimental time-resolved Kerr rotation data for some specific orientations of the bias field the two arrays; (a) S1 at 0°, (b) S1 at 45°, (c) S1 at 60°, (d) S2 at 0°, (e) S2 at 45°, (f) S2 at 60°. (g) and (i) FFT power spectra of experimental time-resolved Kerr rotation data of S1 and S2 for different orientations of the in-plane bias field (g) for S1 at H = 1 kOe, (i) for S2 at H = 1.3 kOe. (h) and (j) FFT power spectra of simulated time-domain magnetization; (h) S1 at H = 1 kOe and (j) S2 at H = 1.3 kOe. Mode numbers are shown in both experimental and simulated power spectra.

Fig. 7.2 (a) – (f) shows the representative background-subtracted experimental time-resolved Kerr rotation data for some specific orientations of the in-plane bias magnetic field for the two antidot arrays. The experimental FFT power spectra for S1 and S2 with φ varying from 0° to 90° (at an interval of 15°) are shown in Fig. 7.2 (g) and (i). As φ and a-values are varied, we observe a distinct variation in the magnetization dynamics. For all φ and a-values, multimodal SW spectra are observed corresponding to the damped nonuniform oscillations [36]. The experimental data of bias-field-angle dependence of SW spectra for S1 has been taken at H = 1.0 kOe, whereas for S2 the data has been taken at H = 1.3 kOe. However, since both of the two field values are well above the saturation field for the Py (base material of the antidot lattice), the variation in bias field magnitude only changes the SW frequency values for the two samples, while the qualitative features of the angular dependence of SW spectra and corresponding SW mode profiles would not be affected by this. The experimental SW spectra for S1 show 3 modes for φ = 0°, 30°, 60° and 90°. The spectra for φ = 0° and 60° are qualitatively similar in nature (though the mode frequencies are not same). Also, there is a qualitative (but not quantitative) agreement between the spectra for 30° and 90°. However, the SW spectra are remarkably different for φ = 15°, 45° and 75° with a drastic increase in the number of modes at φ = 45° and 75°. These indicate a change in the collective nature of the magnetization dynamics with varying φ-values. When we consider S2 with larger a-values, we get a significant

difference in the nature of SW spectra as opposed to S1. Here, instead of large number of modes, only two modes (one dominant mode with a low power shoulder) for almost all the angles are observed (excluding $\varphi = 30°$ where instead of two, only one mode is observed).

The experimental SW spectra are well reproduced by micromagnetic simulations by OOMMF software [37]. The simulated FFT power spectra for S1 and S2 with the variation of φ are shown in Fig. 7.2 (h) and 7.2 (j). As opposed to the experimental technique, which is based on optical excitation of magnetization, the simulation is performed by applying a pulsed magnetic field, which reproduces the experimental conditions successfully. The details of the simulation can be found elsewhere [4]. Similar simulation methods have also previously been used to successfully reproduce and understand the magnetization dynamics and SW mode profiles in different types of magnonic systems [34,36,38]. We have studied arrays of 7 × 7 antidots and discretized the arrays into rectangular prisms of dimensions $4 \times 4 \times 20$ nm^3. The lateral cell size is well below the exchange length of Py (≈ 5.2 nm). The shapes introducing the actual edge roughness of the triangular holes have been derived from SEM images and the material parameters used for Py were gyromagnetic ratio $\gamma' = 17.6$ MHz/Oe, anisotropy field $H_k = 0$, saturation magnetization Ms = 860 emu/cm, and exchange stiffness constant $A = 1.3 \times 10^{-6}$ erg/cm. The material parameters were extracted by measuring the variation of precessional frequency (f) with bias magnetic field H for a Py thin film and by fitting them using Kittel formula,

$$f = \frac{\gamma}{2\pi}\sqrt{(H + H_k)(H + H_k + 4\pi M_s)} \qquad (7.2)$$

The exchange stiffness constant A is obtained from literature [39]. A pulsed field of peak value of 30 Oe, 10 ps rise/fall time and 20 ps pulse duration is used perpendicular to the sample plane, while a damping coefficient $\alpha = 0.008$ is used during dynamic simulations. The experimentally observed SW spectra (FFT of the time-resolved Kerr rotation data) match qualitatively with the simulated SW spectra. But due to some limitations in the micromagnetic simulations, we observe a slight quantitative disagreement between the experimental and simulated spectra [36]. As the triangular antidots have rounded corners, and hence suffer from small asymmetry in their shapes, the simulations have been performed by introducing the actual edge roughness of the triangular antidots. However, the precise edge roughness and deformation could not be reproduced by the finite difference method based micromagnetic simulations used here. The simulations have also been performed on similar antidot arrays after applying a two-dimensional periodic boundary condition (2D-PBC). The simulations with and without application of 2D-PBC show almost identical results. The simulation results with the introduction 2D-PBC are given in Appendix III.

Fig. 7.3 (a) shows the bias magnetic field dependence of the SW frequencies fitted with the Kittel formula for a 20 nm-thick Py blanket film. Fig. 7.3 (b) shows the same extracted from

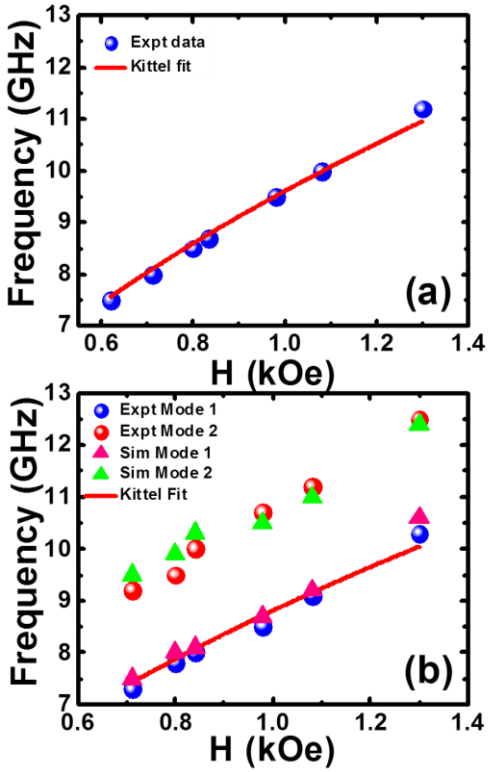

Fig. 7.3: Bias field dependence of precessional frequencies of different SW modes for (a) Py blanket film and (b) antidot lattice S2 with lattice constant 700 nm.

the experimental and simulated FFT spectra for S2. The experimental data points corresponding to mode 1 are well fitted with the Kittel formula. However, the higher frequency mode (mode 2) does not follow the same formula. The M_s value obtained from the Kittel fit of mode 1 is 712 emu/cm^3, while the other magnetic parameters remain same as the Py blanket film. The difference between the simulated and experimental SW mode frequencies may arise due to random demagnetized regions at the edges and rounded corners of the triangular antidots, which is hard to precisely incorporate in the finite difference method based micromagnetic simulations such as OOMMF as used here. Further, we could not fit any of the experimental modes of S1 with the Kittel formula.

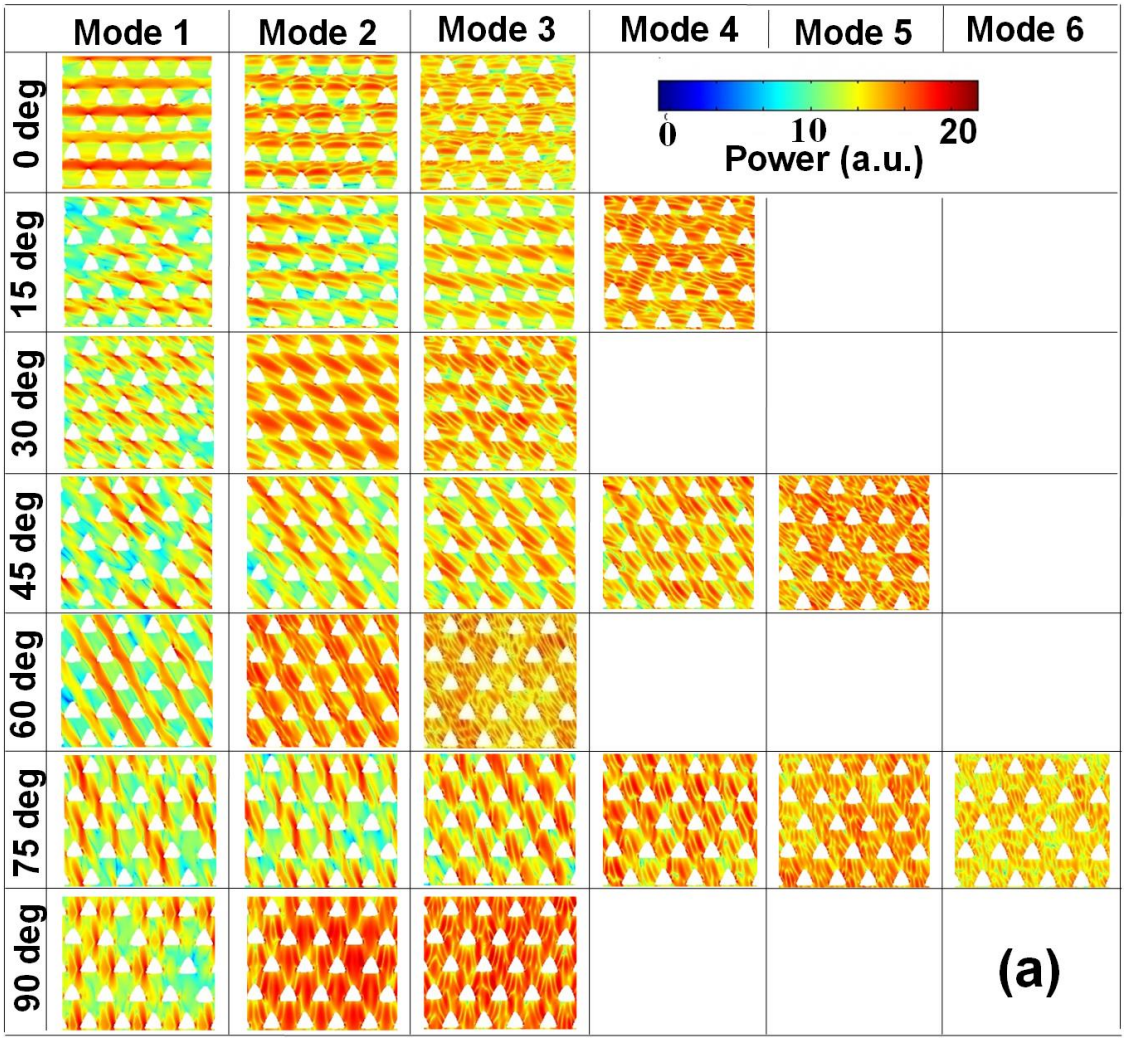
Mode 1
Mode 2
Mode 3
Mode 4
Mode 5
Mode 6
0 deg
15 deg
30 deg
45 deg
60 deg
75 deg
90 deg
0
10
20
Power (a.u.)
(a)

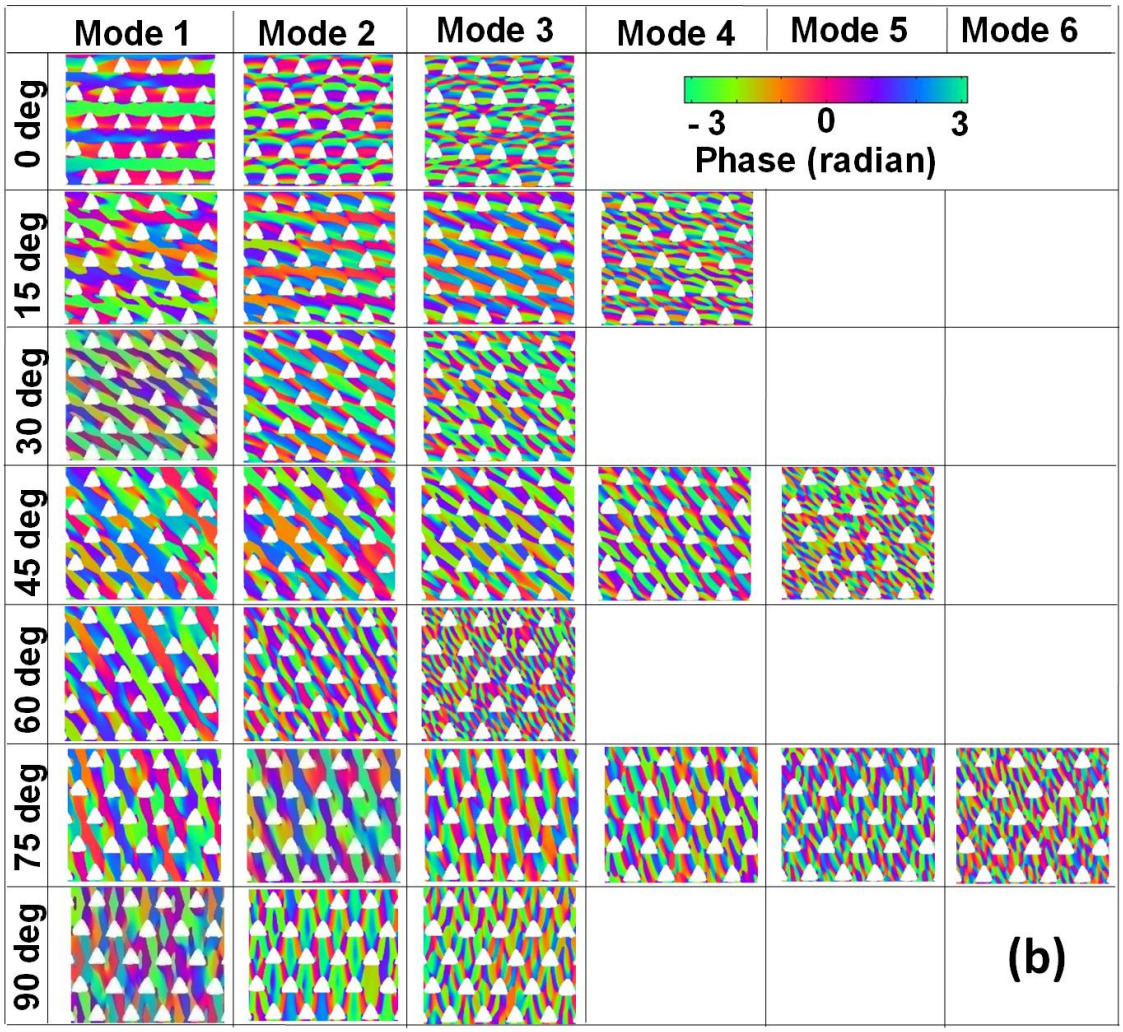

Fig. 7.4: Spin-wave mode profile. (a) Power and (b) phase of S1 for different orientations of the in-plane bias magnetic field. The color maps used for the mode profiles is shown inside the Fig.

We have further simulated the spatial profiles of the resonant modes using a home-built code [40] and the simulated power and phase maps for S1 are shown in Fig. 7.4 (a) and 7.4 (b), respectively. For φ = 0°, mode 1 has an extended character through the horizontal channels between the neighbouring antidot rows in the Damon-Eshbach (DE) geometry (i.e., extended in a direction orthogonal to the applied bias magnetic field). On the contrary, mode 2 is a localized mode where the highest spin-precession amplitude is localized in the same horizontal channels with quantization number n = 3. Mode 3 is again a quantized mode with higher quantization number (n = 5). When φ is rotated to 15°, mode 1 is an edge mode (EM) of the array and the highest spin-precession amplitude associated with this mode is found at the top vertex of each triangular hole. Interestingly, in the simulated profile, mode 2 for φ = 0° is split into two for φ = 15° (modes 2 and 3). These two modes are localized modes between diagonally situated next nearest neighbours but standing waves do not form exactly between the diagonally

situated next nearest neighbours and become asymmetric due to asymmetry in the internal field profile. Mode 4 is the quantized mode with quantization number $n = 5$. When φ is further rotated to 30°, mode 1 is again an EM of the lattice with the highest spin-precession amplitude mainly concentrated due to the demagnetizing regions at the left-most vertex of each triangular antidot. Mode 2 is localized mode and as opposed to $\varphi = 15°$, here the standing wave is symmetric and forms exactly between the diagonally situated next nearest neighbours. Again, mode 3 is the quantized mode with $n = 3$. For $\varphi = 45°$, the lowest frequency mode is split into two modes (modes 1 and 2). For these two modes, overlap between localized modes generates a pseudo-extended mode through the channel marked by the dotted line shown in Fig. 7.1 (a) (diagonally extended channel). The next mode is again split into mode 3 and mode 4 and these two are localized modes along the same channel. Here, the highest frequency mode 5 is quantized with quantization number $n = 5$. Again, for $\varphi = 60°$, the spatial profiles of the SW spectra qualitatively match with that of $\varphi = 0°$. Here, mode 1 is a fully extended mode similar to that for $\varphi = 0°$, but the channel of propagation is different and it flows through the diagonally extended channel. Mode 2 is localized in the same channel with $n = 3$, and mode 3 is a quantized mode with higher quantization number ($n = 7$). Again, at $\varphi = 75°$, each mode is split into two. For the two lowest frequency modes (mode 1 and 2), the highest spin-precession amplitude is concentrated at the left-most vertex of the triangular antidots. These two are localized modes and seem to be running parallel through the diagonally extended channel of the array. The next higher frequency modes are quantized modes with quantization numbers increasing from mode 3 to mode 6. For $\varphi = 90°$, due to the unavailability of continuous channels along the vertical direction, mode 1 is again an EM of the lattice with the highest spin-precession amplitude mainly concentrated due to the demagnetizing regions at the left-most vertex of each triangular antidots. Mode 2 is a localized mode as compared to $\varphi = 30°$ and here the standing wave is symmetric and forms exactly between the vertically situated next nearest neighbours. Mode 3 is again a quantized mode with higher quantization number ($n = 5$).

In S2, we observed a remarkable variation in the SW mode profiles as shown in Fig. 7.5. In addition to horizontally and diagonally extended continuous channels, we also observed continuous channels in the vertical direction (which was unavailable in S1) and fully extended modes in DE geometry are obtained through the horizontal, diagonal and vertical channels for $\varphi = 0°$, 60° and 90°, respectively. For the other angles, the lower frequency extended, pseudo-

extended or EMs (present in S1) are not present here and we observed localized and/or quantized modes.

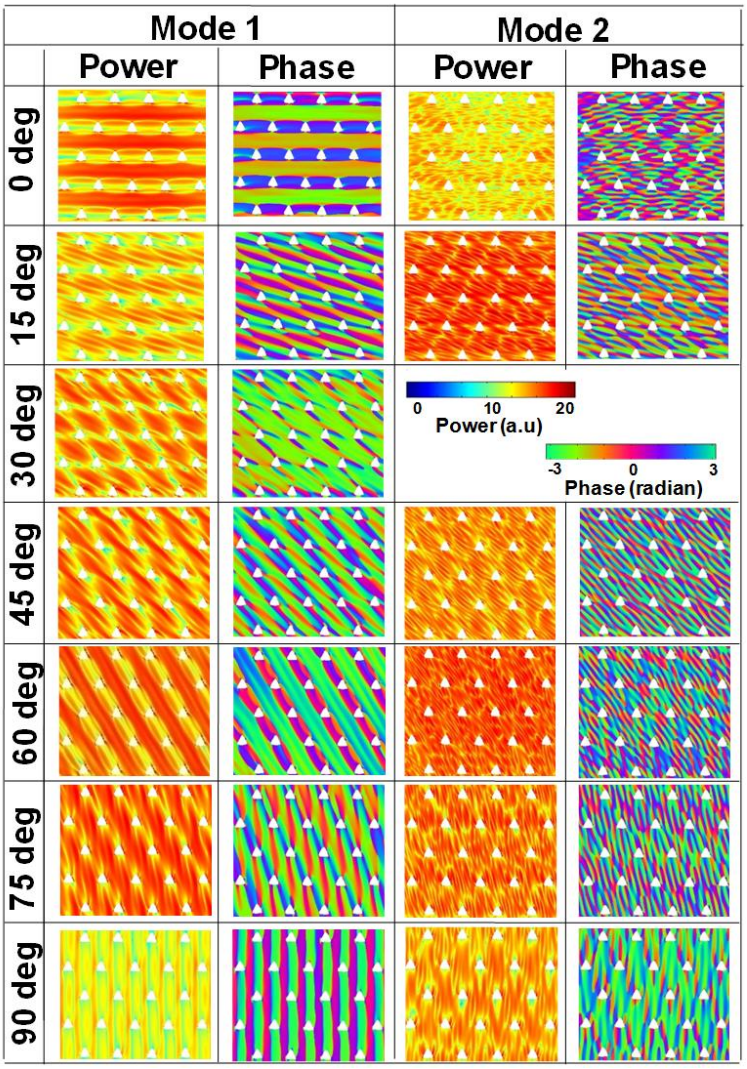

Fig. 7.5: Spin-wave mode profile (power and phase) of S2 for different orientations of the in-plane bias field. The color maps used for the mode profiles are shown inside the Fig.

We have further simulated the magnetostatic field distribution of the antidot arrays by using the LLG micromagnetic simulator [41]. Fig. 7.6 shows the magnetization maps (domain plot) and the contour plots of simulated magnetostatic field distributions for the two arrays, at some specific orientations of the in-plane bias field. This reveals the demagnetized regions and internal-field distribution around the antidots for different values of φ. For different φ-values, the surface charges at the boundaries between the antidots and magnetic layer lead to the formation of different types of domains through the demagnetization field. Due to the triangular shape of the antidots, the demagnetized regions, as well as magnetostatic field distributions

around the arrays, are not symmetrical. As φ is varied, the domain structure and the internal field lines change considerably. This leads to the variation in the SW mode structures as well as the mode frequencies.

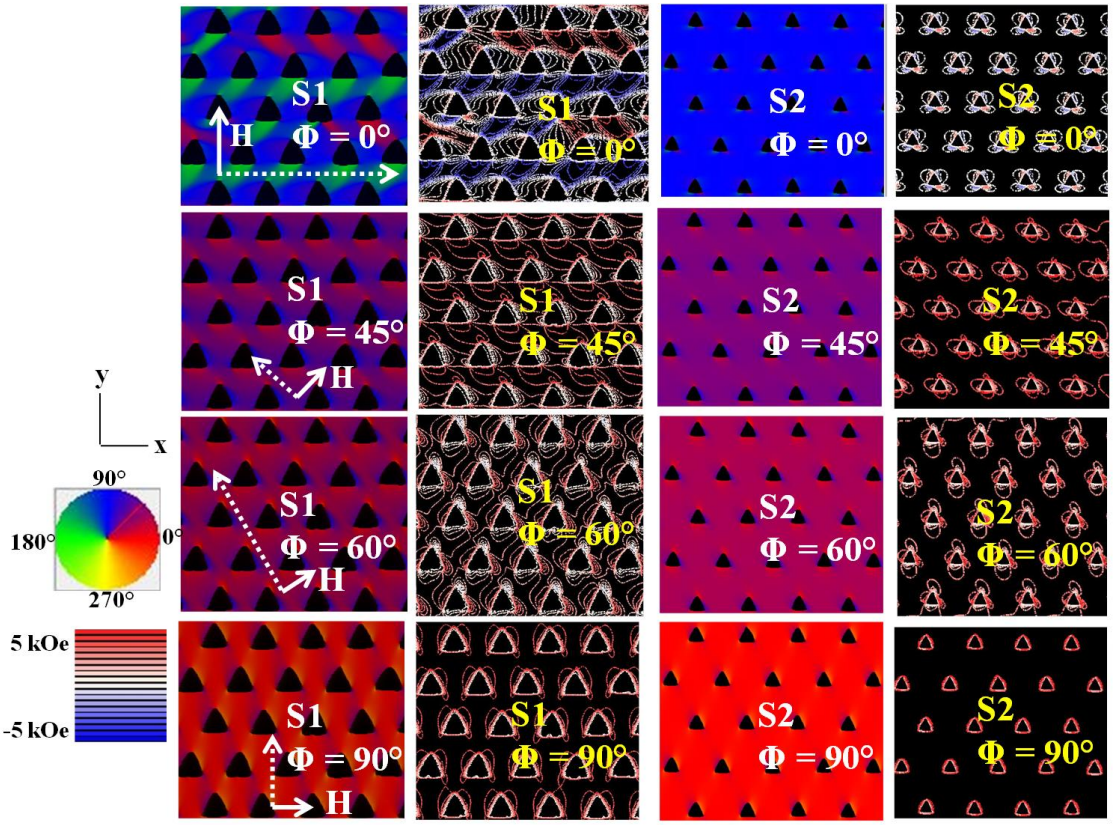

Fig. 7.6: Magnetization distribution and the contour maps of simulated magnetostatic field distribution of the two arrays for some specific orientations of the in-plane bias magnetic field obtained by micromagnetic simulations. The solid arrow lines indicate the direction of applied bias field and the dotted arrow lines (perpendicular to the direction of applied bias field) indicate the direction through which SWs are supposed to propagate. Color maps for both magnetization distribution and contour plot are shown in the left side of the Fig.

For S1 at $\varphi = 0°$, domains with magnetization reaching ±45° with respect to the y-axis (direction of applied bias magnetic field) are located within the regions between the base and the top apex of the vertically nearest neighbour triangular antidots. But due to the triangular shape of the holes and the small lattice constant, all the ±45° domains are not symmetrically situated. The domains with magnetization along the applied field are located within the central area of the unit cell. From the contour plot it is evident that the density of the internal field lines in the region between the base and top apex of vertically situated triangular holes (i.e., along the horizontal channel) is large. The hexagonal geometry gives the extended nature of the SW modes through the horizontal channel shown in Fig. 7.1. For S1 at $\varphi = 60°$, the density of the

internal field lines deceases along the horizontal channel but increases along the diagonal channel as small domains with magnetization directed nearly along y-axis are located at the left and right apex and domains with magnetization directed nearly along x-axis are located at the top-apex of each triangle. But along the diagonally extended channel, the magnetization points along the direction of applied field and SW shows an extended nature through this channel. Again, for S1 at φ = 45°, the density of the internal field lines is less compared to φ = 0° and 60°, along the horizontal and diagonal channels, respectively. Domains with magnetization directed nearly along the x-direction are located along the horizontal channel (between the base and top-apex of vertically situated nearest neighbours) and domains with magnetization directed nearly along the y-direction are located between horizontally situated nearest neighbours. But in this orientation of the bias field, the extended nature of SW is suppressed due to the absence of a channel along which only one type of domain could be observed. For S1 at φ = 90°, the density of the internal field lines reduces significantly, and the demagnetizing regions become asymmetric around the triangular holes. In most of the regions, the magnetization points along the direction of the applied field. Only very small domains with magnetization pointing nearly along the y-axis are located at the corners of the triangular holes. But in this orientation, the extended nature of the SWs is not observed due to the hexagonal geometry of the lattice with a small lattice constant.

The domain structure changes when we consider the array S2 with a larger lattice constant. For φ = 0°, the asymmetric nature of the domain structure found in S1 is not observed in S2, all the domains almost coalesce, and very small ±45° domains are located only at the corners of the triangular holes for S2. In most of the regions, the magnetization points along the direction of the applied magnetic field and as the horizontal channels consist of only one type of domain, the power of the extended mode through this horizontal channel is considerably higher than that for S1. Similarly, in other orientations also, the domains coalesce more and only one type of domain is observed in most of the regions except for the triangular corners. Hence, in case of S2, we do not observe EMs as obtained in S1 and for all other orientations of the bias magnetic field we observe either quantized or extended modes with comparatively higher power than S1.

7.4. Conclusion

In conclusion we have investigated the effects of the orientation of the bias-magnetic field and lattice constant on the ultrafast magnetization dynamics and magnetostatic field distribution in a periodic array of triangular nanoholes forming a hexagonal antidot lattice in a thin Py film by

using time-resolved Kerr microscopy. The experimental results reveal that the magnetization dynamics can be effectively tuned by the systematic variation of the orientation of the in-plane bias-magnetic field and lattice constant. Micromagnetic simulations successfully repro- duced the experimental results and a fully extended SW mode is found to transform to quantized ones and vice versa simply by changing the in-plane orientation of the bias field. For the antidot lattice S1 (lattice constant 400 nm), the channels for SW propagation are found to be opened at φ = 0° and 60°. For φ = 45°, we observe a pseudo-extended nature of SW modes along the diagonally extended channel, whereas for the other angles, due to unavailability of continuous propagation channels, the powers of SWs are found to be concentrated at specific edges of the triangular holes. Interestingly, for S2 (lattice constant 700 nm), due to the increased inter-antidot separation, an additional SW propagation channel at φ = 90° gets opened. For other angles, the low-power edge modes are not present here due to the increased lattice constant, and for those angles, we mainly observe quantized and/or localized modes. The observed variation in the collective magnetization dynamics with the orientation of the in-plane bias field is attributed to the variation of the internal field distribution between the triangular shaped antidots. The observed tunability of the magnetization dynamics and SW spectra with the variation in the orientation of the in-plane bias field and lattice constant is anticipated to be important for nanoscale magnonic crystal based technology.

References

[1] V. V. Kruglyak, S. O. Demokritov, D. Grundler, J. Phys. D: Appl. Phys. **43**, 264001 (2010).
[2] B. Lenk, H. Ulrichs, F. Garbs, M. Münzenberg, Phys. Rep. **507**, 107 (2011).
[3] S. Jung, B. Watkins, L. DeLong, J. B. Ketterson, V. Chandrasekhar, Phys. Rev. B **66**, 132405 (2002).
[4] B. Rana, D. Kumar, S. Barman, S. Pal, Y. Fukuma, Y. Otani, A. Barman, ACS Nano **5**, 9559 (2011).
[5] S. Pal, S. Saha, M. V. Kamalakar, A. Barman, Nano Res. **9**, 1426 (2016).
[6] C. C. Wang, A. O. Adeyeye, N. Singh, Nanotechnology **17**, 1629 (2006).
[7] S. Neusser, B. Botters, M. Becherer, D. Schmitt-Landsiedel, D. Grundler, Appl. Phys. Lett. **93**, 122501 (2008).
[8] S. Neusser, G. Duerr, H. G. Bauer, S. Tacchi, M. Madami, G. Woltersdorf, G. Gubbiotti, C. H. Back, D. Grundler, Phys. Rev. Lett. **105**, 067208 (2010).
[9] G. Ctistis, E. Papaioannou, P. Patoka, J. Gutek, Fumagalli, P. Giersig, Nano Lett. **9**, 1 (2009).
[10] L. Torres, L. Lopez-Diaz, O. Alejos, J. Appl. Phys. **87**, 5645 (2000).
[11] M. Sushruth, J. Ding, J. Duczynski, R. C. Woodward, R. A. Begley, H. Fangohr, R. O. Fuller, A. O. Adeyeye, M. Kostylev, P. J. Metaxas, Phys. Rev. Appl. **6**, 044005 (2016).
[12] J. W. Kłos, D. Kumar, J. Romero-Vivas, H. Fangohr, M. Franchin, M. Krawczyk, A. Barman, Phys. Rev. B **86**, 184433 (2012).
[13] J. W. Klos, D. Kumar, M. Krawczyk, A. Barman, Sci. Rep. **3**, 2444 (2013).
[14] E. K. Semenova, D. V. Berkova, J. Appl. Phys. **114**, 013905 (2013).
[15] M. Madami, G. Gubbiotti, S. Tacchi, G. Carlotti, S. Jain, Physica B **435**, 152 (2014).
[16] T. Schneider, M. Langer, J. Alekhina, E. Kowalska, A. Oelschlägel, A. Semisalova, A. Neudert, K. Lenz, K. Potzger, M. P. Kostylev, J. Fassbender, A. O. Adeyeye, J. Lindner, R. Bali, Sci. Rep. **7**, 41157 (2017).
[17] L. Torresa, L. L. Diaz, O. Alejos, J. Inigues, J. Appl. Phys. **85**, 6208 (1999).
[18] N. G. Deshpande, M. S. Seo, X. R. Jin, S. J. Lee, Y. P. Lee, J. Y. Rhee, K. W. Kim, Appl. Phys. Lett. **96**, 122503 (2010).
[19] S. McPhail, C. M. G*ü*rtler, J. M. Shilton, N. J. Curson, J. A. C. Bland, Phys. Rev. B **72**, 094414 (2005).
[20] R. Mandal, S. Barman, S. Saha, Y. Otani, A. Barman, J. Appl. Phys. **118**, 053910 (2015).
[21] S. Tacchi, M. Madami, G. Gubbiotti, G. Carlotti, A. O. Adeyeye, S. Neusser, B. Botters, D. Grundler, IEEE Trans. Mag. **46**, 1440 (2010).
[22] H. Ulrichs, B. Lenk, M. Munzenberg, Appl. Phys. Lett. **97**, 092506 (2010).
[23] S. Pal, J. W. Klos, K. Das, O. Hellwig, P. Gruszecki, M. Krawczyk, A. Barman, Appl. Phys. Lett. **105**, 162408 (2014).
[24] S. Choudhury, S. Barman, Y. Otani, A. Barman, ACS Nano **11**, 8894 (2017).
[25] R. Mandal, P. Laha, K. Das, S. Saha, S. Barman, A. K. Raychaudhuri, A. Barman, Appl. Phys. Lett. **103**, 262410 (2013).
[26] S. Tacchi, B. Botters, M. Madami, J. W. Kłos, M. L. Sokolovskyy, M. Krawczyk, G. Gubbiotti, G. Carlotti, A. O. Adeyeye, S. Neusser, D. Grundler, Phys. Rev. B **86**, 014417 (2012).
[27] A. Manzin, O. Bottauscio, J. Phys. D: Appl. Phys. **45**, 095001 (2012).
[28] G. Gubbiotti, S. Tacchi, M. Madami, G. Carlotti, S. Jain, A. O. Adeyeye, M. P. Kostylev, Appl. Phys. Lett. **100**, 162407 (2012).
[29] S. Choudhury, S. Saha, R. Mandal, S. Barman, Y. Otani, A. Barman, ACS Appl. Mater. Interf. **8**, 18339 (2016).

[30] N. Tahir, M. Zelent, R. Gieniusz, M. Krawczyk, A. Maziewski, T. Wojciechowski, J. Ding, A. O. Adeyeye, J. Phys. D: Appl. Phys. **50**, 025004 (2017).
[31] F. Haering, U. Wiedwald, S. Nothelfer, B. Koslowski, P. Ziemann, L. Lechner, A. Wallucks, K. Lebecki, U. Nowak, J. Grafe, E. Goering, G. Schutz, Nanotechnology **24**, 465709 (2013).
[32] A. Manzin, G. Barrera, F. Celegato, M. Coïsson, P. Tiberto, Sci. Rep. **6**, 22004 (2016).
[33] A. Barman, and A. Haldar, Solid State Physics **65**, 1 (2014).
[34] S. Saha, S. Barman, S. Sugimoto, Y. Otani, A. Barman, RSC Adv. **5**, 34027 (2015).
[35] G. Malinowski, F. Dalla Longa, J. H. H. Rietjens, P. V. Paluskar, R. Huijink, H. J. M. Swagten, B. Koopmans, Nat. Phys. **4**, 855 (2008).
[36] S. Mondal, S. Choudhury, S. Barman, Y. Otani, A. Barman, RSC Adv. **6**, 110393 (2016).
[37] M. Donahue, and D. G. Porter, OOMMF User's guide, version1.0, Interagency Report NISTIR 6376, National Institute of Standard and Technology, Gaithersburg, MD,1999.
[38] A. De, S. Mondal, C. Banerjee, A. K. Chaurasiya, R. Mandal, Y. Otani, R. K. Mitra, A. Barman, J. Phys. D: Appl. Phys. **50**, 385002 (2017).
[39] K. H. J. Buschow, J.: Handbook of Magnetic Materials, North Holland, Amsterdam, **18**, 168 (2009).
[40] D. Kumar, O. Dmytriiev, S. Ponraj, A. Barman, J. Phys. D: Appl. Phys. **45**, 015001 (2012).
[41] Scheinfein, M. R.; LLG Micromagnetic Simulator, http://llgmicro.home.mindspring.com (1997).

Chapter 8

8. Magnonic Crystals with Complex Geometry

8.1. Introduction

The emergence of magnonics [1-3] has promised a paradigm shift in the on-chip data communication and processing for future computing devices. Subsequent development of combination of magnonics with other systems have unearthed greater functionalities in the form of magnon-spintronics [4], magphonics [5] and magnon-polaritronics [6] which may give rise to next-generation devices with superior energy efficiency, speed and miniaturization. The magnon current generated by the collective motion of magnetic moments or spin waves (SWs, quanta of which are known as magnons) does not involve the motion of charge carriers, and therefore, have lesser dissipation as compared to the spin polarized current and even pure spin current. The short wavelength SWs with about 50 nm wavelength has been demonstrated to propagate a distance over 60 μm with a group velocity as high as 2.6 km/s [7] and has bright future to generate miniaturized, faster, and more energy-efficient technological implementations. Further evolution of hybrid magnonics [8,9] offers the possibility of quantum transduction and quantum entanglement using magnons.

Ferromagnetic antidot lattices (ADLs) [10, 11] with non-magnetic holes periodically grooved in a continuous ferromagnetic film are of profound interest in magnonics for potential applications in designed magnon waveguides [12], filters [13] amplifiers [14], couplers [15], multiplexers [16], phase shifters [17], interferometers [18], transistors [19] as well as magnonic logic devices [20]. A flurry of investigations on standing and propagating SWs in ferromagnetic ADLs have been performed by varying a number of parameters such as antidot shape [21], lattice constant [22], lattice symmetry [23], base material [24, 25] as well as the strength and orientation of the applied magnetic field [26]. Early experiments on Co ADLs showed the attenuation of uniform ferromagnetic resonance (FMR) mode due to the excitation of nonuniform SW modes [27]. Observations of field controlled confinement, localization, and propagation of SWs [28], splitting of resonant modes [29], mode crossover [30], mode hopping [30], mode softening [31], as well as the formation of magnonic mini band [32] in ADLs were important developments in this area.

Quasiperiodicity is an important problem in solid state physics because quasiperiodic crystals possess long-range ordering without any periodicity, complex form of frustration leading to glassy behavior, their diffraction patterns exhibit symmetry that are forbidden by crystallographic restrictions and they show exotic rotational symmetry [33]. Artificial quasicrystals have been extensively studied in photonics [34] and phononics [35] for a long time. Recently magnonic quasicrystals (MQC) [36] have become a burgeoning research topic due to various interesting properties like branching features in the band structure [37], appearance of pass band [38], allowed bulk band in place of band gaps [39] etc. Concepts of self-generation of dissipative solitons in MQC active ring resonators have been reported [40]. Bhat *et al*. showed the MQCs comprising of $Ni_{80}Fe_{20}$ interconnected nanobars arranged in Penrose P2, P3 and Ammann tiling exhibit distinct sets of FMR modes with eight- and ten-fold rotational symmetries with varying in-plane magnetic field orientations [41]. Experimental observation of emergent magnon motifs and Conway worm-like nanochannels in MQCs created via nanoholes arranged in Penrose P2 and P3 tiling have been reported [42]. Construction of numerous types of MQCs with Fibonacci sequences [43], and different variants of Penrose tiling, oblique tiling, Kite and Dart tiling [44] and Ammann-Beenker tiling [45, 46] may offer unprecedented tunability of the SW dynamics and magnonic band structure due to the lack of translational symmetry.

MQCs in the form of octagonal lattice of ferromagnetic nanodots [47, 48] and antidots [49] with broken translational symmetry have been featured in few earlier works. The whole space of an octagonal lattice cannot be covered with only one kind of tile. Instead rhombic tiles along with octagonal tiles are required to cover the whole space. Choudhury *et al*. observed an eight-fold rotational symmetry in octagonal lattice of circular shaped $Ni_{80}Fe_{20}$ antidots [49]. Introduction of complex basis to such MQCs may result in richer and more complex SW dynamics. However, a combination of MQC with a complex basis is absent in the literature. Along with the aperiodicity of octagonal lattice we have added an asymmetric basis of triangular shaped antidots with lack of reflection or mirror symmetry. Such complex network of antidots may be considered as interesting testbed for providing new phenomena and stern challenges.

We investigate the high-frequency SW dynamics of two-dimensional arrays of asymmetric triangular shaped $Ni_{80}Fe_{20}$ antidots arranged in octagonal lattices with varying lattice constant. We have further compared the results with the most primitive Bravais lattice having square symmetry. A strong eight-fold anisotropy superposed with a weak three-fold anisotropy in the SW frequency is observed for the octagonal lattice, whereas, a strong four-fold anisotropy

superposed with a weak three-fold anisotropy is observed for the square lattice. The micromagnetic simulations revealed a mode conversion from extended to quantized standing-wave pattern and vice versa with the variation of the orientation of the in-plane bias magnetic field. The strong modifications of the asymmetric demagnetizing regions as well as the internal field profiles around the triangular antidots can explain the observed variation of the SW dynamics in such complex antidot lattice.

8.2. Methods

Triangular-shaped antidots were patterned on a 20-nm-thick $Ni_{80}Fe_{20}$ (Py) film by using a combination of electron-beam lithography (EBL), electron-beam evaporation (EBE), and ion milling [23]. The antidots with a fixed edge length (d) of 200 nm and variable lattice constants (a) of 400 nm, 500 nm, 600 nm, and 700 nm are arranged in square and octagonal symmetries with total array dimensions of 25 × 25 μm^2, as shown in the scanning electron micrographs (SEMs) of Figs. 8.1 (a) and (b). Both the edge lengths and the lattice constants of these antidots suffer from ±5% deviations. At first a continuous Py film of 20 nm thickness was deposited on self-oxidized silicon (Si) [100] substrate by EBE at a base pressure of ~ 2×10^{-8} Torr. On top of the Py film, a 5-nm-thick protective layer of Al_2O_3 was deposited to protect the samples from external contamination of the environment, degradation with time, and also from direct exposure to the femtosecond laser. A bi-layer MMA/PMMA (methyl methacrylate/ polymethyl methacrylate) was used for EBL to prepare the resist pattern on the continuous Py film. Finally, argon ion milling was carried out for 6 min at a base pressure of ~1×10^{-4} Torr and beam current of ~60 mA to etch out the Py film from everywhere except the unexposed resist pattern to create the triangular shaped antidots.

The ultrafast magnetization dynamics of the samples was measured by a custom-built time-resolved magneto-optical Kerr effect (TR-MOKE) microscope based upon a two-color collinear pump–probe setup [50]. A small part of the fundamental laser output (λ = 800 nm, fluence = 2 mJ/cm^2, pulse width ~80 fs, spot size ~800 nm) generated from a mode locked Ti-sapphire laser (Tsunami, Spectra Physics) was exploited to probe the magnetization dynamics of the sample. Another part of this fundamental laser output was frequency doubled (λ = 400 nm, fluence = 20 mJ/cm^2, pulse width ~100 fs, spot size ~1 μm) and was used as the pump beam to excite the magnetization dynamics of the sample. The probe beam was time delayed with respect to the pump beam and both of them fall upon the sample collinearly through a single microscope objective (MO) with numerical aperture (N.A.) of 0.65. The back reflected

beams from the sample were collected by the same MO. The probe beam was steered to an optical bridge detector (OBD) after filtering out the pump beam using a spectral filter. The OBD measures the transient reflectivity and Kerr rotation by two separate lock-in amplifiers in phase sensitive manner ensuring no breakthrough of one into another. The pump beam was modulated at 2 kHz frequency by a mechanical chopper, the frequency output of which was used as reference frequency to the lock-in amplifiers. The sample was scanned by an *x*-*y*-*z* piezoelectric scanning stage to position the pump and probe beams at the desired location of the ADLs. This gives high stability to the sample in presence of feedback loops. An external magnetic field was applied at a small angle (~10°) from the sample plane, the in-plane component of which is defined as the bias magnetic field *H*. We varied the azimuthal angle (φ) of *H* between 0° and 180° during the measurement. The measurement geometry is schematically depicted in Fig. 1(c).

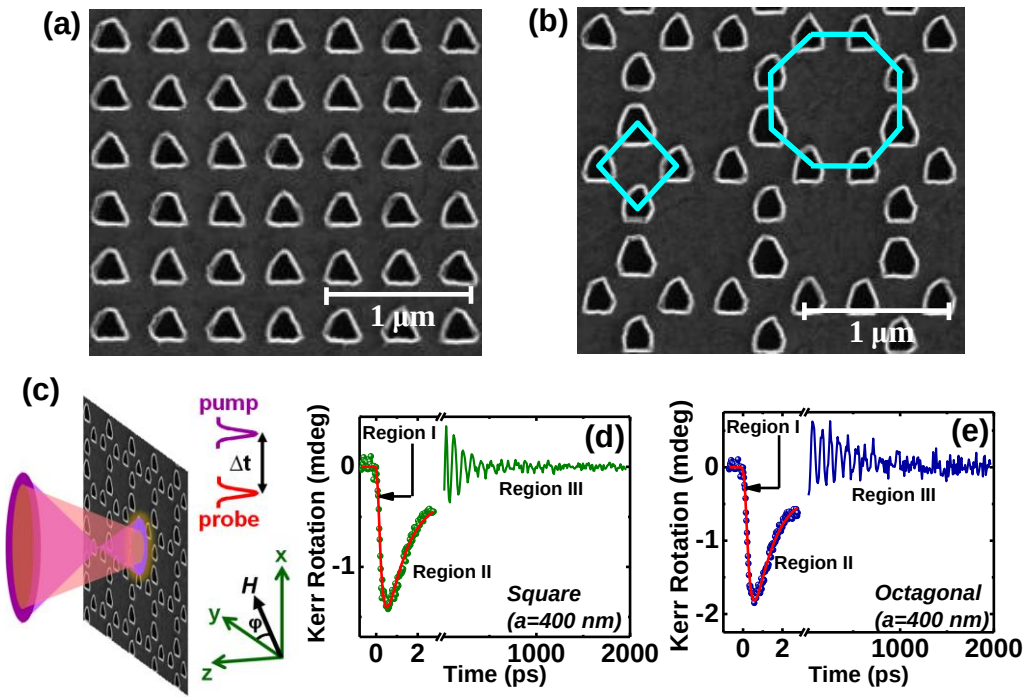

Fig. 8.1: Scanning electron micrographs (SEM) of the antidot lattices with (a) square, (b) octagonal symmetry. The edge length (*d*) of the triangular antidots is 200 nm and the lattice constant (*a*) is 400 nm for both lattice. The length scale bars are shown in the images. (c) Schematic of the TR-MOKE microscope showing the pump and probe beams and the geometry of the measurement. Typical time-resolved Kerr rotation data for the (d) square and (e) octagonal lattice with a = 400 nm at H = 1 kOe and φ = 0°.

The experimental data has been reproduced by finite difference method (FDM) based micromagnetic simulations using the Object Oriented Micromagnetic Framework (OOMMF) software [51], considering arrays of 7 × 7 antidots for each sample to take care of the long range

magnetostatic interaction. To validate these simulation results we have also performed test simulations on the square and octagonal lattice after application of two-dimensional periodic boundary condition (2D-PBC). The test simulation results for a particular lattice constant (a = 400 nm) with 2D-PBC are presented in Fig. A4.1 of the Appendix IV. The simulations with and without application of 2D-PBC show nearly identical results. Each sample was discretized into rectangular prism like cells with dimensions of 4 × 4 × 20 nm^3, with the lateral cell size kept well below the exchange length of Py (≈ 5.2 nm) to include the exchange interaction effect. The shapes of the triangular antidots with the actual edge roughness were derived from the SEM images. The magnetic parameters used in the simulations were: exchange stiffness constant A = 1.3×10^{-6} erg/cm, saturation magnetization M_s = 860 emu/cm^3, damping coefficient α = 0.008, gyromagnetic ratio γ = 17.6 MHz/Oe and the magnetocrystalline anisotropy constant K = 0. Here M_s, γ, and K were extracted from the Kittel fit of the bias-field-dependent precession frequency of a 20-nm-thick Py blanket film deposited under the same condition as the ADLs, while A was obtained from the literature [52]. The dynamic simulations were carried out by first obtaining a static magnetic configuration under a bias magnetic field in the experimental geometry and subsequently applying a pulsed magnetic field with peak magnitude of 30 Oe, rise/fall time of 10 ps and pulse duration of 20 ps over the whole array. For understanding the spatial nature of the observed SW modes, we have further calculated the power and phase maps of these SW modes using a homebuilt Matlab based code named DotMag [53].

8.3. Results and Discussion

Fig. 8.1 (d) and (e) shows the representative time-resolved Kerr rotation traces of the square and octagonal lattice, respectively, with d = 200 nm and a = 400 nm with in-plane bias magnetic field H = 1.0 kOe at φ = 0°. The curves reveal three important temporal regimes. The regime I corresponds to the ultrafast demagnetization (τ_M) due to the incoherent interaction after the pump pulse excites the electrons and the spin subsystems [54]. In regimes II and III, a fast relaxation (s_1) followed by a slow relaxation (s_2) occur due to the relaxation of electron and spin energies to the lattice (s_1), followed by the relaxation of lattice energy to the substrate and the surroundings (s_2) [55, 56]. The damped precessional oscillation is superimposed on the slow relaxation process. We have further performed high-resolution time-resolved Kerr rotation measurements for about 3 ps from the zero delay with 25 fs temporal resolution and fitted the data with the phenomenological three temperature model (3TM) [57]. This accounts for the energy redistribution among electron, spin and the lattice subsystems after the absorption of the

laser by the electronic system, leading to an increase in the spin temperature, causing a loss of magnetization. The expression is:

$$-\frac{\Delta M}{M} = \left\{\left[\frac{A_1}{(1+t/\tau_0)^{1/2}} - \frac{A_2\tau_E - A_1\tau_M}{\tau_E - \tau_M}e^{-t/\tau_M} - \frac{\tau_E(A_1 - A_2)}{\tau_E - \tau_M}e^{-t/\tau_E}\right]H(t) + A_3\delta(t)\right\} \otimes G(t) \qquad (8.1)$$

Here, A_1 represents the amplitude of magnetization after equilibrium between electron, spin and lattice is restored, A_2 is proportional to the maximum rise in the electronic temperature and A_3 represents the state filling effects. $H(t)$ is the Heaviside step function, $\delta(t)$ is the Dirac delta functions and $G(t)$ is a Gaussian function which corresponds to the laser pulse. From the fit we have obtained τ_M = 209 ± 4 fs and 226 ± 6 fs, and s_1 = 962 ± 10 fs and 955 ± 9 fs for the square and octagonal lattices with a = 400 nm, respectively.

Fig. 8.2 (a) shows the fast Fourier transformed (FFT) power spectra of background subtracted experimental time-resolved Kerr rotation data for the ADLs arranged in square symmetry with varying a, taken at H =1.0 kOe and φ = 0°. The square lattice with a = 400 nm shows a rich band of three SW modes, namely *, Δ and # with frequencies ranging from 7.8 to 13.4 GHz. Out of these three modes, the lowest frequency mode has relatively higher power. With the increase of a to 500 nm, we observe a frequency upshift of the modes * and Δ and a frequency downshift of the mode #. As a consequence, the width of the SW band reduces. The power of the intermediate frequency mode Δ also decreases with the increase of a. For a = 600 nm, the mode Δ disappears leaving only two modes. With further increase of a to 700 nm, the frequency gap between the modes * and # decreases further and the width of the SW band is reduced further to be between 9.5 and 11.1 GHz. Fig. 8.2 (b) shows the simulated SW spectra for the square lattice in good agreement with the experimental SW spectra except for the peak width, the relative mode intensities and peak frequencies. The slight disagreements between the experimental and simulated modes can be attributed to the difficulty in precise accounting for the detailed roughness and edge deformation of the real samples in the FDM-based micromagnetic simulations, which may give rise to complex demagnetizing regions at the edges and rounded corners of the triangular antidots. The disagreement may also arise due to the limitation in total time window to ~2 ns taken during the experiment, while the simulated spectra are obtained for 4 ns.

Fig. 8.2 (c) and (d) shows the experimental and simulated SW spectra, respectively, for the ADLs arranged in octagonal symmetry with varying a, taken at H = 1.0 kOe and φ = 0°. Three clear SW modes, namely *, Δ and # are observed for the densest sample with a = 400 nm. Out of these, the intermediate frequency mode Δ has the highest power. With the increase in a (500 nm), the highest frequency mode # undergoes a frequency downshift and merges with the Δ

mode at a = 600 nm. The mode * also undergoes a frequency upshift with the increase in a. With further increase in a, the mode * merges with the mode Δ, leaving only a single mode at a = 700 nm.

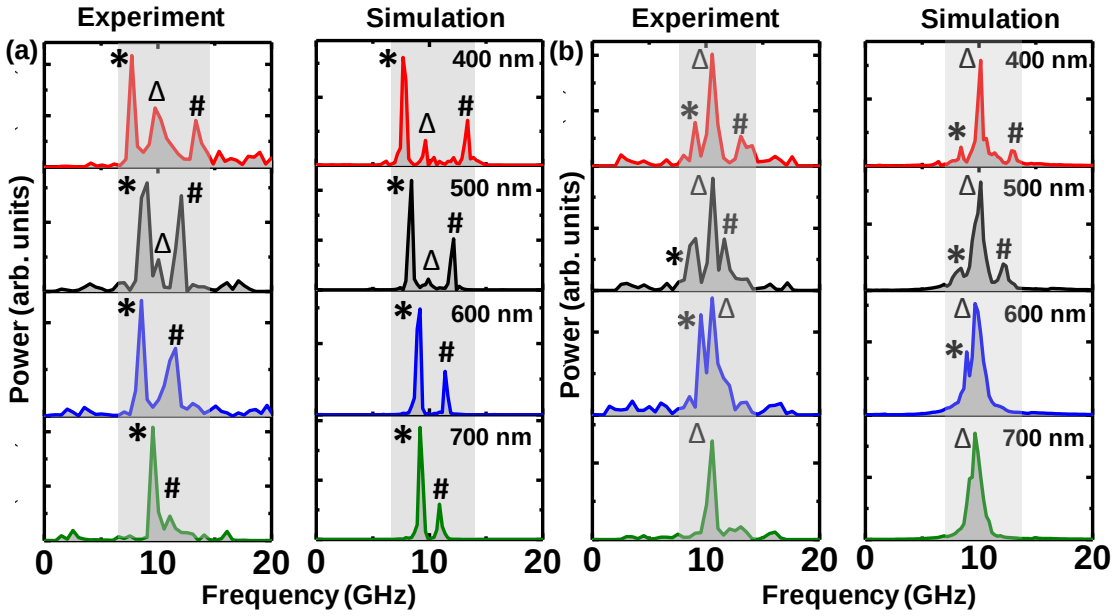

Fig. 8.2: The FFT power spectra of the experimental background subtracted time-resolved Kerr rotation data (left panel) along with the simulated spectra (right panel) obtained for (a) the square and (b) the octagonal lattice at H = 1.0 kOe and φ = 0°. The lattice constants are mentioned at the right-hand side of each panel. The gray shade indicates the maximum width of the SW band for a = 400 nm.

Fig. 8.3 shows the variation of the SW mode frequencies for the square and the octagonal lattice as a function of a. Fig. 8.3 (a) reveals that with the increase in a the intermediate frequency mode Δ of the square lattice disappears and the frequency gap between the modes * and # decreases, leading to an overall reduction of the width of the SW band. On the contrary, for the octagonal lattice (Fig. 8.3 (b)), we observe a merger of both * and # modes with the intermediate frequency mode Δ with the increase of a.

Fig. 8.4 shows the power and phase profiles of the SW modes for the ADLs arranged in the square and the octagonal symmetry with varying a, calculated at H = 1.0 kOe and φ = 0°. We observe different types of extended and quantized standing SW modes for both the lattices due to the formation of confining potentials by the asymmetric demagnetizing regions around the triangular antidots. Different quantization numbers either in the backward volume (BV) geometry or in the Damon−Eshbach (DE) geometry are assigned to the SW modes depending upon the number of antinodes.

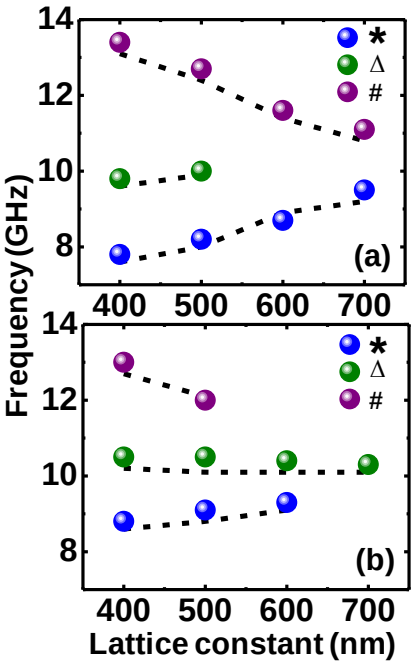

Fig. 8.3: Variation of SW mode frequencies of (a) the square and (b) the octagonal lattice with lattice constant (*a*). The solid symbols correspond to the experimental SW mode frequencies and the dashed lines represent the simulated frequencies.

Fig. 8.4 (a) and (b) shows the power and phase profiles, respectively, for the SW modes of the square lattice. In order to maintain the uniformity in describing the nature of the observed standing SW modes, we have assigned quantization number *n* for the modes forming standing waves in the region between the two consecutive antidots along the y- direction. It is evident that the mode * for the square lattice with a = 400 nm has an extended nature between the neighboring antidot rows along x-direction, i.e., in the DE geometry. The mode Δ also extends through the channel while forming a standing wave pattern with n = 3 between two consecutive antidot rows. For these two modes negligible power outside the channels are observed. The mode # forms a crisscross-like pattern with an even quantization number (n = 4). It is worth mentioning that inside the channels between the neighbouring antidot rows in the x-direction, the potential is not symmetric due to the occurrence of base of a triangle on one side and vertex of another triangle on the other side. Generally, in a symmetric potential, odd modes (with odd number of nodal planes) are observed, whereas, asymmetric potential can accommodate even modes too [58].

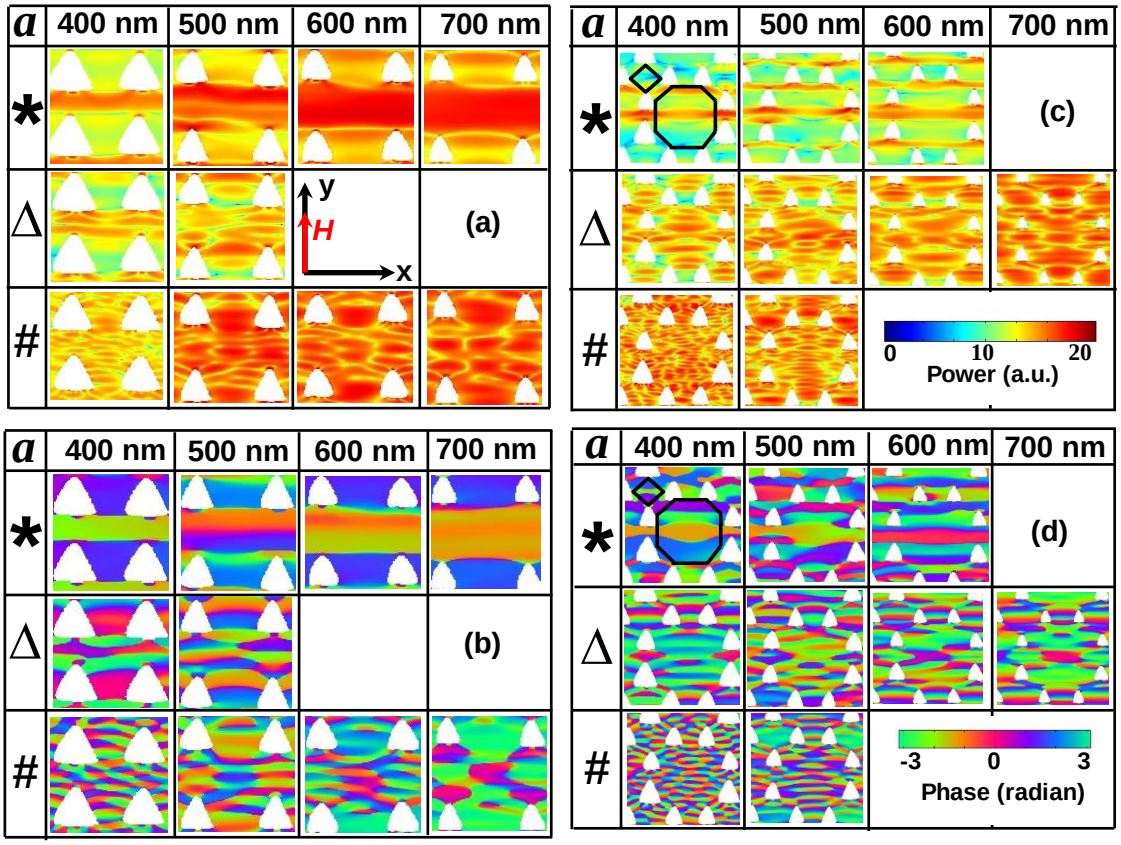

Fig. 8.4: Simulated power and phase maps of different SW modes obtained at H = 1.0 kOe applied at φ = 0°, for the ADLs. The color bars are shown inside the figure. (a) Power and (b) phase profiles for the square lattice and (c) power and (d) phase profiles for the octagonal lattice with varying a.

For a = 500 nm, the mode * has an extended nature in the DE geometry along the channels between the neighbouring antidot rows along the x-direction with a mixed BV nature with n = 2. The mode Δ has n = 5, whereas the mode # is again a crisscross-like mode with n = 6. The mode * has a similar mixed DE-BV nature along the channels with n = 2 and 3 for both a = 600 and 700 nm, respectively. On the other hand, mode # shows crisscross-like nature with n = 7 and 3 for a = 600 and 700 nm, respectively. It is to be noted that power of mode # is located both in the channels and the space between the two consecutive antidots along the x-direction. Notably the spatial uniformity of the power of mode # increases with the increase in a, while the phase profile indicates a gradual conversion form a more quantized mode to a more uniform mode with the increase in a. This may explain the gradual decrease in the frequency of mode #, which eventually approaches that of mode *.

The power and phase profiles of the SW modes for the octagonal lattice are presented in Fig. 8.4 (c) and (d). In this case, depending upon the confinement region of the SWs, two different

quantization numbers, *m* and *n*, are assigned. The quantization of SWs along the y-direction inside the octagonal unit defined by the black octagonal box is represented by *m*, while the quantization of the SWs along the y-direction inside the rhombic unit between two such consecutive octagonal units defined by the black rhombic box is represented by *n*. The modes are generally localized, but some modes extend through the available channels through the neighbouring antidots. The mode numbers (*m*, *n*) for the mode * are (5, 3), (6, 3) and (7, 4) for a = 400, 500 and 600 nm, respectively. Due to the asymmetric potential and the complex lattice geometry, the width of this mode is modulated along the channel in the x-direction. The mode Δ has (*m*, *n*) of (11, 5), (11, 5), (9, 6), and (7, 4) for a = 400, 500, 600 and 700 nm, respectively. The mode # has (*m*, *n*) of (19, 7) and (15, 3) for a = 400 and 500 nm, respectively. Both the Δ and # modes form complex crisscross pattern both within the octagonal and rhombic units. With the increase in *a*, the quantization number of mode # decreases inside the octagonal unit, while it transforms from highly quantized to nearly uniform mode in the rhombic unit. This may explain the decrease in frequency of this mode with the increase in *a*. The phase profiles of the Δ mode also becomes more uniform with the increase in *a*. The spatial power profiles of these two modes also become more uniform. Consequently, their frequencies decrease and seem to approach that of mode *.

For the ADL with square symmetry, the lowest frequency mode *, having an extended nature through the nanochannels, possesses the highest power. This is attributed to the fact that, SW extension through the nanochannels within the neighbouring antidot rows occurs most naturally for the square lattice. On the contrary, SW localization within the octagonal and rhombic units occurs most naturally for the octagonal lattice due to the scarcity of nanochannels allowing the SW propagation. Consequently, the intermediate frequency mode Δ having more localized nature appears with highest power as opposed to the lower or higher frequency modes.

To investigate the SW anisotropy in these samples, we have measured the SW dynamics of the square and octagonal lattices (a = 400 nm), by varying the azimuthal angle (φ) of the bias magnetic field at a fixed strength of H = 1.0 kOe. The bias magnetic field (H) dependence of the SW frequencies at $\varphi = 0°$ and the experimental and simulated FFT power spectra at different values of φ for these samples are presented in Fig. A4.2 and A4.3, respectively of the Appendix IV [52]. The angular dispersions of the precessional frequencies of different SW modes as a function of φ varying from 0° to 180° for the square lattice are shown in Fig. 8.5 (a). The solid symbols represent the experimental frequencies, the hollow symbols represent the simulated frequencies, while the solid lines correspond to the theoretical fits using harmonic functions with different rotational symmetries. It is clear that, while the * and Δ modes appear for almost

all values of φ, the # mode shows a discontinuous angular dispersion appearing only for $0° \leq \varphi \leq 25°$ and $55° \leq \varphi \leq 90°$ and disappearing in between. The modes *, Δ and # exhibit a stronger four-fold anisotropy superposed with a weaker three-fold anisotropy, while the rotational anisotropy of the highest frequency mode (#) is in opposite phase with the other two modes. A combination of triangular shaped antidots arranged on square lattice symmetry gives rise to the observed three- and four fold rotational anisotropy in the SW frequencies of these modes. The anisotropic behavior of the frequency of mode * of the octagonal lattice is shown in Fig. 8.5 (b). The mode * possesses a superposition of strong eight- and weak three-fold anisotropies. The other modes do not exhibit any specific anisotropic behavior. The eight-fold rotational anisotropy arises from the octagonal lattice symmetry, whereas the weak three-fold anisotropy arises due to the triangular shape of the antidots. The eight-fold symmetry is a signature of the quasiperiodicity of the octagonal lattice as reported before [49].

The power profiles of the SW modes for the square and octagonal lattice are shown in Fig. 8.5 (c) and (d), respectively. The mode * for both the lattices undergoes significant modification with the variation of φ. This mode for the square lattice, having an extended nature at $\varphi = 0°$, converts into quasi-extended and localized modes for the intermediate angle before converting back to a flipped extended mode for $\varphi = 90°$. This behavior is repeated periodically in consonance with the observed four-fold rotational anisotropy of this mode. For the octagonal lattice, the mode * also exhibits SW mode conversion between extended and quasi-extended modes having extended nature at 0°, 45° and 90°. This behavior is again repeated periodically in consonance with the observed eight-fold rotational anisotropy of this mode.

The mode Δ shows extended nature for $\varphi = 0°$ and 90°, while being purely localized at 45° in the square lattice. However, this mode shows a peculiar behavior in the octagonal lattice, being extended at 45° and 90°, while being localized at 0°. Apparently, this is due to the lack of channel formation due to the demagnetizing field around the triangular holes at 0°. The crisscross-like mode # also shows a mode conversion between extended (0° and 90°) and localized modes (intermediate angles) in square lattice but no apparent mode conversion is observed in the octagonal lattice for this mode. For both square and octagonal symmetries, a new mode ○ appears in the lower frequency regime at some specific values of φ, with its power primarily concentrated at the sharp corners of the triangular antidots. This mode appears mainly due to the asymmetric demagnetizing regions around the triangular antidots and does not show any specific anisotropic behavior. The appearance of such lower frequency edge localized mode in triangular antidots has been reported earlier [59].

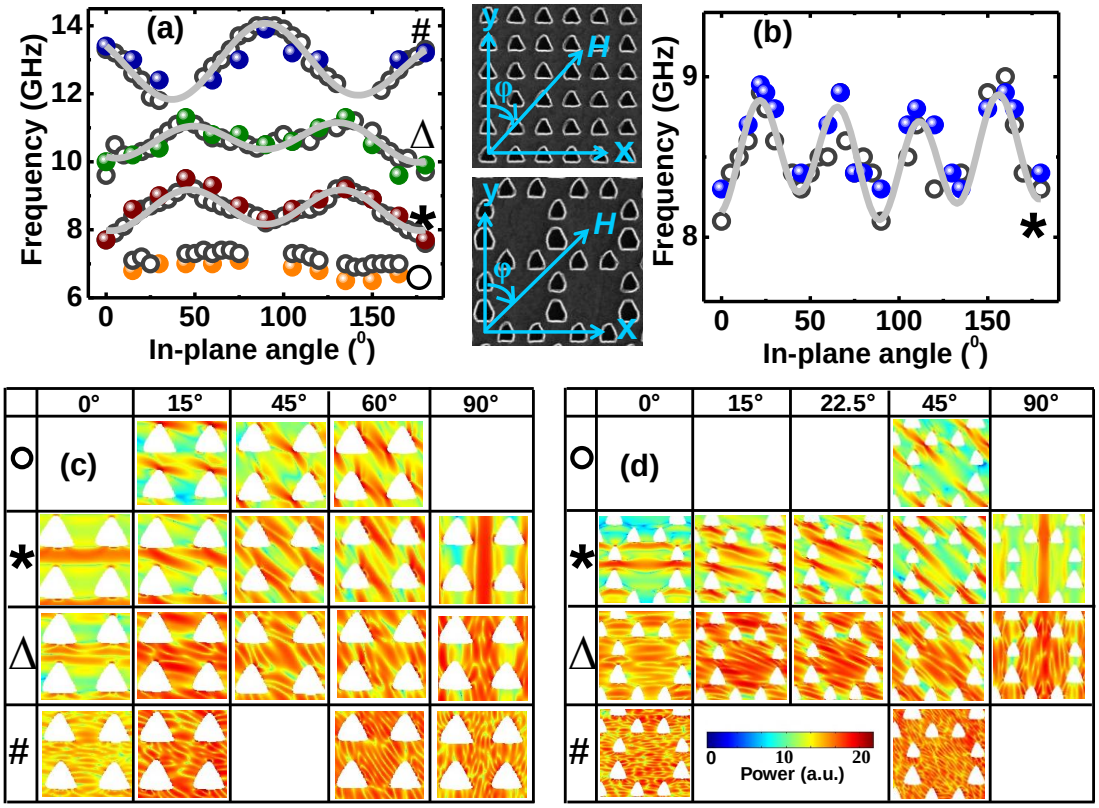

Fig. 8.5: Variation of SW frequencies with the azimuthal angle (φ) of *H* varying from 0° to 180° for (a) the square and (b) the octagonal lattice symmetry with *a* = 400 nm at *H* = 1.0 kOe. The solid symbols represent the experimental data points and the hollow symbols represent the simulated data points. The solid lines describe the sinusoidal fits for the observed anisotropic SW modes. Simulated power profiles of the SW modes for (c) the square and (d) the octagonal lattice symmetry with *a* = 400 nm at some specific values of *φ*. The color bar is shown inside the Fig.

In order to gain more insights into the variation of the SW modes with varying *a* in these ADLs with square and octagonal symmetry, we have calculated the magnetization maps and the magnetostatic field distributions of these lattices using the LLG micromagnetics simulator [60]. The magnetization maps (domain plot) around the triangular antidots for the square lattice with different *a*, at *H* = 1.0 kOe are shown in Fig. 8.6 (a) and (b), whereas, the contour plots of simulated internal field distributions are shown in Fig. 8.6 (c) and (d). The internal field lines around the antidots clearly indicate an asymmetric potential across the channel of extension of the SWs. The demagnetizing regions, as well as the density of field lines around the antidots reduce with the increase in *a*. The internal field strengths (B_{in}) are obtained by taking line scans along the dashed lines in y-direction as shown in Fig. 8.6 (c) and (d). Fig. 8.6 (e) shows the variation of B_{in} with distance for *a* = 400 and 700 nm. It is evident from Fig. 8.6 (f) that B_{in} increases significantly from ~ 9.6 kOe to ~ 10.7 kOe with the increase in *a* within the channels

of SW extension due to the systematic decrease in the overlapping between the demagnetizing fields around the antidots. The increase in B_{in} with a is responsible for the similar increase in the frequencies of modes * and Δ with a as observed in Fig. 8.3 (a).

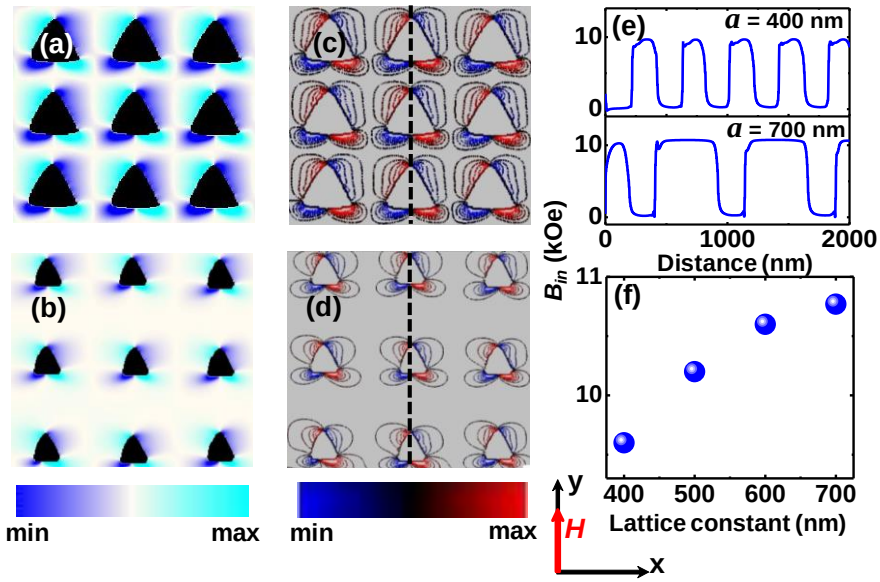

Fig. 8.6: Magnetization maps for the square lattice with (a) a = 400 nm and (b) a = 700 nm. Contour plots of the simulated internal field distributions for the square lattice with (c) a = 400 nm and (d) a = 700 nm. The corresponding color maps and the schematic of H are shown at the bottom of the figure. (e) Line scans of the simulated internal field (B_{in}) of the two lattices taken along the dotted lines as shown in (c) and (d). The values of a are mentioned in the Fig. (f) The variation of B_{in} with a.

We have further investigated the magnetization maps (Fig. 8.7 (a) and (b)) and the contour plots of simulated internal field distributions (Fig. 8.7 (c) and (d)) for the octagonal lattice for different values of a, at H = 1.0 kOe. We have calculated the B_{in} by taking line scans in different region of the lattice as shown in Fig. 8.7 (c) and 8.7 (d). It is evident from Fig. 8.7 (e) that for the densest octagonal lattice with a = 400 nm, B_{in} is significantly lower (~9.3 kOe) in region 1 as compared to the regions 2 (~10.5 kOe) and 3 (~10.3 kOe). This prominent modification in B_{in} arises from the overlapping of complex demagnetizing field in this dense lattice having different magnetic environment in different regions stemming from its octagonal symmetry as well as triangular holes. However, due to the decrease in the overall effective demagnetizing fields, B_{in} increases with a, and becomes identical in all three regions (Fig. 8.7 (f)) at a = 700 nm, leading towards the merging of the three modes *, Δ and # to a single mode for a = 700 nm. The variations of B_{in} with a in all three regions of the octagonal lattice are shown in Fig. 8.7 (g). The sharp increase in B_{in} with a in region 1 (channel) is responsible for the increase in frequency of the mode * with a. On the contrary, B_{in} increases very gently with a inside region

2 (rhombic unit) and remains nearly constant inside region 3 (octagonal unit). This might be responsible for the negligible variation of the frequency of mode Δ with *a*.

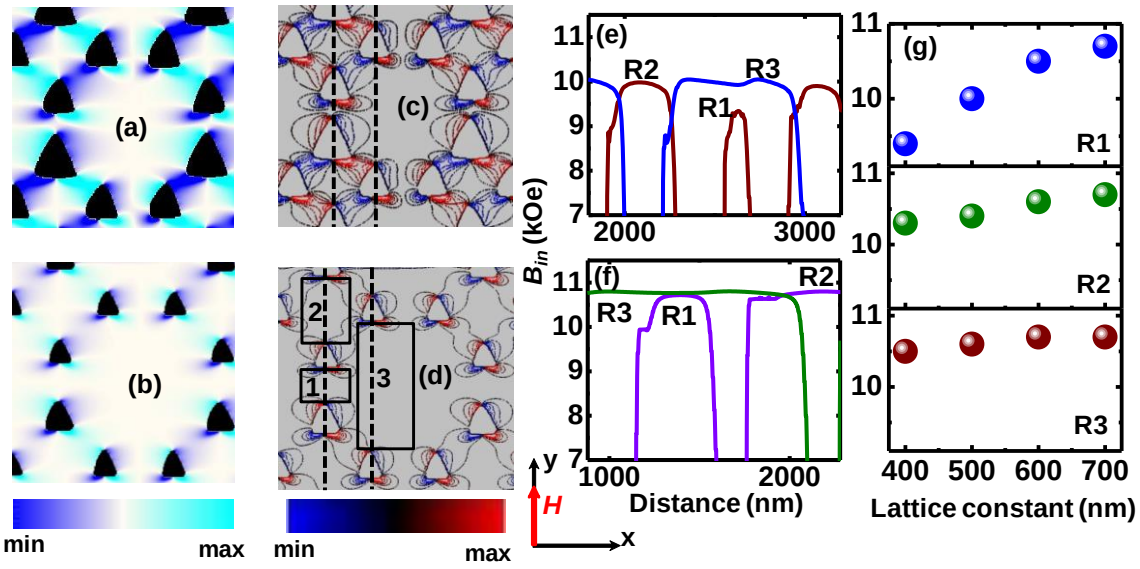

Fig. 8.7: Magnetization maps for the octagonal lattice with (a) *a* = 400 nm and (b) *a* = 700 nm. Contour plots of the simulated internal field distributions for the octagonal lattice with (c) *a* = 400 nm and (d) *a* = 700 nm. The corresponding color maps and the schematic of *H* are shown at the bottom of the figure. (e) Line scans of the simulated internal field (B_{in}) for *a* = 400 nm and (f) *a* = 700 nm taken along the black dotted lines as shown in (c) and (d). (g) The variation of B_{in} with *a*, at three different regions as shown by black boxes in (d).

8.4. Conclusion

In conclusion, we have studied antidot magnonic crystals with complex geometry in the form of octagonal lattice with a triangular shaped basis lacking reflection symmetry and compared its SW dynamics with that of a square lattice. Rich multimodal SW spectra are obtained for the most densely packed lattice, whereas the number of SW modes reduces systematically with the increase in lattice constant approaching towards a nearly thin film-like behavior due to the reduction of the demagnetizing field around the antidots in both lattice symmetries. A combination of the triangular shaped antidots arranged in octagonal symmetry exhibits a strong eight-fold anisotropy superposed with a weak three-fold anisotropy, whereas, a strong four-fold anisotropy superposed with a weak three-fold anisotropy is observed in the square lattice. The experimental observations have been reproduced by micromagnetic simulations and the spatial profiles of the anisotropic SW modes unveiled mode conversion between extended, quasi-extended and quantized standing SW modes with the variation of in-plane bias magnetic field orientation, along with the appearance of some localized edge modes at some specific bias

magnetic field orientation due to the presence of the sharp triangular corners of the antidots. The internal fields including the demagnetization field distributions interpret the origin of the observed SW modes. Our findings offer new potentials in magnonic crystals with complex geometry that are expected to provide exotic SW propagation properties to pave way for the advancement of reprogrammable magnonics.

References

[1] S. Neusser and D. Grundler, Adv. Mater. **21**, 2927 (2009).
[2] V. V. Kruglyak, S. O. Demokritov and D. Grundler, J. Phys. D: Appl. Phys. **43**, 264001 (2010).
[3] B. Lenk, H. Ulrichs, F. Garbs and M. Münzenberg, Phys. Rep. **507**, 107 (2011).
[4] A. V. Chumak, V. I. Vasyuchka, A. A. Serga and B. Hillebrands, Nat. Phys. **11**, 453 (2015).
[5] P. Graczyk and M. Krawczyk, Phys. Rev. B **96**, 024407 (2017).
[6] W. Yu, T. Yu and G. E. W. Bauer, Phys. Rev. B **102**, 064416 (2020).
[7] C. Liu, J. Chen, T. Liu, F. Heimbach, H. Yu, Y. Xiao, J. Hu, M. Liu, H. Chang, T. Stueckler, S. Tu, Y. Zhang, Y. Zhang, P. Gao, Z. Liao, D. Yu, K. Xia, N. Lei, W. Zhao and M. Wu, Nat. Commun. **9**, 738 (2018).
[8] D. L. Quirion, Y. Tabuchi, A. Gloppe, K. Usami and Y. Nakamura, Appl. Phys. Exp. **12**, 070101 (2019).
[9] Y. Li, W. Zhang, V. Tyberkevych, W. K. Kwok, A. Hoffmann and V. Novosad, J. Appl. Phys. **128**, 130902 (2020).
[10] S. Neusser, B. Botters and D. Grundler, Phys. Rev. B **78**, 054406 (2008).
[11] P. Vavassori, G. Gubbioti, G. Zangari, C. T. Yu, H. Yin, H. Jiang and G. J. Mankey, J. Appl. Phys. **91**, 7992 (2002).
[12] V. E. Demidov, M. P. Kostylev, K. Rott, J. Münchenberger, G. Reiss and S. O. Demokritov, Appl. Phys. Lett. **99**, 082507 (2011).
[13] S. K. Kim, K. S. Lee and D. S. Han, Appl. Phys. Lett. **95**, 082507 (2009).
[14] Y. Acremann, X. W. Yu, A. A. Tulapurkar, A. Scherz, V. Chembrolu, J. A. Katine, M. J. Carey, H. C. Siegmann and J. Stohr, Appl. Phys. Lett. **93**, 102513 (2008).
[15] H. Yu, G. Duerr, R. Huber, M. Bahr, T. Schwarze, F. Brandl and D. Grundler, Nat. Commun. **4**, 2702 (2013).
[16] K. Vogt, F. Y. Fradin, J. E. Pearson, T. Sebastian, S. D. Bader, B. Hillebrands, A. Hoffmann and H. Schultheiss, Nat. Commun. **5**, 3727 (2014).
[17] Y. Au, M. Dvornik, O. Dmytriiev and V.V. Kruglyak, Appl. Phys. Lett. **100**, 172408 (2012).
[18] K. S. Lee and S. K. Kim, J. Appl. Phys. **104**, 053909 (2008).
[19] A. V. Chumak, A. A. Serga and B. Hillebrands, Nat. Commun. **5**, 4700 (2014).
[20] T. Schneider, A. A. Serga, B. Leven and B. Hillebrands, Appl. Phys. Lett. **92**, 022505 (2008).
[21] R. Mandal, P. Laha, K. Das, S. Saha, S. Barman, A. K. Raychaudhuri and A. Barman, Appl. Phys. Lett. **103**, 262410 (2013).
[22] R. Mandal, S. Saha, D. Kumar, S. Barman, S. Pal, K. Das, A. K. Raychaudhuri, Y. Fukuma, Y. Otani and A. Barman, ACS Nano **6**, 3397 (2012).
[23] R. Mandal, S. Barman, S. Saha, Y. Otani and A. Barman, J. Appl. Phys. **118**, 053910 (2015).
[24] S. Pal, J. W. Klos, K. Das, O. Hellwig, P. Gruszecki, M. Krawczyk and A. Barman, Appl. Phys. Lett. **105**, 162408 (2014).
[25] S. Mallick, S. Mondal, T. Seki, S. Sahoo, T. Forrest, F. Maccherozzi, Z. Wen, S. Barman, A. Barman, K. Takanashi and S. Bedanta, Phys. Rev. Appl. **12**, 014043 (2019).
[26] A. De, S. Mondal, S. Sahoo, S. Barman, Y. Otani, R. K. Mitra and A. Barman, Beilstein J. Nanotechnol. **9**, 1123 (2018).
[27] O. N. Martyanov, V. F. Yudanov, R. N. Lee, S. A. Nepijko, H. J. Elmers, R. Hertel, C. M. Schneider and G. Schonhense, Phys. Rev. B **75**, 174429 (2007).
[28] S. Neusser, B. Botters, M. Becherer, D. Schmitt-Landsiedel and D. Grundler, Appl. Phys. Lett. **93**, 122501 (2008).

[29] K. Adhikari, S. Barman, R. Mandal, Y. Otani and A. Barman, Phys. Rev. Appl. **10**, 044010 (2018).
[30] S. Choudhury, S. Majumder, S. Barman, Y. Otani and A. Barman, Phys. Rev. Appl. **10**, 064044 (2018).
[31] F. Montoncello, L. Giovannini and M. Krawczyk, J. Appl. Phys. **112**, 033911 (2012).
[32] S. Neusser, G. Duerr, S. Tacchi, M. Madami, M. L. Sokolovskyy, G. Gubbiotti, M. Krawczyk and D. Grundler, Phys. Rev. B **84**, 094454 (2011).
[33] D. Levine and P. J. Steinhardt, Phys. Rev. B **34**, 596 (1986).
[34] M. C. Rechtsman, H. C. Jeong, P. M. Chaikin, S. Torquato and P. J. Steinhardt, Phys. Rev. Lett. **101**, 073902 (2008).
[35] A. L. Chen, Y. S. Wang, Y. F. Guo and Z. D. Wang, Solid State Commun. **145**, 103 (2008).
[36] D. Shi, Z. Budrikis, A. Stein, S. A. Morley, P. D. Olmsted, G. Burnell and C. H. Marrows, Nat. Phys.**14**, 309, (2018).
[37] C. H. Chen, R. Z. Qiu, C. H. Chang and W. J. Hsueh, AIP Adv. **4**, 087102 (2014).
[38] C. H. O. Costa, M. S. Vasconcelos and E. L. Albuquerque, J. Appl. Phys. **109**, 07D319 (2011).
[39] C. H. O. Costa, M. S. Vasconcelos, P. H. R. Barbosa and F. F. Barbosa Filho, J. Magn. Magn. Mater. **324**, 2315 (2012).
[40] S. V. Grishin, E. N. Beginin, M. A. Morozova, Y. P. Sharaevskii and S. A. Nikitov, J. Appl. Phys. **115**, 053908 (2014).
[41] V. S. Bhat and D. Grundler, Phys. Rev. B **98**, 174408 (2018).
[42] S. Watanabe, V. S. Bhat, K. Baumgaert and D. Grundler, Adv. Funct. Mater. **2**, 2001388 (2020).
[43] F. Lisiecki, J. Rychły, P. Kuświk, H. Głowiński, J. W. Kłos, F. Groß, N. Träger, I. Bykova, M. Weigand, M. Zelent, E. J. Goering, G. Schütz, M. Krawczyk, F. Stobiecki, J. Dubowik and J. Grafe, Phys. Rev. Appl. **11**, 054061 (2019).
[44] B. Farmer, V. S. Bhat, A. Balk, E. Teipel, N. Smith, J. Unguris, D. J. Keavney, J. T. Hastings and L. E. De Long, Phys. Rev. B **93**, 134428 (2016).
[45] M. Senechal, Quasicrystals and Geometry (Cambridge University Press, Cambridge, 1996).
[46] M. Gardner, Penrose Tiles to Trapdoor Ciphers and the Return of Dr Matrix MAA Spectrum Mathematical Association of America Spectrum Series (Cambridge University Press, 1997), p. 41, ISBN: 0883855216, 9780883855218.
[47] S. Saha, R. Mandal, S. Barman, D. Kumar, B. Rana, Y. Fukuma, S. Sugimoto, Y. Otani and A. Barman, Adv. Funct. Mater. **23**, 2378 (2013).
[48] S. Mondal, S. Barman, S. Choudhury, Y. Otani and A. Barman, J. Magn. Magn. Mater. **95**, 458 (2018).
[49] S. Choudhury, S. Barman Y. Otani, and A. Barman, ACS Nano **11**, 8814 (2017).
[50] A. Barman and A. Haldar, Solid State Phys. **65**, 1 (2014).
[51] M. Donahue, D. G. Porter, NIST Interagency Report No. 6376; National Institute of Standard and Technology, Gaithersburg, MD, URL: http://math.nist.gov/oommf: (1999).
[52] K. H. J. Buschow, Handbook of Magnetic Materials; North Holland: Amsterdam, Netherlands, **18**, 168 (2009).
[53] D. Kumar, O. Dmytriiev, S. Ponraj, and A. Barman, J. Phys. D: Appl. Phys. **45**, 015001 (2012).
[54] E. Beaurepaire, J. C. Merle, A. Daunois and J.-Y. Bigot, Phys. Rev. Lett. **76**, 22 (1996).
[55] A. Laraoui, J. Venuat, V. Halte, M. Albrecht, E. Beaurepaire and J.-Y. Bigot, J. Appl. Phys. **101**, 09C105 (2007).
[56] A. Barman and J. Sinha, Spin Dynamics and Damping in Ferromagnetic Thin Films and Nanostructures, Springer International Publishing AG, 1 (2018).

[57] U. Atxitia, O. Chubykalo-Fesenko, J. Walowski, A. Mann and M. Münzenberg, Phys. Rev. B **81**, 174401 (2010).
[58] B. K. Mahato, B. Rana, D. Kumar, S. Barman, S. Sugimoto, Y. Otani and A. Barman, Appl. Phys. Lett. **105**, 012406 (2014).
[59] A. De, S. Mondal, S. Choudhury, S. Sahoo, S. Majumder, S. Barman, Y. Otani and A. Barman, J. Magn. Magn. Mater. **487**, 165263 (2019).
[60] LLG Micromagnetics Simulator, developed by M. R. Scheinfein, http://llgmicro.home.mindspring.com (accessed March 8, 2018).

Chapter 9

9. Magnetic Configuration Driven Femtosecond Spin Dynamics in Synthetic Antiferromagnets

9.1. Introduction

The phenomenon of ultrafast demagnetization has attracted intense interest since its discovery in nickel thin films in 1996 by the pioneering experiment of Beaurepaire *et al.* [1] followed by a flurry of other reports in various systems [2-4]. The possibility of optically manipulating spins on femtosecond time scales promises potential applications in spintronic devices such as all-optical switching [5-6]. However, the underlying mechanism of this phenomenon is still debatable. The femtosecond laser induced ultrafast demagnetization in alloys and multilayers is even more challenging and a topic of recent interest after the introduction of an optically induced spin transfer (OISTR) effect [7-8]. Indeed, a wide range of theoretical and experimental investigations have been carried out and several models have been proposed to explain this ultrafast modification of magnetization. Zhang and Hübner explained the ultrafast demagnetization process from the exchange interaction and spin-orbit coupling (SOC) [9] and later as a cooperative effect of laser field and SOC field [10]. Subsequently, various models based on the conservation of angular momentum relying upon phonon- [11-13], electron- [14,15], magnon-[16] mediated, direct laser induced [17] or relativistic [18] spin-flip scattering (SFS) processes have emerged. Koopmans *et al.* [11] first explained ultrafast demagnetization by electron-phonon SFS via the Elliott-Yafet (EY-SFS) mechanism, due to an angular momentum transfer from <S> to <L>. Later, some other theoretical studies have also shown that the demagnetization occurs due to electron-phonon scattering in *fcc*-Ni, *bcc*-Fe and *fcc*-Co [12, 13]. Some reports have claimed by theoretical calculations that electron-electron Coulomb-like scattering [14, 15] in systems with high SOC is responsible for the ultrafast demagnetization. Investigation on Fe thin films [16] suggested that the ultrafast demagnetization is determined by the rate of magnon emission by scattering with excited electrons, where the crystal acts as a perfect sink for angular momentum. This study disproved the influence of the EY-SFS mechanisms. Further reports have also suggested that optically induced demagnetization cannot be explained exclusively by electron-phonon or electron-

magnon scattering, but that the combination of these two processes may give larger demagnetization rates [19]. The Einstein-de Haas effect has also been discussed in the context of ultrafast demagnetization phenomena [20] and it has been argued that phonon-phonon or phonon-magnon scattering mechanisms are too slow for an ultrafast demagnetization to occur [21]. Evidence of THz emission accompanied with ultrafast demagnetization has also been reported [22]. In 2010, a new model based on the superdiffusive transport of optically induced spin current has been proposed. Malinowski *et al*. [23] first showed that the excited hot electron spin transport (ST) enhances and speeds up the demagnetization in a spin valve structure. Thereafter, Battiato *et al*. proposed a theoretical model based on transport of optically excited spin polarized electrons in the superdiffusive regime [24]. Afterwards, several experimental observations demonstrated that ST, rather than SFS, plays a crucial role in ultrafast demagnetization [25, 26]. Recently, simultaneous presence of both direct and indirect excitations has been shown to lead to ultrafast demagnetization in ferromagnetic multilayers [27, 28].

Antiferromagnets (AFM) have recently generated a huge interest for emerging high-speed spintronics [29] due to their very fast dynamics, ability to generate and detect spin-polarized electric currents, and their robustness against external magnetic fields. They are routinely used as a pinning layer to fix the magnetic orientation of the ferromagnetic (FM) reference layer in spin valves and magnetic tunnel junctions. As opposed to FM magnons, the AFM magnons show polarization as an additional degree of freedom, which could be useful for information processing [30]. Synthetic antiferromagnets (SAF) are built from FM layers periodically interleaved with metallic or insulating spacers, where the magnetization of adjacent FM layers alternate owing to the AFM interlayer exchange coupling (IEC). For metallic spacers, IEC is achieved via a Ruderman-Kittel-Kasuya-Yosida (RKKY)–type exchange interaction mediated by spin-polarized charge carriers in the spacer [31]. For insulating spacers, the IEC depends on the spin-polarized tunnelling, and its strength decays exponentially with the spacer layer thickness [32]. The IEC in SAF is much weaker than the direct exchange or superexchange coupling in atomic AFMs, which allows for manipulation of the AFM order more easily in SAFs [33]. The control of the IEC strength and the full understanding of the domain structure and the reversal of such structures under external fields is of high interest and has been extensively studied in recent years [34-36]. Recently engineering of AFM-IEC in all-perovskite-based $La_{2/3}Ca_{1/3}MnO_3/CaRu_{1/2}Ti_{1/2}O_3$ and $La_{2/3}Sr_{1/3}MnO_3/CaRu_{1/2}Ti_{1/2}O_3$ superlattices has been reported where sharp step-like hysteresis loops with magnetization plateaus depending on the repetition number of the stacking bilayers have been observed [37].

Hitherto, very few reports on the study of ultrafast spin dynamics in SAFs exist. Interlayer ST has been explored for studying the ultrafast demagnetization in $[Co–Pt]_n$ multilayers with SOC, which are antiferromagnetically coupled through a metallic Ru spacer or insulating NiO spacer [23]. A recent report showed fundamentally different behavior in femtosecond laser pulse induced ferro- and antiferromagnetic dynamics in one and the same material - metallic dysprosium [38]. The AFM order was found to be significantly faster and much more efficiently reduced by optical excitation than its FM counterpart.

In this article, by using time-resolved magneto-optical Kerr effect (TR-MOKE) magnetometry we have investigated the ultrafast magnetization dynamics in a series of perpendicular magnetic anisotropy (PMA) SAF multilayers (p-SAF), in the form of $\{[Co/Pt]_{X-1}/Co/Y\}_{N-1}/[Co/Pt]_X$, where Y corresponds to Ru or Ir spacer layers, 'X' is the number of bilayer repeats and 'N-1' corresponds to the number of spacer layers in the SAF samples [34, 39]. We have experimentally observed the evidence of simultaneous presence of both SFS and ST mechanisms controlling the ultrafast demagnetization process in these samples. The ultrafast demagnetization time strongly depends on the magnetic state of the samples and the relative orientation of magnetization between the layers. Moreover, the respective contributions of the two mechanisms can also be controlled by specially designing the sample, changing the intermediate spacer layers and changing the excitation fluence.

9.2. Methods

The samples have been prepared with a confocal dc magnetron sputter system, ATC-2200, from AJA International. The base pressure was less than 3×10^{-7} Torr, and the Ar sputtering gas pressure was set to 3 mTorr. For homogenous growth, the sample holder was rotated at about 1 Hz frequency, and deposition rates of ~ 0.1 nm/s were chosen. The multilayers were deposited on substrates of thermally oxidized Si with 100 nm SiO_2 surface oxidation layer. A seed-layer structure of Ta(0.5 nm)/Pt(20 nm) was used, where the amorphous Ta serves for adhesion and Pt provides a strong (111) texture, upon which Co/Pt grows well with high PMA. A capping layer of Pt (2 nm) has been deposited on top of each multilayer to prevent oxidation.

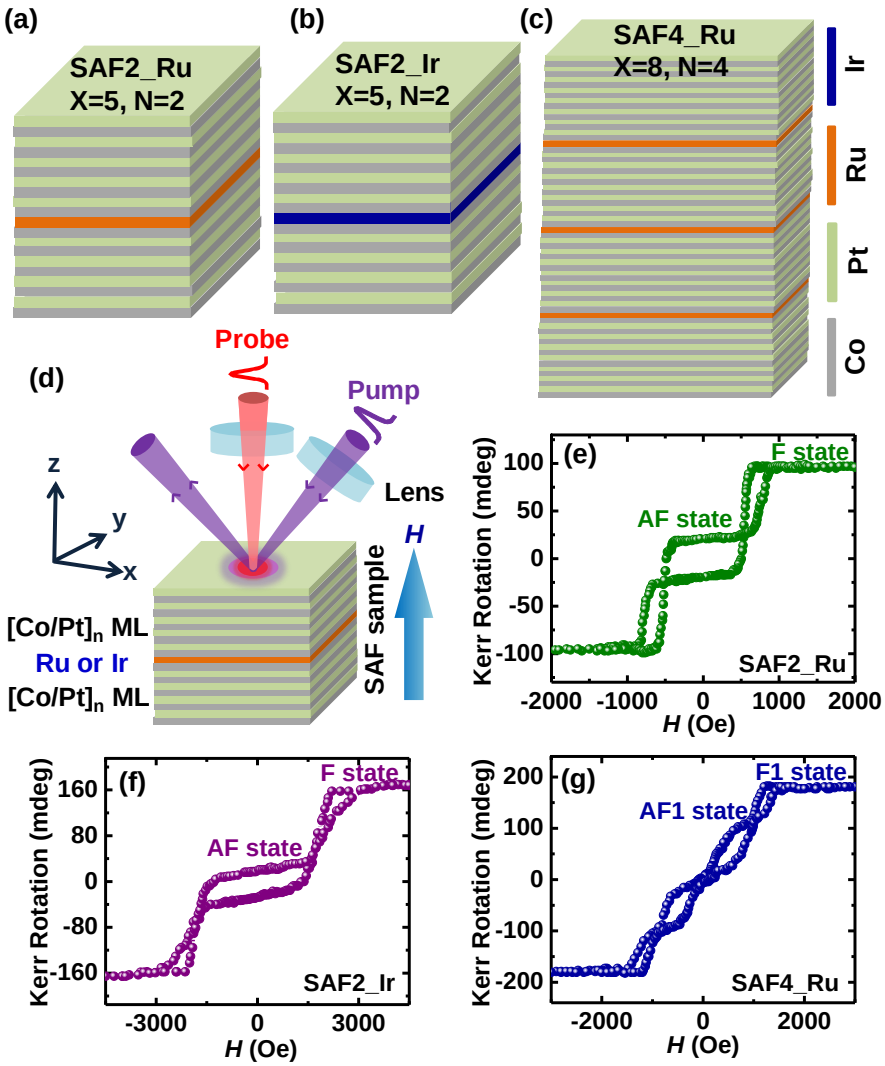

Fig. 9.1: (a) Schematic of the (a) SAF2_Ru sample, where two [Co/Pt] ML stacks are separated by a single Ru spacer, (b) SAF2_Ir sample, where two [Co/Pt] ML stacks are separated by a single Ir spacer, and (c) SAF4_Ru sample, where four [Co/Pt] ML stacks are separated by three Ru spacers. Here, 'X' is the number of Co/Pt bilayer repeats and 'N-1' corresponds to the number of spacer layers in the SAF samples. Different colors representing different materials are indicated in the right- hand side of the figure (d) Schematic of the experimental geometry in the TR-MOKE experiment. Static MOKE hysteresis loops for the (e) SAF2_Ru, the (f) SAF2_Ir, and the (g) SAF4_Ru sample.

To study the ultrafast magnetization dynamics of this sample, we use a custom-built TR-MOKE magnetometer based on two color non-collinear optical pump-probe technique. The fundamental output from an amplified femtosecond laser system with wavelength, $\lambda = 800$ nm, repetition rate = 1 kHz , pulse width ~ 40 fs (Libra, Coherent Inc.) is used as a probe to detect the time-resolved polar Kerr signal from the sample, whereas its second harmonic signal ($\lambda =$ 400 nm, pulse width > 40 fs) is used as a pump to excite the magnetization dynamics of the sample. The temporal resolution of the measurement is limited by the cross-correlation between the pump and probe pulses (~ 100 fs). The diameter of the probe beam is ~ 100 μm and is

incident normally on the sample, whereas the pump beam is kept slightly defocused (the spot size is ~ 300 μm) and is incident obliquely (~ 30° to the normal to the sample plane) on the sample maintaining an excellent spatial overlap with the probe spot. A time-resolved Kerr signal is collected from the uniformly excited part of the sample and slight misalignment during the course of the experiment does not significantly affect the pump-probe signal. The pump beam is chopped at a frequency of 373 Hz and the dynamic signal in the probe pulse is detected by using a lock-in amplifier in a phase-sensitive manner. Simultaneous time-resolved reflectivity and Kerr rotation data are measured and no significant breakthrough of one into the other is found. A variable external magnetic field (*H*) is applied in the OOP direction of the sample. The probe fluence is kept constant at 2 mJ/cm^2 during the measurement to avoid any additional contribution to the modulation of spin dynamics via laser heating. The experiments have been performed for varying pump fluence from 13 to 58 mJ/cm^2 to study the fluence-dependent modulation in magnetization dynamics. All the experiments have been performed under ambient conditions and room temperature.

9.3. Results and Discussion

We have investigated three sets of samples, namely SAF2_Ru (overall SAF thickness = 13.1 nm) consisting of Pt(20 nm)/{[Co(0.4 nm)/P t(0.7 nm)]$_4$/Co(0.4 nm)/Ru (0.8 nm)}/[Co(0.4 nm)/Pt(0.7 nm)]$_5$/Pt(2 nm), SAF2_Ir (overall SAF thickness = 12.8 nm) consisting of Pt(20 nm)/{[Co(0.4 nm)/Pt(0.7 nm)]$_4$/Co(0.4 nm)/Ir(0.5 nm)}/[Co(0.4 nm)/Pt(0.7 nm)]$_5$/Pt(2 nm) and SAF4_Ru (overall SAF thickness = 37.5 nm) consisting of Pt (20 nm)/{[Co(0.4 nm)/Pt(0.7 nm)]$_7$/Co(0.4 nm)/Ru(0.8 nm)}$_3$/[Co(0.4 nm)/Pt(0.7 nm)]$_8$/Pt(2 nm). The schematic of the sample stacks is shown in Fig. 9.1 (a), (b) and (c). Figs. 9.1 (e) - (g) represent the hysteresis loops of SAF2_Ru, SAF2_Ir and SAF4_Ru samples, respectively, measured by the static magneto-optical Kerr effect (SMOKE) magnetometer at room temperature. The static MOKE loops were obtained by using the probe laser (λ = 800 nm, repetition rate = 1 kHz, pulse width ~ 40 fs from Libra, Coherent Inc.) of the optical pump-probe experiment as described later in this article. This is to ensure that the optical absorption profiles during the static MOKE and the TR-MOKE measurements are identical. An out-of-plane (OOP) direction magnetic field with respect to the sample plane was varied to measure MOKE loops in the polar Kerr geometry. For all three samples stepped hysteresis loops were observed which indicate distinct switching fields separated by AF plateaus for these samples. For the SAF2_Ru (Fig. 9.1 (e)) and SAF2_Ir (Fig. 9.1 (f)) samples, where two [Co/Pt]$_n$ ML blocks are separated by a single Ru or Ir spacer,

the hysteresis loops show a two step reversal. On the contrary, a four-stepped reversal has been observed for the SAF4_Ru sample (Fig. 9.1 (g)), as a consonance of the four [Co/Pt] ML blocks periodically separated by three Ru spacers. It is also evident that the IEC strength is higher in SAF2_Ir (AF plateau between ±1500 Oe) as opposed to SAF2_Ru (AF plateau between ±500 Oe), indicating that the Ir-based SAF is strongly coupled, whereas the Ru-based SAF is significantly weaker coupled. It is worth mentioning that the MOKE loops show finite values of the Kerr rotation in the AF plateaus presumably due to the varying absorption profile in the multilayer, which may lead to different Kerr sensitivities in each layer. Earlier works have confirmed through experiment and calculation that the MOKE signal stemming from the magnetization reversal of different multilayers is similar to the light absorption ratio within those layers [23]. From the MOKE hysteresis loops we extracted the relative changes in the Kerr rotations in both F (F1) and AF (AF1) states of the three samples, which was further used to estimate the values of the transient magnetization quenching ($\Delta M/M$ vs. time) in different magnetic states of the samples.

The main focus of this article is to investigate the laser induced ultrafast demagnetization of the p-SAF structures. A TR-MOKE magnetometer with a two-color optical pump-probe experiment in non-collinear geometry has been used to measure the dynamic Kerr rotation. The fundamental output from an amplified femtosecond laser system with wavelength, $\lambda = 800$ nm, repetition rate = 1 kHz, pulse width ~ 40 fs (Libra, Coherent Inc.) is used to probe the dynamics, whereas, its second harmonic signal ($\lambda = 400$ nm, pulse width > 40 fs) is used to pump the sample magnetization. The pump beam is modulated by a mechanical chopper at 372 Hz for lock-in detection of the pump-induced Kerr rotation. The time varying Kerr rotation data ($\Delta\theta$) is normalized with θ, where 2θ corresponds to the change in Kerr rotation for complete reversal of magnetization (+M to -M). Subsequently $\Delta\theta/\theta$ is considered to be equal to $\Delta M/M$, i.e. transient variation of magnetization. We have also verified that the relative variation in transient Kerr rotation is about one to two orders of magnitude larger than the relative variation in transient reflectivity. This confirms that the optical effects barely influence the Kerr rotation signal in our samples (Fig. A5.1 of Appendix V). A variable external magnetic field is applied in the OOP direction of the sample and the experiments have been performed for varying pump fluence from 13 mJ/cm^2 to 58 mJ/cm^2 and a fixed probe fluence of 2 mJ/cm^2. The time-resolved $\Delta M/M$ traces have been captured in both, the ferromagnetically saturated state, where the magnetizations of different [Co/Pt] ML stacks in the SAF are in parallel alignment (F state) and the antiferromagnetic plateau region, where their magnetization directions are antiparallel (AF state). The experimental time-resolved data capturing both the ultrafast demagnetization and

the subsequent fast magnetization recovery within a few picoseconds are fitted with a phenomenological expression, obtained by solving the equations of the three-temperature model (3TM) [23, 40], to extract the ultrafast demagnetization (τ_M) and fast relaxation (τ_E) times. This phenomenological model pictures how energy is redistributed among electrons, spins and the lattice after the laser power has been absorbed by the electronic system. The energy flow ultimately leads to an increase in the spin temperature, thereby reducing the magnetization. The expression is:

$$-\frac{\Delta M}{M} = \left\{\left[\frac{A_1}{(1+t/\tau_0)^{1/2}} - \frac{A_2\tau_E - A_1\tau_M}{\tau_E - \tau_M}e^{-t/\tau_M} - \frac{\tau_E(A_1 - A_2)}{\tau_E - \tau_M}e^{-t/\tau_E}\right]H(t) + A_3\delta(t)\right\}\otimes G(t) \quad (1)$$

which is obtained by solving the energy rate equation in between three different degrees of freedom, e.g. electron, spin, and lattice under low pump fluence condition. Here, A_1 represents the amplitude of magnetization after equilibrium between electron, spin and lattice is restored, A_2 is proportional to the maximum rise in the electronic temperature and A_3 represents the state filling effects during pump-probe temporal overlap described by a Dirac delta function. $H(t)$ is the Heaviside step function, $\delta(t)$ is the Dirac delta distribution and $G(t)$ is a Gaussian function which corresponds to the laser pulse. The convolution of the exponential decay function with the Gaussian laser pulse with 100 fs of full width at half maximum helps in determining an accurate value of the demagnetization time. The schematic of the measurement geometry is shown in Fig. 9.1(d).

Fig. 9.2 (a) presents the experimental ΔM/M vs. time showing the ultrafast demagnetization for the SAF2_Ru sample up to 3.5 ps both in F (H ~ 2000 Oe) and AF state (H ~ 500 Oe) at a pump fluence of 13 mJ/cm^2. A striking difference in τ_M is observed between the demagnetization curves measured in the two states. A much larger (~93% increase) τ_M is observed in the F state (189±6 fs) as opposed to the AF state (98±4 fs). Earlier Mallinowski *et al*. [23], also reported faster demagnetization time in the AF state of [Co/Pt] MLs with Ru spacer. They interpreted their results by the direct transfer of spin angular momentum between the two [Co/Pt] MLs through the majority spin channels in the F state, but neglected the presence of interface-dependent SFS. Later, Vodungbo *et al.* [41] also showed that the laser induced demagnetization process could be faster for antiparallel spin orientation in $[Co/Pd]_{30}$ multilayer having a nanometric magnetic domain structure due to the transfer of angular momentum between the neighbouring domains. Another report showed that the demagnetization time is higher in

[Co/Pt] MLs as opposed to Co due to the presence of Pt with high SOC, causing increased SFS rate [42].

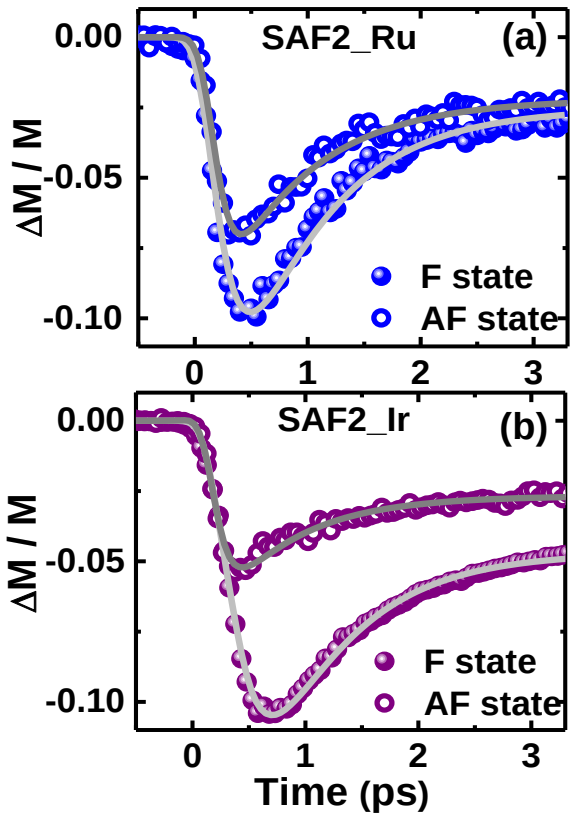

Fig. 9.2: Ultrafast demagnetization traces in the F and AF states for (a) SAF2_Ru sample and (b) SAF2_Ir sample at a pump fluence of 13 mJ/cm^2 and probe fluence of 2 mJ/cm^2.

The observation of the higher value of τ_M in the F state as opposed to the AF state can be interpreted by the simultaneous role of both SFS and ST in the demagnetization process. The interpretation is schematically depicted in Fig. 9.3. Following excitation of the sample by a femtosecond laser pulse, hot electrons are created in both ferromagnetic layers. The pump laser (λ = 400 nm) penetration depth is ~18 nm and probe laser (λ = 800 nm) penetration depth is ~28 nm in these samples [43-45]. The optical penetration depth as a function of incidence angle is expressed by, $\left[2Im\left(\frac{\omega}{c}\sqrt{(n+ik)^2 - sin^2\theta}\right)\right]^{-1}$, where ω is the angular frequency of light, c is the speed of light through vacuum, and n and k are the refractive index and extinction coefficient of the material, respectively. The notation '*Im*' corresponds to the imaginary part of a complex number. In the calculation, we have only considered the [Co/Pt] ML stacks and neglected the ultrathin Ru or Ir spacer layers due to the lack of their available parameters and very small thickness. Hence, both the incident pump and probe pulse penetrate through the

whole sample stack down to the substrate for the SAF2_Ru sample of overall thickness ~13 nm. The metallic Ru spacer does not provide a barrier to the flow of spin current [23] and hence the laser excited spins can be transported from one ML block to another through the Ru spacer layer. In the F state, magnetization orientations of the two FM layers are parallel; hence the majority spins are the same in both top and bottom [Co/Pt] MLs. The velocities and lifetimes of spin majority electrons are greater than the spin minority electrons [46, 47]. Due to small spin-dependent scattering (SDS) at the interface, the optically excited majority spins can easily move from the top to the bottom ML block and vice versa through the majority spin channel. On the other hand, in the AF state, magnetization orientations of the two MLs are antiparallel to each other. Hence, the majority spins in the top ML are opposite to those in the bottom ML and large SDS occurs at the interfaces. Consequently, the transport in individual optically excited spins from one ML to another reduces dramatically. The SFS process within a ML block however remains unaffected by the relative magnetization alignment of the top and bottom ML and has a similar effect in demagnetization. Consequently, τ_M is greater in the F state (where both SFS and ST mechanisms are simultaneously present) as opposed to the AF state (where only the SFS mechanism is present).

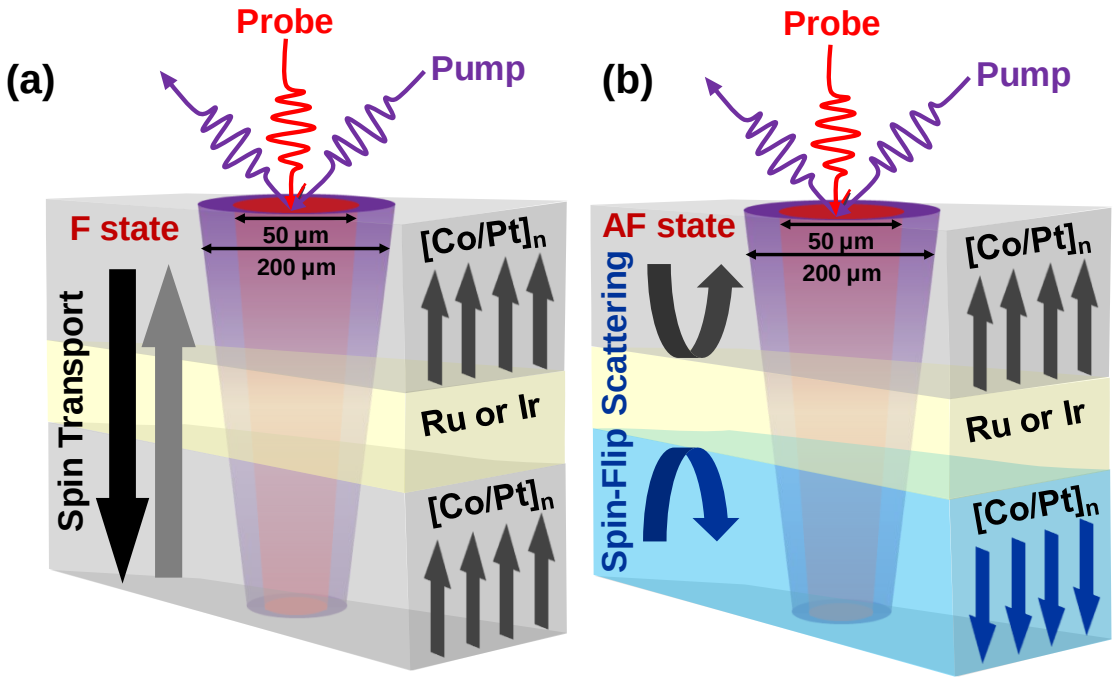

Fig. 9.3: Schematic of (a) spin transport and (b) spin-flip scattering mechanisms controlling the ultrafast demagnetization processes in the parallel (F state) and antiparallel (AF state) spin configurations of the SAF2 samples.

Fig. 9.2 (b) shows the ultrafast demagnetization curves measured for the SAF2_Ir sample for both the F state (H ~ 5000 Oe) and the AF state (H ~ 1500 Oe) at the same pump fluence of 13 mJ/cm^2. In this sample also, both the incident pump and probe pulse penetrate through the whole sample stack of thickness ~12.8 nm and a similar gradient of pump beam across the thickness exists as for the SAF2_Ru sample. However, Ir is a heavy metal (Z = 77) with stronger SOC than Ru (Z = 44). Earlier reports [48, 49] showed that an Ir spacer layer in a p-SAF structure yields higher IEC coupling energy density (J_{ex}) than that of Ru. It was concluded that an Ir spacer is superior to the conventional Ru spacer in p-SAF structures and is a very stable reference layer for perpendicularly magnetized magnetic tunnel junctions (p-MTJs) in spin-transfer torque (STT) switched magnetoresistive random access memory (STT-MRAM). The experimental hysteresis loops also confirm that our Ir-based SAF is more strongly coupled as compared to the Ru-based SAF. Fig. 9.2 (b) reveals that in SAF2_Ir, τ_M increases significantly as opposed to SAF2_Ru in the F state (τ_M = 218±3 fs), but does not show any remarkable change in the AF state (τ_M = 100±4 fs). This corresponds to a 118% increase in τ_M in the F state from its AF state. Due to an increase of Z, the ST between the two ML blocks increases in SAF2_Ir. Consequently, τ_M increases in the F state. However, as mentioned earlier, the contribution of ST is negligible in the AF state. Thus, as the SFS within the individual ML blocks does not change significantly, τ_M does not show any discernible change between Ru and Ir spacer SAF in the AF state.

We have next investigated the ultrafast demagnetization of the SAF4_Ru sample. Fig. 9.4 (a) presents ΔM/M as a function of time in the positive saturation (F1 state, H ~ 5000 Oe) and at the first plateau (3 up, 1 down; denoted as AF1 state, H ~ 1200 Oe) at a pump fluence of 13 mJ/cm^2. The extracted values of τ_M are 245±4 fs in the F1 state and 119±4 fs in the AF1 state, which means an increase by ~105% from the AF1 to F1 state. It can also be noted that τ_M has increased in both F1 and AF1 states in the SAF4_Ru sample as compared to the SAF2_Ru sample. These observations can be interpreted as follows.

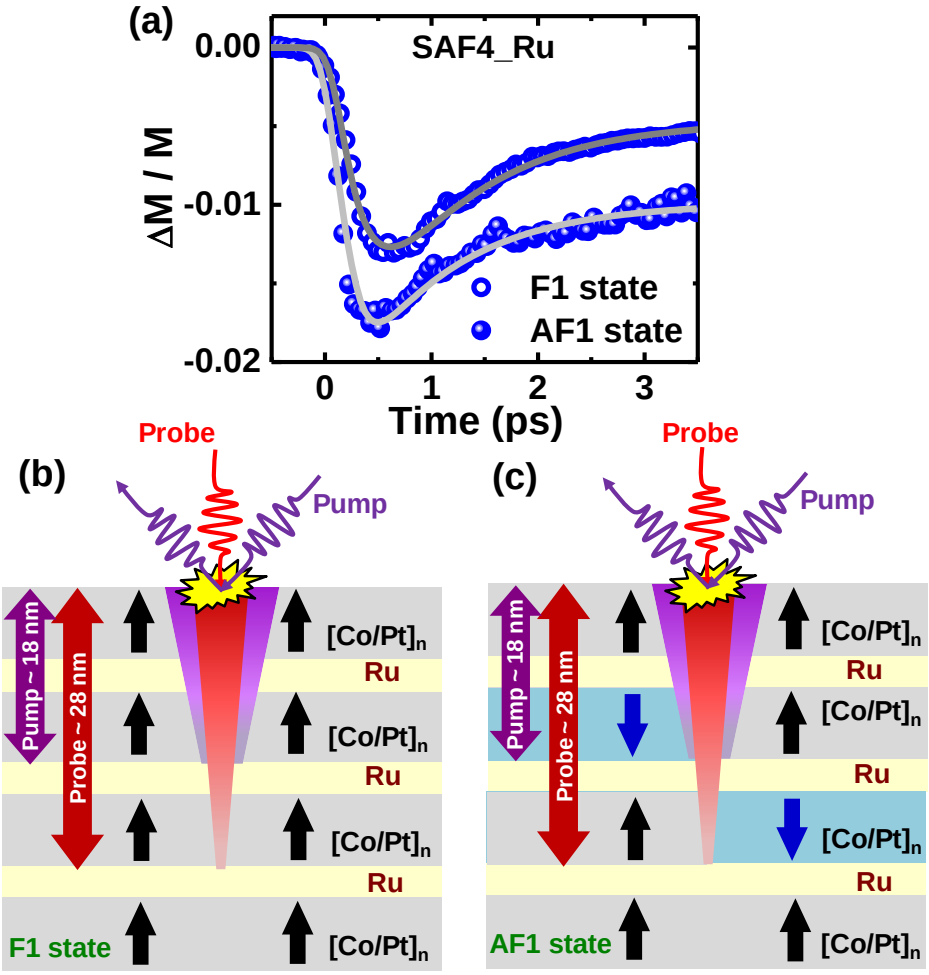

Fig. 9.4: (a) Ultrafast demagnetization traces in the F1 and AF1 states for SAF4_Ru sample at fixed pump fluence of 13 mJ/cm^2 and probe fluence of 2 mJ/cm^2. The schematic showing the spin configurations of the SAF4_Ru sample in the (b) F1 and (c) AF1 state along with the penetration depths of the pump and probe pulses.

As mentioned earlier, the penetration depths of pump and probe lasers are ~18 nm and ~28 nm in the studied samples. Hence, only the top two [Co/Pt] ML blocks are directly excited by the pump laser, whereas the top three [Co/Pt] ML blocks are probed. In the F1 state of SAF4_Ru, all the top three MLs are ferromagnetically coupled, i.e. the magnetization orientations of all three [Co/Pt] MLs are parallel and hence the majority spins are same in these MLs, as shown in Figure 4(b). Consequently, ST mechanism will occur efficiently between these three ML blocks. When the top two MLs are directly excited by the pump pulse, the majority spins from these two blocks should also be transported to the third ML block via the majority spin channels. Hence, the overall effect of ST in SAF4_Ru must be greater than SAF2_Ru, and consequently τ_M should also be greater in the F1 state of SAF4_Ru, as observed experimentally. On the

contrary, the magnetization orientations of the [Co/Pt] ML blocks in SAF4_Ru sample in the AF1 state can be quite complex. Here, the centre blocks are expected to reverse first since they have twice the exchange of the surface blocks [34]. From our static MOKE loop and from the previous literature [34], it appears that this sample exhibits a mixed reversal behavior with about 50% second ML block reversed (up-down-up-up) and 50% third ML block reversed (up-up-down-up) state, as shown schematically in Fig. 9.4 (c). If the second block is reversed in the AF1 state (left hand panel of Fig. 9.4 (c)), the top three blocks become antiparallel to each other, and hence, ST through the MLs becomes negligible. On the contrary, if the third block is reversed (right hand panel of Fig. 9.4 (c)), the top two blocks are parallelly aligned, while, the third block is antiparallelly aligned to its neighbor blocks. Hence, although ST can occur between the top two MLs, the majority spins from these top two blocks cannot be transported to the third ML block, due to the SDS at the interface. Hence, overall the ST in the AF1 state is much smaller as compared to that in the F1 state. Consequently, we observe a large difference in τ_M between the F1 and AF1 state. The increase in τ_M in the AF1 state of SAF4_Ru as opposed to the AF state of SAF2_Ru can be attributed partly to the enhancement of SFS in individual [Co/Pt] MLs because the number of [Co/Pt] bilayer repeats (X) has increased from 5 to 8 from SAF2_Ru to SAF4_Ru causing an overall increase in the SFS within the individual ML blocks [42], and partly to the ST between the top two ML blocks. The increase of τ_M in the F1 state of the SAF4_Ru as opposed to SAF2_Ru can be attributed partly to the increased SFS process within the individual ML blocks and partly to the enhanced ST to the third ML block from the top two MLs. The values of τ_M in different spin configurations for the three SAF samples are tabulated in Table 9.1.

Table 9.1: The ultrafast demagnetization time (τ_M) of three SAF samples in the parallel magnetic configurations (F or F1 state) and antiparallel magnetic configurations (AF or AF1 state) for a pump fluence of 13 mJ/cm^2.

Samples	τ_M **(F/F1 state)**	τ_M **(AF/AF1 state)**
SAF2_Ru	189 ± 6 fs	98 ± 4 fs
SAF2_Ir	218 ± 3 fs	100 ± 4 fs
SAF4_Ru	245 ± 4 fs	119 ± 4 fs

We have next investigated the effects of pump fluence on τ_M in the SAF samples for both F and AF states. For the samples, τ_M is found to increase sharply with pump fluence in the F state, whereas, it increases gently in the AF state. The ultrafast demagnetization curves of the SAF2_Ru sample for varying pump fluences from 13 to 58 mJ/cm^2 are presented in Fig. 9.5 (a) (F state) and (b) (AF state). The variation of τ_M with fluence in the F and AF state, are presented in Figs. 9.5 (c) and (d). While τ_M is found to increase sharply from 189±6 fs to 254±5 fs within the said pump fluence range in the F state, it increases gently from 98±4 fs to 115±3 fs in the AF state.

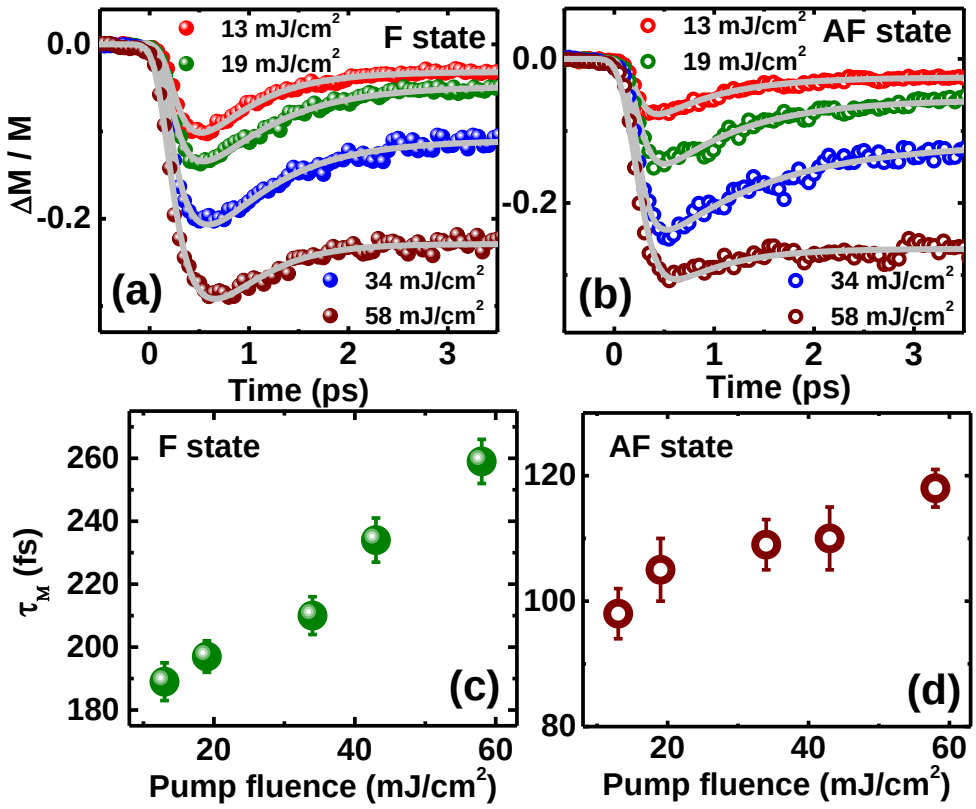

Fig. 9.5: Pump fluence dependent of ultrafast demagnetization traces of SAF2_Ru sample in (a) F state and (b) AF state. The solid circles represent experimental data points and the solid lines are fitted curves. Pump fluences are mentioned in the Fig. The variation of τ_M as a function of pump fluence in the (c) F state and (d) AF state.

The increased pump fluence leads to the generation of more excited carriers and thereby increasing SFS within individual ML blocks and steadily escalating the ST mechanism between the MLs. Thus, the demagnetization in the F state caused by the simultaneous presence of both SFS and ST also increases steadily, leading to a sharp increase of τ_M with pump fluence. On the contrary, as mentioned earlier, SFS is the primary demagnetization mechanism in the AF state.

Hence, only a gentle increase of τ_M with pump fluence is observed in the AF state due to the enhanced spin fluctuations and enhanced SFS at much higher elevated temperature of the spin system [41, 42]. For the SAF2_Ir sample τ_M is found to increase from 218±3 fs to 266±5 fs in the F state and from 100±4 fs to 116±4 fs in the AF state for varying pump fluencies from 13 to 58 mJ/cm^2. Similarly, for the SAF4_Ru sample, τ_M increases from 245±4 fs to 290±5 fs in the F1 state and from 119±4 fs to 138±4 in the AF1 state in the said pump fluence range. The effects of pump fluence on τ_M in these two samples are provided in Figs. A5.2 and A5.3 of the Appendix V. It can be noted that our results on the difference in τ_M between F and AF configurations are in qualitative congruence with the work of Malinowski *et al.* [23] despite the fact that we observed a much larger difference of about a factor of two in all three samples and at all fluences as opposed to a marginal change in their only sample. On the other hand, at higher pump fluence, the magnetization quenching in the F and AF states show similar results to what was reported by Malinowski *et al.* at a single fluence for Ru based SAF [23]. We believe our results will trigger more pervasive studies on a range of systems and at varying experimental parameters to obtain a more conclusive understanding of the ultrafast spin dynamics in synthetic antiferromagnets.

9.4. Conclusion

In conclusion, we have investigated the ultrafast demagnetization in synthetic antiferromagnets (SAFs) consisting of high perpendicular magnetic anisotropy [Co/Pt] multilayers separated by metallic Ru or Ir spacer layers to explore the underlying mechanisms behind the demagnetization. We have observed a large reduction in ultrafast demagnetization time in the AF state of the SAF samples in comparison with the F state. Due to the concurrent presence of both the spin-flip scattering (SFS) and optically excited spin transport (ST) process occurring through the majority spin channels, the demagnetization time of the whole SAF sample is larger in the F state. On the contrary, restricted ST reduces the demagnetization time in the AF state. However, when the Ru spacer is replaced by Ir, an increase in ST between the MLs occurs due to an increase of Z. Consequently, the demagnetization time increases in the F state of the Ir-based SAF as opposed to the Ru-based SAF. Finally, a SAF sample with four [Co/Pt] ML stacks periodically separated by three Ru spacers exhibits larger demagnetization time than single Ru spacer SAF, which is interpreted by the increase in both ST and SFS mechanisms. We understand that both SFS and interlayer ST processes play important roles in optically driven ultrafast demagnetization in SAF structures. Moreover, their respective strengths can be

controlled externally by changing the magnetic orientation using a magnetic field and internally by engineering the design of the sample. Nonetheless, further extensive and systematic studies on SAF structures will be needed to strongly corroborate the ultrafast demagnetization process in order to take full advantage of the variety of tuning and optimization possibilities available in such complex and flexible systems.

References

[1] E. Beaurepaire, J. –C. Merle, A. Daunois, and J. –Y. Bigot, Phys. Rev. Lett. **76**, 4250 (1996).
[2] J. Hohlfeld, E. Matthias, R. Knorren, and K. H. Bennemann, Phys. Rev. Lett. **78**, 4861 (1997).
[3] G. Ju, A. V. Nurmikko, R. F. C. Farrow, R. F. Marks, M. J. Carey, and B. A. Gurney, Phys. Rev. Lett. **82**, 3705 (1999).
[4] B. Koopmans, M. van Kampen, J. T. Kohlhepp, and W. J. M. de Jonge, Phys. Rev. Lett. **85**, 844 (2000).
[5] M. L. M. Lalieu, R. Lavrijsen, and B. Koopmans, Nat. Commun. **10**, 110 (2019).
[6] C-H. Lambert, S. Mangin, B. S. D. Ch. S. Varaprasad, Y. K. Takahashi, M. Hehn, M. Cinchetti, G. Malinowski, K. Hono, Y. Fainman, M. Aeschlimann, and E. E. Fullerton, Science **345**, 1337 (2014).
[7] J. K. Dewhurst, P. Elliott, S. Shallcross, E. K. U. Gross, and S. Sharma, Nano Lett. **18**, 1842 (2018).
[8] M. Hofherr, S. Hauser, J. K. Dewhurst, P. Tengdin, S. Sakshath, H. T. Nembach, S. T. Weber, J. M. Shaw, T. J. Silva, H. C. Kapteyn, M. Cinchetti, B. Rethfeld, M. M. Murnane, D. Steil, B. Stadtmuller, S. Sharma, M. Aeschlimann, and S. Mathias, Sci. Adv. **6**, eaay8717 (2020).
[9] W. Hubner, and G. P. Zhang, Phys. Rev. B **58**, R5920(R) (1998).
[10] G. P. Zhang, and W. Hubner, Phys. Rev. Lett. **85**, 3025 (2000).
[11] B. Koopmans, J. J. M. Ruigrok, F. Dalla Longa, and W. J. M. de Jonge, Phys. Rev. Lett. **95**, 267207(4) (2005).
[12] K. Carva, M. Battiato, and P. M. Oppeneer, Phys. Rev. Lett. **107**, 20720 (2011).
[13] S. Essert, and H. C. Schneider, Phys. Rev. B **84**, 224405 (2011).
[14] M. Krauß, T. Roth, S. Alebrand, D. Steil, M. Cinchetti, M. Aeschlimann, and H. C. Schneider, Phys. Rev. B **80**, 180407 (2009).
[15] J. Hong, and D. L. Mills, Phys. Rev. B **62**, 5589 (2000).
[16] E. Carpene, E. Mancini, C. Dallera, M. Brenna, E. Puppin, and S. De Silvestri, Phys. Rev. B **78**, 174422 (2008).
[17] J. –Y. Bigot, M. Vomir, and E. Beaurepaire, Nat. Phys. **5**, 515 (2009).
[18] R. Mondal, M. Berritta, K.Carva, and P. M. Oppeneer, Phys. Rev. B **91**, 174415 (2015).
[19] C. Illg, M. Haag, and M. Fahnle, Phys. Rev. B **88**, 214404 (2013).
[20] B Koopmans, M van Kampen, and W J M de Jonge, J. Phys.: Condens. Matter **15**, S723 (2003).
[21] M. Fahnle, M. Haag, and C. Illg, J. Magn. Magn. Mater. **347**, 45 (2013).
[22] E. Beaurepaire, G. M. Turner, S. M. Harrel, M. C. Beard, J.-Y. Bigot, and C. A. Schmuttenmaer, Appl. Phys. Lett. **84**, 34653467 (2004).
[23] G. Malinowski, F. Dalla Longa, J. H. H. Rietjens, P. V. Paluskar, R. Huijink, H. J. M. Swagten, and B. Koopmans, Nat. Phys. **4**, 855 (2008).
[24] M. Battiato, K. Carva, and P. M. Oppeneer, Phys. Rev. Lett. **105**, 027203 (2010).
[25] A. Eschenlohr, M. Battiato, P. Maldonado, N. Pontius, T. Kachel, K. Holldack, R. Mitzner, A. Fohlisch, P. M. Oppeneer, and C. Stamm, Nat. Mat. **12**, 332 (2013).
[26] D. Rudolf, C. La-O-Vorakiat, M. Battiato, R. Adam, J. M. Shaw, E. Turgut, P. Maldonado, S. Mathias, P. Grychtol, H. T. Nembach, T. J. Silva, M. Aeschlimann, H. C. Kapteyn, M. M. Murnane, C. M. Schneider, and P. M. Oppeneer, Nat. Commun. **3**, 1037 (2012).
[27] E. Turgut, C. La-o-vorakiat, J. M. Shaw, P. Grychtol, H. T. Nembach, D. Rudolf, R. Adam, M. Aeschlimann, C. M. Schneider, T. J. Silva, M. M. Murnane, H. C. Kapteyn, and S. Mathias, Phys. Rev. Lett. **110**, 197201 (2013).
[28] S. Pan, O. Hellwig, and A. Barman, Phys. Rev. B **98**, 214436 (2018).

[29] T. Jungwirth, X. Marti, P. Wadley, and J. Wunderlich, Nat. Nanotechnol. **11**, 231 (2016).
[30] R. Cheng, M. W. Daniels, J. G. Zhu, and D. Xiao, Sci. Rep. **6**, 24223 (2016).
[31] M. D. Stiles, J. Magn. Magn. Mater. **200**, 322 (1999).
[32] J. Faure-Vincent, C. Tiusan, C. Bellouard, E. Popova, M. Hehn, F. Montaigne, and A. Schuhl, Phys. Rev. Lett. **89**, 107206 (2002).
[33] R. A. Duine, K. J. Lee, S. S. P. Parkin, and M. D. Stiles, Nat. Phys. **14**, 217 (2018).
[34] O. Hellwig, A. Berger, J. B. Kortright, and E. E. Fullerton, J. Magn. Magn. Mater. **319**, 13 (2007).
[35] R. Lavrijsen, A. Fernandez-Pacheco, D. Petit, R. Mansell, J. H. Lee, and R. P. Cowburn, Appl. Phys. Lett. **100**, 052411 (2012).
[36] S. Bandiera, R. C. Sousa, S. Auffret, B. Rodmacq, and B. Dieny, Appl. Phys. Lett. **101**, 072410 (2012).
[37] B. Chen, H. Xu, C. Ma, S. Mattauch, D. Lan, F. Jin, Z. Guo, S. Wan, P. Chen, G.Gao, F. Chen, Y. Su, and W. Wu, Science **357**, 191 (2017).
[38] N. T. Kuhn, D. Schick, N. Pontius, C. Trabant, R. Mitzner, K. Holldack, H. Zabel, A. Fohlisch, and C. S. Langeheine, Phys. Rev. Lett. **119**, 197202 (2017).
[39] O. Hellwig, T. L. Kirk, J. B. Kortright, A. Berger, and E. E. Fullerton, Nat. Mater. **2**, 112 (2003).
[40] U. Atxitia, O. Chubykalo-Fesenko, J. Walowski, A. Mann, and M. Munzenberg, Phys. Rev. B **81**, 174401 (2010).
[41] B.Vodungbo, J. Gautier, G. Lambert, A. Barszczak Sardinha, M. Lozano, S. Sebban, M. Ducousso, W. Boutu, K. Li, B. Tudu, M. Tortarolo, R. Hawaldar, R. Delaunay, V. Lopez-Flores, J. Arabski, C. Boeglin, H. Merdji, P. Zeitoun, and J. Luning, Nat. Commun. **3**, 999 (2012).
[42] K. C. Kuiper, T. Roth, A. J. Schellekens, O. Schmitt, B. Koopmans, M. Cinchetti, and M. Aeschlimann, Appl. Phys. Lett. **105**, 202402 (2014).
[43] Y. Miyasaka, M. Hashida, T. Nishii, S. Inoue, and S. Sakabe, Appl. Phys. Lett. **106**, 013101 (2015).
[44] P. B. Johnson, and R. W. Christy, Phys. Rev. B **6**, 4370 (1972).
[45] M. N. Poliyanskiy, Refractive Index Database, https:// refractiveindex.info (unpublished).
[46] V. P. Zhukov, E. V. Chulkov, and P. M. Echenique, Phys. Rev. Lett. **93**, 093401 (2004).
[47] N. Moisan, G. Malinowski, J. Mauchain, M. Hehn, B. Vodungbo, J. Luning, S. Mangin, E. E. Fullerton, and A. Thiaville, Sci. Rep. **4**, 4658 (2014).
[48] K. Yakushiji, H. Kubota, A. Fukushima, and S. Yuasa, Appl. Phys. Exp. **8**, 083003 (2015).
[49] K. Yakushiji, A. Sugihara, A. Fukushima, H. Kubota, and S. Yuasa, Appl. Phys. Lett. **110**, 092406 (2017).

Chapter 10

10. Anisotropic Variation of the Spin-Wave Dynamics in Antidot Lattices on $[Co/Pd]_8$ Multilayers with Perpendicular Magnetic Anisotropy

10.1. Introduction

Ferromagnetic multilayers (MLs) offer immense versatility in quantum magnetic properties, including spin-dependent scattering [1], spin tunnelling [2], exchange anisotropy [3], perpendicular magnetic anisotropy (PMA) [4], interfacial Dzyaloshinskii-Moriya (iDMI) interaction [5], spin Hall effect (SHE) [6], Rashba-Edelstein effect [7, 8], spin Seebeck effect [9], voltage controlled magnetic anisotropy (VCMA) [10], topological spin textures [11], etc. Ferromagnetic MLs with PMA [12, 13] are prospective candidates for bit patterned media and nanostructured MLs with PMA have become building blocks of magnetic recording technology [14]. The origin of PMA remained a subject of interest, and several evidences suggest that strong and localized *d*–*d* band hybridization at the interface of ferromagnetic (FM) metals (like Co, Fe) and heavy metals (HM) (like Pt, Pd) is responsible for PMA, which decreases sharply with the increase of layer thicknesses. Although significant works on the magnetization dynamics of thin film ferromagnetic MLs with PMA have been reported [15-17], but the dynamics of nanostructured MLs with PMA have rarely been explored. Few reports exist on magnetization reversal and domain wall (DW) study with defects and edge corrugations [18], increase of coercive field [19] in antidots carved on [Co/Pd] MLs and DW pinning in antidots carved on [Co/Pt] MLs [20]. Theoretical study of SWs in patterned MLs with PMA using discrete dipole approximation (DDA) showed that magnetic inhomogeneity along the central axis splits the magnetostatic SWs into two bands, and the exchange SWs into a number of bands as a result of the underlying long- and short-range interactions, respectively [21]. The magnetization reversal in perpendicularly magnetized nanostructures has been reported to be highly dependent on the nature and condition of the edges [22]. The first experimental observation of spin-wave (SW) dynamics in such system came in 2014, when Pal *et al*. observed a decrease in SW frequency with increasing density of antidots, down to values well below the FMR frequency of the continuous ML, in a series of $[Co(0.75\ nm)/Pd(0.9\ nm)]_8$ antidot lattice (ADLs) with PMA [23]. This was modelled by assuming nanoscale rim-like shell regions

surrounding the antidots created by the Ga+ ion bombardment during patterning using focused ion beam (FIB) milling technique. The decrease of SW frequencies is found to be driven by a dynamical coupling between the localized modes within the narrow shells, most likely by tunnelling and exchange interactions. The shape of the antidots has been observed to play decisive roles in the in-plane domain structure and the ensuing edge-localized SW spectra, their mutual interactions and interaction with bulk SW excitations [24]. The existence of such localized SWs may offer new possibilities for their exploitation as nano-oscillators [25]. Demidov *et al.* demonstrated the construction of spin-Hall nano-oscillators (SHNOs) with a ferromagnetic ML and explained the intriguing mechanism for a single nanomagnet [26]. Furthermore, the role of interactions between the edge localized and bulk SW excitations in nanomagnet array, or other type of SWs, like the Winter type modes [27, 28] localized at the 90° domain wall between the shell and the bulk regions have been reported. The formation of artificial skyrmions and antiskyrmions via localized ion irradiation of [Co/Pt] multilayers, to create circular regions with in-plane magnetization set into the surrounding PMA film have also been observed [29]. These possibilities open prospects for exploiting collective dynamics in patterned multilayer systems with modified local properties to form bicomponent magnonic crystals (BMCs) by ion irradiation [30]. Furthermore, it has been demonstrated that by controlling the PMA strength, one can suppress the nonlinear magnetic damping in order to achieve decay-free propagation and probable amplification of SWs [31].

We have investigated the SW excitations in diamond shaped ADLs fabricated on [Co(0.75 nm)/Pd(0.9 nm)]$_8$ MLs with PMA using time-resolved magneto-optical Kerr effect (TR-MOKE) microscopy. Rich SW spectra are observed in this system, which changes significantly with the orientation of the applied bias magnetic field. To interpret the experimental results we have performed micromagnetic simulations assuming a narrow shell region around the antidots with reduced PMA [23, 24]. Consequently, the demagnetizing field aligns the magnetization of the shell in the film plane, thus forming a localized in-plane domain structure, which changes sharply with the orientation of the applied bias magnetic field. The variety of the magnetization states in the shells leads to the remarkable modulation of the SW dynamics with the bias magnetic field orientation.

10.2. Methods

The [Co(0.75 nm)/Pd(0.9 nm)]$_8$ ML structures were deposited by dc magnetron sputtering using a confocal sputter up geometry, in which the targets tilted and arranged in a circle around a central target (Pd). During deposition, the substrate rotates at a frequency of 3 Hz. The base pressure of the chamber was 2×10^{-8} mbar and the deposition was performed at room temperature and 4 μbar of Ar pressure. The antidots were patterned on the Co/Pd MLs by focused ion beam (FIB) milling using liquid Ga^+

ions at a voltage of 30 kV and at a beam current of 20 pA. At first, a pattern of antidots with the desired shape, covering an area of 8 × 8 μm^2 was created on the ML sample. Subsequently, the material was milled out by exposing the patterned part to the Ga^+ ion beam source. The initial milling was performed by a raster scan of the focused ion beam in a single pass, followed by the cleaning of residual resists from the ADLs in multipass (about 200 passes) [24]. We have fabricated diamond shaped antidots arranged in square lattice symmetry as shown by the scanning electron microscope (SEM) images in Fig. 10.1 (a). The antidot diameter (*d*) is 200 nm and the edge-to-edge separation (*s*) is 300 nm. The atomic force microscopy (AFM) image of the ADL is shown in Fig. 10.1 (b).

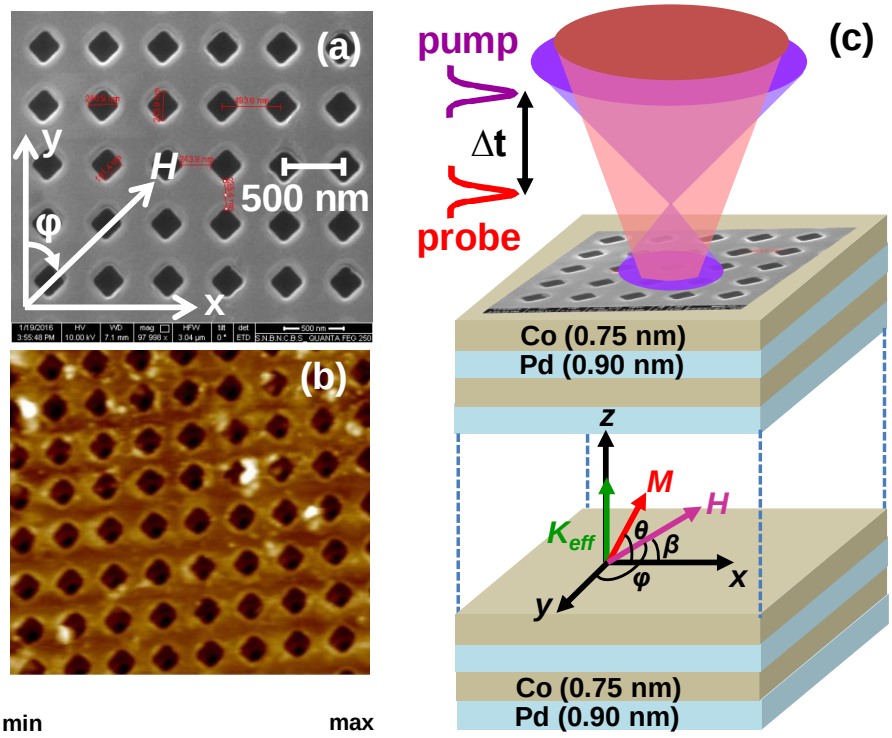

Fig. 10.1: (a) The SEM image of the antidot lattice. (b) The AFM image of the same lattice (c) Schematic of the sample geometry showing the direction of the bias magnetic field along with the pump and probe beams of the TR-MOKE microscope.

The ultrafast magnetization dynamics are measured by a custom-built TR-MOKE microscope in collinear two-color pump-probe geometry [32, 33]. The second harmonic (λ = 400 nm, spot size ~1 μm, fluence ~ 20 mJ/cm^2) of a Ti-sapphire oscillator output was used to pump the dynamics, whereas the time delayed fundamental laser (λ = 800 nm, spot size ~800 nm, fluence ~ 2 mJ/cm^2) was used to probe the dynamics. The Kerr rotation was measured by an optical bridge detector (OBD) as a function of the time-delay between the pump and probe beams. An external magnetic field (*H*), tilted at a small angle (β ~ 20°) to the surface normal of the sample, was applied to saturate its magnetization during the dynamic measurements. The measurement geometry is schematically depicted in Fig. 10.1 (c).

To interpret the experimental results, we have performed micromagnetic simulations using the object oriented micromagnetic framework (OOMMF) software [34] assuming an effective medium across the entire thickness of the ML sample with the following parameters: volume magnetization M_S = 0.81 × 10^6 A/m, anisotropy energy density K_u = 4.2 × 10^5 J/m^3, exchange stiffness constant A = 1.3 × 10^{-11} J/m, and gyromagnetic ratio γ = 187 GHz/T, and the Gilbert damping constant α = 0.008 [24]. The simulations have been performed on arrays of 7 × 7 antidots and the sample has been discretized into rectangular prism-like cells with dimensions of 2 × 2 × 4.4 nm^3. We have assumed a uniform shell-like region around each antidot, with constant width (20 nm) and shape corresponding to the shape of the respective antidots, where the magnetic anisotropy has been reduced to zero (K_u = 0). The other parameters for the shell regions are chosen as, M_S = 0.3 × 10^6 A/m, and A = 1.3 × 10^{-11} J/m from previous study on similar materials but with different geometry [23]. During the FIB milling process of the MLs for the creating the antidots, some scattered ions may have penetrated through the sidewalls of the antidots, causing a degradation of the structural and magnetic properties over the shell region. As a consequence, the effective magnetization, exchange interactions, and especially the PMA field in the shell regions are decreased [24]. Hence, we may consider that the ADL consists of two magnetic components: one with the properties of the continuous ML and the other with degraded properties inside the shell regions around the antidots. The dynamic simulations were performed by first obtaining a static magnetic configuration under the bias magnetic field of ~ 1.7 kOe in the experimental geometry and subsequently applying a pulsed magnetic field with peak magnitude of 20 Oe, rise/fall time of 10 ps and pulse duration of 20 ps over the whole array. We have further calculated the spatial distributions of these modes using a homebuilt Matlab-based code named DotMag [35].

10.3. Results and Discussion

The background subtracted experimental time-resolved Kerr rotation data for 0° ≤ φ ≤ 90° at an interval of 15° taken at H = 1.7 kOe are shown in Fig. 10.2 (a). The multimodal power spectra obtained from fast Fourier transform (FFT) of the Kerr oscillations are shown in Fig. 10.2 (b). For φ = 0°, a rich SW spectrum consisting of five modes with varying power are obtained, out of which the highest frequency has the highest power too. The SW spectra for φ = 15° also consists of five SW modes with slightly different relative mode power. However, the spectra for φ = 30°, 45° and 60° are remarkably different, with a drastic reduction in the number of SW modes. In these cases, only three modes appear. For φ = 45°, the power of the intermediate frequency mode is much larger as compared to the higher and lower frequency modes on either side. Again at φ = 75° and 90°, rich SW spectra consisting of five modes with varying power are observed. These indicate a gradual variation in the collective nature of the SW dynamics with varying φ-values. Fig. 10.2 (c) shows the simulated SW spectra of the

sample, which is in qualitative agreement with the experimental spectra except for quantitative values of the linewidth, the relative mode power and peak frequencies. These deviations may be attributed to the differences between the experimental and simulated samples. The precise value of the shell width is difficult to characterize, besides in the real sample, the values of anisotropy and saturation magnetization may vary continuously, while these quantities are assumed as step function in the simulations.

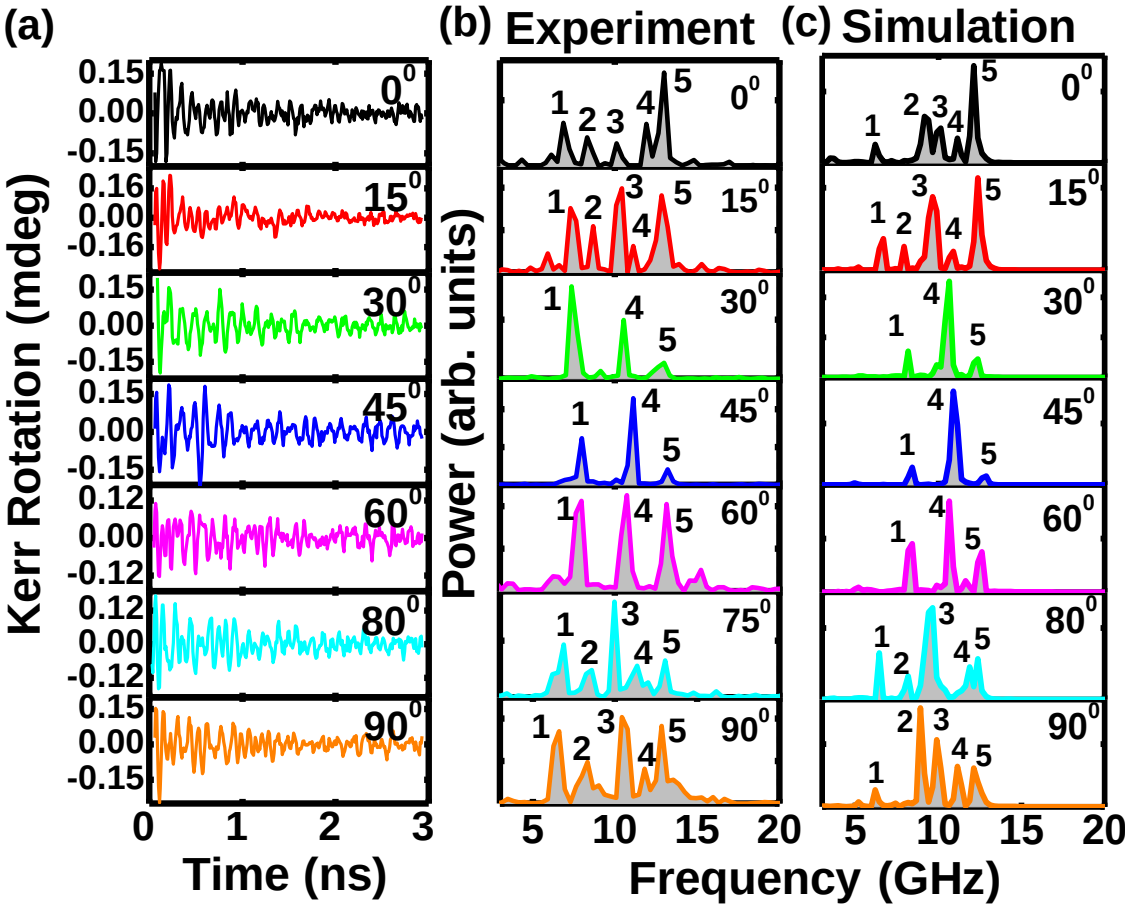

Fig. 10.2: (a) Background subtracted experimental time-resolved Kerr rotation data for some specific orientations of the bias magnetic field. The value of the magnetic field orientation is written in the corresponding plot. (b) The corresponding FFT power spectra showing the SW modes. Mode numbers are shown in the figure. (c) The FFT power spectra of simulated time-domain magnetization.

Fig. 10.3 (a) shows the bias magnetic field (H) dependence of the SW frequencies (f) extracted from the experimental FFT spectra at $\varphi = 0°$. We observe that the higher frequency modes exhibit significant dispersion with H, whereas, the lower frequency modes show weak dispersion with H. The frequencies corresponding to the modes M4 and M5 are in agreement with the Kittel formula (Eq. (1)) giving effective magnetization (M_{eff}) of 405 ± 15 emu/cm^3 and 560 ± 21 emu/cm^3, respectively.

$$f = \frac{\gamma\mu_0}{(1+\alpha^2)}\left[H\frac{sin\beta}{sin\theta} + 2\frac{K_{eff}}{\mu_0 M_S} - M_S\right] \qquad (1)$$

where γ is the gyromagnetic ratio, α is the damping coefficient, θ and β are the angles made by the equilibrium magnetization (M), and the bias magnetic field (H) with x-axis and K_{eff} is the effective magnetic anisotropy. θ is obtained by minimizing the total energy of the system, while β is known from the experimental geometry, as shown in Fig. 10.1(c). α is taken from literature [17]. The angular dispersions of the precessional frequencies of different SW modes as a function of φ varying from 0° to 180° are shown in Fig. 10.3 (b). The solid symbols represent the experimental frequencies, the dashed lines represent the simulated frequencies, while the solid lines correspond to the theoretical fits using harmonic functions with different rotational symmetries. It is evident that the modes M1, M4 and M5 are present at almost all values of φ, whereas the modes M2 and M3 exhibit a discontinuous angular dispersion appearing only for $0° \leq \varphi \leq 15°$ and $75° \leq \varphi \leq 90°$ and disappear in between. This behavior is repeated periodically. Theoretical fits of the variation of the frequencies of M1, M4 and M5 with φ (solid line) show a four-fold anisotropy, while while the rotational anisotropy of the mode M4 is in anti phase with the other two modes.

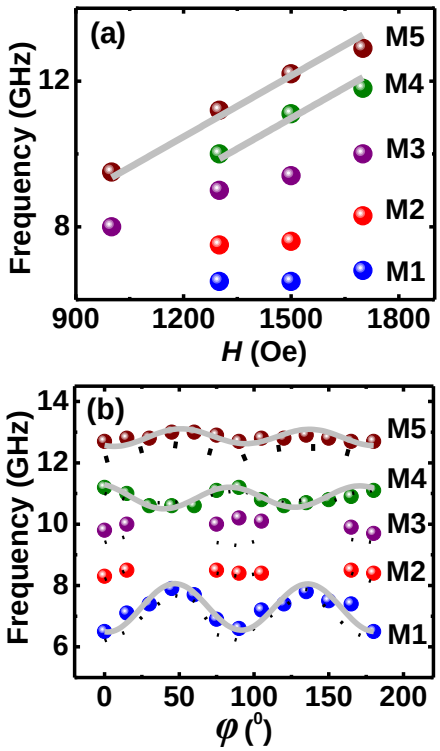

Fig. 10.3: (a) Bias magnetic field dependent precessional frequencies of different SW modes of the ADL. The solid lines represent the Kittel fits to the modes M4 and M5. (b) Variation of frequencies of the SW modes with the bias magnetic field orientation φ between 0° and 180° at a fixed value of H = 1.7 kOe. The symbols represent the experimental data, the dashed lines represent the simulated data and the solid lines describe the theoretical fits with sinusoidal function.

Fig. 10.4 (a) shows the static magnetic configuration around a single antidot, while Fig. 10.4 (b) shows the phase profiles of the SW modes from the central part of the ADL at different values of φ. Fig. 10.4

(c) shows the corresponding power maps of the SW modes. The lack of the PMA in the shell region allows the demagnetizing field to align the magnetization into an in-plane domain structure around the antidots. Besides, we have applied a bias magnetic field tilted at a small angle ($\beta \approx 20°$) from the sample plane. Consequently, the in-plane domains do not remain constrained within the shell regions only, but spills slightly outside the shells forming a gradient of the in-plane domains in the bulk regions just outside the shells.

The static magnetic configuration changes sharply with the variation in φ. For $\varphi = 0°$, head-to-head and tail-to-tail domains are observed along the sides of the diamond antidots just outside the shells. At $\varphi = 15°$, the magnetization is rotated and the head-to-head and tail-to-tail domains spill more into the bulk regions outside the shells. At $\varphi = 30°$, the magnetization is further rotated and the head-to-head and tail-to-tail domains disappear. In this case, the domains only at two diagonally opposite sides of the diamond antidots are extended slightly inside the bulk regions, whereas the domains at two other sides remain localized inside the shells only. However, at $\varphi = 45°$, the domains are localized strictly within the shell regions. The drastic variation of the magnetic configuration of the shells and the adjacent bulk regions with the orientation of the bias magnetic field is manifested in the observed variation of the SW spectra. From the spatial profiles it is evident that the lowest frequency mode M1 at $\varphi = 0°$, has the highest power concentrated at the top and bottom corners of the antidots. The intermediate frequency modes M2 and M3 have backward volume (BV)-like nature with quantization number $n = 3$ and 5, respectively. For these two modes, the highest power is mainly concentrated in the in the area of the reduced anisotropy of the domains along the sides of the antidots. The mode M4 has BV-like nature with $n = 7$. The highest frequency mode M5 forms a complex crisscross-like pattern with a mixed Damon-Eshbach (DE)-BV nature with mode quantization number (m, n) of (5, 9). For both M4 and M5, the power is uniformly distributed over the whole lattice. At $\varphi = 15°$, the spatial profiles of the SW modes remain qualitatively similar with their symmetry axes gradually shifted with the variation of φ. However, at $\varphi = 30°$ and 45°, the spatial profiles of the lower frequency SW modes undergo a significant change. The highest power of M1 becomes concentrated only along the two diagonally opposite sides of the antidots. However, the spatial profiles of the higher frequency modes remain unchanged. The mode M4 has a BV-like nature and the mode M5 forms complex crisscross-like pattern with a mixed DE-BV nature both at $\varphi = 30°$ and 45°. The shell magnetization can stabilize in different configurations similar to isolated rings having larger width and made up of soft ferromagnetic materials. With the changing of shell width, the coupling between fundamental and shell modes change, resulting in a change of frequencies of the localized SWs [24]. The variety of the magnetization states in these shells gives opportunity for further exploitation of the edge localized SW spectra, which can be controlled by the magnetization configuration. This is accomplished by developing protocols of the remagnetization with the in-plane component of the applied magnetic

field, as in the case of isolated rings based on soft ferromagnetic materials of circle, square, triangle, and diamond shapes [36]. The interactions between the edge localized and bulk SW excitations for different orientations of applied magnetic field in antidots of various other shapes may be interesting. Furthermore, combining our study with chirality-controlled dot structures in similar PMA MLs will be worth exploring in the future.

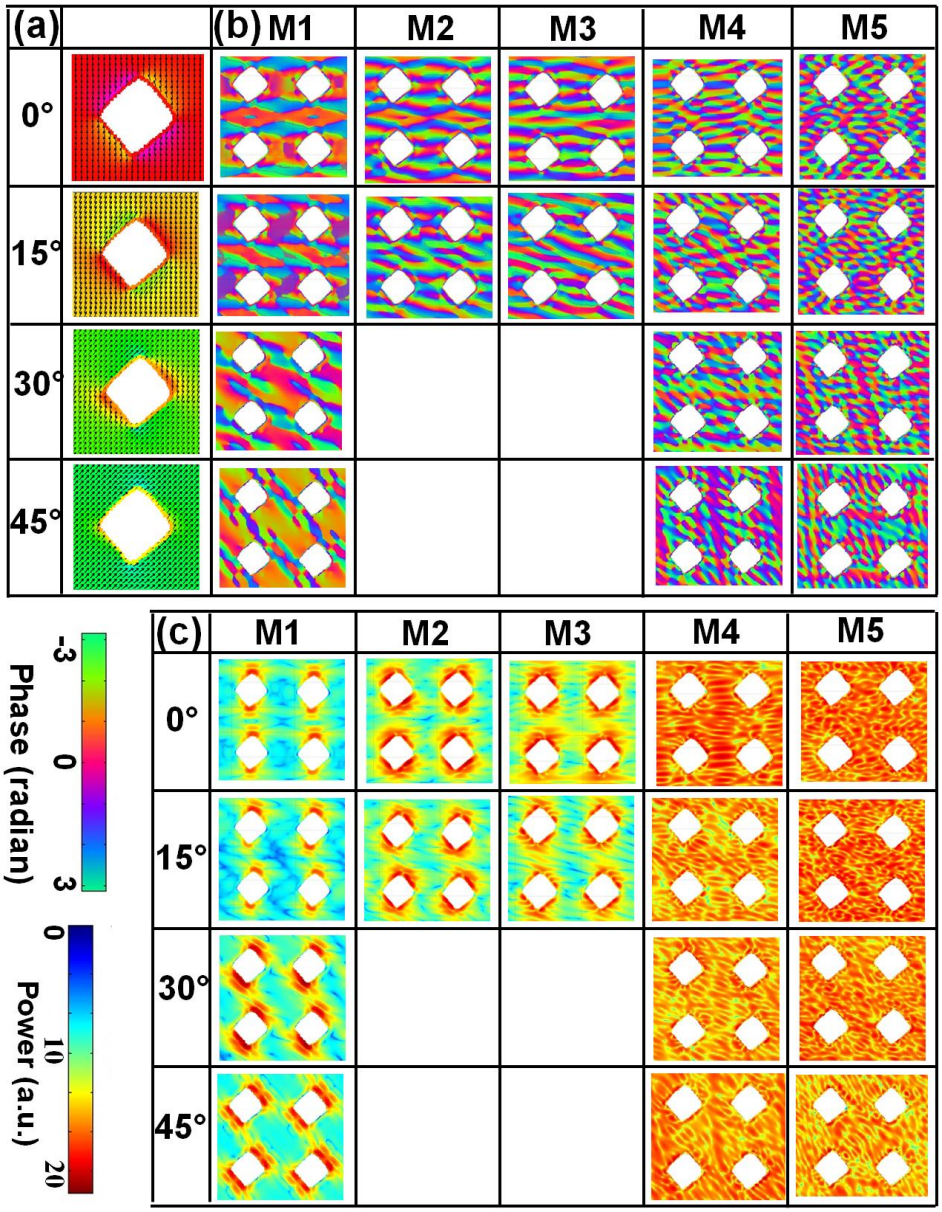

Fig. 10.4: (a) Simulated static magnetic configurations around a single antidot and the (b) phase and (c) power profiles of the SW modes at different values of φ. The color bars are shown inside the Fig.

10.4. Conclusion

In conclusion, we have experimentally investigated the SW excitations in diamond shaped ADLs fabricated on $[Co/Pd]_8$ multilayers having PMA using a TR-MOKE microscope. With the aid of micromagnetic simulations we propose that the emergence of narrow shell regions with reduced PMA around the antidots is responsible for the experimentally observed SW modes at lower frequencies. The shells with reduced PMA are formed presumably due to the Ga+ ion irradiation during the FIB milling process of antidot fabrication. When the PMA in the shells reduce to zero, the magnetization around the antidot edges rotate towards the sample plane. Furthermore, the in-plane direction of the shell magnetization changes sharply with the change of the orientation of the applied bias magnetic field, leading to the stark variation of the SW modes localized within the in-plane domains around the antidots. The efficient modulation of these localized SWs with bias magnetic field orientation can offer new prospects for their exploitation as spin-texture driven magnonic as well as spintronic devices.

References

[1] X. Waintal, E. B. Myers, P. W. Brouwer, and D. C. Ralph, Phys. Rev. B, **62**, 12317 (2000).
[2] T. Song, X. Cai, M. W.-Y. Tu, X. Zhang, B. Huang, N. P. Wilson, K. L. Seyler, L. Zhu, T. Taniguchi, K. Watanabe, M. A. McGuire, D. H. Cobden, D. Xiao, W. Yao, X. Xu, Science, **360**, 1214 (2018).
[3] S. Maat, K. Takano, S. S. P. Parkin, and E. E. Fullerton, Phys. Rev. Lett. **87**, 087202-1 (2001).
[4] P. F. Carcia, A. D. Meinhaldt, and A. Suna, Appl. Phys. Lett. **47**, 178 (1985).
[5] N. S. Gusev, A. V. Sadovnikov, S. A. Nikitov, M. V. Sapozhnikov, and O. G. Udalov, Phys. Rev. Lett. **124**, 157202 (2020).
[6] J.-C. Rojas-Sanchez, P. Laczkowski, J. Sampaio, S. Collin, K. Bouzehouane, N. Reyren, H. Jaffres, A. Mougin, and J.-M. George, Appl. Phys. Lett. **108**, 082406 (2016).
[7] H. Nakayama, Y. Kanno, H. An, T. Tashiro, S. Haku, A. Nomura, and K. Ando, Phys. Rev. Lett. **117**, 116602 (2016).
[8] Y. Du, H. Gamou, S. Takahashi, S. Karube, M. Kohda, and J. Nitta, Phys. Rev. Appl. **13**, 054014 (2020).
[9] G. M. Choi, C. H. Moon, B. C. Min, K. J. Lee and D. G. Cahill, Nat. Phys. **11**, 576, (2015).
[10] P. K. Amiri and K. L. Wang, Spin **2**, 1240002 (2011).
[11] W. Jiang, G. Chen, K. Liu, J. Zang, S. G. E. te Velthui, A. Hoffmann, Phys. Rep. **704**, 1 (2017).
[12] O. Hellwig, S. Maat, J. B. Kortright, E. E. Fullerton, Phys. Rev. B **65**,144418 (2002).
[13] O. Hellwig, T. Hauet, T. Thomson, E. Dobisz, J. D. Risner-Jamtgaard, D. Yaney, B. D. Terris, E. E. Fullerton, Appl. Phys. Lett. **95**, 232505 (2009).
[14] S. N. Piramanayagam, J. Appl. Phys. **102**, 011301 (2007).
[15] A. Barman, S. Wang, O. Hellwig, A. Berger, E. E. Fullerton, and H. Schmidt, J. Appl. Phys. **101**, 09D102 (2007).
[16] S. Mizukami, E. P. Sajitha, D. Watanabe, F. Wu, T. Miyazaki, H. Naganuma, M. Oogane, and Y. Ando, Appl. Phys. Lett. **96**, 152502 (2010).
[17] S. Pal, B. Rana, O. Hellwig, T. Thomson, and A. Barman, Appl. Phys. Lett. **98**, 082501 (2011).
[18] M. Krupinski, P. Sobieszczyk, P. Zieliński, and M. Marszałek, Sci. Rep**. 9**, 13276 (2019).
[19] D. Tripathy and A. O. Adeyeye, New J. Phys **13**, 023035 (2011).
[20] M. T. Rahman, N. N. Shams, C. H. Lai, J. Fidler, and D. Suess, Phys. Rev. B **81**, 014418 (2010).
[21] M. Krawczyk, S. Mamica, J. W. Kłos, J. Romero-Vivas, M. Mruczkiewicz, and A. Barman, J. Appl. Phys. **109**, 113903 (2011).
[22] J. M. Shaw, S. E. Russek, T. Thomson, M. J. Donahue, B. D. Terris, O. Hellwig, E. Dobisz, and M. L. Schneider, Phys. Rev. B **78**, 024414 (2008).
[23] S. Pal, J. W. Klos, K. Das, O. Hellwig, P. Gruszecki, M. Krawczyk, and A. Barman, Appl. Phys. Lett. **105**, 162408 (2014).
[24] S. Pan, S. Mondal, M. Zelent, R. Szwierz, S. Pal, O. Hellwig, M. Krawczyk, and A. Barman, Phys. Rev. B **101**, 014403 (2019).
[25] N. Sato, K. Schultheiss, L. Körber, N. Puwenberg, T. Mühl, A. A. Awad, S. S. P. K. Arekapudi, O. Hellwig, J. Fassbender, and H. Schultheiss, Phys. Rev. Lett. **123**, 057204 (2019).
[26] V. E. Demidov, S. Urazhdin, H. Ulrichs, V. Tiberkevich, A. Slavin, D. Baither, G. Schmitz, and S. O. Demokritov, Nat. Mater. **11**, 1028 (2012).
[27] A. A. Awad, A. Lara, M. García Hernández, V. Metlushko, K. Y. Guslienko, and F. G. Aliev, J. Supercond. Nov. Magn. **26**, 2057 (2013).
[28] F. G. Aliev, A. A. Awad, D. Dieleman, A. Lara, V. Metlushko, and K. Y. Guslienko, Phys. Rev. B **84**, 144406 (2011).
[29] S. Zhang, A. K. Petford-Long, and C. Phatak, Sci. Rep. **6**, 31248 (2016).
[30] P. Kuswik, I. Sveklo, B. Szymanski, M. Urbaniak, F. Stobiecki, A. Ehresmann, D. Engel, P. Mazalski, A. Maziewski, and J. Jagielski, Nanotechnology **23**, 475303 (2012).
[31] B. Divinskiy, S. Urazhdin, S. O. Demokritov, and V. E. Demidov, Nat. Commun. **10**, 5211 (2019).

[32] A. Barman, and A. Haldar, Solid State Phys. **65**, 1 (2014).
[33] A. Barman and J. Sinha, Spin Dynamics and Damping in Ferromagnetic Thin Films and Nanostructures, Springer International Publishing AG, 2018.
[34] M. Donahue, D. G. Porter, NIST Interagency Report No. 6376; National Institute of Standard and Technology, Gaithersburg, MD, URL: http://math.nist.gov/oommf: (1999).
[35] D. Kumar, O. Dmytriiev, S. Ponraj, A. Barman, J. Phys. D: Appl. Phys. **45**, 015001 (2012).
[36] M. D. Mascaro, H. S. Körner, C. Nam, B. G. Ng, and C. A. Ross, Appl. Phys. Lett. **98**, 252506 (2011).

Chapter 11

Surface Acoustic Wave Modulated Magnetization Dynamics in a Two-Phase Multiferroic Nanomagnet Array

11.1. Introduction

Magnetoelasticity (ME) or inverse magnetostriction has emerged as a powerful tool to couple magnons and phonons since the magnetization precession in ferromagnetic magnetostrictive materials is affected by elastic stress [1-5] and hence by surface acoustic waves (SAW) [6, 7] which are propagating strain (elastic) waves consisting of acoustic phonons. SAW-induced precession of magnetization in magnetostrictive nanomagnets has been studied extensively [8, 9] and SAW-induced magnetization rotation and domain-wall motion in magnetostrictive nanomagnets have been harnessed for energy-efficient hybrid writing schemes for non-volatile memory [10, 11]. Over the last decade, SAW in the GHz frequency regime has been used to excite or manipulate spin waves (SWs) in magnetic thin films [2, 12] and nanostructures [13, 14] through ME interactions. In this work, we demonstrate, using time-resolved magneto-optical Kerr effect (TR-MOKE) microscopy, that SAW can strongly influence the magnetization dynamics (and hence magnon modes) in a two-dimensional (2D) densely packed array of interacting elliptical magnetostrictive Co nanomagnets, fabricated on a piezoelectric 128° Y-cut $LiNbO_3$ substrate. This is a system of 2-phase (magnetostrictive + piezoelectric) multiferroic nanomagnets. The interplay between the demagnetizing field arising from the shape anisotropy of the nanomagnets and the dipolar coupling field generated by the strong magnetostatic inter-element interaction trigger incoherent magnetization precession within the array at zero bias magnetic field (remanent state) causing the emergence of intrinsic SW (magnonic) modes. We call them ‘intrinsic modes’ since they are intrinsic to the array and do not depend on any external bias magnetic field or other types of excitation like a SAW. When a SAW is launched into the 2D array, we observe two effects: (i) amplification of an existing (intrinsic) SW mode’s power when the SAW frequency is resonant with that mode’s frequency, and (ii) generation of a new extrinsic ME mode at the SAW frequency when the latter is not resonant with the frequency of any intrinsic mode. We call the new modes “extrinsic” since they are generated by the SAW and would be absent otherwise. Our experimental observations are in good agreement with predictions from micromagnetic

simulations that model the ME coupling with an effective time-varying magnetic field which is proportional to the time-varying stress [15].

11.2. Methods

The $LiNbO_3$ substrate is cleaned in ethanol and Au electrodes for launching the SAW are delineated using optical lithography. After delineation of the electrodes, the substrate is spin-coated (spinning rate ~2500 rpm) with bilayer polymethyl methacrylate (PMMA) resists of two different molecular weights and subsequently baked at 110 °C for 5 min. Next, electron beam lithography is performed using a Hitachi SU-70 scanning electron microscope (accelerating voltage of 30 kV, beam current 60 pA) with a Nabity NPGS lithography attachment to open windows for deposition of the nanomagnets. The resists are finally developed in methyl isobutyl ketone and isopropyl alcohol (MIBK-IPA, 1:3) for 270 s, which is followed by a cold IPA rinse. A 5-nm-thick Ti adhesion layer is deposited on the patterned substrate using electron beam evaporation (base pressure ~ 2×10^{-7} Torr), followed by the electron beam deposition of 6-nm-thick Co. The lift-off is carried out by remover PG solution. We have used solid rectangular shaped electrodes to launch SAW in the substrate, instead of inter-digitated transducers (IDT), thereby sacrificing some coupling efficiency, because IDTs are narrow-band filters and our intention was to launch a broad band of SAW frequencies, for which IDTs would not have been functional. A time-varying voltage with frequency in the GHz range is applied between the electrodes which results in a time-varying strain in the region pinched between the electrodes owing to d_{31} and d_{33} coupling. The time varying strain produces an acoustic wave which is very different from the traditional Rayleigh, Sezawa, Lamb or Love modes. Fig. 11.1 (a) shows the scanning electron microscopy (SEM) image of the nanomagnet array comprising elliptical nanomagnets with major axis dimension ~ 360 nm, minor axis dimension ~ 330 nm and thickness ~ 6 nm. The edge-to-edge separation between the nanomagnets is ~ 65 nm in the direction of the major axes and ~ 40 nm in the direction of the minor axes.

The ultrafast magnetization dynamics were measured by a custom-built time-resolved magneto optical Kerr effect (TR-MOKE) microscope [16, 17] in a collinear two-color pump-probe setup. The second harmonic (λ = 400 nm, spot size ~1 μm, fluence ~12 mJ/cm^2) of a Ti-sapphire oscillator was used to excite the dynamics, whereas the time-delayed fundamental laser (λ = 800 nm, spot size ~800 nm, fluence ~1 mJ/cm^2) was used to probe the dynamics. The probe beam samples approximately four nanomagnets since the lateral dimensions of the nanomagnets is ~350 nm. The polar Kerr rotation was measured by an optical bridge detector as a function of the time delay between the pump and probe beams. A large magnetic field was first applied along the minor axes of the nanomagnets to saturate the magnetization and then removed. The sample was scanned by a piezoelectric x-y-z stage to position

the pump and probe beams at the desired location of the sample. RF signal from a signal generator (Rohde & Schwarz SMB100A, frequency range: 100 kHz to 20 GHz) was launched on the sample through high-frequency and low noise coaxial cable (Model No. N1501A-203). The measurement geometry is schematically depicted in Fig. 11.1 (b).

The micromagnetic simulations were performed using object oriented micromagnetic framework (OOMMF) software [18] on a 7×7 array of nanomagnets, discretizing the samples into rectangular prisms of dimensions $2 \times 2 \times 6$ nm^3. First, the static magnetic state was obtained under experimental field configuration. Subsequently, the magnetization dynamics was triggered in the simulation using different excitation fields. The optical excitation was mimicked by a pulsed magnetic field excitation (peak amplitude = 20 Oe and pulse duration = 10 ps) perpendicular to the sample plane, whereas the effect of SAW was mimicked by an additional sinusoidal excitation field (peak amplitude = 5 Oe and frequency corresponding to the SAW frequency) in the direction of the major axis throughout the whole simulation time. This field is related to the generated stress as,

$$\boldsymbol{H_{stress}(t) = \frac{3\lambda_S \sigma(t)}{2\mu_0 M_S}} \tag{11.1}$$

where μ_0 is the magnetic permeability of free space, M_s is the saturation magnetization of the nanomagnets (1 MA/m), λ_s is the saturation magnetostriction and $\sigma(t)$ is the sinusoidal time-varying stress due to the SAW [15].

To calculate the amplitude of the stress $\sigma(t)$, generated by the S AW, we follow the recipe of an earlier work [19] for a plane surface wave:

$$\boldsymbol{\sigma = \sqrt{2PZ_0}\ ;\ Z_0 = \sqrt{c_{11}\rho}} \tag{11.2}$$

where P is the power in the wave per unit area, Z_0 is the characteristic acoustic impedance, c_{11} is the first diagonal element of the elasticity tensor and ρ is the mass density. The cross-sectional area through which the wave passes is the penetration depth times the width of the electrodes. The penetration depth is approximately the wavelength (which varies with the SAW frequency), but we will take its average value to be ~1 mm. Therefore, the cross-sectional area of the wave is roughly 1 μm × 2 mm = 2×10^{-9} m^2. Since the power coupled into the substrate is 4.5 μW (calculated earlier), the power per unit cross-sectional area P = 2.25 kW/m^2. For $LiNbO_3$, c_{11} = 202 GPa and ρ = 4650 Kg/m^3. This yields $Z_0 = 9.7 \times 10^8$ N.s /m^3. Therefore, the stress generated is 1.55 MPa. There is a wide spread in the reported values of the saturation magnetostriction of Co, λ_s ranging from 30 ppm [20] to 150 ppm [21]. Taking the higher value in view of the fact that magnetostriction may increase in nanoparticles [22] and assuming M_s = 1 MA/m, we obtain from the previous equation that the amplitude is 277.5 A/m which is about 3.5 Oe. This is of the same order as 5 Oe assumed in the simulation.

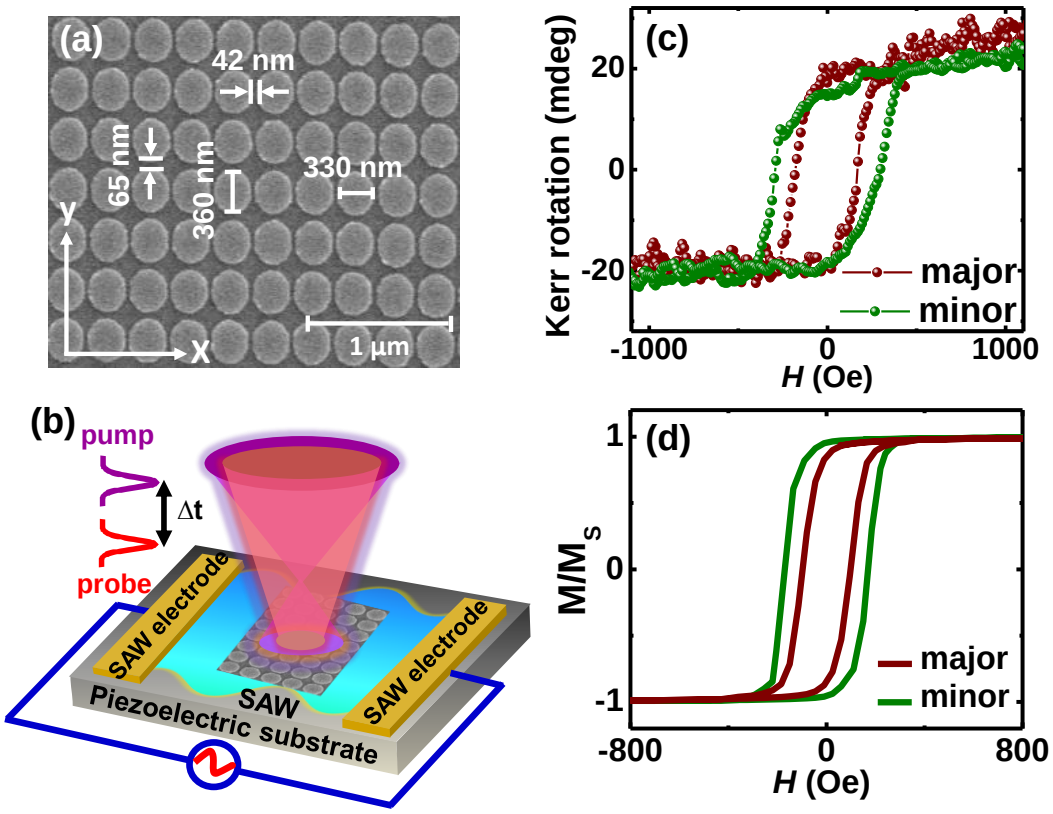

Fig. 11.1: (a) Scanning electron microscopy (SEM) image of the nanomagnet array. (b) Schematic of the measurement geometry showing the launched SAW along with the pump and probe beams of the TR-MOKE measurement. (c) Experimental and (d) Simulated magnetic hysteresis loop of the sample.

Within each nanomagnet, the SAW amplitude is assumed to be spatially invariant and so is the effective magnetic field H_{stress} associated with it. The wavelength of the SAW in the frequency range 1 – 10 GHz is a few hundreds of nm to few micrometers. The major axes of the nanomagnets are ~360 nm while the minor axes are ~330 nm. Hence, at the lower frequencies, the assumption of spatially invariant H_{stress} amplitude is justified since the nanomagnet's lateral dimension is an order of magnitude smaller than the wavelength, but it is definitely questionable at the higher frequencies. Since taking the spatial variation of the amplitude of $H_{stress}(t)$ into account would have been computationally prohibitive, we ignored this effect, but understand that it could make some difference. Material parameters used in the simulations were gyromagnetic ratio γ = 17.6 MHz/Oe, anisotropy field H_k = 0 saturation magnetization M_{eff} = 1400 emu/cc, and exchange stiffness constant A = 3.0 × 10^6 erg/cm. The spatial profiles of the SW modes were calculated using an in-house Matlab code named DotMag [23].

11.3. Results and Discussion

The experimental hysteresis loops of the sample for two mutually perpendicular orientations of the magnetic field are presented in Fig. 11.1 (c). The coercivity is □100 Oe higher when the magnetic field is directed along the horizontal axis which is parallel to the minor axes of the elliptical nanomagnets. The simulated hysteresis loops of the sample for two mutually perpendicular orientations of the magnetic field are presented in Fig. 11.1 (d). The simulated results are in qualitative agreement with the experimental MOKE loops corroborating the presence of configurational anisotropy in the sample.

The time-resolved reflectivity and Kerr rotation signals in the absence of any bias magnetic field or SAW are shown in Fig. 11.2 (a) and (b), respectively. The fast Fourier transformed (FFT) power spectra of the experimental and simulated time-domain magnetization are shown in Fig. 11.2 (c) and (d), respectively. The FFT power spectrum of the time-resolved reflectivity signal is shown in the inset of Fig. 11.2 (c). The simulated static spin configuration of the nanomagnet array at remanence is shown in the inset of Fig. 11.2 (d). In the absence of any bias magnetic field or SAW, the magnetization of a nanomagnet precesses around an effective magnetic field determined by the strong magnetostatic interaction between nanomagnets in the array, the shape anisotropy, and any stress caused by the differential thermal expansion/contraction of the nanomagnets and the substrate (as a consequence of laser heating). The resulting SW modes are the intrinsic SW modes of the array. The experimental intrinsic SW spectrum (spectrum of Kerr oscillations) reveals four distinct intrinsic SW modes ~3.1 GHz (M1), ~4.2 GHz (M2), ~7.1 GHz (M3) and ~10.2 GHz (M4) with the powers of lower frequency modes M1 and M2 much larger than those of higher frequency modes M3 and M4. Interestingly, the FFT power spectrum of the time-resolved reflectivity signal also shows a dominant peak at around M2 with two weaker peaks at around M1 and M3. However, the time-resolved reflectivity data measured from the bare $LiNbO_3$ substrate reveals no clear oscillation, exhibiting only a noisy FFT power spectrum as shown in section A6.1 of the Appendix VI. This is probably due to the fact that the laser heating and cooling effect sets up noisy strain-field oscillations in the bare substrate, which are captured in the reflectivity data. If there is any signal submerged in the measured data, we do not have sufficient sensitivity to capture it.

Before simulating the intrinsic SW dynamics of the nanomagnet array to compare with experiments, we have simulated the intrinsic SW dynamics of a single isolated Co nanomagnet as shown in section A6.2 of the Appendix VI. The static spin configuration of a single nanomagnet forms an '*S*' state and its simulated SW spectrum reveals four clear modes whose spatial profiles show standing wave patterns along the major axis. The axes of quantization of the modes are rotated owing to the asymmetric '*S*' state spin configuration. However, the static spin configuration is significantly

modified in the multi-nanomagnet array with the spins inside the nanomagnets getting aligned primarily along the major (easy) axes of the nanomagnets (inset of Fig. 11.2 (d)).

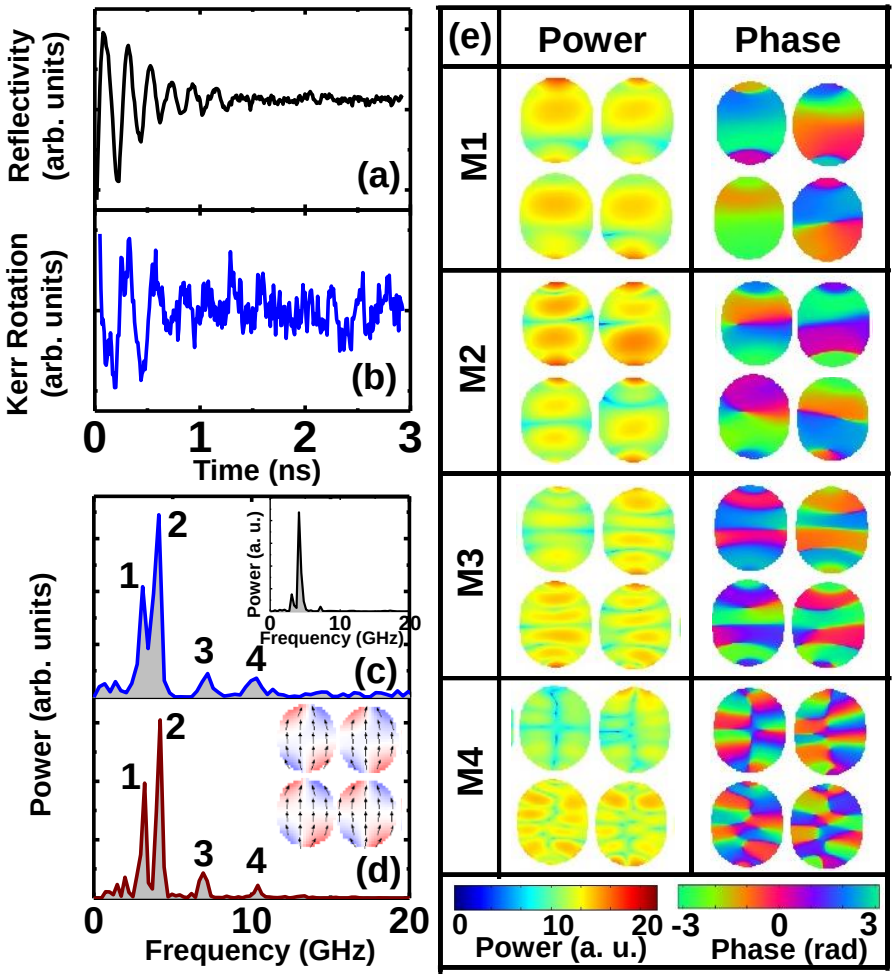

Fig. 11.2: Background subtracted experimental time-resolved (a) reflectivity and (b) Kerr rotation data in the absence of SAW and any bias magnetic field. (c) FFT power spectrum of the experimental time-resolved Kerr rotation (FFT of time-resolved reflectivity in the inset). (d) FFT power spectrum of simulated time-resolved magnetization showing excellent agreement with the experimental data in 2(c). The simulated static magnetic configuration of a part of the nanomagnet array at remanence is shown in the inset. (e) Power and phase profiles of the SW modes of the nanomagnet array. The corresponding color bars are shown in the Fig.

The simulated SW spectrum of the array again shows four clear peaks in qualitative agreement with the experimental spectrum (Fig. 2(c) and (d)). The slight discrepancies between the theoretical and experimental peak frequencies can be attributed to the difficulty of precisely accounting for the roughness and edge deformations of the real sample in the micromagnetic simulation. The spatial profiles of the simulated intrinsic SW modes of the array are shown in Fig. 11.2 (e). The modes M1, M2 and M3 form standing wave patterns along the major axis with quantization numbers n = 3, 4 and 6, respectively. The highest frequency intrinsic mode M4 has a complex character with mixed quantization along both major (n = 6) and minor (m = 2) axes of the nanomagnet. We notice that the

deformed SW patterns in the single nanomagnet become more symmetric in the array due to the strong interelement magnetostatic coupling.

SAW driven dynamics: Finally, we apply SAW to the sample in the geometry shown in Fig. 11.1 (c) with varying frequencies (f_{SAW}) in the range, 1 GHz $\leq$ $f_{SAW} \leq$ 10 GHz at a fixed power P_{SAW} = -10 dBm (0.1 mW). The SAW propagates along the major axes of the nanomagnets. Fig. 11.3 (a) shows the experimental SW spectra after the application of SAW. The simulated SW spectra corresponding to this case was obtained with a sinusoidal time-varying magnetic field H_{stress} applied along the major axis of the nanomagnets to replicate the time-varying stress field caused by the SAW. The simulation results (Fig. 11.3 (b)) are in good qualitative agreement with the experimental SW spectra. The launched SAW periodically expands and contracts the Co nanomagnets and modifies their magnetization precession owing to the inverse magnetostrictive (Villari) effect.

Non-resonant excitation: When the SAW frequency is not resonant with any intrinsic mode frequency, the SAW would generate a new ME mode at its own frequency. These are the extrinsic modes which are synchronous with the SAW. For example, at f_{SAW} = 1 GHz, a new (extrinsic) mode appears at ~1 GHz in addition to the existing intrinsic SW modes. This new mode was not present in the absence of the SAW and is therefore generated exclusively by the SAW. However, characterization of precise elastic and magnetic components present in this mode is beyond the scope of this article [24]. Nevertheless, this is an exciting observation since the new SW mode would couple to a radiating electromagnetic wave and therefore radiate an electromagnetic wave of the same frequency as the driving SAW. This is the basis of a microwave frequency (1 GHz) magnetoelastic antenna [25].

Resonant Excitation: When the SAW frequency is resonant with one of the intrinsic SW mode frequencies, the SAW drives the nanomagnets into ME resonance, amplifying the power of that intrinsic mode significantly. This type of resonance phenomenon has been predicted theoretically from micromagnetic simulations [26]. At f_{SAW} = 3 GHz (4 GHz), the power of M1 (M2), which is resonant with the SAW, is amplified while other modes are suppressed. Consequently, we observe a SW spectrum having one dominant resonantly amplified mode with a low power shoulder on the left or the right side. The frequencies of the suppressed modes M3 and M4 are actually resonant with f_{SAW} = 7 GHz, and 10 GHz respectively, and hence, their powers are significantly amplified at those SAW frequencies. On the other hand, when f_{SAW} is adjacent (6 GHz or 8 GHz) to M3, it excites an extrinsic mode at the SAW frequency by nearly annihilating M3, as shown by the red dotted box in Fig. 11.3 (a) and b. These observations show that we can always generate SW modes at the frequency of the SAW and if the latter happens to be resonant with an intrinsic SW mode (i.e. a mode which is present in the absence of SAW), then that mode is amplified by the SAW.

Fig. 11.3 (c) shows the power and phase profiles of selected modes after the application of SAW. The power and phase profiles of the SW modes whose frequencies are resonant with the SAW frequencies become more uniform upon application of SAW (as shown in Fig. 11.3 (c) for M* and M3 and Fig. A6.3 of appendix VI for M1, M2 and M4). Therefore, the SAW has a smoothing effect on the profiles of those modes that it drives resonantly. However, the nature of those modes, including mode quantization number, remains unaffected. The SAW-generated new extrinsic modes at 6 and 8 GHz also exhibit standing wave pattern along the major axis of the ellipse with n = 5 and 7, respectively, as shown in Fig. 11.3 (c).

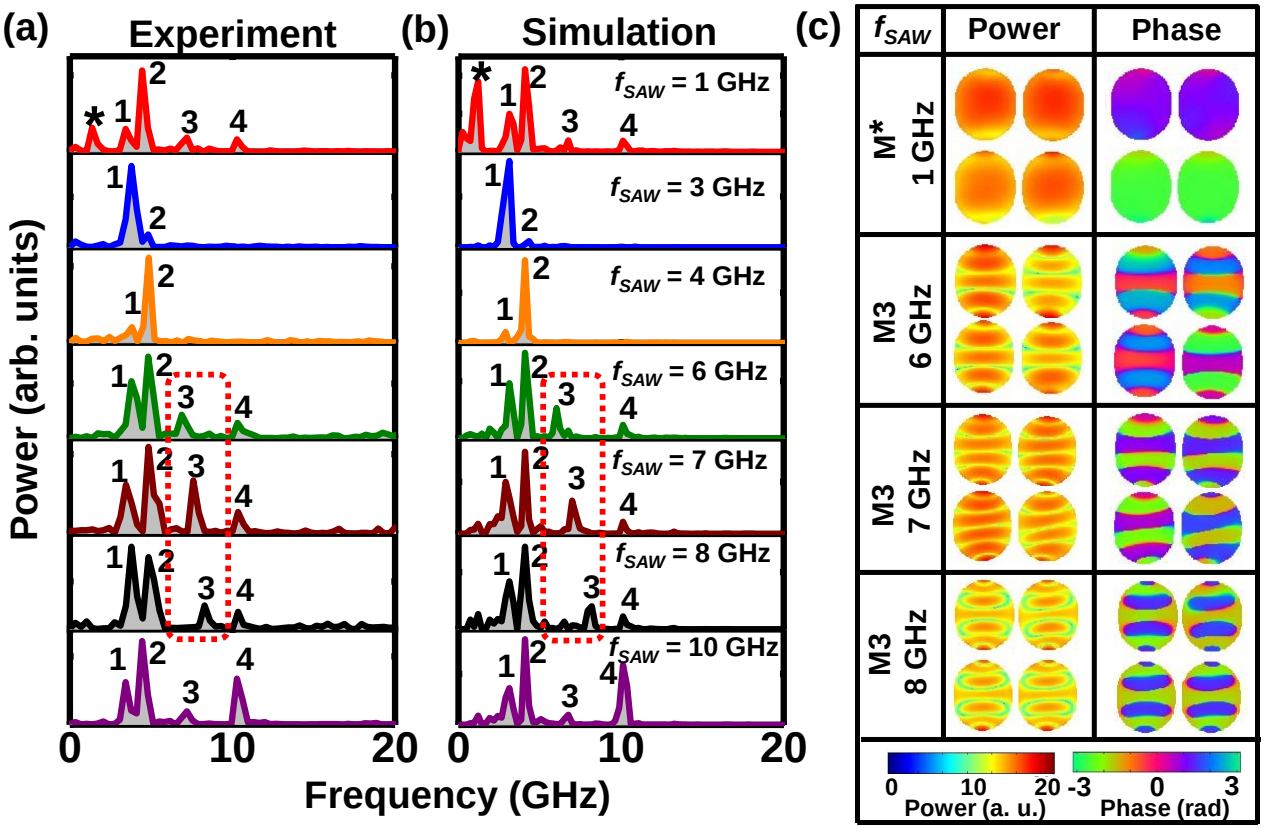

Fig. 11.3: (a) The experimental and (b) simulated SW spectra of the nanomagnet array at different values of SAW frequency f_{SAW}, with SAW propagation along the major axis of the nanomagnets (c) The power and phase profiles of selected SW modes at different values of f_{SAW}. The color bars are shown at the bottom.

In order to check the anisotropic nature of the SAW coupling (magnon-phonon coupling), we have further simulated the SW dynamics of the array at remanence with the sinusoidal field $H_{stress}(t)$ applied along the minor axis of the elliptical nanomagnets. Fig. 11.4 (a) shows the simulated time-domain magnetization ($M_z(t)$) at three different frequencies of $H_{stress}(t)$ and Fig. 11.4 (b) shows the corresponding FFT power spectra. A drastic change in the SW spectra is observed with a single dominant extrinsic SW mode appearing at the frequency of the SAW in all three cases. The intrinsic SW modes of the array at remanence are completely annihilated when excited by SAW in this

geometry and replaced by the extrinsic mode. This shows the strongly anisotropic nature of the SAW coupling. This is also a very exciting result since it shows that in this configuration, it may be possible to implement a nearly 'monochromatic' magnetoelastic antenna which would be radiating almost exclusively at the SAW excitation frequency without any sideband. In future, we will verify this result experimentally. The magnon-phonon coupling (between SW and SAW) studied here is not necessarily optimal. Optimal coupling requires phase matching between the two waves where the wavevectors of the two waves will be equal. We do not currently know the wavevectors of the SW at the SAW frequencies since we do not know their dispersion relations. We are obtaining these dispersion relations using Brillouin light scattering (BLS) and would attempt to study phase matching scenarios in the future.

In order to gain more insight into the observed dynamics, we have further simulated the magnetostatic field distribution of the array by using LLG micromagnetic simulator [27]. Fig. 11.4 (c) shows the contour plots of the magnetostatic fields of the nanomagnet array at remanence. The arrows represent the magnetization inside the dots. Strong inter-element interacting field lines are observed along the major axes of the nanomagnets, indicating dominant dipolar contribution from the magnetostatic stray field along this direction. To quantify the inter-element interaction, we have taken line scans of the magnetostatic fields along both major and minor axes of the nanomagnets as shown by the black dotted lines in Fig. 11.4 (c). From Fig. 11.4 (d), it is evident that the magnitude of the inter-element stray field along the major axes is ~2.2 kOe, whereas, along the minor axes it is negligibly small. This indicates stronger inter-element interaction along the major axes than along the minor axes of the nanomagnets, despite the fact that the center-to-center separation between nearest neighbor nanomagnets in the array is 425 nm along the major axis and smaller (370 nm) along the minor axis. This is due to the abundance of free magnetic poles at the edges of the nanomagnets along the major axis, which causes a significantly large stray magnetic field along that direction. long the minor axis, the free magnetic poles are negligible causing negligibly small stray magnetic field. This property (anisotropic dipole interaction in a 2D array) has been exploited in devising nanomagnet-based computing platforms, such as image processors [28] and anti-correlators/correlators for Bayesian networks [29]. Here, the anisotropy makes the extrinsic (SAW-driven) SW dynamics very different along the two directions.

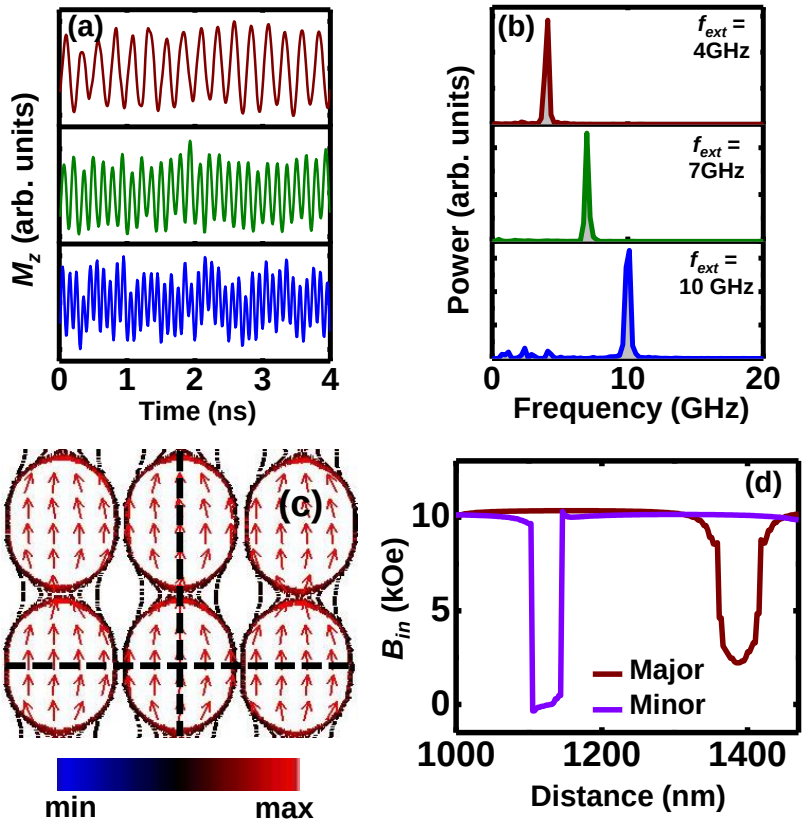

Fig. 11.4: (a) Simulated time-domain magnetization (M_z) when the sinusoidal field mimicking the SAW is applied along the minor axes of the nanomagnets (corresponding to SAW propagation along the minor axis) and (b) the corresponding FFT power spectra. (c) Contour plot of the simulated magnetostatic field distribution of the nanomagnet array at remanence and (d) line scans of the magnetostatic field taken along the black dotted lines as shown in (c). The color bar is shown below the plot in (c).

11.4. Conclusion

In conclusion, the magnetodynamics in a densely packed 2D array of elliptical Co magnetostrictive nanomagnets fabricated on a piezoelectric $LiNbO_3$ substrate has been probed in the absence of any bias magnetic field and without/with SAW excitation. A SAW launched into the array amplifies the intrinsic SW modes if their frequencies are resonant with the applied SAW frequencies. New SW (extrinsic) modes are spawned by the SAW at the SAW frequencies when they are not resonant with the intrinsic modes. The coupling between SW and SAW is highly anisotropic in nature. All observed features are qualitatively reproduced by micromagnetic simulations. Our findings provide fundamental insight into bias-field free magnonics [30], which offer exciting potentials for the design of energy efficient spin-wave filters and strain-controlled magnonic nano-devices.

References

[1] W. Rushforth, E. De Ranieri, J. Zemen, J. Wunderlich, K.W. Edmonds, C.S. King, E. Ahmad, R. P. Campion, C. T. Foxon, B. L. Gallagher, K. Výborný, J. Kučera, T. Jungwirth, Phys. Rev. B **78**, 085314 (2008).
[2] M. Weiler, L. Dreher, C. Heeg, H. Huebl, R.Gross, M. S. Brandt, S. T. B. Goennenwein, Phys. Rev. Lett. **106**, 117601 (2011).
[3] A. V. Scherbakov, A. S. Salasyuk, A. V. Akimov, X. Liu, M. Bombeck, C. Bruggemann, D. R. Yakovlev, V. F. Sapega, J. K. Furdyna, M. Bayer, Phys. Rev. Lett. **105**, 117204 (2010).
[4] M. Bombeck, A. S. Salasyuk, B. A. Glavin, A. V. Scherbakov, C. Bruggemann, D. R.Yakovlev, V. F. Sapega, X. Liu, J. K. Furdyna, A. V. Akimov, M. Bayer, Phys. Rev. B **85**, 195324 (2012).
[5] A. Barman, S. Mondal, S. Sahoo, A. De, J. Appl. Phys. **128**, 170901 (2020).
[6] A. Biswas, S. Bandyopadhyay, J. Atulasimha, Appl. Phys. Lett. **103**, 232401 (2013).
[7] V. Sampath, N. D'Souza, D. Bhattacharya, G. M. Atkinson, S. Bandyopadhyay, J. Atulasimha, Nano Lett. **16**, 5681 (2016).
[8] C. Berk, M. Jaris, W. Yang, S. Dhuey, S. Cabrini, H. Schmidt, Nat. Commun. **10**, 2652 (2019).
[9] Z. Xiao, R. Lo Conte, M. Goiriena-Goikoetxea, R. V. Chopdekar, C.-H. A. Lambert, X. Li, A. T. N'Diaye, P. Shafer, S. Tiwari, A. Barra, A. Chavez, K. P. Mohanchandra, G. P. Carman, K. L. Wang, S. Salahuddin, E. Arenholz, J. Bokor, R. N. Candler, ACS Appl. Mater. Interfaces **12**, 6752 (2020).
[10] W. Edrington, U. Singh, M. A. Dominguez, J. R. Alexander, R. Nepal, S. Adenwalla, Appl. Phys. Lett. **112**, 052402 (2018).
[11] S. Davis, A. Baruth, S. Adenwalla, Appl. Phys. Lett. **97**, 232507 (2010).
[12] M. Foerster, F. Macia, N. Statuto, S. Finizio, A. S. Hernandez-Mínguez, S. Lendínez, P. V. Santos, J. Fontcuberta, J. M. Hernàndez, M. Klaui, L. Aballe, Nat. Commun. **8**, 407 (2017).
[13] Y. Yahagi, B. Harteneck, S. Cabrini, H. Schmidt, Phys. Rev. B **90**, 140405 (R) (2014).
[14] S. Mondal, M. A. Abeed, K. Dutta, A. De, S. Sahoo, A. Barman, S. Bandyopadhyay, ACS Appl. Mater. Interfaces **10**, 43970 (2018).
[15] M. S. Fashami, J. Atulasimha, S. Bandyopadhyay, Nanotechnology **23**, 105201 (2012).
[16] A. Barman, A. Haldar, Solid State Phys. **65**, 1 (2014).
[17] A. Barman, J. Sinha, Springer International Publishing AG, 2018.
[18] M. Donahue, D. G. Porter, OOMMF User's guide, Version 1.0, Interagency Report NISTIR 6376, National Institute Standard and Technology, Gaithersburg, MD (1999); http://math.nist.gov/oommf.
[19] S. Datta, Prentice Hall, Englewood Cliffs, New Jersey, 1986.
[20] Z. Nishiyama, Sci. Rep. Tohoku Imp. Univ. Ser. 1 **18**, 341 (1929).
[21] R. M. Bozorth, *Phys. Rev.* **96**, 311 (1954).
[22] S. J. Zhao, Nanomaterials 1 (2015).
[23] D. Kumar, O. Dmytriiev, S. Ponraj, A. Barman, J. Phys. D: Appl. Phys. **45**, 015001 (2012).
[24] F. Vanderveken, J. Mulkers, J. Leliaert, B. Van Waeyenberge, B. Soree, O. Zografos, F. Ciubotaru, C. Adelmann, arXiv:2011.10326 [cond-mat.mes-hall].
[25] J. L. Drobitch, A. De, K. Dutta, P. K. Pal, A. Adhikari, A. Barman, S. Bandyopadhyay, Adv. Mater. Tech. **5**, 2000316 (2020).
[26] W. A. Misba, M. M. Rajib, D. Bhattacharya, J. Atulasimha, Phys. Rev. Appl. **14**, 014088 (2020).
[27] LLG Micromagnetics Simulator, developed by M. R. Scheinfein http://llgmicro.home.mindspring.com (accessed March 8, 2018).
[28] M. A. Abeed, A. K. Biswas, M. M. Al-Rashid, J. Atulasimha, S. Bandyopadhyay, IEEE Trans. Elec. Dev. 64, 2417 (2017).
[29] M. T. McCray, M. A. Abeed, S. Bandyopadhyay, Sci. Rep. **10**, 12361 (2020).
[30] A. Haldar, D. Kumar, A. O. Adeyeye, Nature Nanotechnol. **11**, 437 (2016).

Chapter 12

Summary and Future Perspectives

12.1 Summary

In this thesis, we have investigated the quasi-static and dynamic magnetization processes in ferromagnetic patterned nanostructures and multilayers. The motivation for such research is to promote the potential of SW devices for future data storage and information processing technology. The growth of ferromagnetic thin films and multilayers and nanopatterning of magnetic nanostructures were carried out by using rf/dc magnetron sputtering, electron beam evaporation, electron beam lithography and focused ion beam milling, as applicable. The preliminary characterizations of these samples were carried out using scanning electron microscopy (SEM), atomic force microscopy (AFM) and energy dispersive X-ray spectroscopy (EDX). The static magnetic properties, such as, magnetization reversal, saturation magnetization, saturation field, coercivity, anisotropy, domain features were explored by using static magneto optical Kerr effect (S-MOKE) magnetometry and magnetic force microscopy (MFM). The magnetization dynamics were probed by some state-of-the-art techniques namely, custom-built all-optical time-resolved magneto-optical Kerr effect (TR-MOKE) microscopy (in time domain) based on mode-locked fs oscillator system in a collinear geometry, a two-color optical pump probe technique based on femtosecond amplifier system in noncollinear geometry and Brillouin light scattering (BLS) spectroscopy (in wave vector domain), respectively. The experimental observations were modelled to interpret the underlying physics for the respective systems with the aid of micromagnetic simulations (i.e., OOMMF and LLG simulator) and plane wave method (PWM).

We investigated the magnetization dynamics in a binary magnonic crystal (BNM) comprised of $Ni_{80}Fe_{20}$ diatomic nanodot array (two different sized nanodots placed in close proximity to each other forming a complex double-dot unit cell). A distinct variation of SW mode characteristics for different in-plane bias magnetic field applied along two different orientations of the lattice was observed. Micromagnetic simulations reproduced the observed dynamical behavior and revealed the variation of spatial distribution of collective modes of constituent single nanodots with different diameter and a diatomic unit forming the large array to understand the evolution of the magnetization dynamics from a single dot to the large array via a diatomic unit. The changes in mode frequency, spatial profiles of the modes, and appearance of new modes in a diatomic unit and its array from that of the constituent single dots indicated the strong magnetostatic interaction among the dots within the diatomic unit.

Also, the occurrence of the new interacting mode at different frequencies for different orientations of the bias field indicated the change in the nature of interaction among the dots within the diatomic unit with bias magnetic field. We subsequently investigated the SW dispersion and reconfigurable magnonic band structure in this BNM. The dynamic dipolar coupling between the nanodots of two different diameters plays crucial role by substantially affecting the magnonic band structure, including the slope of the dispersion curves in two orthogonal orientations of the applied bias magnetic field. A detailed micromagnetic investigation using local excitation was performed to obtain a deeper insight into the nature of the SW propagation in this system. Iso-frequency contours calculated from plane-wave method, further revealed the origin of the anisotropic properties of the SW eigenmodes.

We further investigated the magnetization dynamics in 2D MCs with complex geometry in the form of antidot arrays by tuning the lattice arrangements from periodic to quasi-periodic regime. For this study we specifically selected asymmetric triangular-shaped antidots with lack of reflection or mirror symmetry along a particular axis, arranged in various lattice symmetry. Firstly, the SW dynamics in hexagonally arranged antidot systems was explored by controlling the strength and orientation of the bias magnetic field. Hexagonally arranged antidot lattices are interesting because they offer the highest packing density among all Bravais and non-Bravais lattices. A remarkable variation in the SW modes with the orientation of in-plane bias magnetic field was found to be associated with the conversion of extended SW modes to quantized ones and vice versa. Next, the high-frequency SW dynamics in a magnonic quasicrystal (MQC) with complex basis was studied, the quasiperiodicity of octagonal lattice was added to the asymmetric basis of triangular shaped antidots. We further compared the SW dynamics of this MQC with that of the most primitive square lattice. The number of SW modes reduced systematically with increasing lattice constant, approaching towards a thin-film like behavior, due to the reduction of the demagnetizing field around the antidots. Micromagnetic simulations revealed the presence of SW modes with both even and odd quantization numbers, because of the asymmetric potential energy landscapes. The SW extension through the nanochannels between the antidots occured most naturally for the square lattice, whereas, the SW localization within the octagonal and rhombic units occured most naturally for the octagonal lattice, due to the scarcity of nanochannels. The combination of the complex triangular basis along with the octagonal unit cell exhibited a strong eight-fold anisotropy superposed with a weak three-fold anisotropy. This is in sharp contrast to a strong four-fold anisotropy superposed with a weak three-fold anisotropy observed in the most primitive square lattice. We interpreted the origin of the diversity of SW dynamics from the stark modulation of the internal field strengths and asymmetric demagnetizing field profiles surrounding the antidots.

The underlying mechanisms of femtosecond laser induced ultrafast demagnetization in synthetic antiferromagnets (SAFs) comprised of Co/Pt multilayers periodically interleaved by Ru or Ir spacers

and its external control by the magnetic configuration was also investigated in this thesis. Our investigation conclusively showed that both spin flip scattering (SFS) as well as the spin transport (ST) of optically excited carriers through majority spin channels have significant contributions to the ultrafast demagnetization of the SAF multilayers. The demagnetization time can be as fast as sub-100 fs and it can be easily controlled by externally controlling the magnetic state of the samples, i.e. the relative orientation of magnetization between the layers. An active control over different demagnetization mechanisms can be achieved by specially designing the samples, altering the external magnetic field and the excitation fluence.

The anisotropic variation of SW dynamics in diamond shaped antidot lattices patterned on Co/Pd multilayers with PMA was then investigated in this thesis. By employing micromagnetic simulations we showed that formation of narrow shell-like regions around the antidots caused the emergence of in-plane domain structures as the magnetic anisotropy in these regions is reduced due to the Ga+ ion irradiation during the focused ion beam (FIB) milling process of the antidot fabrication. The in-plane direction of the shell magnetization changes sharply with the change of the bias magnetic field orientation, leading to the stark variation of the SW modes in such perpendicularly magnetized systems.

Surface-acoustic-wave (SAW) induced resonant amplification of intrinsic SW modes, as well as generation of new extrinsic modes at applied SAW frequency was demonstrated in a densely packed two-dimensional array of elliptical Co nanomagnets fabricated on a piezoelectric $LiNbO_3$ substrate, forming a two phase (magnetostrictive + piezoelectric) multiferroic. The strong magnon-phonon coupling (between SW and SAW) was found to be highly anisotropic in nature. Our findings lay the groundwork for the bias-field-free magnonics, which offer exciting potentials in the design of energy efficient on-chip microwave devices and extreme sub-wavelength ultra-miniaturized microwave antennas for embedded applications.

12.1 Future Perspectives

The current advancement in nanofabrication techniques has made it possible to grow periodically patterned nanostructures and thin film heterostructures with high quality and resolution while the experimental realization of various theoretically proposed effects in these novel systems have opened new pathways to understand the fundamental physics and potential applications in last few decades.

The investigation of magnetization dynamics of arrays of ferromagnetic nanodots and antidots can play a pivotal role in future spin-based communication technology due to their efficient tunability as a function of various geometric parameters such as shape, size, lattice arrangement and periodicity. Introduction of binary or ternary basis to ferromagnetic nanodots and antidots can enrich the SW

spectra, mode profiles and magnonic band structures in future. An interesting aspect for future can be the investigation of spin dynamics in quasiperiodic and defective nanostructures. Defects can also play important roles in MCs. Numerical studies showed that the magnonic spectra of a hexagonal array of antidot is quite robust to random defects [1]. On the other hand, introduction of a line defect, showed elevated frequency of the fundamental mode due to the increase in internal field in antidot-free region and generation of a new extended mode with wider profile [2]. The defects or disorders reforms the local magnetic properties, which may drastically reconstruct the magnonic band structure by introducing new SW modes, phase shifts, minibands with tailored magnonic band gap and SW group velocities due to the breaking of translational symmetry. Quasicrystals possess long-range ordering without any periodicity and their diffraction patterns exhibit symmetry forbidden by crystallographic restrictions. MQCs can possess salient properties like branching in the band structure, self-similarity and scaling properties in the transmission spectra. Construction of numerous types of bi-component or multi-component MQCs with aperiodic geometries, such as different variants of penrose tiling, oblique tiling, and Ammann–Beenker tiling may offer unprecedented tunability of the magnonic band structure besides a stark modulation of SW group velocity due to the lack of translational symmetry. MCs with "fractal" geometries can be included as a new member of the family of artificial crystals offering intriguing high frequency dynamics. Another interesting polytope of MC can be "Voronoi cell"-like nanostructures, which retains the lattice symmetry but offers more independent choice of the basis [3].

The study of laser induced modification of ultrafast magnetization dynamics in ferromagnetic multilayers reveals that the dynamic parameters can be controlled reversibly with pump induced rapid heating and simultaneous cooling in ultrafast time scale, which may find application in future heat assisted data writing technology. Using an optical parametric amplifier (OPA), lasers of different wavelengths having different penetration depths can be generated. Exploiting those as pump, rich physics related to ultrafast demagnetization and remagnetization in SAF multilayers can be explored in future.

In case of the magneto-elastic (ME) coupling of magnetostrictive nanomagnets, the energy can be transferred from the SAW to the SW very efficiently (ideally up to 100% efficiency) if the coupling is strong. In this case, the energy will not remain mostly in the elastic domain any more, but will go into the spin domain. Phase matching is required for most efficient coupling and that occurs when the wave vectors (and hence the wavelengths) of the SAW and SW match. This is well-known from coupled mode theory. For such optimal magnon-phonon coupling, we need to know the wave vectors of the SWs at the SAW frequencies. Investigation of dispersion relations of such nanomagnet array using Brillouin light scattering (BLS) technique to study phase matching scenarios would be an

important future problem. Further investigation of the effect of SAWs on the SW dynamics of these nanomagnets in presence of applied magnetic field would also be worth exploring in future.

The SW dynamics in nanostructures can be more interesting if those are patterned on top of heavy metal with high spin-orbit coupling (SOC). To excite and control the SW dynamics by the application spin current generated spin-orbit torque (SOT) in such nanostructures would be interesting. The generation of spin current and its effect on adjacent ferromagnetic layer can be studied in various emerging systems, such as, topological insulator, Weyl semimetal, doped heavy metals etc. which may provide exceptionally high charge to spin conversion efficiency and giant modulation of damping leading towards energy efficient magnetic switching.

References

1. A. Barman, J. Phys. D Appl. Phys. **43**, 195002 (2010).
2. M. Madami, G. Gubbiotti, S. Tacchi, G. Carlotti, and S. Jain, Physica B **435**, 152 (2014).
3. M. Senechal, Quasicrystals and Geometry (Cambridge University Press, Cambridge, 1996).

Appendix I

Micromagnetic Simulations of the Diatomic Nanodot Arrays with the Introduction of Actual Edge Roughness

The introduction of edge deformation causes modifications of the spin-wave modes and we studied the same for the two single dots of different size, diatomic unit and the array. The FFT spectra of the simulated time-domain magnetization for the rough-edged samples in the two orientations of the bias field have been shown in Figs. A1.1 (a) and (b). The power and phase profiles have been shown in Figs. A1.2 and A1.3. In comparison to the ideal sample, in the smaller dot for φ = 0°, mode 1 is significantly modified with larger frequency of 4.3 GHz and spatial character (asymmetric edge mode) due to the edge deformation while the two higher frequency modes remain nearly unaltered. Similarly, for φ = 90°, the modes are drastically different with an EM (mode 1 at 4.0 GHz) and two BV-like modes with n = 5 (mode 2 at 6.4 GHz) and n = 7 (mode 3 at 8.2 GHz). For the larger dot three lower frequency modes (6.4, 7.4 and 8.0 GHz) are modified for φ = 0° with mode number as n = 7, 7 and 9 for mode 1, 2 and 3, respectively. For φ = 90° the two lower frequency modes (mode 1, 6.2 GHz and mode 2, 7.2 GHz) and the highest frequency mode (mode 4, 12.5 GHz) remains unaltered (in comparison with the ideal sample) as BV-like mode with n = 5 and 7 and the complex mode with mixed BV-DE like character, respectively, despite of edge deformations. However, mode 3 for the smooth edged/ideal larger dot which is a BV-like mode with n = 9, almost disappears (see Fig. 5.4 (c) of the chapter 5 for comparison) and the most dominant mode (mode 3 for rough edged larger dot, 8.6 GHz) shows primarily uniform character as CM superposed with a quantized mixed BV-DE like character. These modes are again modified in a diatomic unit due to the variation of the internal field and the stray magnetic field as a result of the edge deformation. For φ = 0°, the number of modes and their frequencies remain unaltered (as compared to the ideal array) by the edge deformation but the spatial nature of modes 1 and 3 are significantly modified, while other modes remain similar (see Fig. 5.4 (b) and 5.5 of the chapter 5 for comparison). For φ = 90°, mode 1 being the EM of both the dots nearly vanishes due to the edge deformation, while other modes remain qualitatively similar to those of the diatomic unit with smooth edge (see Figs. 5.4 (c) and 5.6 of the chapter 5 for comparison).

In the array, the modes are further modified. For φ = 0°, mode 1 of the ideal array (with dots of smooth edges) nearly disappears (Fig. A1.1 (a)) as also observed in the experimental spectrum (Fig. 5.4 (a) of the chapter 5). Consequently, mode 1 of the rough-edged sample corresponds to the mode 2 of the ideal sample and similarly modes 2 and 4 of the rough-edged sample correspond to modes 3 and 4 of the ideal sample, respectively. A new shoulder-like mode (mode 3) appears in the rough array at

around 11.6 GHz, which is again a BV-like mode with quantization number n = 22 in the larger one and n = 10 in the smaller one. The simulated spectra of the rough array reproduce the experimental spectra better than the ideal array. For φ = 90°, the experimental spectra is even better reproduced by the rough array than the ideal array. Here mode 1, which was not prominent in the ideal array, is now clearly observed and corresponds to the BV-like modes in the two dots with n = 5 for the larger dot and n = 3 for the smaller dot. The other three modes remain qualitatively similar as the ideal array (see Figs. 5.4 (c) and 5.6 of the main article for comparison).

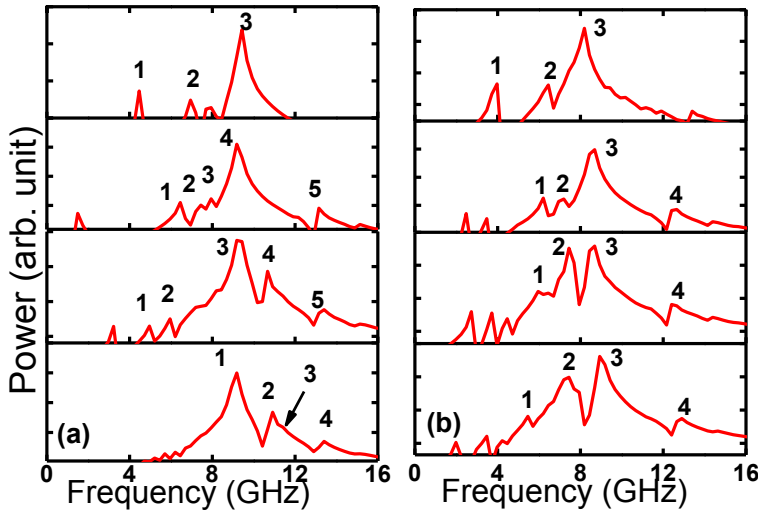

Fig. A1.1: FFT power spectra of the simulated time-domain magnetization of rough-edged array S1 at (a) φ = 0°and (b) φ = 90°. Each column contains four panels corresponding to the simulated spectra of smaller dot, larger dot, a diatomic unit and an array with periodic boundary condition.

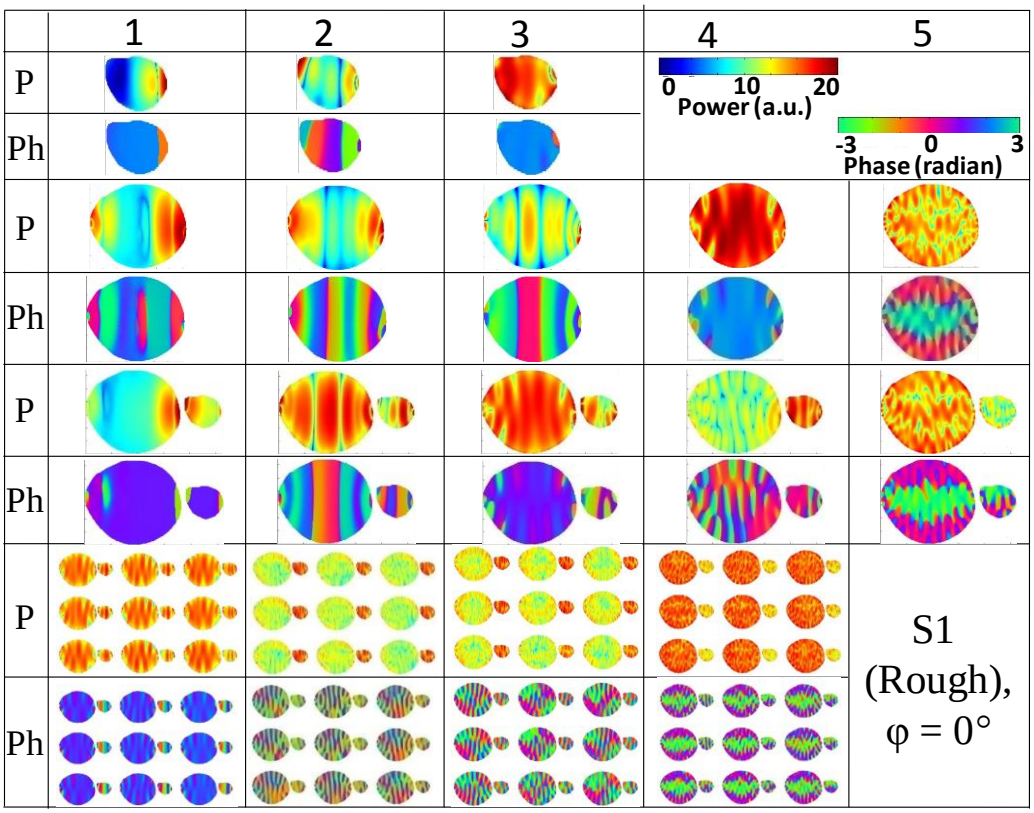

Fig. A1.2: The power and phase maps for different spin-wave modes of rough-edged nanodots, diatomic unit and diatomic array (S1) for H = 1 kOe applied at φ = 0° showing the evolution of the modes from individual nanodots to the array via a diatomic unit. The color maps for the power and phase distributions are as shown at the top. Sizes of the dots are not in scale.

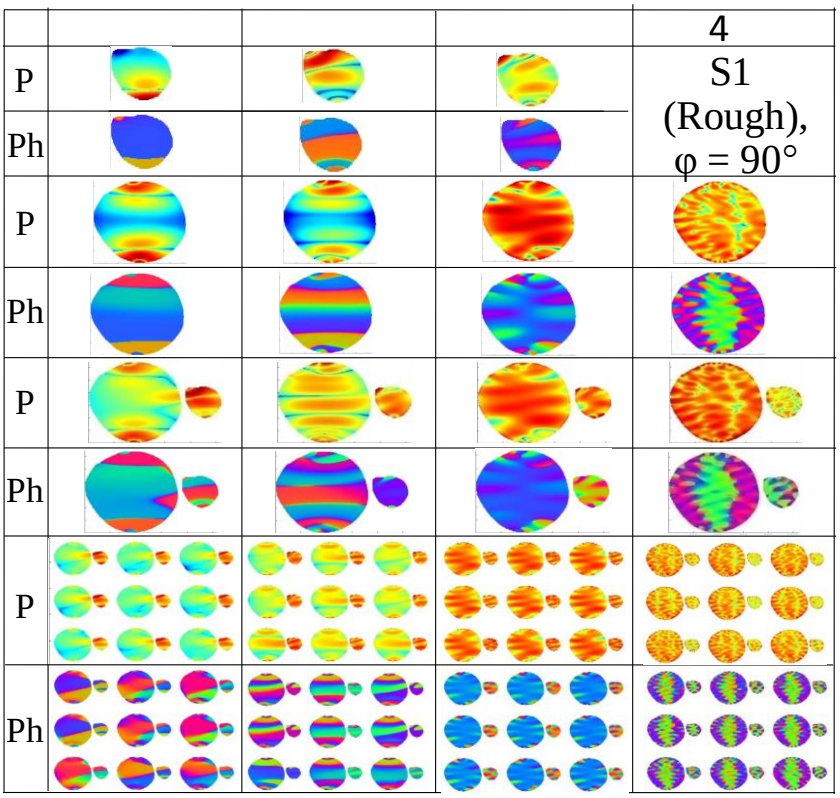

Fig. A1.3: The power and phase maps for different spin-wave modes of rough-edged nanodots, diatomic unit and diatomic array (S1) for H = 1 kOe applied at φ = 90° showing the evolution of the modes from individual nanodots to the array via a diatomic unit. The color maps for the power and phase distributions are as shown in figure S2. Sizes of the dots are not in scale.

Appendix II

Variation of Spin-Wave Dynamics with In-Plane Applied Magnetic Field Orientation for the Diatomic Nanodot Array

The role of dynamic magnetic coupling between the dots is discussed here by studying the frequency evolution as a function of in-plane orientation of the applied bias magnetic field in detail. This revealed the phenomena of mode hopping and four-fold anisotropy of the sample. We have analyzed the dependence of SWs at $q = 0$ wave vector with the variation of the in-plane angle φ (at an interval of 15°) of the applied magnetic field. The representative BLS spectra for three different in-plane angles are shown in Fig. A2.1 (a). The variation of different modes with φ, extracted from the experiment (circular symbols) and simulations (solid lines) is shown in Fig. A2.1 (b). The frequency of the 1st or the lowest frequency mode (indicated by red color) first decreases as φ increases from 0°, attains a minimum value at $\varphi = 45°$ and it again increases and attains a maximum at $\varphi = 90°$. This mode appears due to the unsaturated spins at the edges, which strongly depends on the edge roughness of the dots. Also, the orientation of the spins differs substantially for 0° and 90°. Consequently, the frequency of this mode is not same for $\varphi = 0°$ and 90° and it shows asymmetric nature with the variation of the in-plane angle of the magnetic field. Interestingly, the curvature is reversed for the 2nd mode (indicated by magenta color in Fig. A2.1 (b) which is the uniform mode as observed from the spatial profiles). The frequency of this mode first increases as φ increases from 0°, attains a maximum at $\varphi = 45°$ and it again decreases and attains a minimum at $\varphi = 90°$. Theoretical fitting of both of these modes with φ shows four-fold anisotropy. Although, the anisotropic variation of the 1st mode is greater than the 2nd mode. The 3rd mode (indicated by blue color in Fig. A2.1 (b)) shows a hopping nature. Its frequency is around 10.5 GHz (frequency blue shifted compared to the 2nd mode) for $\varphi < 30°$. For $\varphi > 30°$, it gets red shifted as compared to the 2nd mode and jumps to a frequency of around 8 GHz. The two higher frequency modes remain almost constant in frequency with the variation of φ, though a slight gradual downshift in frequency value for both the modes is observed with increasing φ.

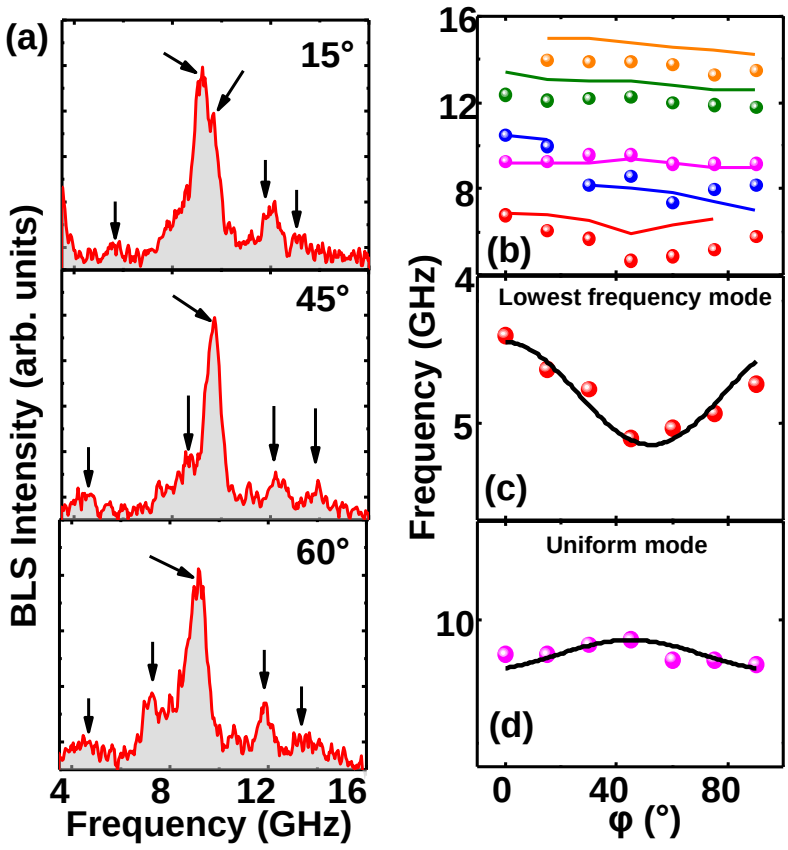

Fig. A2.1: (a) The Stokes side of BLS spectra taken at different values of the in-plane applied magnetic field. (b) The angular variation of different SW eigenmodes. (c) Magnified view of the lowest frequency mode showing the anisotropy. (d) Magnified view of the uniform mode showing the anisotropy.

Appendix III

Micromagnetic Simulations of the Triangular Shaped Ferromagnetic Antidot Arrays with Hexagonal Symmmetry by Applying Two-Dimensional Periodic Boundary Condition

The simulation results with application of two-dimensional periodic boundary condition (2D-PBC) shows almost similar results as compared to those without the application of 2D-PBC. The simulations with 2D-PBC have been performed on the arrays with the introduction of actual edge deformation to the triangular antidots. The FFT power spectra of the antidot array S1, for φ = 0°, 45° and 60° are shown in Fig. A3.1 and the corresponding power and phase profiles are shown in Figs. A3.2 (a) and (b) respectively. As compared to the spectra without the application of 2D-PBC, in this case also the spectra for φ = 0° and 60° are qualitatively similar in nature (though the mode frequencies are not same). In both cases we observe three modes and the number of modes increases to five for φ = 45°. However, the mode frequencies are slightly different as compared to the spectra without the application of 2D-PBC. For φ = 0°, mode 1 at 8.2 GHz has an extended character through the horizontal channels between the neighbouring antidot rows in the Damon-Eshbach (DE) geometry (i.e. extended in a direction orthogonal to the applied bias field). On the contrary, mode 2 at 10.2 GHz is a localized mode where highest spin-precession amplitude localiszd in the same horizontal channels with quantization number n = 3. Mode 3 at 11.5 GHz is again a quantized mode with higher quantization number (n = 5). Again, for φ = 60°, the spatial profile of the spin-wave spectra qualitatively matches with that of φ = 0°. Here, mode 1 at 7.5 GHz is a fully extended mode similar to that for φ = 0°, but the channel of propagation is different and it flows through the diagonally extended channel. Mode 2 at 10.2 GHz is localized in the same channel with n = 3, and mode 3 at 13.8 GHz is quantized mode with higher quantization number (n = 7). For φ = 45°, the lowest frequency mode is split into two modes (mode 1 at 8.1 GHz and mode 2 at 8.7 GHz). For these two modes, overlap between localized modes generates a pseudo-extended mode through the diagonally extended channel. The next mode is again split into modes 3 and 4 (at 9.8 GHz and 10.5 GHz respectively) and these two are localized modes (n = 3 for mode 3 and n = 5 for mode 5) along the same channel. Here, the highest frequency mode 5 at 12.2 GHz has a quantized nature with quantization number n = 7.

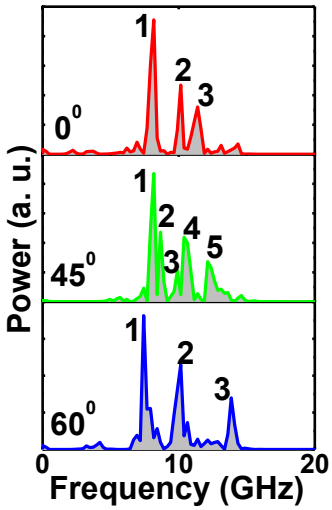

Fig. A3.1: FFT power spectra of the simulated time-domain magnetization of the antidot array S1 after the application of 2D-PBC for bias field applied along φ = 0°, 45° and 60°.

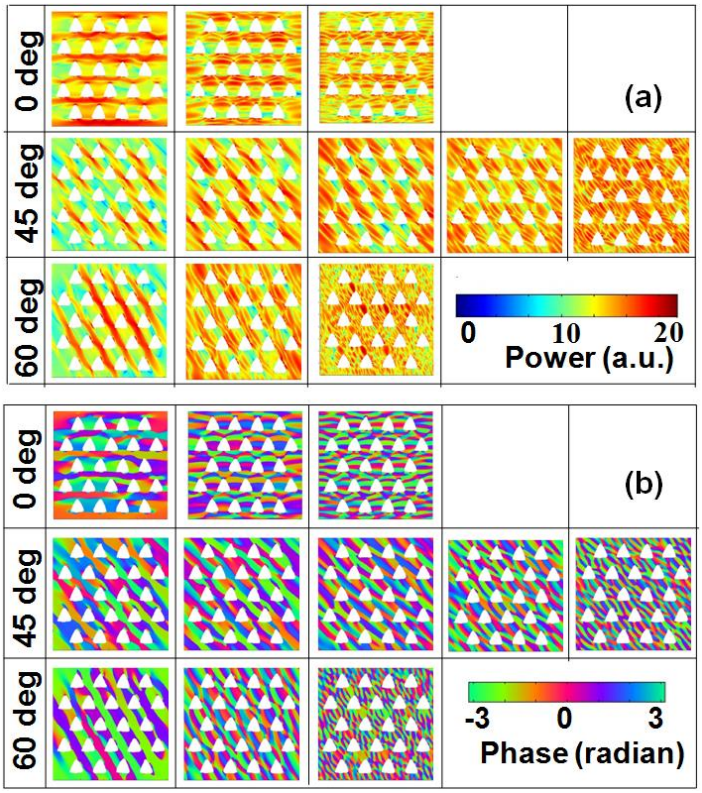

Fig. A3.2: SW mode profiles: (a) power and (b) phase of S1 after the application of 2D-PBC for bias field applied along φ = 0°, 45° and 60°. The color maps used for the mode profiles are shown inside the respective Fig.

Appendix IV

A4.1. Micromagnetic Simulations of the Triangular Shaped Ferromagnetic Antidot Arrays with Square and Octagonal Symmetry by Applying Two-Dimensional Periodic Boundary Condition

In order to verify the validity of the micromagnetic simulation results presented in the manuscript, we have performed further test simulations on the square and the octagonal lattice having a = 400 nm after application of two-dimensional periodic boundary condition (2D-PBC) while keeping all other simulation parameters unchanged. The test simulation results with 2D-PBC show nearly identical results to those performed considering large array without the application of 2D-PBC. The FFT power spectra of the simulated time-resolved magnetization (with 2D-PBC) of the square and the octagonal lattice having a = 400 nm taken at H = 1.0 kOe and φ = 0° are presented in Fig. A4.1 (a) and (b), respectively. Both the lattices show three modes namely *, Δ and #. For the square lattice, the lowest frequency mode * appears with highest power, whereas, for the octagonal lattice, the intermediate frequency mode Δ has the highest power. The reasons behind the observed features are discussed in the manuscript. The simulated power and phase profiles of the SW modes for the square and the octagonal lattice are shown in Fig. A4.1 (c) and (d), respectively. The mode profiles are also identical to those obtained without the application of 2D-PBC, as presented in the manuscript.

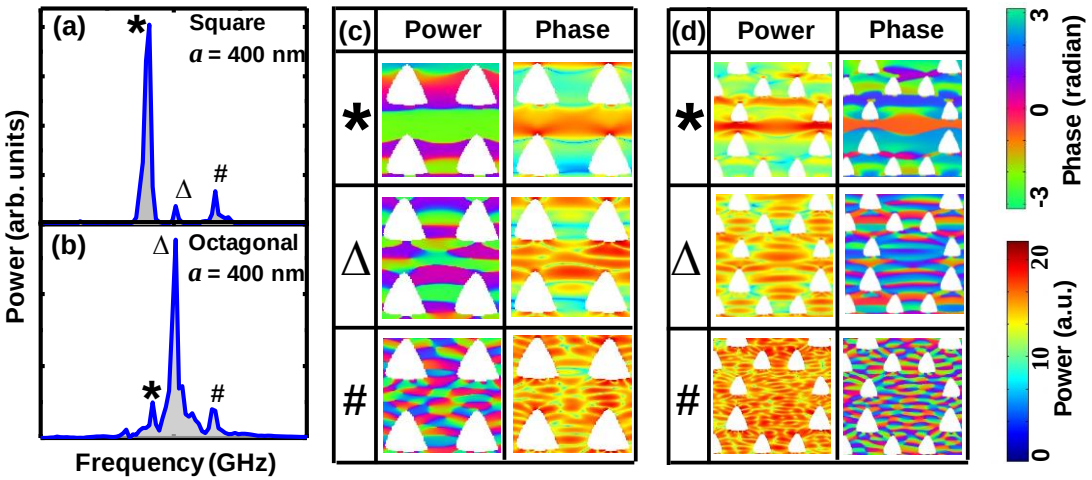

Fig. A4.1: FFT power spectra of the simulated time-resolved magnetization for (a) the square and (b) the octagonal lattice having a = 400 nm with 2D-PBC at H = 1.0 kOe and φ = 0°. The simulated power and phase profiles of the SW modes for (c) the square and (d) the octagonal lattice. The color bars are shown on the right-hand side of the figure.

A4.2. Bias Magnetic Field Dependence of the Spin-Wave Frequencies of the Triangular Shaped Ferromagnetic Antidot Arrays with Square and Octagonal Symmetry

Fig. A4.2 shows the bias magnetic field (H) dependence of the SW frequencies for the square and the octagonal lattice, respectively with a = 400 nm taken at φ = 0°. From Fig. A4.2 (a) we find that for the square lattice, the SW frequencies corresponding to the lowest frequency mode * is well fitted with the Kittel formula given by:

$$f = \frac{\gamma}{2\pi}\sqrt{(H + H_k)(H + H_k + 4\pi M_{eff})} \qquad (1)$$

where, γ is the gyromagnetic ratio, H is bias magnetic field and H_k is the anisotropy field. From the fit, we obtain the effective magnetization M_{eff} = 592 ± 17 emu/cm^3 and H_k = 0 for the * mode. The other modes, despite showing significant dispersion with the bias magnetic field, do not follow the Kittel formula. Fig. S2 (b) shows the Kittel fit to the bias field variation of mode * for the octagonal lattice, giving rise to M_{eff} = 635±14 emu/cm^3 and H_k = 0. The other modes for this lattice again do not follow the Kittel formula.

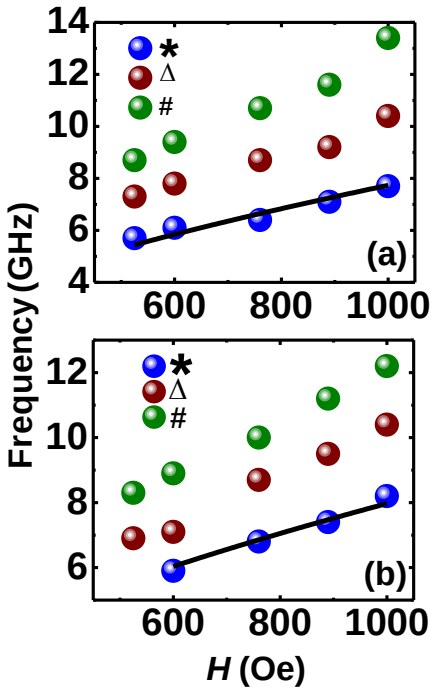

Fig. A4.2: Bias magnetic field (H) dependence of SW frequencies for (a) the square and (b) the octagonal lattice with a = 400 nm taken at φ = 0°. The symbols represent the experimental SW frequencies and the solid line represents the Kittel fit to the data points.

A4.3. Variation of Spin-Wave Spectra with the Azimuthal Angle of the Bias Magnetic Field of the Triangular Shaped Ferromagnetic Antidot Arrays with Square and Octagonal Symmetry

Fig. A4.3 shows the FFT power spectra of the background subtracted experimental time-resolved Kerr rotation data along with the simulated spectra for the square and the octagonal lattice with a = 400 nm taken at H = 1.0 kOe and different values of φ. From Fig. A4.3 (a), we observe that modes * and the Δ for the square lattice appear at almost all values of φ, although the power of these modes varies significantly with φ. However, mode # shows an interesting behavior. This mode exists only for specific angular ranges such as $0° \leq \varphi \leq 25°$ and $55° \leq \varphi \leq 90°$ and disappears in between. Furthermore, at some specific values φ, a new mode named ○ appears in the lower frequency regime.

We have further investigated the SW spectra for the octagonal lattice. Fig. A4.3 (b) reveals that modes * and Δ appear at all values of φ, while mode Δ is generally the highest power mode for the full angular range. The mode # appears only for specific values of φ in the higher frequency regime. Occasionally, another mode ○ appears in the lower frequency regime.

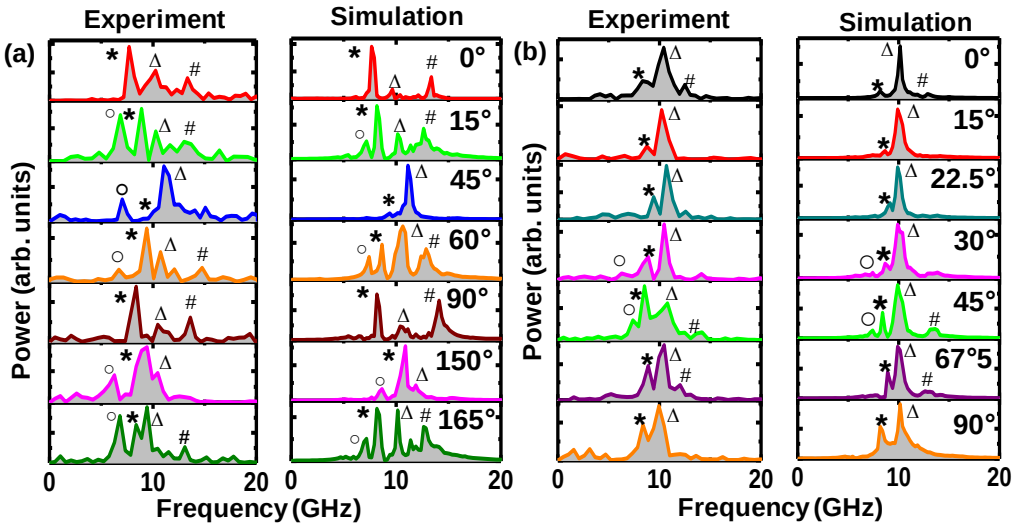

Fig. A4.3: The experimental (left panel) and simulated (right panel) FFT power spectra obtained for (a) the square and (b) the octagonal lattice taken at H = 1.0 kOe and different values of φ.

Appendix V

A5.1. Possible Nonmagnetic Contributions to Kerr Rotation of the Synthetic Antiferromagnets

Before analyzing the demagnetization curves, it is necessary to understand the possible contributions of the nonmagnetic and optical effects superposed with the true magnetic information. This is crucial particularly when the system is in highly excited state within hundreds of femtoseconds from zero delay. A precise method to estimate the true demagnetization from the magneto-optical Kerr signal is to measure the complex Kerr rotation, which contains both the Kerr rotation and ellipticity, followed by extracting the actual demagnetization time from there.

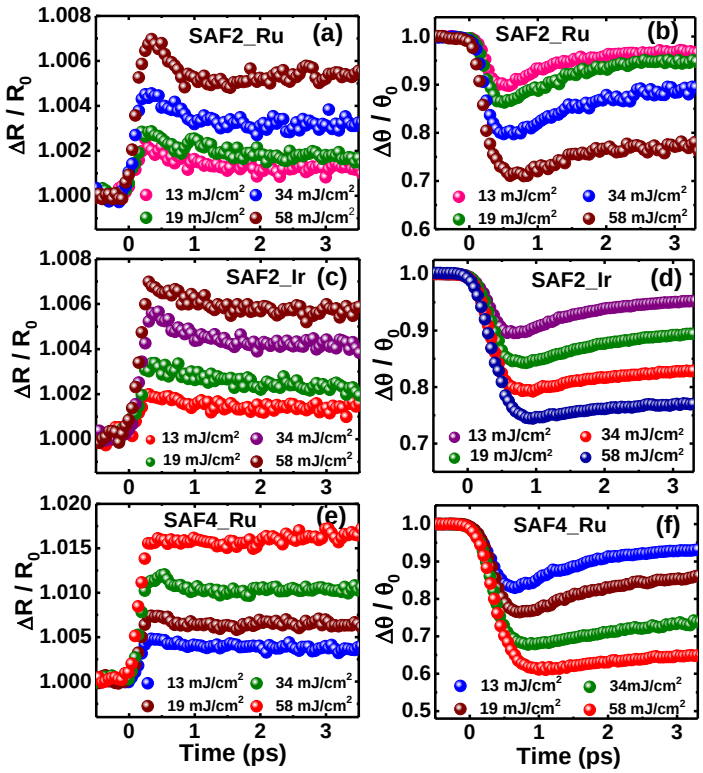

Fig. A5.1. Normalized variation of transient reflectivity and Kerr rotation in the F (F1) state of the three SAF samples at different pump fluences. The names of the samples are mentioned in the corresponding graphs.

However, the nonmagnetic contributions can be considered as negligible if the relative variation in transient reflectivity is much smaller than the relative variation in transient Kerr rotation. The transient variation of the reflectivity and Kerr rotation traces normalized by their values in the negative delay (i.e. in the saturation magnetic state) are shown in Fig. A5.1 (a) – (f). It is clear from the graphs that the relative variation in Kerr rotation is about one to two orders of magnitude larger than the relative

variation in reflectivity. This implies that the optical effects barely influence the Kerr rotation signal in our samples. Thus, we can conclude that the transient Kerr rotation signal is dominated by the genuine magnetic contribution.

A5.2. Fluence Dependent Ultrafast Demagnetization in SAF2_Ir and SAF4_Ru Samples

We have also investigated the effects of pump fluence on the demagnetization time (τ_M) in the SAF samples. The ultrafast demagnetization curves of the SAF2_Ir sample in the F and AF state for varying pump fluences from 13 to 58 mJ/cm^2 are presented in Fig. A5.2 (a) and (b), respectively. The variation of τ_M with pump fluence for the F and AF state is shown in Fig. A5.2 (c) and (d), respectively. For SAF2_Ir sample, τ_M is found to increase steadily with pump fluence from 218±3 fs to 266±5 fs in the F state, whereas, it increases slightly from 100±4 fs to 116±4 fs in the AF state. The ultrafast demagnetization curves of the SAF4_Ru sample in the F1 state and AF1 state for the said fluence range is presented in Fig. A5.3 (a) and (b), respectively, whereas the variation of τ_M is presented in Fig. A5.3 (c) and (d). For the SAF4_Ru sample τ_M increase from 245±4 fs to 290±5 fs in the F1 state and from 119±4 fs to 138±4 in the AF1 state in the said fluence range. The possible interpretation behind the observed variation with pump fluence is discussed in the article.

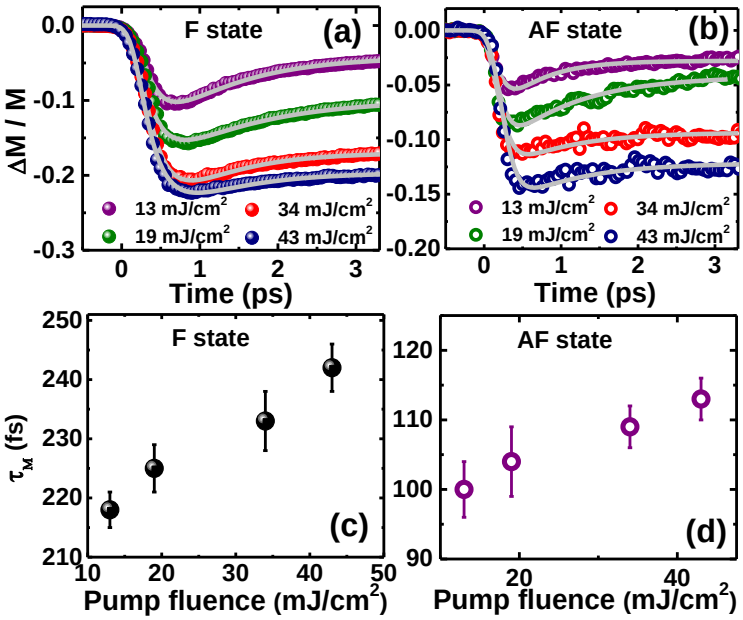

Fig. A5.2: Pump fluence dependent of ultrafast demagnetization traces of SAF2_Ir sample in (a) F state and (b) AF state. The symbols represent experimental data points and the solid lines are fitted curves. Pump fluences are mentioned in the Fig. The variation of τ_M as a function of pump fluence in the (c) F state and (d) AF state.

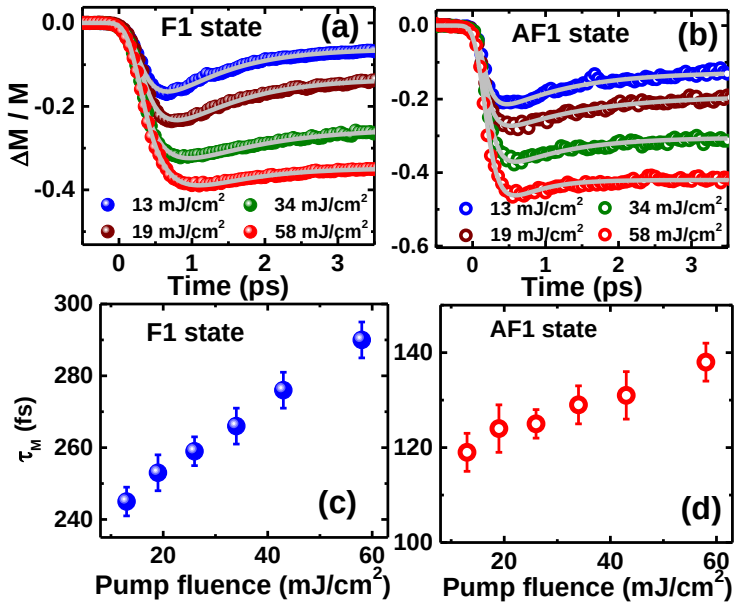

Fig. A5.3: Pump fluence dependent of ultrafast demagnetization traces of SAF4_Ru sample in (a) F 1 state and (b) AF1 state. The symbols represent experimental data points and the solid lines are fitted curves. Pump fluences are mentioned in the Fig. The variation of τ_M as a function of pump fluence in the (c) F1 state and (d) AF1 state.

Appendix VI

A6.1: Time-Resolved Reflectivity Data from Piezoelectric $LiNbO_3$ Substrate

The time-resolved reflectivity signal measured from the bare $LiNbO_3$ substrate is shown in Fig. A6.2 (a) and the corresponding FFT power spectrum is shown in Fig. A6.2 (b). The data measured from the bare substrate reveals no clear oscillation exhibiting only a noisy FFT power spectrum. This is presumably due to the fact that the laser heating and cooling effect sets up noisy strain-field oscillations in the substrate as captured in the reflectivity data.

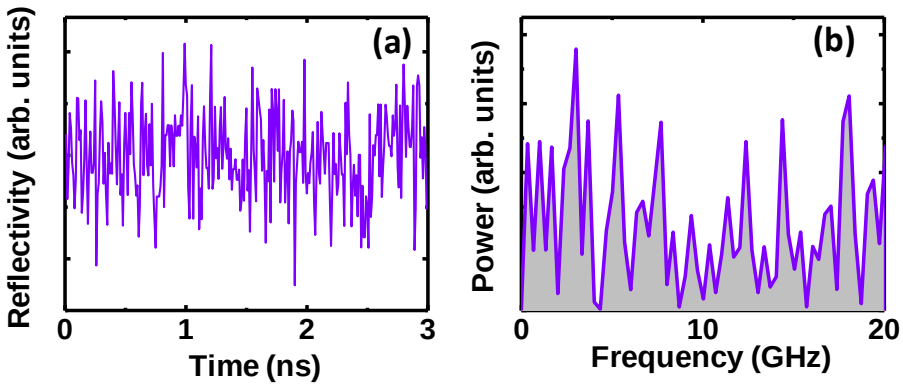

Fig. A6.1: (a) Experimental time-resolved reflectivity data taken from the substrate and (b) the corresponding FFT power spectrum.

A6.2. Micromagnetic Simulations of a Single Co Nanomagnet at Remanence

We have simulated the magnetization of a single nanomagnet with no dipole coupling with neighbors, to understand the modulation of the SW dynamics within an isolated nanomagnet distinct from that of the array where inter-magnet dipole coupling plays a significant role. Fig. A6.3 (a) reveals that the ground state spin configuration of the single nanomagnet at remanence forms an '*S*' state. The fast Fourier transformed (FFT) power spectra of the simulated time-domain magnetization for the single nanomagnet as shown in Fig. A6.3 (b) reveals four distinct SW modes at ~3.1 GHz (M1), ~4.1 GHz (M2), ~8.3 GHz (M3) and ~11.5 GHz (M4). Among them, the powers of modes M1 and M2 are much higher than those of the modes M3 and M4. The spatial profiles of the SW modes are shown in Fig. A6.3 (c). It is evident that the modes

M1 and M2 form standing wave patterns along the major axis of the ellipse, with quantization number n = 3. The mode M3 also forms a standing wave pattern in the same geometry with higher quantization number (n = 5). The highest frequency mode M4 forms a complex crisscross pattern with n = 7. It is noteworthy to mention that the spatial profiles of the SW modes are not symmetric. The axes of quantization of these modes are rotated due to the asymmetric '*S*' state spin configuration at remanence.

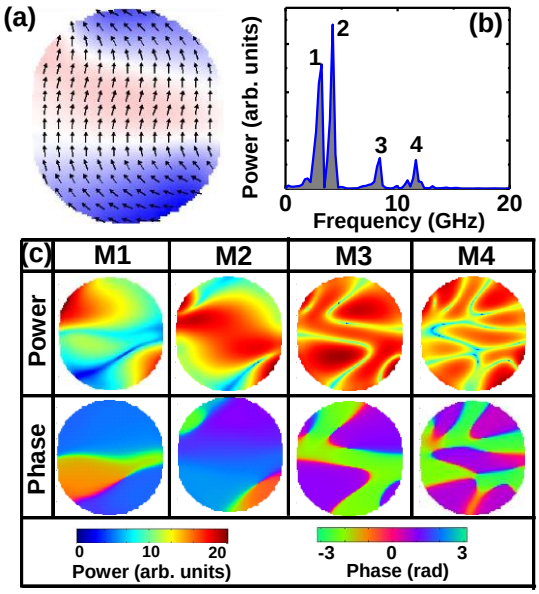

Fig. A6.2: (a) Simulated ground state spin configuration within an isolated nanomagnet, (b) the FFT power spectra of the simulated time domain magnetization of the isolated nanomagnet, and (c) the power and phase profiles of the SW modes of the single isolated nanomagnet at remanence. The color bars are shown at the bottom.

A6.4. Spatial Profiles of the Intrinsic Spin-Wave Modes of the Nanomagnet Array (M1, M2 and M4) After Application of Surface Acoustic Waves

The spatial profiles of the intrinsic SW modes (M1, M2 and M4) after application of SAW whose frequencies are in resonance with those of the modes are shown in Fig. A6.4. We have observed that the intrinsic SW modes whose frequencies are resonant with the SAW frequencies become more spatially uniform upon application of SAW. The modes M1 and M2 form standing wave patterns along the major axes with n = 3, and 4 respectively, whereas, the mode M4 has a complex characteristic with quantization occurring along both major (n = 6) and minor (m = 3) axis of the nanomagnet. The quantization numbers of M1 and M2 remain

unaffected upon application of the SAW. However, for M4, the quantization along the minor axis changes after the application of SAW, while remaining unaffected along the major axis.

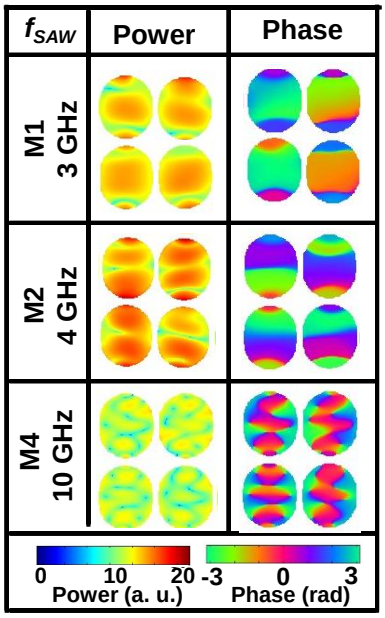

Fig. A6.3: The spatial profiles of the resonant SW modes at different values of f_{SAW}. The color bars are shown in the figure.